Numerical study of laminar and turbulent flames propagating in a fan-stirred vessel

Adrien Bonhomme

THÈSE

En vue de l'obtention du

DOCTORAT DE L'UNIVERSITÉ DE TOULOUSE

Délivré par :

Institut National Polytechnique de Toulouse (INP Toulouse)

Discipline ou spécialité :

Energétique et Transferts

Présentée et soutenue par :

M. ADRIEN BONHOMME

le vendredi 23 mai 2014

Titre :

NUMERICAL STUDY OF LAMINAR AND TURBULENT FLAME PROPAGATING IN A FAN-STIRRED VESSEL

Ecole doctorale :

Mécanique, Energétique, Génie civil, Procédés (MEGeP)

Unité de recherche :

Institut de Mécanique des Fluides de Toulouse (I.M.F.T.)

Directeur(s) de Thèse :

M. THIERRY POINSOT

M. LAURENT SELLE

Rapporteurs :

M. BRUNO RENOU, INSA ROUEN

M. DENIS VEYNANTE, ECOLE CENTRALE PARIS

Membre(s) du jury :

M. STÉPHANE MOREAU, UNIVERSITE DE SHERBROOKE QUEBEC, Président

M. CHRISTIAN ANGELBERGER, INSTITUT FRANCAIS DU PETROLE (IFP), Membre

M. FABIEN HALTER, UNIVERSITE D ORLEANS, Membre

M. LAURENT SELLE, INP TOULOUSE, Membre

M. THIERRY POINSOT, INP TOULOUSE, Membre

Abstract

Fossil energy is widely used since the 1900s to satisfy the global increasing energy demand. However, combustion is a process releasing pollutants such as CO_2 and NO_x. One of the major challenges of the 21^{th} century is to reduce these emissions and car manufacturers are involved in this race. To increase fuel efficiency of piston engines, some technical solutions are developed such as downsizing`. It consists in reducing the engine size while maintaining its performances using a turbocharger to increase the trapped mass in the combustion chamber. Unfortunately, downsizing can lead to abnormal combustions: intense cycle to cycle variations can appear, the fresh mixture can auto-ignite (ignition before spark-plug ignition) leading to knock or rumble. Large Eddy Simulation has proven to be a reliable tool to predict these abnormal combustions in real engines. However, such computations are performed using models to predict the flame propagation in the combustion chamber. Theses models are generally based on correlations derived in cases where turbulence is assumed to be homogeneous and isotropic. Defining theoretically or numerically such a turbulence is a simple task but experimentally it is more challenging. This thesis focuses on a apparatus used in most experimental systems: fans stirred vessel. The objective of this work is twofold:

- characterize the turbulence generated inside the vessel to check wether it is homogeneous and isotropic or not,
- finely characterize laminar and turbulent combustion in this setup in order to increase the knowledge in this field, and thereby improve models used.

First, a laminar flame propagation study has been conducted to address both confinement and curvature effects on the laminar flame speed in a spherical configuration. The main difficulty to perform the simulation of the whole configuration consists in finding a numerical method able to compute accurately the flow generated by one fan and able to handle six fans simultaneously too. Two numerical methodologies have been tested. First an Immersed Boundaries method was implemented. Despite good results obtained on academic test cases, this method was shown to be unadapted to compute accurately the flow generated by one fan. On the other hand, a numerical approach, coming from turbomachinery calculations and based on code coupling (called MISCOG), demonstrates its ability to do it and it is used to compute the flow generated by the six fans inside the closed vessel. Non-reacting flow is first analyzed and reveals a zone at the vessel center of around 6 cm of diameter where mean velocity is near zero and turbulence is almost homogeneous and isotropic. After that, the premixed fresh mixture is ignited depositing a hot gases kernel at the vessel center and the turbulent propagation phase is analyzed. In particular, it is shown that the amount of energy deposited at ignition is a critical parameter.

Keywords: fan-stirred vessel, premixed flames, immersed boundaries, code coupling, turbulence, ignition

Résumé

Les énergies fossiles sont largement utilisées depuis les années 1900 pour satisfaire l augmentation mondiale de la demande d énergie. Cependant, la combustion est un procédé qui libère des polluants comme le CO_2 et les NO_x. Un des principaux challenges du $21^{ème}$ siècle est de réduire ces émissions et les constructeurs automobiles sont impliqués dans cette course. Pour augmenter le rendement des moteurs à pistons, des solutions techniques, tels que le downsizing , sont développées. Cette technique consiste à réduire la cylindrée des moteurs tout en maintenant leurs performances grace à un turbocompresseur qui permet d augmenter la masse enfermée dans la chambre de combustion. Malheureusement, l augmentation de la pression dans les cylindres induite par le turbocompresseur est à l origine de combustions anormales: des variations cycles à cycles importantes apparaissent, les gaz frais peuvent s auto-allumer (allumage avant le claquage de la bougie) entrainant des phénomènes de cliquetis ou de rumble. La Simulation aux Grandes Echelles (SGE) a déjà prouvé qu elle était un outil fiable pour prédire ces combustions anormales. Cependant ces calculs reposent sur des modèles pour prédire la propagation de la flamme dans la chambre de combustion. Ces modèles sont généralement issus de corrélations réalisées dans des cas où la turbulence est supposée homogène et isotrope. Définir théoriquement ou numériquement une telle turbulence est relativement simple mais expérimentalement la tache est plus délicate. Cette thèse s intéresse à un dispositif classiquement utilisé: une enceinte fermée dans laquelle la turbulence est générée par des ventilateurs. L objectif de ce travail est donc double:

- caractériser la turbulence générée dans ce type d enceinte pour vérifier si elle est homogène et isotrope.
- caractériser finement la combustion, laminaire et turbulente, afin d enrichir les connaissances dans ce domaine et ainsi améliorer les modèles utilisés.

Une première étude sur la propagation des flammes laminaires a été menée. Elle présente les effets de l étirement et du confinement sur la vitesse de flamme laminaire. La principale difficulté pour la simulation de l enceinte complète consiste à trouver une méthode numérique permettant de reproduire précisément l écoulement généré par un ventilateur mais aussi d en gérer plusieurs simultanément. Deux méthodes ont alors été testées. Premièrement, une méthode type Frontières Immergées a été implémentée dans le code de calcul AVBP. Malgré les bons résultats obtenus sur des cas tests simples, cette méthode ne s est pas montrée adaptée pour reproduire précisément l écoulement généré par un seul ventilateur. Une autre approche, provenant du monde du calcul des turbomachines, et basée sur le couplage de codes (appelée MISCOG), a quant à elle démontré ses capacités à le faire et est donc utilisée pour calculer l écoulement généré par les six ventilateurs à l intérieur de l enceinte. L écoulement non réactif est d abord analysé: les résultats montrent qu il existe une zone d environ 6 cm de diamètre au centre de l enceinte dans laquelle la vitesse moyenne de l écoulement est proche de zéro et dans laquelle la turbulence est quasiment homogène et isotrope. Enfin, le pré-mélange de gaz frais est allumé en déposant un noyau de gaz chauds au centre de l enceinte et la phase de propagation turbulente est analysée. En particulier, il est montré que la température

des gaz brulés déposés au moment de l allumage est un paramètre critique.

Mots clés: enceinte agitée par ventilateurs, flammes de pré-mélange, frontières immergées, couplage de codes, turbulence, allumage

Acknowledgement

Le voilà enfin...le moment que tout thésard attend: l écriture des remerciements. Ils symbolisent la fin d une aventure, peut etre un peu folle, mais tellement passionnante et enrichissante. Un travail de thèse est très personnel mais pour y parvenir aussi faut-il savoir s entourer. Je vais donc essayer de remercier tous ceux qui ont participé, de près comme de loin, à ce projet car leur aide a été précieuse.

Tout d abord, je tiens à adresser mes sincères remerciements à mes encadrants Thierry Poinsot et Laurent Selle. Au cours de ces trois années de recherche, j ai pu apprécier vos compétences scientifiques et votre rigueur dans le suivi de mes travaux mais aussi la sympathie qui vous caractérise. Vous avez su me guider tout en me laissant la liberté nécessaire pour mes initiatives. Ces années à vos cotés m ont permis de grandir et je vous en suis très reconnaissant. Encore Merci à vous!

Je remercie tous les membres de mon jury pour l intéret qu ils ont porté à mon travail de recherche. Je suis en particulier reconnaissant aux rapporteurs de ma thèse Bruno Renou et Denis Veynante pour leurs lectures attentives de mon manuscrit et leurs rapports qui m ont permis de prendre un meilleur recul sur ma thèse. Je remercie de plus Christian Angelberger, Fabien Halter et Stéphane Moreau (qui a fait le déplacement depuis le Canada pour cette occasion) pour avoir accepté d etre examinateurs. Je garderai un excellent souvenir de ma soutenance.

J ai réalisé cette thèse à l IMFT dans l équipe PSC. C est toujours avec plaisir que j allais travailler car je savais que j allais y retrouver des personnes de qualité, que ce soit pour parler de science mais aussi de tout le reste! Je remercie tous ceux qui sont à l origine de la bonne ambiance qui régnait dans cette équipe :

- Nicolas G. (merci de m avoir pris sous ton aile à mes débuts à l IMFT lors de mon stage),
- les anciens d jeuns Aurélien, Marion L., Florian, Guillaume M., Nicolas N., J-F, Marion P. pour toutes les discussions autour de la table le midi,
- la fine équipe de thésards : Adrien J. (numéro #2 ou Jeannot, ne change rien), Guillaume L., (à quand la prochaine virée à Candie?), François, Zhiad, Maxence, Marie-Charlotte (une partie de coinche pour décompresser un peu? ou une virée au ski?) , Tom, Emilien (dit Coco, c était vraiment cool de bosser avec toi, j espère que l on pourra remettre ça un jour), Adama & Blaise (ces deux là on ne peut dire qu ils ne branlent rien), Lucas, Solene.....je vous souhaite à tous beaucoup de réussite pour la suite!
- et mes collègues de bureau : le premier, Djé (tu as vraiment été un moteur pour mon début de thèse), puis Romain (vive le moteur pop-pop, la YBR, le dériveur, le ski, les vide-greniers...), et enfin Dani (qu est ce que tu as pu nous faire rire avec toutes tes histoires improbables...et ton BMX) et Anna.
- Merci aussi à tous les permanents du groupe pour leur accueil, en particulier Enrica

(je garderai un super souvenir de notre atelier pate à pizza et des nos discussions sur la turbulence) et Oliver pour ton initiation (périlleuse) au ski de rando , les sorties VTT (sans portage c est pas une vraie sortie) et notre belle 5^{eme} place au Raid ABS.

Bien sur, je souhaite remercier tous ceux sans qui le laboratoire ne fonctionnerait pas si bien: Florence, Céline, Muriel, André, le service informatique, le service COSINUS et bien d autres encore.

L utilisation et le développement dans le code AVBP m a permis de collaborer avec l équipe CFD du CERFACS. Je souhaite remercier en particulier Antoine Dauptain, Olivier Vermorel, Florent Duchaine et Gabriel Staffelbach pour l aide scientifique et technique qu ils m ont apporté. Merci aussi à toute l équipe de thésards pour votre accueil lors de mes journées passées au CERFACS.

Mes remerciements s adressent aussi à tous mes amis extérieurs à l IMF avec qui je suis sur, ou presque, de ne pas parler de méthodes numériques et de modèles de sous-maille: Audrey, Thibaut, Laura, Julien, Aurelia, Vincent, Catherine, Sébastien, Amandine, Eloi, Marine, Jeremy, Alex, Alice, Marion, Anaïs, Cédric, Aurélie, Arnaud .... J ai aussi une pensée à tous les coursiers du Balma Vélo Sprint : c est un vrai plaisir de partager une sortie en peloton avec vous sur les routes du Lauragais.

Pour terminer, mes remerciements les plus chers s adressent à ma famille : notamment mes parents pour m avoir toujours encouragé et soutenu tout au long de mes études, et Carole, qui a accepté de devenir ma femme. Tu as été mon rayon de soleil quotidien, je ne t en remercierai jamais assez. Et notre fils Louis, né le 17 février 2014, que je félicite d avoir assisté sagement à ma soutenance. L avenir nous réserve plein de belles choses, j en suis sur! Je vous dédie tout particulièrement ce travail.

CONTENTS

NOMENCLATURE

Roman characters

Symbol	Definition
$\Delta h^0_{f\,k}$ [J/kg]	mass enthalpy of formation of species k at $T = T_0$, *p.14*
$F_{p\,i}$ [N.m^{-3}]	i-component of the source term added in the momentum equation for IBM, *p.73*
Q_p [kg.m^{-1}.m^{-3}]	source term added in the energy equation for IBM, *p.73*
λ [W.K^{-1}.m^{-1}]	heat conduction coefficient, *p.19*
$\vec{d_f}$ [-]	fan direction-vector, *p.42*
B_0 [-]	bomb center, *p.43*
C_D [-]	drag coefficient, *p.89*
C_L [-]	lift coefficient, *p.89*
D_k [m^2.s^{-1}]	molecular diffusion coefficient of species k in the mixture, *p.55*
D_{th} [m^2.s^{-1}]	thermal diffusion coefficient, *p.55*
F [-]	thickening factor, *p.33*
f_i^n [kg.m.s^{-2}]	i-component of the forcing term (before projection on the grid nodes), *p.75*
$J_{i\,k}$ [kg.m^{-2}s^{-1}]	i-component of the diffusive flux of species k, *p.14*
$L_{\tau\,exp}$ [m]	experimental integral length scale at the bomb center, *p.118*
Le_k [-]	Lewis number of species k, *p.19*

M [-]	normalized parameter of the proportional controller, *p.76*
M_p [kg]	mass of product p, *p.54*
N [-]	normalized parameter of the integral controller, *p.76*
N_c^b [-]	number of cores allocated to the bomb instance, *p.121*
N_c^f [s]	number of cores allocated to the fan instances, *p.121*
N_{fan} $[tr.mn^{-1}]$	fan rotation speed, *p.42*
P [Pa]	static pressure, *p.14*
R $[m]$	flame radius, *p.50*
R_0 [m]	radius of the experimental vessel, *p.42*
R_f [m]	flame radius based on the mass of fuel, *p.55*
R_p [m]	flame radius based on the mass of product p, *p.54*
R_c [-]	ratio of the number of cores allocated to the bomb instance to the number of cores allocated to the fan instances, *p.121*
s_c [m.s^{-1}]	consumption flame speed, *p.53*
s_c^f [m.s^{-1}]	flame speed based on fuel conservation, *p.55*
$s_c^{p\ expe}$ [m.s^{-1}]	classical` flame speed used experimentally. Based on conservation of burnt gases and constant densities assumption, *p.54*
s_c^p [m.s^{-1}]	flame speed based on conservation of burnt gases, *p.54*
s_L [m.s^{-1}]	laminar flame speed, *p.51*
s_L^0 $[m.s^{-1}]$	unstretched laminar flame speed, *p.50*
S_{ij} $[J/m^3]$	deformation tensor, *p.14*
Sc_k [-]	Schmidt number of species k, *p.19*
St [-]	Strouhal number, *p.89*
T_c [s]	computational time, *p.120*
T_c^b [s]	bomb standalone computational time, *p.120*
T_c^f [s]	fan standalone computational time, *p.120*
T_e [s]	exchanging time, *p.120*

T_w [s]	waiting time, *p.120*
T_{it}^b [s]	time needed by the bomb to compute one iteration, *p.120*
T_{it}^f [s]	time needed by each fan to compute one iteration, *p.120*
u_i [m.s^{-1}]	i-component of the velocity, *p.14*
$u_{rms\ exp}$ [m.s^{-1}]	experimental velocity fluctuations at the bomb center, *p.118*
V_i^c [m/s]	i-component of the correction velocity, *p.14*
V_m [m^3]	fictitious volume surrounding each grid node, *p.75*
X_k [-]	mass fraction of species k, *p.14*
y^+ [-]	non-dimensional wall distance, *p.110*
Y_k [-]	mass fraction of species k, *p.14*

Greek characters

Symbol	**Definition**
α [kg.s^{-1}]	parameter of the proportional controller, *p.75*
β [kg.s^{-2}]	parameter of the integral controller, *p.75*
$\mathcal{L}$ [m]	Markstein length, *p.51*
δ_l^0 [m]	thermal flame thickness, *p.55*
$_k$ [$kg.m^{-3}s^{-1}$]	reaction rate of species k, *p.14*
$_T$ [W/m^3]	heat release due to combustion, *p.14*
η_{exp} [m]	experimental Kolmogorov length scale at the bomb center, *p.118*
κ [s^{-1}]	stretch, *p.51*
Φ [-]	equivalence ratio, *p.55*
τ [s]	experimental integral time scale at the bomb center, *p.118*
τ_I [s^{-1}]	response time of the integral controller, *p.76*
τ_P [s^{-1}]	response time of the proportional controller, *p.76*
τ_{ij} [J/m^3]	viscous tensor, *p.14*

Ξ [-]	efficiency function, *p.34*

Short names

Symbol	**Definition**
ALE	Arbitrary Lagrangian Eulerian, *p.70*
BC	Body Conformal, *p.70*
BL	Bomb Limited case, *p.120*
BOMB	configuration to mimic a flame propagating in a closed vessel, *p.52*
DNS	Direct Numerical Simulations, *p.16*
FL	Fan Limited case, *p.120*
IBM	Immersed Boundaries Method, *p.70*
INF	configuration to mimic a flame propagating in an infinite medium, *p.52*
LES	Large Eddy Simulations, *p.16*
MISCOG	Multi Instances Solver Coupled on Overlapping Grids, *p.106*
PIV	Particle Image Velocimetry, *p.43*
RANS	Reynolds Average Navier-Sokes, *p.16*

INTRODUCTION

The number of combustion systems used in power generation and transportation industries is growing rapidly. Today, combustion of fossil and biofuels provides more than 90% of the world s energy [1]. However, burning these fuels causes very dramatical environmental problems in our society. It is known that anthropological activities are the leading cause of air pollution and global warming. Despite the global energy consumption increase, pollutant emissions and greenhouse gases must be controlled that is why players in the energy sector must produce energy with systems as efficient as possible. It is clear that an improvement of the performance - even of a few percent - of devices using combustion leads to huge decrease of pollutant emissions.

Transport industry is involved in this challenge and especially the road transport. Indeed, the worldwide passenger car production increase linearly since 1945, end of the second world war, to reach more than 80 millions of units today (see Fig. 1). In Europe the production reaches near 15 millions cars even tough it was affected by the 1993 and 2009 crisis. According to the European Environment Agency, 93% of greenhouse gas emissions from transport came from road transport in 2004. To face this environmental issue, European standards in term of pollutant emissions (see Tab. 1) were setup in 1992 to make car manufacturers do more and more efficient engines. In addition, the French government implemented in 2010 a bonus/penalty system on CO_2 emissions: one the one hand, if the car does not reach the objective clients have to pay a fee; on the other hand, if the car emits few pollutants clients receive a financial aid. Moreover the fuel price has still increased since 1990 (see Fig. 2) which encourages consumers to buy the most fuel-efficient car possible. Regarding all reasons described before, car manufacturers have to develop new solutions to make piston engines as efficient as possible to remain competitive: at the beginning of september 2013, the French president François Hollande presented the national industrial priorities. These priorities are organized in 34 recovery plans. The second of these 34 plans - highlighting its importance - consists in developing a car consuming less than 2 liters of fuel per 100 km. This challenge can be handled only if new technological breakthroughs are found.

Internal combustion piston engines can be classified into two categories: spark-ignition (SI) engines (typically gasoline engines) where ignition is controlled by a spark from a

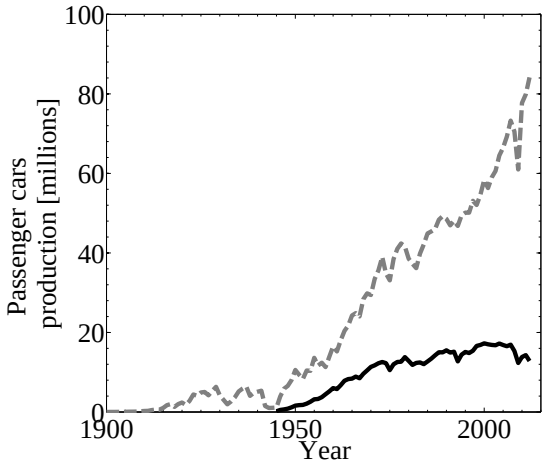

Figure 1: European (——) and worldwide (- - - -) passenger cars production in millions of units.

European Standard		**Euro 1**	**Euro 2**	**Euro 3**	**Euro 4**	**Euro 5**	**Euro 6**
Year		1992	1996	2000	2005	2009	2014
Nitrogen Oxides (NO_x)	Diesel	-	-	500	250	180	80
	Gasoline	-	-	150	80	60	60
Carbon monoxide (CO)	Diesel	2720	1000	640	500	500	500
	Gasoline	2720	2200	2200	1000	1000	1000
Hydrocarbures (HC)	Diesel	-	-	-	-	-	-
	Gasoline	-	-	200	100	100	100
Particles	Diesel	140	80	50	25	5	5
	Gasoline	-	-	-	-	5	5
$HC + NO_x$	Diesel	970	700	560	300	230	170
$HCNM$	Gasoline	-	-	-	-	68	68

Table 1: European standards in terms of pollutant emission in mg/km when driving the New European Driving Cycle (NEDC) source : http://www2.ademe.fr

spark plug and compression-ignition (CI) engines (typically diesel engines) where pressure and temperature conditions inside the combustion chamber leads to auto-ignition. In France, diesel engines represent about 70% of the automotive fleet. But the Euro 6 standard enforces a drastic reduction (50 %) for diesel engines in term of nitrogen oxides NO_x emissions. Moreover, the recent controversy on particles produced by diesel engines have been classed by the World Health Organization in 2012 as one of most carcinogen substances. For the reasons mentioned above, this trend is changing and new development for gasoline engines are encouraging this reversal. This thesis focuses only on gasoline engines.

The operating principle of spark-ignition engines is described in the next paragraph.

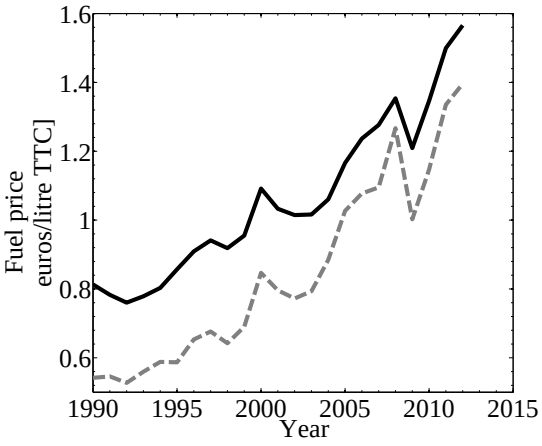

Figure 2: Evolution of fuel prices: Unleaded-Petrol (——) and diesel (- - - -) source: www.developpement-durable.gouv.fr

The spark-ignition (SI) engine

Basically, the SI engine transforms chemical energy into mechanical energy according to combustion process. Most of SI engines are based on a four-stroke cycle describes below (see Fig. 3):

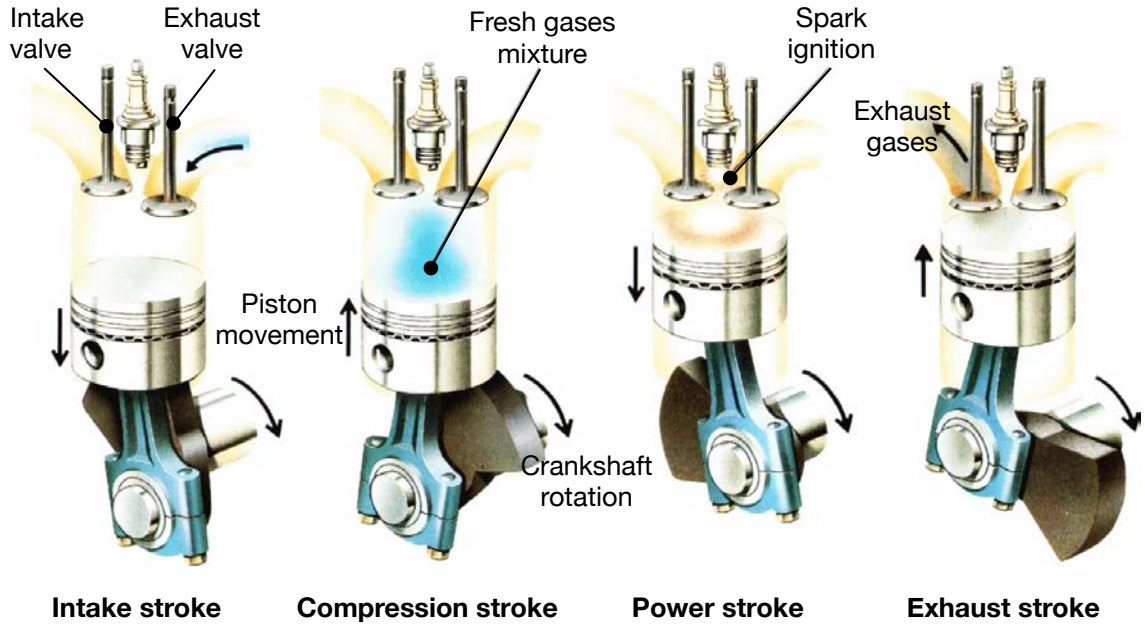

Figure 3: Four-stroke cycle of a spark-ignition engine.

1. Intake Stroke. During this stroke the piston moves downward forcing the air into combustion chamber through the intake valve. The exhaust valve remains closed

in this stroke.

2. Compression Stroke. The piston moves upward and intake and exhaust valve remain closed so that the fresh gases mixture is compressed. Just a little before the end of the compression stroke, the mixture is ignited by a spark produced by the spark plug.
3. Power Stroke. The air-fuel mixture which burns at the end of compression stroke expands due to heat of combustion. Under this impulse the piston moves downward thus doing useful work. Intake and exhaust valves remain closed during this stroke.
4. Exhaust Stroke. During this stroke the intake valve remains closed while the exhaust valve opens. The greater part of burnt gases escape because of their own expansion. The upward movement of piston pushes the remaining gases out of the open exhaust valve.

In the early development of gasoline engines, engines work at atmospheric pressure and a stoichiometric premixed mixture was generated using a carburetor and introduced in the combustion chamber. In the last twenty years, new strategies and technical solutions were developed to improve the efficiency of these engines and are described below:

Direct injection and stratified combustion: Nowadays, stratified combustion using direct fuel injection are commonly used in gasoline engines instead of injecting fuel in the intake pipe (see Fig. 4). Thanks to direct injection, the gasoline engine can work

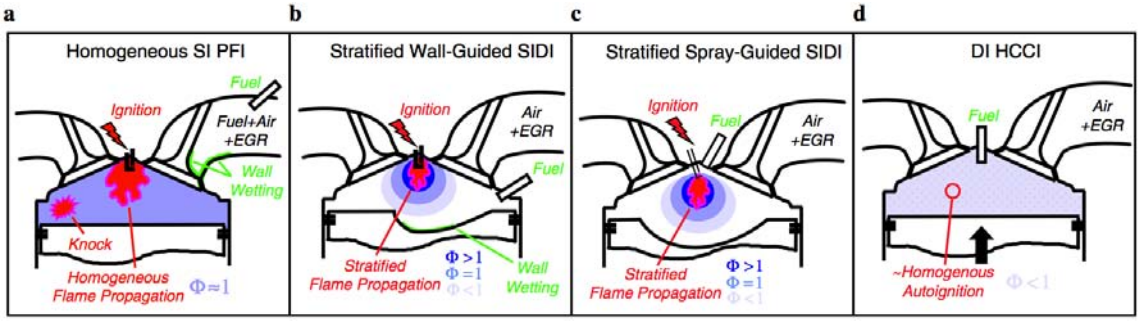

Figure 4: Gasoline engine types classified by fuel-injector location, ignition mode, and combustion mode. (a) Port-fuel-injection. (b) Wall-guided spark-ignition direct-injection. (c) Spray-guided spark-ignition direct-injection. (d) Homogeneous-charge compression-ignition [2].

with a global equivalence ratio lower than the unity: the flame propagates in a stoichiometric zone near the spark-plug while a very lean mixture takes place in the rest of the combustion chamber.

Controlled auto-ignition: Auto-ignition is used for diesel engine but this ignition mode can be used for gasoline engines. Homogeneous-charge compression-ignition (HCCI), see Fig. 4, is now used because this technology can achieve up to 15% fuel savings and generate lower peak temperature leading to lower pollutant emissions.

Downsizing: From the point of view of CO_2, gasoline engines suffer from an handicap in comparison to diesel engines due to a lower efficiency. Size reduction of gasoline engines appears to be a promising way to improve engines efficiency [3]. For gasoline engines, the power depends on the mass of fresh gases to burn. In order to balance the reduction of the size of the engine, a turbocharger is added to increase the mass of fresh gases in the combustion chamber and thus maintain the engine power. However, the pressure increase in the combustion chamber can lead to abnormal combustions such as important cycle-to-cycle variations and auto-ignition leading to knock or rumble.

Objectives and motivations of this work

This work is part of a project funded by the French National Agency denoted ICAM-DAC[1] involving the IFP Énergies Nouvelles, the laboratory PRISME at Orléans, CERFACS, PSA Peugeot Citroën, Renault and the Institut de Mécanique des Fluides de Toulouse (IMFT) in order to study instabilities and abnormal combustions in downsized gasoline piston engines. In this project, the objective at IMFT is to use DNS and high resolution LES to study the ignition and propagation phase of laminar and turbulent premixed flames which is one of the key-point in CFD codes and especially in piston engine computations. As previously shown by L. Thobois [4], B. Enaux [5] and V. Granet [6], one of the critical phase in gasoline engines, in terms of abnormal combustions, is the ignition and flame propagation in the combustion chamber (power stroke in Fig. 3)

Turbulence has been studied for decades in its most canonical form: homogeneous isotropic turbulence (HIT) [7, 8, 9, 10, 11, 12, 13]. This limit case is the cornerstone of multiple theoretical approaches as well as the building brick of Large Eddy Simulation (LES) models where the Kolmogorov cascade assumption allows to model the effects of small scales from information available for the resolved ones [14, 15]. HIT is also the only generic case where the interaction of other phenomena with turbulence can be defined using a limited number of parameters: evolution of large droplets in HIT [16, 17, 18], interaction of evaporating droplets with HIT [19], flame / turbulence interaction [20, 21, 22].

While defining HIT theoretically or numerically is a reasonably simple and clear task, creating HIT experimentally is more challenging. This thesis focuses first on one classical technique used to generate HIT: fan-stirred closed vessels. Sometimes these apparatus are called `bombs , a denomination that will be used in this report. Stirring vessels with fans to study turbulent flame propagation has been used for more than a century (see Laffitte s book [23]). A classical paper where this turbulence was qualified as HIT is due to Semenov [24] who showed that properly designed bombs with multiple fans were able to generate reasonable HIT in a zone located near the center of the chamber where the mean flow is almost zero and turbulence is homogeneous and isotropic. A significant amount of work has been based on correlations obtained in such bombs. The most famous example is probably the quest for `turbulent flame speed correlations in which the speed s_T of premixed turbulent flames is expressed as a function of the initial turbulent velocity u'.

[1] from the original French name: Instabilités et Combustions Anormales dans les Moteurs Downsizés à Allumage Commandé.

Such correlations continue to be frequently published [25, 26, 27, 28, 29] and interestingly, few of them agree. One reason for this may be that the notion of a generic turbulent flame speed depending only on a limited number of flow and flame parameters may not be relevant [20]. Another one could be that the initial turbulence in such bombs is not really close to HIT and that more parameters should be taken into account. Therefore, since most models are based on measurements performed in bombs, an interesting question is to study whether the flow created in a fan-stirred bomb really mimics HIT and over which spatial extent. This question has been investigated experimentally [24, 30, 31] but using CFD would be a useful addition.

Even though the largest CFD simulations to date have been published for HIT with meshes up to 64 billions points [32], all of them were performed in simple cubic meshes, initialized with a flow which has all the properties of theoretical HIT. None of these simulations address the question of how HIT is created (if it is) in a real fan-stirred bomb. This question is much more complicated and existing experimental diagnostics are not always sufficient to guaranty that the flow in this situation matches all properties of theoretical HIT: in a bomb, fans obviously induce a strong mean, pulsated flow. In the center of the vessel, the mean flow is expected to be zero and turbulence assumed to diffuse to a central zone where HIT is expected. This involves a series of questions which are rarely addressed:

- By which mechanisms does turbulence transfer from the fan region to the central zone?
- Since the number of fans is usually limited, are there preferential straining axes in the bomb which could affect isotropy near its center?
- The fans flow being by nature unsteady, is turbulence at the center of the apparatus sensitive to the pulsating nature of the flow created by the blades rotation?
- How large is the zone where HIT is obtained?

The two main objectives of this work, in order to answer issues presented above, are the following:

- to compute the full geometry of the fan-stirred vessel experiment conducted in the PRISME laboratory in Orléans, including the fans geometry, using high-resolution LES to check whether turbulence is homogeneous and isotropic or not. This simulation is used to complement experimental diagnostics.
- finely characterize laminar and turbulent combustion in this setup in order to increase the knowledge in this field, and thereby improve models used.

Here again, instead of producing extensive sets of results for various fuels, pressure and temperature this work focuses on methodologies and questions the accuracies of the methods used in these vessels. For example, the methods used to extract flame speeds from measurements of spherical flame radii versus time will be specifically discussed. Similarly, we will discuss initialization methods used to create the first flame kernels in DNS and LES and show that this part, which is often viewed as a secondary element of the simulation, actually plays an important role.

Outline of the manuscript

This manuscript is divided into seven chapters. These chapters are briefly described below and Fig. 5 presents a graphic overview of the actions performed to achieve the project:

1. Chapter 1 gives a general introduction to Computational Fluid Dynamics, presents the concept and the governing equations for Large Eddy Simulations of turbulent reactive flows. This chapter describes models used in fluid mechanics codes and thereby in the AVBP code. In particular, turbulent combustion modeling and mesh movement are briefly described.
2. Chapter 2 presents the Orléans bomb configuration conducted in the PRISME laboratory. The geometry of the experiment is presented before describing the operating procedure. This apparatus is a spherical closed vessel where turbulent or laminar premixed flames propagates. This setup is the target numerical configuration.
3. Chapter 3 discusses methods used to obtain laminar flame speeds in spherical laminar premixed flames. Most recent studies express the laminar flame consumption speed as $\rho_b/\rho_u dR/dt$, where R is the flame radius and ρ_b/ρ_u is the ratio of the burnt to the fresh gas density (ρ_b is evaluated at chemical equilibrium and supposed to be constant). This chapter investigates the validity of this assumption by reconsidering it in a more general framework. Other formulae (first proposed by Bradley and Mitcheson in 1976) are derived and tested on a DNS of cylindrical flames.
4. In order to compute the flow inside the closed vessel stirred by six fans, a numerical method able to deal with rotating parts must be setup. First an Immersed Boundaries Method (IBM) was implemented in the AVBP code and is presented in Chapter 4. The formalism implemented in the code is described. Several academic test-cases of increasing complexity were successfully performed and are presented in this chapter. Finally, the IBM is tested on a configuration with one isolated fan. It is shown that the IBM implemented is not able to compute this flow which shows that this method can not be used to compute the full geometry (vessel with the six fans).
5. Since IBM can not be used to compute the flow generated by one fan, another technique coming from the framework of turbomachinery calculations is presented in Chapter 5. The method is based on running multiple instances of the same solver, working on different subdomains and communicating through small overlapping zones where interpolations allow to handle moving meshes. First the accuracy of this Multi Instances Solver Coupled on Overlapping Grids (MISCOG) approach is evaluated for the convection of a single vortex. Then the configuration with one isolated fan is computed. Results show a reasonable agreement between numerical simulations and experimental data (in terms of mean and fluctuating velocities) which confirms that the MISCOG approach can be used to compute the full geometry.
6. In Chapter 6, the MISCOG approach is applied to the LES of the six fan-stirred

configuration: then non-reacting flow inside the closed vessel is computed. Mean and fluctuating velocity fields obtained by LES are compared to experimental data. The structure of the turbulence generated at the center of the vessel is studied and the mechanisms allowing turbulence to travel from fans to the center of the vessel are analyzed. The parallel efficiency of MISCOG is discussed in this chapter too.

7. Chapter 7 presents well resolved LES of the flame propagation and compares turbulent and laminar flame propagation in the closed vessel. The turbulent flame propagates in the turbulence generated by fans computed in Chapter 6. The influence of the velocity field and the temperature in the burnt gases kernel imposed at the ignition time is studied.

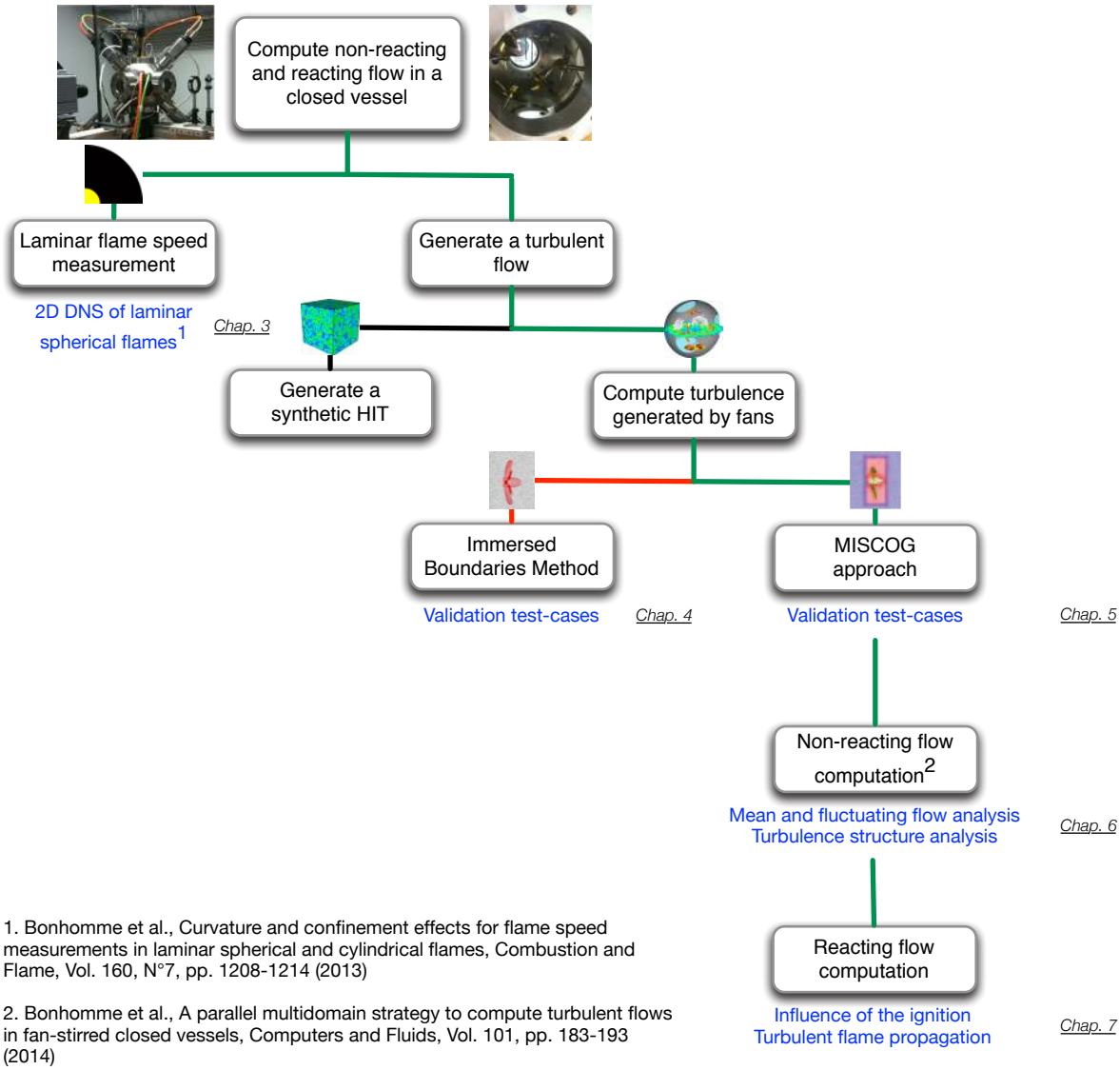

1. Bonhomme et al., Curvature and confinement effects for flame speed measurements in laminar spherical and cylindrical flames, Combustion and Flame, Vol. 160, N°7, pp. 1208-1214 (2013)

2. Bonhomme et al., A parallel multidomain strategy to compute turbulent flows in fan-stirred closed vessels, Computers and Fluids, Vol. 101, pp. 183-193 (2014)

Figure 5: Work Breakdown structure. —— : non-investigated branch ; —— : unsuccessful branch ; —— : successful branch

CHAPTER 1

GOVERNING EQUATIONS FOR LES OF TURBULENT REACTIVE FLOWS

Contents

This chapter gives a general introduction to Computational Fluid Dynamics, presents the concept and the governing equations for Large Eddy Simulations of turbulent reactive flows. This chapter describes models used in fluid mechanics codes and thereby in the AVBP *code. In particular, a reduced kinetic scheme for octane have been developed and is presented. Transport coefficients for octane / air flame used in the* AVBP *code have been validated and the ignition procedure is presented. Finally, turbulent combustion modeling and mesh movement are briefly described.*

(a) Claude Louis Navier (1785-1836).

(b) George Gabriel Stokes (1819-1903).

1.1 An introduction to Computational Fluid Dynamics

The aim of fluid mechanics is to study liquids and gases properties in various configurations. It starts by being able to predict its motion. The history of the equations governing the motion of a fluid started in 1757 when Leonhard Paul Euler published an important set of equations to describe the motion of inviscid flows that are known as the Euler equations. Then in 1822 Claude-Louis Navier, a French engineer, introduced the notion of viscosity. Finally in 1845 George Gabriel Stokes wrote the final equations describing the motion of a viscous fluid (including the terms proposed by C.L. Navier). These equations are now known as the Navier-Stokes equations . These equations are nonlinear partial differential equations and they are used to study a wide range of situations: the design of aircraft and cars, the study of blood flows, the weather or ocean currents. These nonlinear equations can not be solved analytically, except in some very simple cases that is why they are solved numerically thanks to computers.

This first section is divided in two parts. Section 1.1.1 presents the governing equations in fluid dynamics and a short description of the methods available to solve them is given in Sec. 1.1.2.

1.1.1 The Navier-Stokes equations

All the physics required to predict the exact behavior (including turbulence) of non-reacting and reacting flows in a given configuration is contained in the `full Navier-Stokes equations:

$$\frac{\partial \rho}{\partial t} + \frac{\partial}{\partial x_i}(\rho u_i) = 0 \tag{1.1}$$

$$\frac{\partial \rho u_j}{\partial t} + \frac{\partial}{\partial x_j}(\rho u_i u_j) = -\frac{\partial}{\partial x_j}\left(P\delta_{ij} - \tau_{ij}\right) \tag{1.2}$$

$$\frac{\partial \rho E}{\partial t} + \frac{\partial}{\partial x_j}(\rho E u_j) = -\frac{\partial}{\partial x_j}[u_i(P\delta_{ij} - \tau_{ij}) + q_j] + \quad _T + Q_r \tag{1.3}$$

$$\frac{\partial \rho Y_k}{\partial t} + \frac{\partial}{\partial x_j}(\rho Y_k u_j) = -\frac{\partial}{\partial x_j}(J_{j\,k}) + \quad _k \tag{1.4}$$

with ρ the density, u_i the i-component of the velocity, P the static pressure, τ_{ij} is the viscous tensor, E the energy, q_i the i-component of the the energy flux, $\quad _T$ the heat release due to combustion, Q_r the heat source term due for example to an electric spark, a laser, a radiative flux which must not be confused with the reaction term $\quad _T$, Y_k the mass fraction of species k, $J_{i\,k}$ is the i-component of the diffusive flux of species k and $\quad _k$ the reaction rate of species k.

The viscous tensor for Newtonian fluids is (Boussinesq [33] model):

$$\tau_{ij} = 2\mu\left(S_{ij} - \frac{1}{3}\delta_{ij}S_{kk}\right) \tag{1.5}$$

with μ the dynamic viscosity and S_{ij} is the deformation tensor:

$$S_{ij} = \frac{1}{2}\left(\frac{\partial u_j}{\partial x_i} + \frac{\partial u_i}{\partial x_j}\right). \tag{1.6}$$

The reaction term is expressed as:

$$\quad _T = -\sum_{k=1}^{N} \Delta h^0_{f\,k} \quad _k \tag{1.7}$$

where N is the number of species in the flow, $h^0_{f\,k}$ is the mass enthalpy of formation of species k at $T = T_0$ and $\quad _k$ is the reaction rate of species k. All details on $\quad _k$ are given in Sec. 1.4. The computation of the exact formulation of the diffusive flux of species k, $J_{i\,k}$, is a very difficult and costly task. The best first-order approximation is the Hirschfelder and Curtiss approximation [34]. The diffusive flux of species k, $J_{i\,k}$, is expressed as:

$$J_{i\,k} = -\rho\left(D_k\frac{W_k}{\overline{W}}\frac{\partial X_k}{\partial x_i} - Y_k V_i^c\right),$$

where D_k is not a binary diffusion but an equivalent diffusion coefficient of species k in the rest of the mixture:

$$D_k = \frac{1 - Y_k}{\sum_{j=k} X_j / D_{jk}} \tag{1.8}$$

W_k is the molecular weight of species k and $\overline{W}$ is the mean molecular weight of the mixture. X_k is the mole fraction of species k and Y_k is the mass fraction of species k. V_i^c is a correction velocity to ensure global mass conservation:

$$V_i^c = \sum_{k=1}^{N} D_k \frac{W_k}{\overline{W}} \frac{\partial X_k}{\partial x_i} \tag{1.9}$$

For multi-species flows, an additional heat flux term appears in the diffusive heat flux. This term is due to heat transport by species diffusion. The total heat flux vector then writes:

$$q_i = \underbrace{-\lambda \frac{\partial T}{\partial x_i}}_{\text{Heat conduction}} \underbrace{- \rho \sum_{k=1}^{N} \left(D_k \frac{W_k}{\overline{W}} \frac{\partial X_k}{\partial x_i} - Y_k V_i^c \right) h_{s\,k}}_{\text{Heat flux through species diffusion}} \tag{1.10}$$

where λ is the heat conduction coefficient of the mixture.

1.1.2 How to solve them ?

Unfortunately, the exact resolution of Eqs. 1.1 - 1.4 using Computational Fluid Dynamics (CFD) for turbulent flows in complex geometries is and will remain a challenge for a long time. Indeed, turbulent flows are characterized by a wide range of length scales (eddies): from the integral scale (the largest) to the Kolmogorov` scales (the smallest). The size of the largest eddies $l_t$ is typically of the order of the geometry considered. These structures contain most of the energy of the flow. The smallest eddies are the ones where the energy is dissipated. There is a cascade` of energy from the large scale to the smallest scales because large eddies interact with each other and breakdown into smaller eddies. The size of the Kolmogorov scale is noted η. Kolmogorov showed in 1941 [35] that the ratio between the integral length scale l_t and η is (see Fig. 1.2):

$$\frac{l_t}{\eta} = Re_t^{3/4} = \frac{\rho u' l_t}{\mu} \tag{1.11}$$

where Re_t is the turbulent Reynolds number based on a turbulent velocity u' and the integral length scale. The ratio l_t/η represents the number of points in each direction required to compute all the scales in the flow. Therefore, the total number of points N_{pt} needed to compute the flow in the three dimensions scales as:

$$N_{pt} \simeq \left(Re_t^{3/4} \right)^3 = Re_t^{9/4} \tag{1.12}$$

For example, lets imagine the number of points required to compute the flow around a car moving at $U_{car} = 100$ km/h $\simeq 30$ m/s. The turbulent velocity can be estimated at $u' \simeq 0.1 * U_{car} = 3$ m/s. If the car has a length $L_{car} \simeq l_t \simeq 4$ m, the turbulent Reynolds number is:

$$Re_t = \frac{\rho U_{car} L_{car}}{\mu} = \frac{1.2 * 3 * 4}{1.8.10^{-5}} \simeq 8.10^5 \tag{1.13}$$

According to Eq. 1.12, the total number of grid points needed to compute this configuration is around $N_{pt} = 2.10^{13}$. It is not feasible to compute such huge grids with current computer resources.

Three numerical approaches have been developed to describe flows using CFD:

- the Reynolds Averaged Navier-Stokes (RANS) computations have historically been the first possible approach thanks to their affordable computational costs. RANS techniques were developed to solve the mean values of all quantities. The balance equations for the averaged quantities are obtained by averaging the instantaneous balance of equations and require closure models for turbulence and combustion.
- The second level corresponds to Large Eddy Simulations (LES). The largest scale of the turbulence are explicitly calculated whereas the effects of smaller scales are modeled using subgrid closure rules. The balance of equations for LES are obtained by filtering the instantaneous balance of equations. Opposite to RANS, LES capture instantaneous motions. Not only mean values are calculated.
- The third level of computations is Direct Numerical Simulations (DNS) where the full instantaneous Navier-Stokes equations are solved without any model for turbulent motions: all turbulence scales are explicitly determined. DNS would predict all time variations exactly like a high-resolution sensor would measure in an experiment. This approach have changed the analysis of turbulent combustion. DNS represent a very important computational cost however it is developing thanks to High Performance Computing (HPC). Today, this approach is mainly used to study flows in academic configurations (low Reynolds number, very small configuration).

Figure 1.1 shows an example of the time evolution of local temperature predicted by RANS, LES or DNS for a stabilized flame. RANS capture only the mean value, LES capture the low frequency variations and DNS captures all time variations. These properties can also be presented in terms of energy spectra as shown by Fig. 1.2. All spatial frequencies are resolved in DNS. In LES, the largest scales (up to a cut-off wave number k_c) are computed whereas the smallest are modeled. By construction, LES is expected to tend toward DNS when the cut-off length goes to zero (*ie.* the mesh is fine). In RANS, only mean flow fields are resolved: no turbulent motion is explicitly calculated.

1.2 The LES concept

Large Eddy Simulation is nowadays recognized as an intermediate approach in comparisons to the more classical RANS methodologies and the very expensive DNS. As previously discussed, in RANS, only mean fields are calculated (the derivation of the

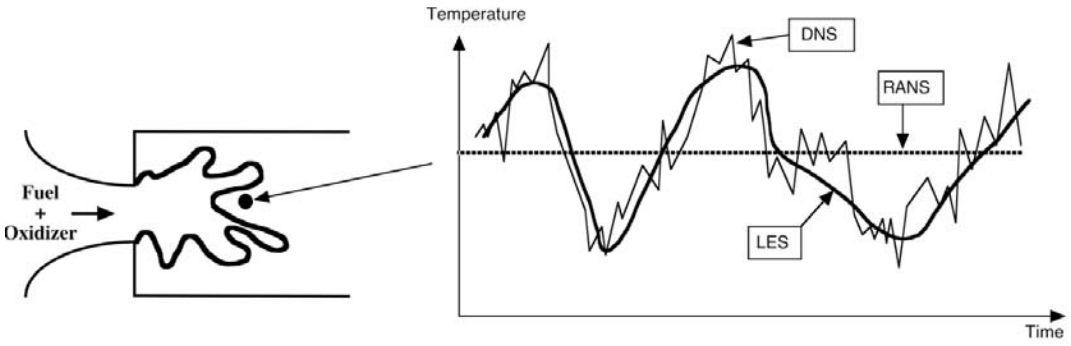

Figure 1.1: Time evolutions of local temperature computed with RANS, LES or DNS in a turbulent brush [20].

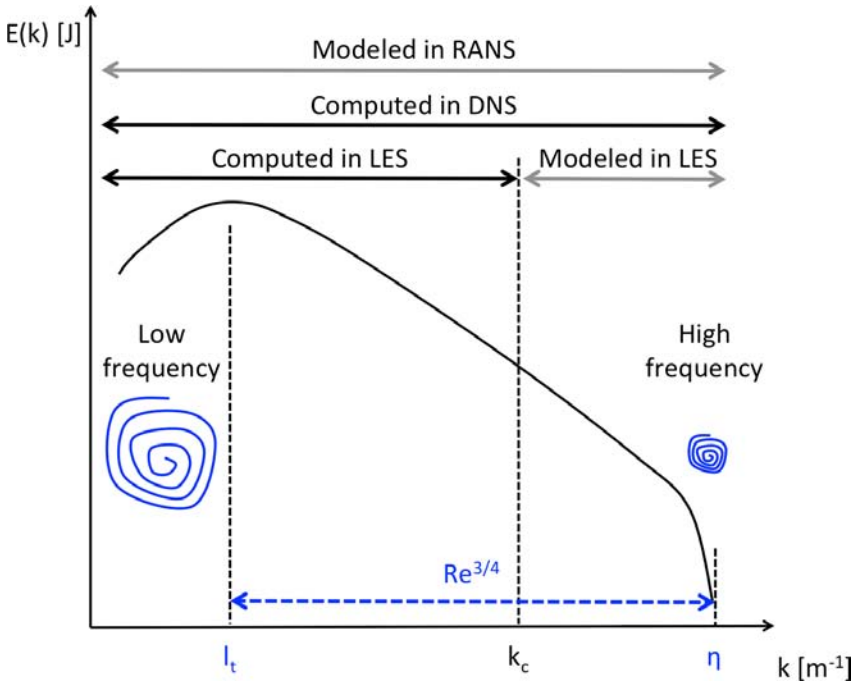

Figure 1.2: Log-log turbulence energy spectrum versus wave number. k_c is the cut-off wave number used in LES.

method consists in a temporal averaging of the Navier-Stokes equations Eqs. 1.1 - 1.4). It means than only a steady state can be expected. The unclosed terms (appearing during the derivation of the mean equations) are representative of the physics taking place over the entire range of frequencies (see Fig. 1.2) and the closure models have a an important forecasting job to do. It explains the big impact of the model on the results. In LES, the operator is a spatially localized time independent filter of given size Δ. Resulting from this spatial average` is a separation between the large (greater than the filter size) and small (smaller than the filter size) scales. The unclosed terms are in LES representative of the physics associated with the small structures (with high frequencies) present in the flow. LES allows a dynamic representation of the large scale motions whose contributions are critical in complex geometries. The LES predictions of complex turbulent flows are henceforth closer to the physics since large scale phenomena such as large vortex shedding and acoustic waves are embedded in the set of governing equations. It was shown for example by Rodi [36], Lübcke et *al.* [37], Cheng et *al.* [38] and Salim et *al.* [39] that significantly better predictions have been obtained with LES methods compared to RANS.

For these reasons, LES has a clear potential in predicting turbulent flows encountered in industrial applications. All simulations performed in this thesis are LES (and DNS for laminar flows). They were realized with the *AVBP* code.

1.3 Multi-species flows

Combustion necessarily involves multi-species flows: at least one fuel (for example methane CH_4) and one oxidizer (for example O_2). In this section, the equation of state, the transport coefficients and the thermodynamical variables (enthalpy, energy and entropy) of such flows are presented.

1.3.1 The equation of state

In a flow composed of N species, the proportion of each species k can be described by its mass fraction Y_k or by its molar fraction X_k. Y_k (resp. X_k) is defined as the mass (resp. the mole number) of species k, m_k (resp. n_k) divided by the total mass m (resp. the total mole number n) in a given volume: $Y_k = m_k/m$ (reps. $X_k = n_k/n$). Necessarily, $_k X_k =$ $_k Y_k = 1$.

The equation of state for an ideal gas mixture writes:

$$P = \rho r T \tag{1.14}$$

where r is the gas constant of the mixture dependent on time and space: $r = R/\overline{W}$ where $\overline{W}$ is the mean molecular weight of the mixture:

$$\frac{1}{\overline{W}} = \sum_{k=1}^{N} \frac{Y_k}{W_k} \tag{1.15}$$

The gas constant r and the heat capacities of the gas mixture depend on the local gas composition as:

$$r = \frac{R}{\overline{W}} = \sum_{k=1}^{N} \frac{Y_k}{W_k} R = \sum_{k=1}^{N} Y_k r_k \tag{1.16}$$

$$C_p = \sum_{k=1}^{N} Y_k C_{p\,k} \tag{1.17}$$

$$C_v = \sum_{k=1}^{N} Y_k C_{v\,k} \tag{1.18}$$

where $R = 8.3143$ J/mol.K is the universal gas constant. The adiabatic exponent for the mixture is given by $\gamma = C_p/C_v$. Thus, the gas constant, the heat capacities and the adiabatic exponent are no longer constant. Indeed, they depend on the local gas composition as expressed by the local mass fractions $Y_k(x,t)$.

The temperature is deduced from the the sensible energy, using Eqs. 1.27 and 1.28.

1.3.2 Transport coefficients

In CFD codes for multi-species flows the molecular viscosity μ is often assumed to be independent of the gas composition. However, it depends on the temperature and a power-law gives a good estimation of this evolution:

$$\mu = \mu_0 \left(\frac{T}{T_0} \right)^b \tag{1.19}$$

with b typically ranging between 0.5 and 1.0. For example $b = 0.76$ for air. The heat conduction coefficient of the gas mixture can then be computed by introducing the molecular Prandtl number of the mixture as:

$$\lambda = \frac{\mu C_p}{Pr} \tag{1.20}$$

The Prandtl number Pr is supposed to be constant in time and space and is given in an input file in the *AVBP* code. For the molecular diffusion coefficients D_k the same approximation can be used in CFD codes. The Schmidt number of species k, Sc_k, is supposed to be constant (in space and time) so that the diffusion coefficient for each species is computed as:

$$D_k = \frac{\mu}{\rho S_{c\,k}} \tag{1.21}$$

An important dimensionless number is defined in combustion: the Lewis number Le. It compares the thermal heat diffusivity $D_{th} = \lambda/(\rho C_p)$ to the molecular diffusivity D_k:

$$Le_k = \frac{D_{th}}{D_k} \tag{1.22}$$

1.3.2.a Octane / air flame transport coefficients

To find the Schmidt number of species k, Sc_k, and the Prandtl number Pr, a reference flame with a complex transport is computed with CANTERA [40]. CANTERA is an object-oriented, open source suite of software tools for reacting flow problems involving detailed chemical kinetics, thermodynamics and transport processes. For example, this software can compute one-dimensional laminar premixed flames with detailed chemistry and complex species transport. Then the same flame is computed with *AVBP* using a one-dimensional mesh. In both codes, flames are computed using a the 2S_C8H18_AB two-step chemical scheme (described in Sec. 1.4.1) for a octane / air flame.

Figure 1.3(a) presents the evolution of the Schmidt number of octane through the flame. With CANTERA, the Schmidt number is not assumed to be constant but in *AVBP* it is. Procedure recommanded by CERFACS to choose a Schmidt value is that the value chosen for *AVBP* should match the value given by CANTERA in the burnt gases. With this value, the diffusion coefficient of octane is well predicted in *AVBP* (see Fig. 1.3(b)). This methodology is applied for all species. The same methodology

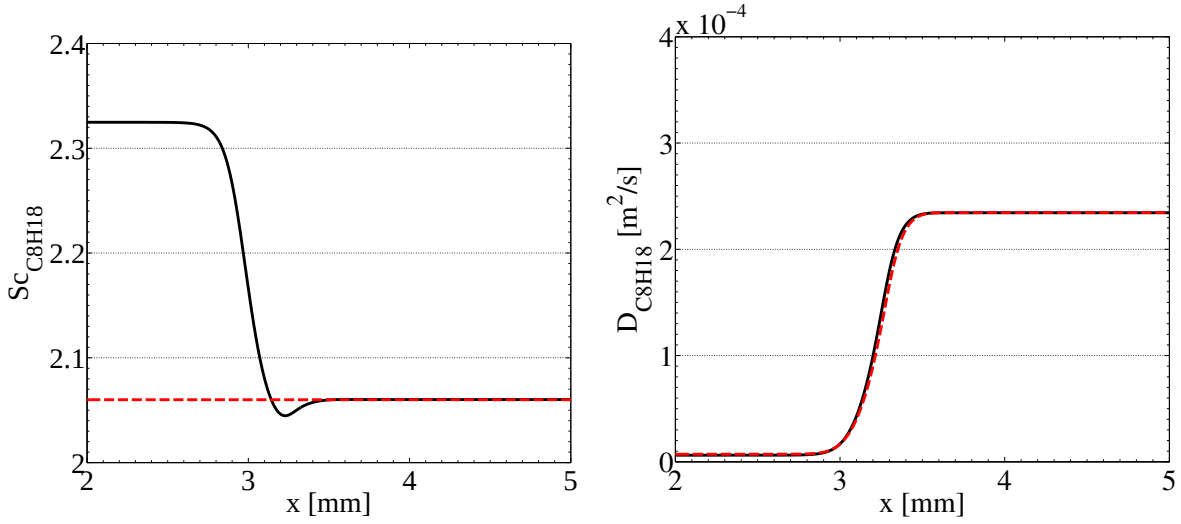

(a) Schmidt number of C_8H_{18}.

(b) Diffusion coefficient of C_8H_{18}.

Figure 1.3: Validation of the diffusion coefficient of octane ($P_0 = 101325$ Pa and $T_0 = 323$ K). —— CANTERA (complex transport) ; ---- *AVBP*.

is followed for the thermal diffusion. Figure 1.4(a) presents the evolution of the Prandtl number through the flame. In *AVBP* this number is constant and is chosen at $Pr = 0.74$. With this value the heat conduction coefficient computed in *AVBP* is in agreement with the coefficient computed in CANTERA.

As a result, Fig. 1.5 compares the same flame computed with *AVBP* and CANTERA. All profiles match very well which means that the approximation which consists in assuming that the Schmidt and the Prandtl numbers are constant is valid (it does not change the flame structure) if these values are well chosen. Table 1.1 summarizes the Schmidt number for each specie.

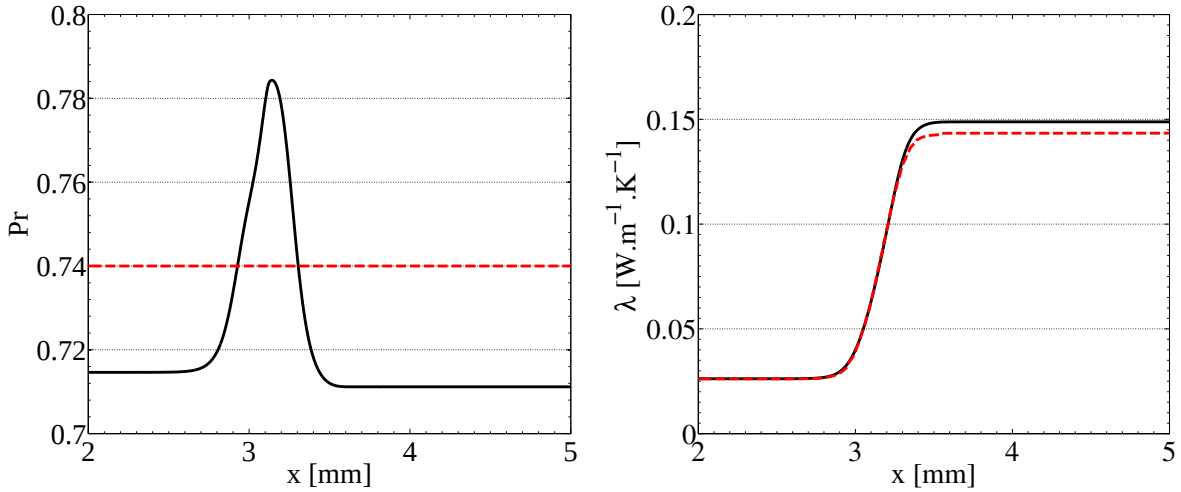

(a) Prandtl number.

(b) Heat conduction coefficient.

Figure 1.4: Validation of the heat conduction coefficient at $P_0 = 101325$ Pa and $T_0 = 323$ K. —— CANTERA (complex transport) ; ---- *AVBP*.

Specie	Sc_k
C_8H_{18}	2.06
CH_4	0.68
0_2	0.74
N_2	0.70
H_20	0.54
CO	0.75
CO_2	0.95

Table 1.1: Schmidt numbers for all species.

The diffusion coefficients characterize the diffusion of each species in the mixture. However, in practice, these values can be used independently of the equivalence ratio since the mixture is mostly represented by air.

1.3.3 Thermodynamical variables

Species energy and enthalpy are defined in reference to a given temperature T_0. Mass enthalpy of species k, h_k, is the sum of a reference enthalpy at $T = T_0$ and a sensible enthalpy $h_{s\,k}$:

$$h_k = \underbrace{h_{s\,k}}_{\text{sensible}} + \underbrace{\Delta h^0_{f\,k}}_{\text{chemical}} \tag{1.23}$$

The internal energy of species k, $e_k = h_k - RT/W_k$, can also be split into a sensible and a chemical contribution $e_k = e_{s\,k} + .\Delta h^0_{f\,k}$.

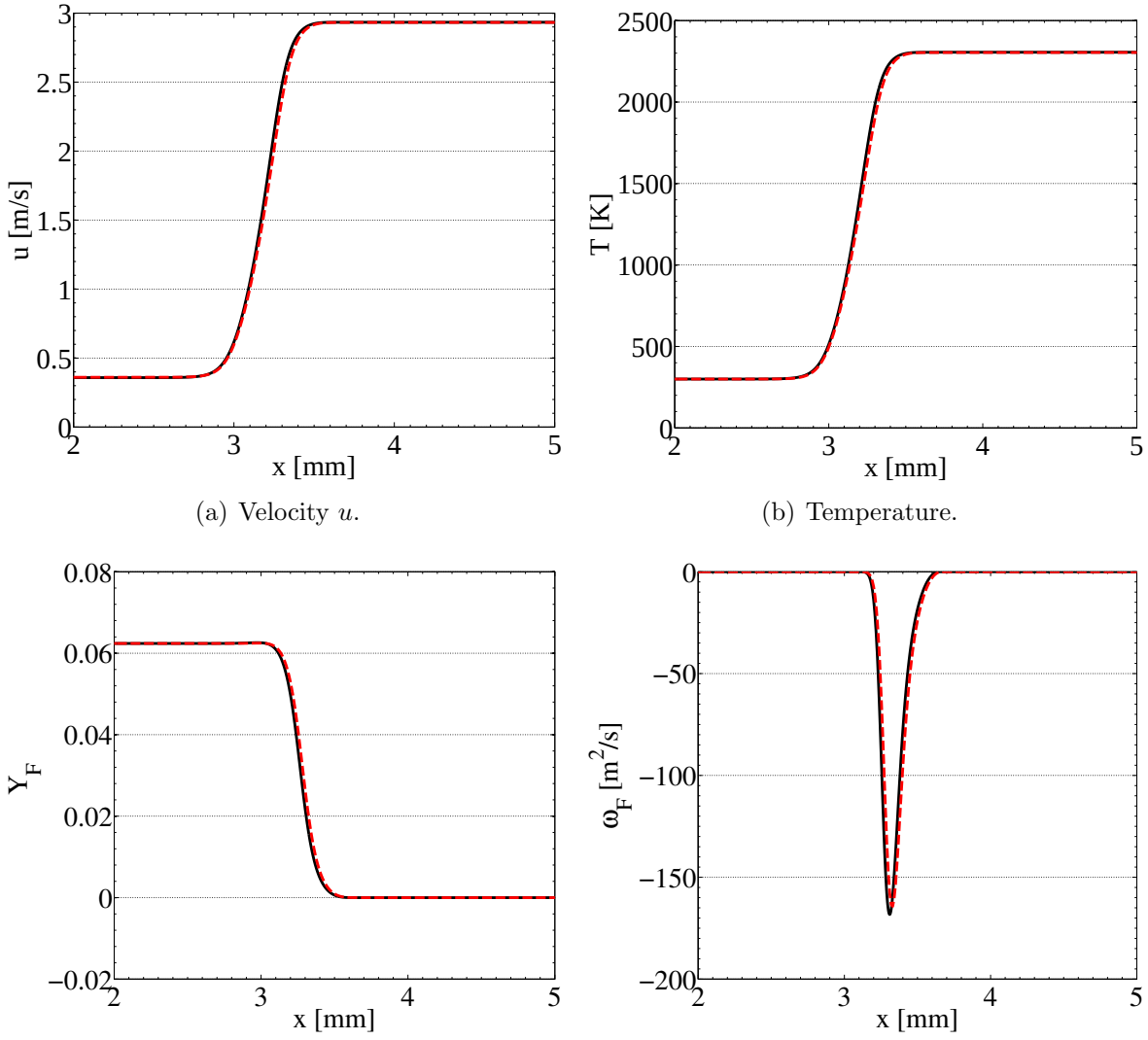

(a) Velocity u.

(b) Temperature.

(c) Mass fraction of C_8H_{18}.

(d) Reaction rate of C_8H_{18}.

Figure 1.5: Validation of species transport for octane / air flames at $P_0 = 101325$ Pa and $T_0 = 323$ K. —— CANTERA (complex transport) ; ---- *AVBP*.

The standard reference state used in *AVBP* is $P_0 = 1$ bar and $T_0 = 0$ K. The sensible mass enthalpies ($h_{s\,k}$) and entropies (s_k) for each species are tabulated for 51 values of the temperature (T_i with $i = 1...51$) ranging from 0K to 5000K with a step of 100 K. Therefore these variables can be evaluated by:

$$h_{s\,k}(T_i) = \int_{T_0=0K}^{T_i} C_{p\,k} dT = \frac{h^m_{s\,k}(T_i) - h^m_{s\,k}(T_0)}{W_k} \tag{1.24}$$

and:

$$s_k(T_i) = \frac{s^m_k(T_i) - s^m_k(T_0)}{W_k} \tag{1.25}$$

The superscript m corresponds to molar values. The tabulated values for $h_{s\,k}(T_i)$ and $s_k(T_i)$ can be found in the JANAF tables [41]. With this assumption, the sensible energy for each species can be reconstructed using the following expression:

$$e_{s\,k}(T_i) = \int_{T_0=0K}^{T_i} C_{v\,k} dT = h_{s\,k}(T_i) - r_k T_i \tag{1.26}$$

Note that the mass heat capacities at constant pressure $C_{p\,k}$ and volume $C_{v\,k}$ are supposed constant between T_i and $T_{i+1} = T_i + 100$. They respectively are defined as the slope of the sensible enthalpy and the slope of the sensible energy ($C_{p\,k} = \partial h_{s\,k}/\partial T$ and $C_{v\,k} = \partial e_{s\,k}/\partial T$). The sensible energy henceforth varies continuously with the temperature and is obtained by using a linear interpolation:

$$e_{s\,k}(T) = e_{s\,k}(T_i) + (T - T_i)\frac{e_{s\,k}(T_{i+1}) - e_{s\,k}(T_i)}{T_{i+1} - T_i} \qquad \text{for T} \in [\mathrm{T_i; T_{i+1}}] \tag{1.27}$$

The sensible energy and enthalpy of the mixture may then be expressed as:

$$\rho e_s = \sum_{k=1}^{N} \rho_k e_{s\,k} = \rho \sum_{k=1}^{N} Y_k e_{s\,k} \tag{1.28}$$

$$\rho h_s = \sum_{k=1}^{N} \rho_k h_{s\,k} = \rho \sum_{k=1}^{N} Y_k h_{s\,k} \tag{1.29}$$

1.4 Kinetics

During combustion, reactants are transformed into products once a sufficiently high energy is available to activate the reaction. This process can be modeled by a global reaction where a budget between reactants and major products is written. For example, the global reaction of octane oxidation is:

$$C_8H_{18} + \frac{25}{2}\ O_2 \quad - \quad 8CO_2 + 9\ H_2O \tag{1.30}$$

Such a global reaction does not describe elementary reactions that effectively occur during combustion process. Combustion of reactants is in fact a set of reactions involving major and minor species. Generally, N species $\mathcal{M}_{kj}$ react through M reactions:

$$\sum_{k=1}^{N} \nu'_{kj}\mathcal{M}_{kj} \rightleftharpoons \sum_{k=1}^{N} \nu''_{kj}\mathcal{M}_{kj}, \qquad j = 1, M \tag{1.31}$$

The reaction rate of species k, $_k$, is the sum of rates $_{kj}$ produced by all M reactions:

$$_k = \sum_{j=1}^{M} {}_{kj} = W_k \sum_{j=1}^{M} \nu_{kj}\mathcal{Q}_j \tag{1.32}$$

where $\nu_{kj} = \nu''_{kj} - \nu'_{kj}$ and $\mathcal{Q}_j$ is the rate progress of reaction j. The total mass conservation gives:

$$\sum_{k=1}^{N} {}_k = 0 \tag{1.33}$$

$\mathcal{Q}_j$ is written:

$$\mathcal{Q}_j = K_{f\,j} \prod_{k=1}^{N} \left(\frac{\rho Y_k}{W_k}\right)^{\nu_{kj}} - K_{r\,j} \prod_{k=1}^{N} \left(\frac{\rho Y_k}{W_k}\right)^{\nu_{kj}} \tag{1.34}$$

$K_{f\,j}$ and $K_{r\,j}$ are the forward and reverse rates of reaction j:

$$K_{f\,j} = A_{f\,j} \exp(-\frac{E_{a\,j}}{\mathcal{R}T}) \tag{1.35}$$

where $A_{f\,j}$ and $E_{a\,j}$ are the pre-exponential factor and the activation energy given in an input file. $K_{r\,j}$ is deduced from the equilibrium assumption:

$$K_{r\,j} = \frac{K_{f\,j}}{K_{eq}} \tag{1.36}$$

where K_{eq} is the equilibrium constant defined by:

$$K_{eq} = \left(\frac{p_0}{\mathcal{R}T}\right)^{\sum_{k=1}^{N} \nu_{kj}} \exp\left(\frac{\Delta S^0_j}{\mathcal{R}} - \frac{\Delta H^0_j}{\mathcal{R}T}\right) \tag{1.37}$$

where $p_0 = 1$ bar. ΔH^0_j and ΔS^0_j are respectively the enthalpy (sensible + chemical) and the entropy changes for reaction j:

$$\Delta H^0_j = h_j(T) - h_j(0) = \sum_{k=1}^{N} \nu_{kj} W_k (h_{s\,k}(T) + \Delta h^0_{f\,k}) \tag{1.38}$$

$$\Delta S_j^0 = \sum_{k=1}^{N} \nu_{kj} W_k s_k(T) \tag{1.39}$$

where $\Delta h^0_{f\,k}$ is the mass enthalpy of formation of species k at temperature $T_0 = 0$ K and is given in an input file (molar value). The heat released by combustion $_T$ in the initial enthalpy equation [20] is calculated as:

$$_T = -\sum_{k=1}^{N} {}_k \Delta h^0_{f\,k} \tag{1.40}$$

1.4.1 2S_C8H18_AB reduced scheme

In real flames, the combustion process involves many species and reactions. For example, the widely used GRI-MECH 3.0 mechanism describes the reaction of methane with air. It consists of 325 reactions that involve 53 species. These full schemes can be used only on very simple configurations (one-dimensional laminar flames for example). In an LES or DNS code, it is nor reasonable neither necessary to transport such a large number of species (the code must solve one conservation equation for each specie). Moreover some of these reactions can be very fast and could limit the time step. One possible solution consists in reducing the true chemistry. Reduced mechanisms are built to reproduce a minimum of flame features. In practice reduced schemes with two reactions are sufficient to reproduce the flame speed, the adiabatic flame temperature and the flame thickness for lean flames. Three criteria are usually sufficient to capture the important kinetic phenomena in most lean premixed turbulent flames.

1. For methane a scheme [42] called 2S_CH4_CM2 is employed.

$$CH_4 + \frac{3}{2}\, O_2 \quad - \quad CO + 2\, H_2O \tag{1.41}$$

$$CO + \frac{1}{2}\, O_2 \quad\quad CO_2 \tag{1.42}$$

2. For octane, a scheme called 2S_C8H18_AB was developed following the same methodology[1].

$$C_8H_{18} + \frac{17}{2}\, O_2 \quad - \quad 8\, CO + 9\, H_2O \tag{1.43}$$

$$CO + \frac{1}{2}\, O_2 \quad\quad CO_2 \tag{1.44}$$

[1]The 2S_C8H18_AB scheme is now available in the chemical library of *AVBP*.

Both schemes account for fuel oxidation through an irreversible reaction at a rate q_1 while a second reaction accounts for the equilibrium between CO and CO_2 with a rate q_2:

$$q_1 = A_1 \left(\frac{\rho Y_F}{W_F}\right)^{n_1^F} \left(\frac{\rho Y_{O_2}}{W_{0_2}}\right)^{n_1^{O_2}} \exp\left(\frac{E_{a\,1}}{RT}\right) \tag{1.45}$$

$$q_2 = A_2 \left(\frac{\rho Y_{CO}}{W_{CO}}\right)^{n_2^{CO}} \left(\frac{\rho Y_{O_2}}{W_{0_2}}\right)^{n_2^{O_2}} - \frac{1}{K_e}\left(\frac{\rho Y_{CO_2}}{W_{CO_2}}\right)^{n_2^{CO_2}} \exp\left(\frac{E_{a2}}{RT}\right) \tag{1.46}$$

where K_e is the equilibrium constant for the CO/CO_2 equilibrium and R the perfect-gas constant. The coefficients for the two schemes are recalled in Tab. 1.2. While the reduced

q_1	A_1	$E_{a\,1}$	n_1^F	$n_1^{O_2}$	
methane	2.00 10^{15}	35000	0.9	1.1	
octane	6.05 10^{11}	41500	0.55	0.9	
q_2	A_2	$E_{a\,2}$	n_2^{CO}	$n_2^{O_2}$	$n_2^{CO_2}$
methane	2.00 10^{9}	12000	1.0	0.5	1.0
octane	4.50 10^{10}	20000	1.0	0.5	1.0

Table 1.2: Coefficients for the reduced kinetic scheme 2S_C8H18_AB. Activation energies are in [cal.mol^{-1}] and pre-exponential constants in [cgs] units.

scheme for methane has already been validated [42], the validation of the 2S_C8H18_AB scheme for octane versus a detailed scheme proposed by Jerzembeck [43] is presented in Fig. 1.6 (the CANTERA code is used to compare these two chemical schemes). For a one-dimensional planar flame at $P_0 = 101325$ Pa and $T_0 = 323$ K, the reduced scheme reproduces accurately the laminar flame speed and burnt gases adiabatic temperature, for equivalence ratios up to $\Phi = 1.2$ which cover all experiments performed in Orléans. Franzelli et *al.* [44] developed a methodology to get better results in terms of flame speed and adiabatic temperature when computing reach flames ($\Phi > 1.2$) with two-step schemes. This is done by introducing two functions $f_1(\Phi)$ and $f_2(\Phi)$ which modify the pre-exponential constants in the chemical scheme: $A_1 = A_1 f_1(\Phi)$ and $A_2 = A_2 f_2(\Phi)$. This strategy is not necessary here and is not employed in this thesis because all computed flames are lean.

1.5 Governing equations for non-reactive LES

As previously discussed, the LES concept consists in applying a spatially localized time independent filter of given size Δ on the Navier-Stokes equations. This filtering inttroduces a separation between the large (greater than the filter size) and small (smaller than the filter size) scales. This operation also exhibits unclosed terms which must be

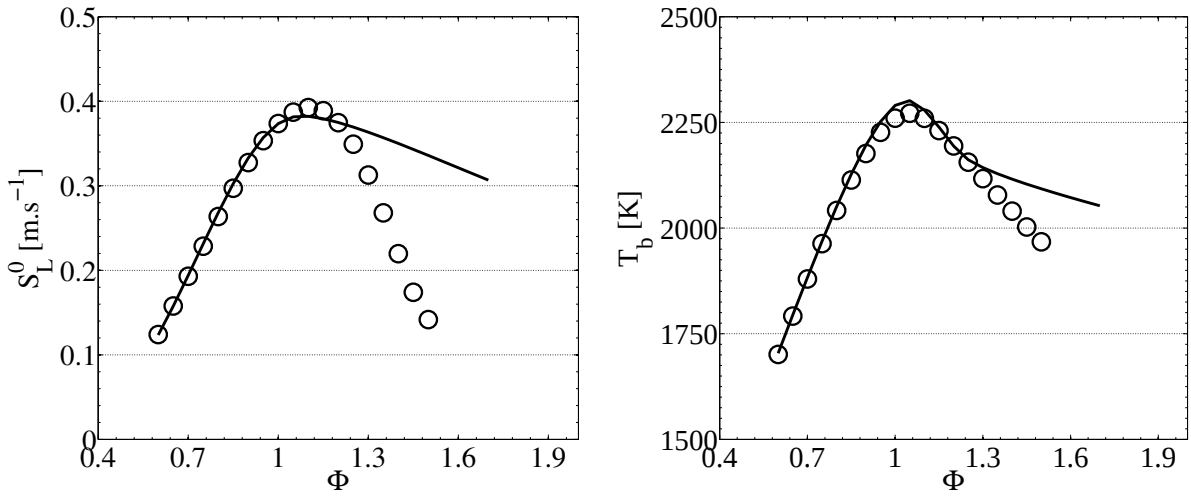

(a) Laminar flame speed.

(b) Adiabatic temperature.

Figure 1.6: Validation of the reduced scheme 2S_C8H18_AB for octane / air flames at $P_0 = 101325$ Pa and $T_0 = 323$ K. ◯ Jerzembeck *et al.* [43], —— 2S_C8H18_AB.

modeled. These equations and the closure models are presented in this section. It is a close transposition of the *AVBP* handbook [2].

1.5.1 The filtering operation

A low-pass (in wavenumber) filter, G_Δ, is applied to the Navier-Stokes equations Eqs. 1.1 - 1.4. Mathematically, it consists of a convolution of any quantity, f, with the filter function G_Δ.

$$\bar{f}(x) = \int f(x')G_\Delta(x - x')dx' \tag{1.47}$$

The resulting filtered quantity, $\bar{f}$, represents the large-scale structures of the flow (*ie.* resolved in the LES) whereas all the structures of size smaller than the filter length, Δ, are contained in the residual field, $f' = f - \bar{f}$. Contrary to RANS averaging, the filtered value of a LES perturbation is not zero: $\overline{f'} = 0$ and the double filtered values are not equal to the filtered values in general: $\overline{\overline{f}} = \overline{f}$. For variable density ρ, a mass-weighted Favre filtering is introduced according to:

$$\bar{\rho}\tilde{f}(x) = \int \rho f(x')G_\Delta(x - x')dx' = \overline{\rho f} \tag{1.48}$$

Filtering the instantaneous balance equations (Eqs. 1.1 - 1.4) leads to the following equations:

$$\frac{\partial \overline{\rho}}{\partial t} + \frac{\partial}{\partial x_i}(\overline{\rho} u_i) = 0 \tag{1.49}$$

[2] *AVBP* handbook: http://www.cerfacs.fr/∼avbp/AVBP_V6.X/HANDBOOK/AVBP/HTML2/main.html

$$\frac{\partial \overline{\rho} u_j}{\partial t} + \frac{\partial}{\partial x_j}(\overline{\rho} u_i u_j) = -\frac{\partial}{\partial x_j}(\overline{P}\delta_{ij} - \overline{\tau}_{ij} - \overline{\tau}^t_{ij}) \tag{1.50}$$

$$\frac{\partial \overline{\rho} E}{\partial t} + \frac{\partial}{\partial x_j}(\overline{\rho} E u_j) = -\frac{\partial}{\partial x_j}[\overline{u_i(P\delta_{ij} - \tau_{ij})} + \overline{q}_j + \overline{q}^t_j] + \overline{\ }_T + \overline{Q}_r \tag{1.51}$$

$$\frac{\partial \overline{\rho} Y_k}{\partial t} + \frac{\partial}{\partial x_j}(\overline{\rho} Y_k u_j) = -\frac{\partial}{\partial x_j}[\overline{J}_{j\,k} + \overline{J}^t_{j\,k}] + \overline{\ }_k \tag{1.52}$$

where u_j, E and Y_k denote the filtered velocity vector, total energy per unit mass and species mass fractions, respectively. A repeated index implies summation over this index (Einstein s rule of summation). Note also that the index k is reserved for referring to the k^{th} species and does not follow the summation rule.

Writing the vector of the filtered conservative variables as follows: $\overline{\mathbf{w}} = (\bar{\rho}u, \bar{\rho}v, \bar{\rho}w, \bar{\rho}E, \bar{\rho}Y_k)$, Eqs. 1.50 - 1.52, can be expressed as:

$$\frac{\partial \overline{\mathbf{w}}}{\partial t} + \nabla \cdot \overline{\mathbf{F}} = \overline{\mathbf{s}} \tag{1.53}$$

where $\overline{\mathbf{s}}$ is the filtered source term and $\overline{\mathbf{F}}$ is the flux tensor which can be divided in three parts:

$$\overline{\mathbf{F}} = \overline{\mathbf{F}}^I + \overline{\mathbf{F}}^V + \overline{\mathbf{F}}^t \tag{1.54}$$

where $\overline{\mathbf{F}}^I$ is the inviscid term, $\overline{\mathbf{F}}^V$ is the viscous term and $\overline{\mathbf{F}}^t$ is the turbulent subgrid-scale term.

1.5.1.a The inviscid term $\overline{\mathbf{F}}^I$

The three spatial components of the inviscid flux tensor are the same as in DNS but based on the filtered quantities:

$$\overline{\mathbf{F}}^I = \begin{array}{c} \bar{\rho}u_i u_j + \overline{P}\delta_{ij} \\ \bar{\rho}E u_j + \overline{P u_j}\delta_{ij} \\ \bar{\rho_k} u_j \end{array} \tag{1.55}$$

1.5.1.b The viscous term $\overline{\mathbf{F}}^V$

The components of the viscous flux tensor take the form:

$$\overline{\mathbf{F}}^I = \begin{array}{c} -\overline{\tau_{ij}} \\ -(\overline{u_i \tau_{ij}}) + \overline{q_j} \\ \overline{J_{j\,k}} \end{array} \tag{1.56}$$

The filtered diffusion terms are:

- Laminar filtered stress tensor $\overline{\tau_{ij}}$ (for Newtonian fluids)

$$\overline{\tau_{ij}} = \overline{2\mu\left(S_{ij} - \frac{1}{3}\delta_{ij}S_{kk}\right)} \tag{1.57}$$

$$\text{approximation:} \quad \overline{\tau_{ij}} \simeq 2\bar{\mu}\left(S_{ij} - \frac{1}{3}\delta_{ij}S_{kk}\right) \tag{1.58}$$

$$\text{with:} \quad S_{ij} = \frac{1}{2}\left(\frac{\partial u_j}{\partial x_i} + \frac{\partial u_i}{\partial x_j}\right) \tag{1.59}$$

$$\text{and:} \quad \bar{\mu} \simeq \mu(T) \tag{1.60}$$

- Diffusive species flux vector $\overline{J_{i\,k}}$

$$\overline{J_{i\,k}} = -\overline{\rho\left(D_k\frac{W_k}{\overline{W}}\frac{\partial X_k}{\partial x_i} - Y_k V_i^c\right)} \tag{1.61}$$

$$\text{approximation:} \quad \overline{J_{i\,k}} \simeq -\bar{\rho}\ \ \overline{D}_k\frac{W_k}{\overline{W}}\frac{\partial X_k}{\partial x_i} - Y_k V_i^c \tag{1.62}$$

$$\text{with:} \quad V_i^c = \sum_{k=1}^{N} \overline{D}_k\frac{W_k}{\overline{W}}\frac{\partial X_k}{\partial x_i} \tag{1.63}$$

$$\text{and:} \quad \overline{D}_k \simeq \frac{\bar{\mu}}{\bar{\rho}Sc_k} \tag{1.64}$$

- Filtered heat flux $\overline{q_i}$

$$\overline{q_i} = -\overline{\lambda\frac{\partial T}{\partial x_i}} + \sum_{k=1}^{N}\overline{J_{i\,k}h_{s\,k}} \tag{1.65}$$

$$\text{approximation:} \quad \overline{q_i} \simeq -\bar{\lambda}\frac{\partial T}{\partial x_i} + \sum_{k=1}^{N}\overline{J_{i\,k}}h_{s\,k} \tag{1.66}$$

$$\text{with:} \quad \bar{\lambda} \simeq \frac{\bar{\mu}\overline{C}_p(T)}{Pr} \tag{1.67}$$

These forms assume that the spatial variations of molecular diffusion fluxes are negligible and can be modeled through simple gradient assumptions.

1.5.1.c The turbulent subgrid-scale term $\overline{\mathbf{F}}^t$

The components of the turbulent subgrid-scale flux take the form:

$$\overline{\mathbf{F}}^I = \begin{matrix} -\overline{\tau_{ij}}^t \\ \overline{q_j}^t \\ \overline{J_{j\,k}}^t \end{matrix} \tag{1.68}$$

As highlighted above, filtering the transport equations leads to a closure problem evidenced by the so called subgrid-scale (SGS) turbulent fluxes. For the system to be solved numerically, closures need to be supplied. Details on the closures are:

- The Reynolds tensor $\overline{\tau_{ij}}^t$

$$\overline{\tau_{ij}}^t = -\bar{\rho}\left(u_i u_j - u_i u_j\right) \tag{1.69}$$

$$\text{modeled as (Boussinesq [33] model)}: \quad \overline{\tau_{ij}}^t = 2\bar{\rho}\nu_t\left(S_{ij} - \frac{1}{3}\delta_{ij}S_{kk}\right) \tag{1.70}$$

$$\text{with:} \quad S_{ij} = \frac{1}{2}\left(\frac{\partial u_j}{\partial x_i} + \frac{\partial u_i}{\partial x_j}\right) - \frac{1}{3}\frac{\partial u_k}{\partial x_k}\delta_{ij} \tag{1.71}$$

In Eq. 1.70, $\overline{\tau_{ij}}^t$ is the SGS tensor, S_{ij} is the resolved rate tensor and ν_t is the SGS turbulent viscosity. The modeling of ν_t is explained in Sec. 1.5.2.

- The subgrid scale diffusive species flux vector $\overline{J_{j\,k}}^t$

$$\overline{J_{i\,k}}^t = -\bar{\rho}\left(u_i Y_k - u_i Y_k\right) \tag{1.72}$$

$$\text{modeled as:} \quad \overline{J_{i\,k}}^t = -\bar{\rho}\quad D_k^t\frac{W_k}{\overline{W}}\frac{\partial X_k}{\partial x_i} - Y_k V_i^{c\,t} \tag{1.73}$$

$$\text{with:} \quad V_i^{c\,t} = \sum_{k=1}^{N} D_k^t\frac{W_k}{\overline{W}}\frac{\partial X_k}{\partial x_i} \tag{1.74}$$

$$\text{and:} \quad D_k^t = \frac{\nu_t}{Sc_k^t} \tag{1.75}$$

The turbulent Schmidt number $Sc_k^t = 0.6$ is the same for all species. Note also that having one turbulent Schmidt number for all the species does not imply, $V_i^{c\,t} = 0$ because of the $W_k/\overline{W}$ term in Eq. 1.73.

- The subgrid scale heat flux vector $\overline{q_j}^t$

$$\overline{q_i}^t = -\bar{\rho}\left(u_i E - u_i E\right) \tag{1.76}$$

$$\text{modeled as:} \quad \overline{q_i}^t = -\lambda_t\frac{\partial T}{\partial x_i} + \sum_{k=1}^{N}\overline{J_{i\,k}}h_{s\,k} \tag{1.77}$$

$$\text{with:} \quad \lambda_t = \frac{\mu_t\overline{C}_p}{Pr^t} \tag{1.78}$$

The turbulent Schmidt number is fixed at $Pr^t = 0.6$.

1.5.2 Models for the subgrid stress tensor

LES models for the subgrid stress tensor (see Eq. 1.70) are derived on the theoretical ground that the LES filter is spatially and temporally invariant. Variations in the filter size due to non-uniform meshes or moving meshes are not directly accounted for in the LES models. Change of cell topology is only accounted for through the use of the local cell volume, that is $\Delta = V_{cell}^{1/3}$.

The filtered compressible Navier-Stokes equations exhibit SGS tensors and vectors describing the interaction between the non-resolved and resolved motions. Generally, the influence of the SGS on the resolved motion is taken into account by a SGS model based on the introduction of a turbulent viscosity, ν_t (Boussinesq [45] model). Such an approach assumes the effect of the SGS field on the resolved field to be purely dissipative. This hypothesis is essentially valid within the cascade theory of turbulence introduced by Kolmogorov [35].

LES models for the subgrid stress tensor only differ through the estimation of ν_t. In this document, only the two models used during the thesis are presented: the Smagorinsky model and the WALE (Wall Adapting Local Eddy-viscosity). More information on the other models implemented in *AVBP* can be found for example in [46].

- The Smagorinsky model

$$\nu_t = (C_S\Delta)^2 \quad \overline{2S_{ij}S_{ij}} \tag{1.79}$$

where Δ denotes the filter characteristic length (cube-root of the cell volume), C_S is the model constant set to 0.18 but can vary between 0.1 and 0.18 depending on the flow configuration. The Smagorinsky model [47] was developed in the sixties and heavily tested for multiple flow configurations. This closure has the particularity of supplying the right amount of dissipation of kinetic energy in homogeneous isotropic turbulent flows. Locality is however lost and only global quantities are maintained. It is known to be too dissipative and transitioning flows are not suited for its use [12].

- The WALE model

$$\nu_t = (C_w\Delta)^2 \frac{\left(s_{ij}^d s_{ij}^d\right)^{3/2}}{\left(S_{ij}S_{ij}\right)^{5/2} + \left(s_{ij}^d s_{ij}^d\right)^{5/4}} \tag{1.80}$$

with:

$$s_{ij}^d = \frac{1}{2}\left(g_{ij}^2 + g_{ji}^2\right) - \frac{1}{3}g_{kk}^2\delta_{ij} \tag{1.81}$$

where Δ denotes the filter characteristic length (cube-root of the cell volume), $C_w = 0.4929$ is the model constant and g_{ij} denotes the resolved velocity gradient. The WALE model [48] was developed for wall bounded flows in an attempt to recover the scaling laws of the wall. Similarly to the Smagorinsky model locality is lost and only global quantities are to be trusted.

1.5.3 Numerical schemes

To resolve equations presented in Sec. 1.5.1, numerical schemes are needed. The *AVBP* solver is based on the finite volume method [49] with a cell-vertex discretization. Because they are less dissipative than non-centered schemes (up-wind or downwind), centered numerical schemes are implemented in *AVBP*. All the numerical schemes developed in *AVBP* are presented in [50]. The two numerical schemes used in this thesis are:

- The Lax-Wendroff (LW) scheme The LW scheme [51] is a finite volume centered scheme. This scheme uses an explicit time integration with a single Runge-Kutta step. Its accuracy in both space and time is of second order. The scheme is quite robust due to a diffusive term that stabilizes it very effectively (even if it is a centered scheme in space). Furthermore, it is characterized by low computational cost.

- The Two step Taylor-Galerkin C` scheme The TTGC scheme [52] is a finite element centered scheme. Its accuracy in both space and time is of third order (4^{th} on regular grids [53]). It is characterized by very good properties regarding dissipation and dispersion making it well-suited for LES applications. However, it is less robust than the LW scheme and approximately 2.5 more expensive in terms of computational cost.

1.5.4 Artificial viscosity

The numerical discretization methods in AVBP are spatially centered. These types of schemes are known to be naturally subject to small-scale oscillations in the vicinity of steep solution variations. This is why it is common practice to add a so-called artificial viscosity (AV) term to the discrete equations, to avoid these spurious modes (also known as wiggles) and in order to smooth very strong gradients. These AV models are characterized by the linear preserving property which leaves unmodified a linear solution on any type of element. The models are based on a combination of a shock capturing term (called 2^{nd} order AV) and a background dissipation term (called 4^{th} order AV). In AVBP, adding AV is done in two steps:

- first a sensor detects if AV is necessary, as a function of the flow characteristics,
- then a certain amount of 2^{nd} and 4^{th} AV is applied, depending on the sensor value and on user-defined parameters.

The 2^{nd} order AV acts just like a classical viscosity activated only in certain regions of the flow. It smoothes local gradients, and introduces artificial dissipation. The 4^{th} order AV is mainly used to control spurious high-frequency wiggles.

1.6 Combustion modeling

As described in Sec. 1.4, combustion is a process in which reactants are transformed into products. The domain where these transformations take place, called the flame front, is very small. Typically a flame thickness at atmospheric pressure for gasoline/air flames is around 0.1 to 0.5 mm. This raises a problem encountered for Large Eddy Simulation of reactive flows: the thickness δ_L^0 of a flame is generally smaller than the standard mesh size Δ used for LES. In order to resolve the flame front correctly, about 5 to 10 points are needed. This leads to very large grids, out of the capacity of the current calculators for large and complex industrial configurations.

Different models have been proposed to approximate the filtered species reaction rates $\overline{\ }_k$ (see Eq. 1.52) for turbulent premixed combustion using the LES approach. They may be separated into two main categories:

1. **Models assuming an infinitely thin reaction zone:** the turbulent premixed flame is modeled by fresh reactants and burnt products separated by an infinitely thin reaction zone. The local structure of the flame is assumed equal to a laminar flame for which the inner structure is not affected by turbulence (flamelet assumption). The Bray-Moss-Libby (BML) models [54], the flame surface density models [55], and G-equation models [56, 57] are some of the most common examples
2. **Models describing the structure of the reaction zone thickness:** the turbulent premixed flame is characterized by a finite thin reaction zone that could interact with the turbulent flow and often behaves as a stretched laminar flame. Some examples are the Probability Density Function (PDF) models [58, 59], the F-TACLES approach (the chemistry is tabulated as a function of a progress variable) developed by Fiorina et *al.* [60] and the artificially Thickened Flame (TF) models [61, 62].

Only the Thickened Flame model is described in details in this document because only this model was used during the thesis.

1.6.1 The Thickened Flame model for LES (TFLES)

An attractive solution to propagate a flame on a coarse` grid consists in artificially thicken this flame. This idea was first proposed by Butler and O Rourke in 1977 [63]. Figure 1.7 presents the concept of this approach. For sufficiently large values of the thickening factor F, the thickened flame front can be resolved explicitly on the grid nodes. Since the reaction rate is still expressed using Arrhenius law, various phenomena can be accounted for without requiring ad-hoc submodels (ignition, flame/wall interactions). Following

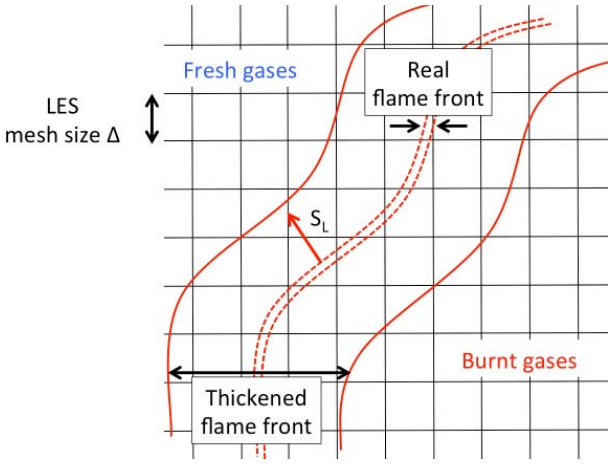

Figure 1.7: Thickened flame approach. The flame is artificially thickened but it flame speed is conserved.

simple theories of laminar premixed flames [64, 65], the flame speed s_L and the flame

thickness δ_L^0 may be expressed as:

$$s_L \quad \sqrt{D_{th}B} \quad ; \quad \delta_L^0 \quad \frac{D_{th}}{s_L} = \quad \frac{\overline{D_{th}}}{B} \tag{1.82}$$

where D_{th} is the thermal diffusivity and B the pre-exponential constant. If the thermal diffusivity is multiplied by a factor F while the pre-exponential constant is divided by F, the flame thickness δ_L^0 is multiplied by a factor F but the flame speed s_L is conserved. So the flame propagates to the good speed on the computational domain.

When the flame is thickened by a factor F, the interaction between the flame and the turbulence is modified: the flame becomes less sensitive to turbulent motions and vortex may affect the reaction zone. This interaction is characterized by the Damköhler number D_a which compares turbulent τ_t to chemical τ_c time scales (for large values of D_a, turbulence is not able to affect the inner flame structure which remains close to a laminar flame wrinkled by turbulence motions):

$$D_a = \frac{\tau_t}{\tau_c} = \frac{l_t}{u'}\frac{s_L}{\delta_L^0} \tag{1.83}$$

It is straightforward to show that increasing the flame thickness by a factor F decreases the D_a number by the same factor F ($D_a^{thick} = D_a/F$). This point has been investigated using DNS by Angelberger et al. [66] and Colin et al. [61] (see Figure 1.8). To account for this unwanted effect, an efficiency function Ξ, corresponding to a subgrid scale wrinkling factor has been derived. This efficiency function depends on velocity (u'/s_L) and length scale ($\Delta/F\delta_L^0$) ratios.

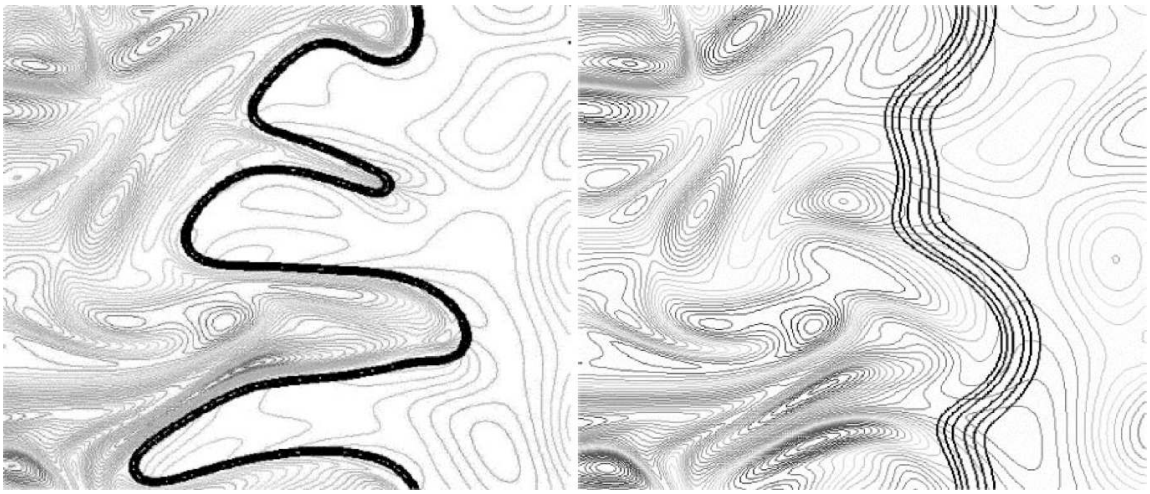

Figure 1.8: DNS of flame turbulence interactions. Reaction rate and vorticity fields are superimposed. Left: Reference flame ; Right: flame artificially thickened by a factor $F = 5$ [20].

In practice, the thickened flame approach is implemented by changing the thermal

diffusivity and the reaction rate according to:

Diffusivity:	D_{th}	FD_{th}	ΞFD_{th}
Pre-exponential constant:	B	B/F	$\Xi B/F$
	thickening	wrinkling	

According to Eq. 1.82, the flame speed s_L and the flame thickness δ_L^0 become respectively:

$$s_T = \Xi s_L \qquad ; \qquad \delta_T = F\delta_L^0 \tag{1.84}$$

This TFLES model has been first developed for perfectly premixed combustion. But applying a uniform thickening in the whole domain accelerates diffusion in non reactive zones, where thickening is not necessary. In other words, the TF model can remain unchanged in the flame zone but must be adapted outside the flame region. So a dynamic thickening procedure [62] (called D-TFLES) depending on the flame position and the local resolution has been developed and is therefore preferred.

The thickening factor F is not a constant any more but it goes to F_{max} in flame zones and decreases to unity in non reactive zones. This is obtained by writing:

$$F = F_{max}\mathcal{S} \tag{1.85}$$

with:

$$F_{max} = \frac{N_c}{\Delta}\delta_L^0 \tag{1.86}$$

N_c being the number of cells used to resolve the flame front (typically $N_c = 5$ guarantees a good behavior). $\mathcal{S}$ is a sensor depending on the local temperature and mass fractions:

$$\mathcal{S} = \tanh(\beta' \frac{\Omega}{\Omega_0}) \tag{1.87}$$

where β' is a constant equal to 500, Ω is a sensor function detecting the presence of a reaction front and Ω_0 corresponds to its maximum value. One possible method to construct Ω is to use the kinetic parameters of the fuel breakdown reaction:

$$\Omega = {Y_F}^{n_F} {Y_O}^{n_O} \exp\left(-\Gamma \frac{E_a}{RT}\right) \tag{1.88}$$

Ω_0 can be found running a 1D premixed non-thickened flame and measuring Ω_0 on it. Γ is used to start the thickening before the reaction, that is why $\Gamma < 1$ (usually $\Gamma = 0.5$).

The main advantages of the TFLES model are its simplicity and its performances for premixed and stratified flames. It has been used successfully in multiple configurations [61, 67, 42, 68, 69] and is also integrated now in commercial softwares such as Fluent or Charles (from Cascade Technologies). In the present work, even though the TFLES was used, grids were sufficiently refined to offer a `DNS-like accuracy. The results will show that most thickening factors were less than 1.4 leading to efficiency functions less than 1.3. For such fine grids, the effect of the TFLES model is clearly very small.

1.6.2 Ignition procedure

In most combustion devices, and especially in gasoline piston engines, spark-plugs are used to ignite flames. A very high-tension ($\sim$ 30 kV) is applied between two electrodes which generates a plasma at a very high temperature containing enough energy to ignite the flame. Physic of this complex process has been widely studied [70, 71, 72, 73] and 4 main phases have been highlighted:

1. The pre-breakdown phase where the electrical discharge occurs.
2. The breakdown phase when voltage decreases and current increases between the two electrodes. A plasma phase at about $60,000$ K is generated at this moment. Then this plasma generates a shock wave which propagates, absorbing a large portion of the initial energy.
3. The arc phase: the volume of the plasma phase increases while its temperature decreases to reach about 6000 K. During this phase, chemical radicals are produced due to high-temperature.
4. The glow phase: during this final phase which last about 1 ms, the gas temperature close to the spark-plug is near 3000 K. It is during this phase that most of the energy is transmitted from the spark-plug to the gas.

The first three phases, where the plasma phase is generated, can not be fully described in a simulation CFD code because they involve very short times and length scales so that models have been developed and are presented below.

To ignite a flame in CFD codes, two classical approaches are commonly used in the combustion community:

1. **The Energy Deposition (ED) model**: A gaussian (in time and space) source term is added in the energy equation [74]. The *AVBP* code can not compute the plasma phase but the ED model mimics the discharge of a spark beginning at the end of the plasma phase.
2. **The kernel deposition**: A burnt gases kernel is artificially imposed in the fresh gases. If the energy contained in the kernel is sufficient, the kernel grows and the flame propagates. This method is used in this thesis and more details are given below.

The ignition with a burnt gases kernel (method 2) raises the problem of the composition of this kernel. Profiles of temperature and species at the instant where the kernel is introduced are supposed to match the flow state after the plasma phase when only a hot sphere of burnt gases is left. Choosing such profiles involves some arbitrariness since the plasma phase can leave certain traces in the flow (temperature higher than the adiabatic flame temperature for example). Here we decided to deposit a kernel at a temperature equal to or larger than the adiabatic temperature. These conditions are sufficient to ignite a flame but *AVBP* is a compressible code and acoustic waves are created if the initial solution is too far from reality. To avoid these acoustic waves a good method consists in using the profiles of a one-dimensional flame previously computed with CANTERA. Thus the species mass fractions, density, temperature are closer to a real flame. Moreover, for laminar spherical propagations, the velocity profile can also be derived and introduced at $t = 0$. Assuming that the velocity is only a function of the radial coordinates r (spherical

symmetry), the mass conservation writes in spherical coordinates:

$$\frac{\partial \rho}{\partial t} + \frac{1}{r^2}\frac{\partial \rho u_r r^2}{\partial r} = 0 \tag{1.89}$$

To solve Eq. 1.89, the three-dimensional density profile is assumed to be the same as the one-dimensional one ρ_{1d} (previously computed with CANTERA) convected at the flame speed velocity $\rho_1/\rho_2 s_L^0$:

$$\rho(r) = \rho_{1d}(r - \frac{\rho_1}{\rho_2} s_L^0 t) \tag{1.90}$$

By injecting Eq. 1.90 in Eq. 1.89 an analytical solution for u_r can be derived:

$$u_r(r) = \frac{1}{\rho_{1d}(r) r^2}\frac{\rho_1}{\rho_2} s_L^0 \int_0^r r^2 \frac{\partial \rho_{1d}(r)}{\partial r}\ \mathrm{dr} \tag{1.91}$$

Equation 1.91 offers a correct behavior for limit cases ($r = 0$ and $r =$): one can show that if $r < R_f$, $u_r = 0$ (burnt gases do not move) and if $r > R_f$:

$$u_r(r = R) = \left(\frac{R_f}{R}\right)^2 \left(1 - \frac{\rho_1}{\rho_2}\right)\frac{dr}{dt} \quad ; \text{with } R > R_f \tag{1.92}$$

which is in agreement with the relation proposed by Poinsot and Veynante [20] for an infinitely thin flame. Figure 1.9 displays the radial velocity profile u_r and the one-dimensional density profile ρ_{1d} used to compute u_r.

1.7 Moving mesh

The computation of turbomachinery or piston engine requires to deal with moving boundaries (a rotation for the blades of the turbomachinery and a translation for the piston). In CFD codes, two numerical approaches are usually found:

1. **The Immersed Boundaries Method method (IMB) [75, 76]:** This method consists in imposing a given speed on an arbitrary surface (or immersed boundary) which does not necessarily coincide with the mesh. This speed is imposed by adding a right-hand-side source term in the momentum equation (see Eq. 4.2). Thus, complex moving geometries can be simulated even on fixed Cartesian grids. But an important drawback is that imposing characteristic boundary conditions is very difficult. During this thesis, one IBM method has been implemented and tested in the *AVBP* code. More details are given in Chapter 4.
2. **Arbitrary Lagrangian Eulerian (ALE) method [77]:** In this method each grid node i has a given displacement speed. This approach was first proposed by Hirt et al. [77] and has been implemented in *AVBP* by Moureau [78, 79]. The development of this method has been motivated by the relative facility to transpose the boundary conditions on fixed mesh to moving mesh. The movement of the mesh is supposed to be linear during a time step Δt so that the grid speed

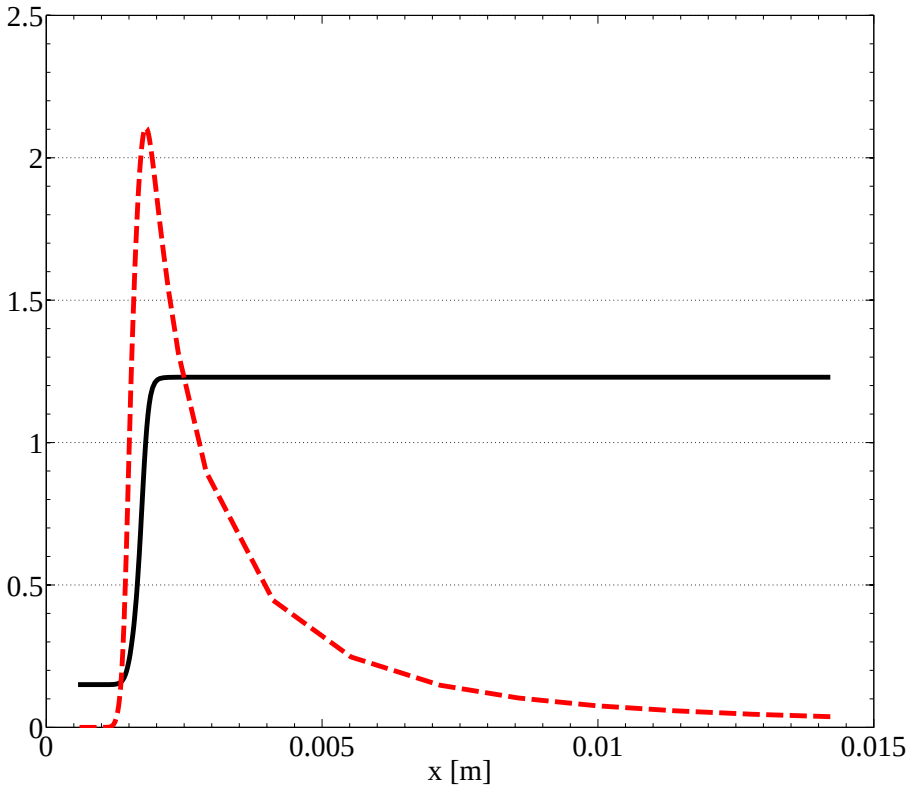

Figure 1.9: Ignition radial velocity profile. —— One dimensional density profile (input from CANTERA) ; ---- Radial velocity profile for a spherical flame.

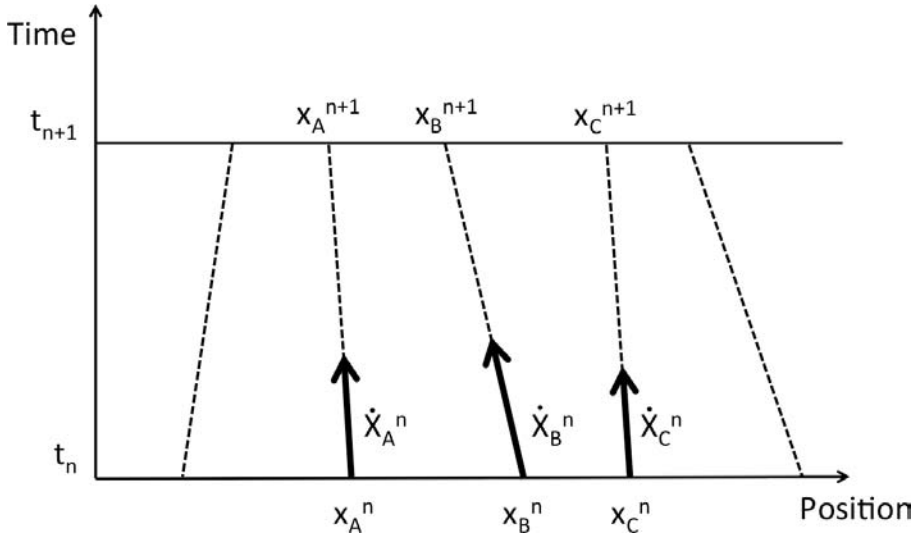

Figure 1.10: ALE method principle. Each grid node i has a given displacement speed X_i^n (constant during the iteration n).

X_i is piecewise constant. This approximation allows to integrate the governing equations on moving node-centered volumes and on moving cell-centered volumes. The ALE method was derived for all convective schemes in *AVBP*. All details of the derivation of the LW and TTGC schemes can be found in [78]. Corrective terms appear in this new formulation of the numerical schemes due to the mesh displacement and the mesh deformation. In this thesis this method is used for moving mesh (the computation of rotating axial fans) but without mesh deformation (more details are given in Chapter 5 where the TurboAVBP code is described).

1.8 Few words about the *AVBP* code

Historically, the *AVBP* code was started at CERFACS in January 1993 as an initiative of Michael Rudgyard and Thilo Schönfeld. The aim of this project was to build an efficient code handling unstructured grids of any cell type. Nowadays, *AVBP* is a parallel CFD code that solves the laminar and turbulent compressible reactive (or non-reactive) Navier-Stokes equations in two and three space dimensions[3]. It is also the baseline code of the ERC (European Research Council) advanced grant won by IMFT in 2013 on thermoacoustics (http://intecocis.inp-toulouse.fr).

The important development of the physical models done at CERFACS is completed by academics studies carried out at the IFP Energies Nouvelles, the EM2C lab of Ecole Centrale Paris (ECP) and the Institut de Mécanique des Fluides de Toulouse (IMFT). The ownership of AVBP is shared with IFP-Energies Nouvelles (IFP-EN), following an agreement of joint code development oriented towards piston engine applications. Important links to industry have been established with Safran Group (Snecma, Snecma DMS, Herakles, Turbomeca), Air Liquide, Gaz de France as well as with Alstom, Ansaldo and Siemens Power Generation.

[3]More details on *AVBP* here: http://www.cerfacs.fr/4-26334-The-AVBP-code.php.

CHAPTER 2

DESCRIPTION OF THE ORLÉANS BOMB CONFIGURATION

This chapter presents the Orléans bomb configuration conducted at the PRISME laboratory. Geometries of the vessel and the fans are presented. The basic operating procedure is described. Average and fluctuating measured velocity fields are also shown (non-reactive case) to illustrate the flow inside the spherical vessel.

The configuration studied in this thesis is the spherical vessel experiment of the PRISME laboratory in Orléans [80] (see Fig. 2.1). This apparatus is used to study both laminar and turbulent premixed spherical flames. The radius of the closed vessel

(a) Overview. (b) Inside view.

Figure 2.1: Experiment setup at PRISME laboratory (Orléans).

R_0 is 100 mm and it has six windows for experimental visualizations. Six fans are placed inside the spherical vessel. A mixture of fresh gases is trapped in the closed vessel and flames are ignited at the bomb center by a spark (electrodes can be seen in Fig. 2.1(b)). For laminar flames, fans are removed so that the flow inside the vessel remains immobile. For turbulent flames, fans rotate at a given speed to generate a turbulent flow inside the vessel. Once steady state is reached, flames are ignited. A wide range of operating points can be handled with this experimental device:

- four fan geometries have been tested,
- the fan rotation speed N_{fan} was varied from 1,000 rpm to 15,000 rpm,
- the pressure P_0 inside the vessel was varied from 1 bar to 10 bar,
- the temperature T_0 from 323 K to 473 K,
- the equivalence ratio Φ was varied from 0.6 to 1.5.

With such an experiment, initial conditions (temperature, pressure, composition, etc.) are well controlled.

In this thesis, only one fan geometry has been computed. Figure 2.2 presents the geometry of the fan. The fan is an axial turbomachinery device with an external diameter of 60 mm, the blade thickness is 0.8 mm and the fan length is 22 mm. At a rotation speed of $N_{fan} = 10,000$ rpm, the Reynolds number, based on tip radius (30 mm) and rotor tip speed (31.5 m/s) is about 60,000.

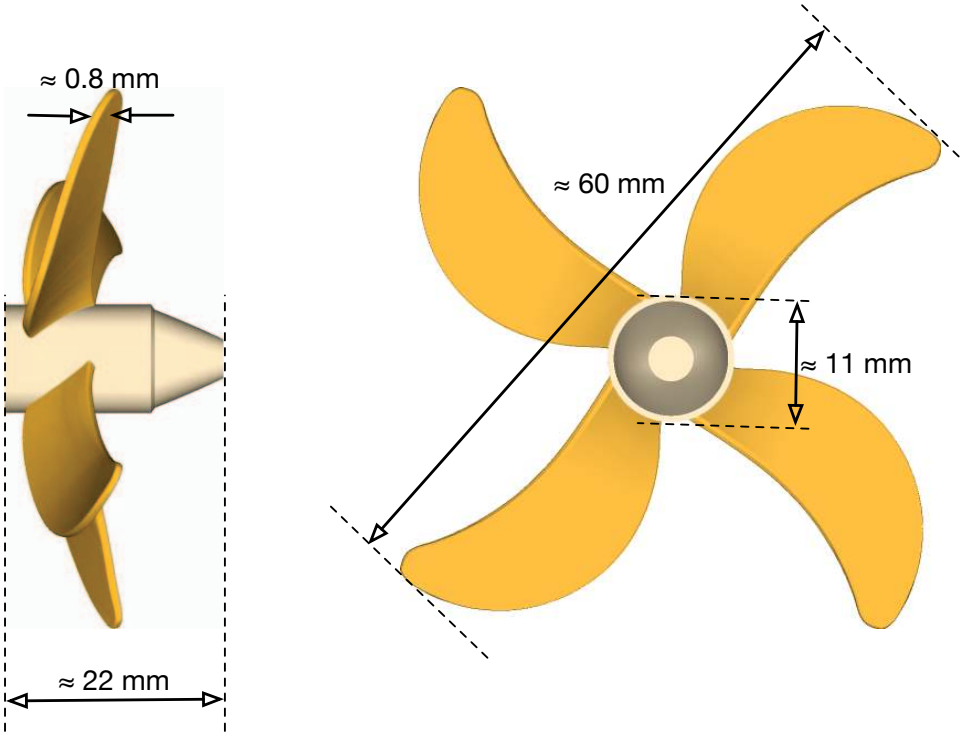

Figure 2.2: Characteristics of the fans.

Table 2.1 gives the position of each fan in the bomb. They are localized by a point F_b and a direction-vector $\vec{d_f}$. F_b is located at the center of the rear face of the fan and the direction-vector is aligned with the fan body (see Fig. 2.3). The point F_f is at the center of the front face of the fan. 4 fans are located in the $y + z = 0$ plane and distributed uniformly (90^o between each fan). The two others are located in the $x = 0$ plane and the axis of these fans ($\vec{d_f}$) is perpendicular to the $y + z = 0$ plane. The distance between two fans diametrically opposed (two times the distance from F_f to the bomb center B_0) is 93 mm and the distance from the wall bomb and fans backside is 31.5 mm.

To place fans in the numerical domain, only one fan is meshed in a reference position: the center of the fan backside F_b is located at the bomb center $B_0 = (0; 0; 0)$ and the fan direction-vector $\vec{d_f}$ is oriented in the $-z$ direction. Then this initial mesh is duplicated and each fan is moved at the right place following geometrical transformations (1 or 2 rotations and 1 translation). Table 2.2 summarizes these transformations for all fans.

Figure 2.4 displays average and fluctuating velocities measured using Particle Image Velocimetry (PIV) in the XY plane. Experimental measurements are performed in this

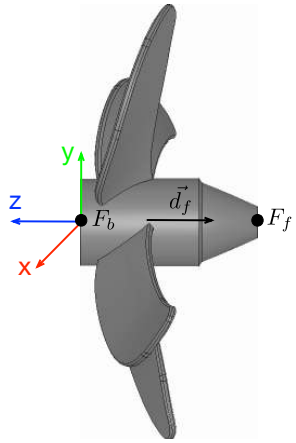

Figure 2.3: Reference initial fan position.

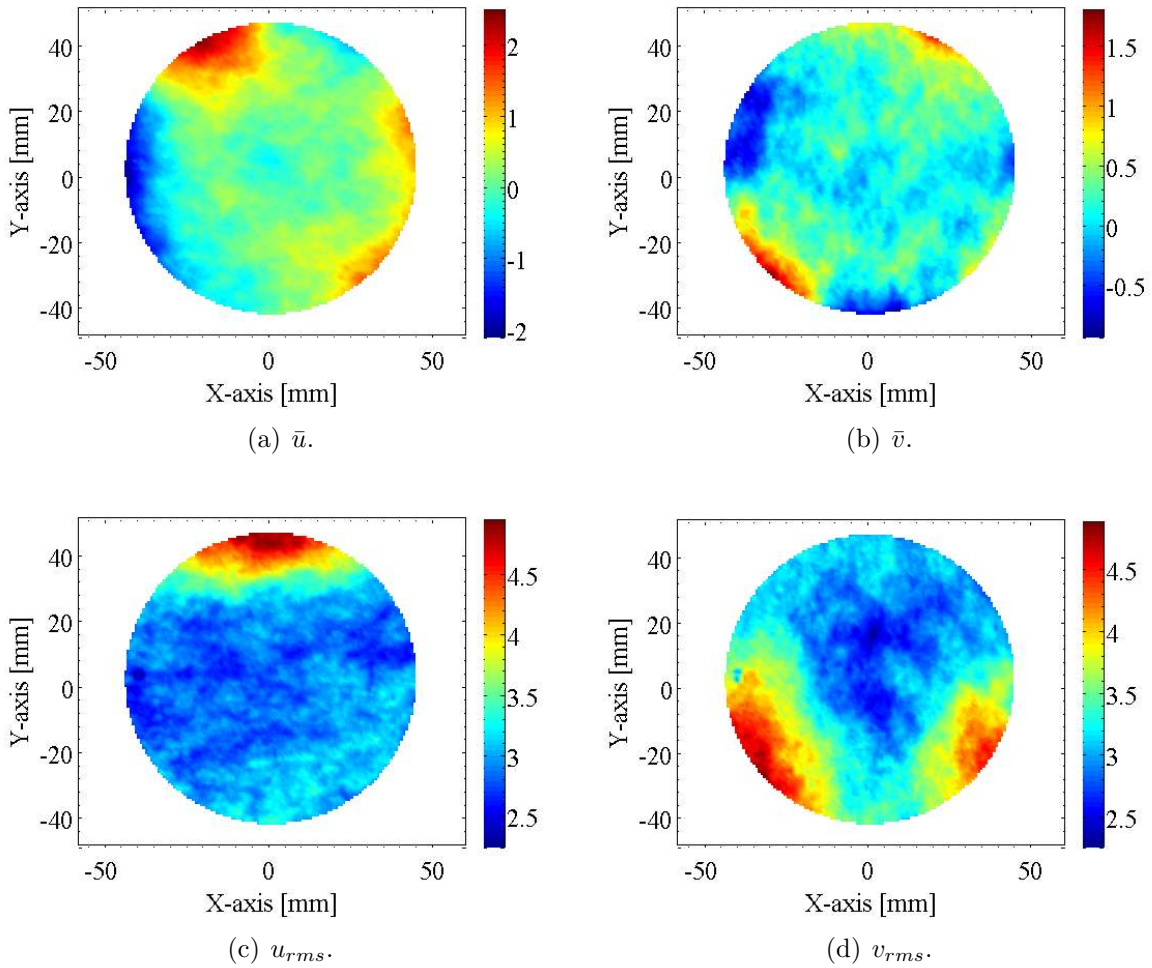

(a) $\bar{u}$. (b) $\bar{v}$.

(c) u_{rms}. (d) v_{rms}.

Figure 2.4: Experimental average and fluctuating velocities measured using PIV. Fans rotation speed is $N_{fan} = 10\ 000$ rpm.

	Direction-vector $\vec{\mathbf{d_f}}$:	Point $\mathbf{F_b}$:
Fan n^o 1	$\mathbf{n_1} = \begin{matrix} 0 \\ \overline{2}/2 \\ \overline{2}/2 \end{matrix}$	$F_b = (0; -48.36; -48.36)$
Fan n^o 2	$\mathbf{n_1} = \begin{matrix} 0 \\ -\ \overline{2}/2 \\ -\ \overline{2}/2 \end{matrix}$	$F_b = (0; 48.36; 48.36)$
Fan n^o 3	$\mathbf{n_1} = \begin{matrix} -0.709 \\ 0.500 \\ -0.497 \end{matrix}$	$F_b = (48.36; -34.20; 34.20)$
Fan n^o 4	$\mathbf{n_1} = \begin{matrix} 0.709 \\ -0.500 \\ 0.497 \end{matrix}$	$F_b = (-48.36; 34.20; -34.20)$
Fan n^o 5	$\mathbf{n_1} = \begin{matrix} 0.709 \\ 0.500 \\ -0.497 \end{matrix}$	$F_b = (-48.36; -34.20; 34.20)$
Fan n^o 6	$\mathbf{n_1} = \begin{matrix} -0.709 \\ -0.500 \\ 0.497 \end{matrix}$	$F_b = (48.36; 34.20; -34.20)$

Table 2.1: Position of each fan in the bomb. Positions are given defined using a direction-vector $\mathbf{d_f}$ and a point located at the center of the rear face of the fan (the coordinates of the bomb center are (0;0;0)).

plane since there is no fan in front of corresponding windows which enable the laser sheet to go through the closed vessel. The full geometry of this experiment is computed in this study: only the rods which maintain fans in the bomb have been removed in simulations compared to the experimental device. This simplification has been done in order to avoid the sliding condition between the rear face of the fan and the extremity of the rod, which is not easy to handle in CFD codes. This simplification should have a very limited impact on the flow inside the vessel. Figure 2.5 presents the numerical configuration.

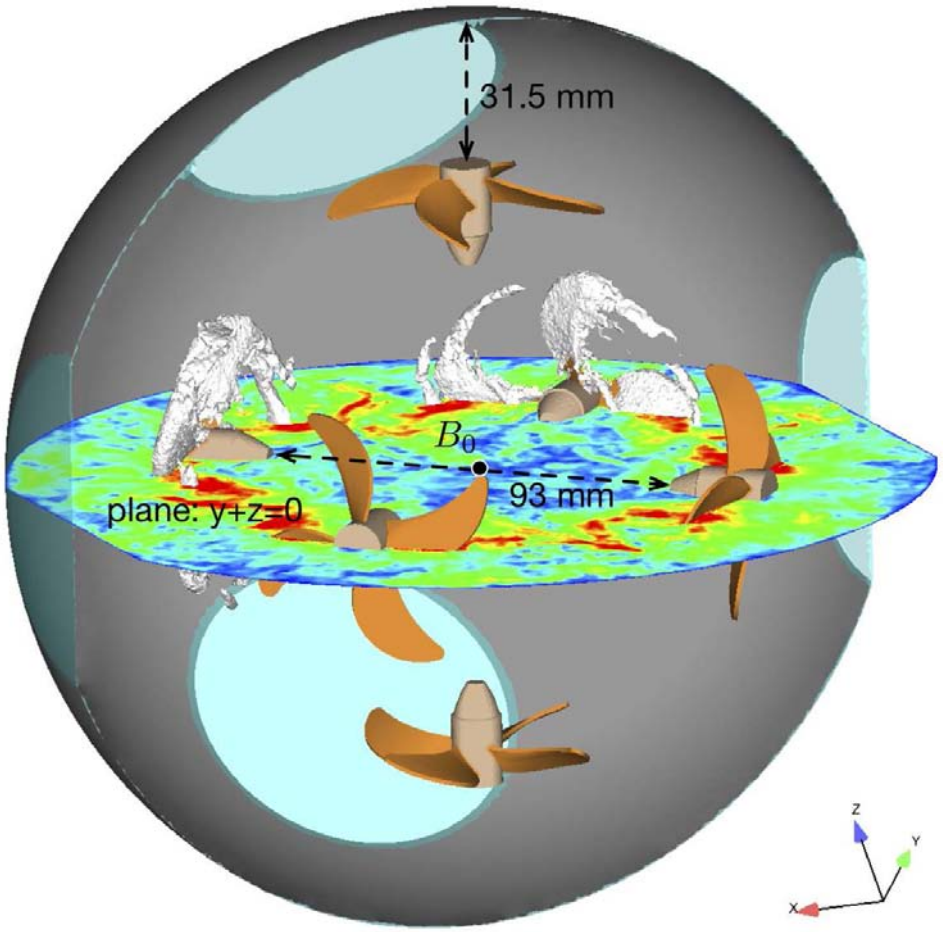

Figure 2.5: Sketch of the geometry computed. Velocity instantaneous field in the central plane and isosurfaces of vorticity in fan regions (for 2 fans only).

	Transformation n^o 1: rotation	**Transformation n^o 2 : rotation**	**Transformation n^o 3: translation (mm)**
Fan n^o 1	$\mathbf{n_1} = \begin{matrix}1\\0\\0\end{matrix}$; $\phi = 135\frac{\pi}{180}$	X	$T = \begin{matrix}0\\-48.36\\-48.36\end{matrix}$
Fan n^o 2	$\mathbf{n_1} = \begin{matrix}1\\0\\0\end{matrix}$; $\phi = -45\frac{\pi}{180}$	X	$T = \begin{matrix}0\\48.36\\48.36\end{matrix}$
Fan n^o 3	$\mathbf{n_1} = \begin{matrix}0\\1\\0\end{matrix}$; $\phi = 55\frac{\pi}{180}$	$\mathbf{n_2} = \frac{1}{\sqrt{(0.7^2+1)}}\begin{matrix}-0.7\\0\\1\end{matrix}$; $\phi = -30\frac{\pi}{180}$	$T = \begin{matrix}48.36\\-34.20\\34.20\end{matrix}$
Fan n^o 4	$\mathbf{n_1} = \begin{matrix}0\\1\\0\end{matrix}$; $\phi = 55\frac{\pi}{180}$	$\mathbf{n_2} = \frac{1}{\sqrt{(0.7^2+1)}}\begin{matrix}-0.7\\0\\1\end{matrix}$; $\phi = -210\frac{\pi}{180}$	$T = \begin{matrix}-48.36\\34.20\\-34.20\end{matrix}$
Fan n^o 5	$\mathbf{n_1} = \begin{matrix}0\\1\\0\end{matrix}$; $\phi = -55\frac{\pi}{180}$	$\mathbf{n_2} = \frac{1}{\sqrt{(0.7^2+1)}}\begin{matrix}0.7\\0\\1\end{matrix}$; $\phi = 30\frac{\pi}{180}$	$T = \begin{matrix}-48.36\\-34.20\\34.20\end{matrix}$
Fan n^o 6	$\mathbf{n_1} = \begin{matrix}0\\1\\0\end{matrix}$; $\phi = -55\frac{\pi}{180}$	$\mathbf{n_2} = \frac{1}{\sqrt{(0.7^2+1)}}\begin{matrix}0.7\\0\\1\end{matrix}$; $\phi = 210\frac{\pi}{180}$	$T = \begin{matrix}48.36\\34.20\\-34.20\end{matrix}$

Table 2.2: Description of the transformations to place fans in the bomb (the coordinates of the bomb center are (0;0;0)).

CHAPTER 3

LAMINAR FLAME PROPAGATING IN A SPHERICAL BOMB

Contents

During the ICAMDAC project, an important part of the work has been devoted to the characterization of turbulent flames in the turbulent bomb of Orléans. Before doing this, performing the same exercise for a laminar flame had to be done both experimentally and numerically, this is what the present chapter describes. Interestingly, even though the determination of the flame speed of a spherical laminar flame might appear as one of the 'easy' problems in combustion science, it is not and multiple controversial issues must be discussed, many of them due to the importance of stretch effects and of the finite thickness of the flame front. These issues were studied during this PhD work and we used theory and simulation to revisit methods which can be used experimentally to analyze data (flame radii vs time and bomb pressure). This chapter discusses this work which has also appeared in Combustion and Flame in 2013 [81].

3.1 Introduction

The experimental determination of the laminar consumption flame speed, s_L^0, is an overarching problem in combustion [82]. Indeed the knowledge of the rate at which the fresh gases are consumed is instrumental in the study of flame dynamics as well as the development of kinetic schemes. For modeling purposes, the laminar flame speed is the central ingredient of most turbulent-combustion models [83, 84, 21, 85, 20].

Despite the apparent simplicity in the formulation of the problem, measuring accurately s_L^0 is a delicate task. Since the early attempts, which date as far back as a hundred and fifty years ago [86, 87, 88, 89, 23], a variety of methods have been devised. These methods find their roots in analytical solutions of reacting fluid mechanics but most of them suffer from approximations or experimental difficulties that strongly affect their precision. For example, the flat flame propagating in a tube is strongly perturbed by instabilities or the presence of walls [90, 91]. Other techniques require extrapolation or correcting factors in order to account for the effects of curvature or strain [92, 93, 64, 94].

In the present work, we revisit the classical technique of the *`spherical flame in a bomb* (Fig. 3.1): in a closed vessel, a mixture of fresh gases is ignited, a spherical flame develops and its radius, $R(t)$, is measured versus time using simple optical methods. Such experiments are fairly easy to conduct. Moreover initial conditions (temperature, pressure, composition, *etc.*) are well controlled and can be extended to high temperatures and pressures.

However, extracting flame speed values from spherical flames is a much more difficult exercise which has lead to multiple controversies in the past [95, 96, 97, 98, 99]. Two quantities can be measured experimentally to construct a flame speed in a bomb: (1) the flame radius evolution $R(t)$ and (2) the bomb pressure $P(t)$. Most existing methods use one of these two quantities (or the two) to deduce flame speeds[1].

Assuming that $R(t)$ and/or $P(t)$ are available, two independent steps are then required

[1]Recent methods using direct flow and front speed measurements have begun in the last two years [100] but they are not discussed here.

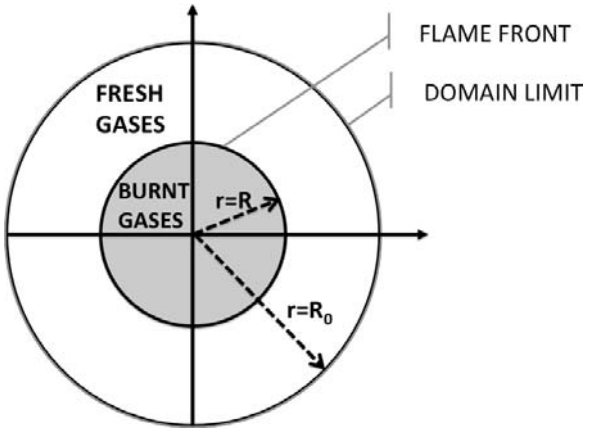

Figure 3.1: Generic configuration for a spherical flame in a bomb.

to obtain flame speeds:

- STEP I: the instantaneous flame speed must be obtained from $R(t)$ and/or $P(t)$,
- STEP II: since a spherical flame is a stretched flame, the speed which is measured in STEP I is not the unstretched laminar flame speed s_L^0 but a stretched flame speed $s_L(\kappa)$ where $\kappa = 2/R\ dR/dt$ is the instantaneous flame stretch. Therefore a model for $s_L(\kappa)$ is needed to obtain s_L^0. This model is usually based on a Markstein-type correlation [98, 101, 102], for example the linear expression:

$$s_L(\kappa) = s_L^0 - \mathcal{L}\kappa \tag{3.1}$$

where $\mathcal{L}$ is the Markstein length which becomes an additional unknown quantity to determine [103]. In the past five years, other expressions have also been proposed to replace Eq. 3.1 (mostly based on the non linear form of s_b advocated by Kelley and Law [104] and the Orléans group [98]).

This work does not discuss STEP II and focuses on STEP I. During this step, approximations between the various flame speeds characterizing a front are utilized and the present work shows that they can have a direct impact on the result. Indeed, the only speed which is unambiguously measured in a bomb is the flame speed of the front relative to the burnt gases $s_b(\kappa) = dR/dt$ because the burned gases do not move.

Obtaining a relation between $s_b(\kappa)$ and $s_L(\kappa)$ is a delicate task because it requires well chosen assumptions. A classical, albeit approximate, relation used in multiple recent studies is:

$$s_L(\kappa) = \frac{\rho_b}{\rho_u} s_b(\kappa) \tag{3.2}$$

where ρ_b is the density of the burnt gases and ρ_u that of the unburnt gases.

In addition to stretch, other factors modify the flame speed in a spherical explosion [104, 98, 105, 106]:

1. In the early stages, the energy of the spark modifies the burnt gases temperature as well as the flame speed.

2. Curvature effects induce preferential diffusion phenomenon (for non unity Lewis number) which also influence the evolution of the flame and the burnt gases temperature. In Eq. 3.2, most authors recognize that s_b depends on stretch but neglect the influence of stretch on ρ_b. However, the burnt gases density, like the burnt gases temperature, is affected by stretch too. And even if this effect is smaller than the effect of κ on s_L it must be taken into account.
3. For large radii, the confinement of the flame in a closed vessel influences ρ_u and ρ_b and therefore changes the flame speed.

The objective of this chapter is to revisit the formulation of Eq. 3.2 and to propose theoretical expressions for the consumption flame speed that alleviate the problems of Eq. 3.2. The derivations are presented in Sec. 3.2 and Direct Numerical Simulations (DNS) are conducted in Sec. 3.3 where the formulae can be compared to the true consumption speed based on the integral of the reaction rate [20] in the case of a cylindrical flame. All derivations are performed in two cases (see Fig. 3.2): (1) INF where the flame propagates in an infinite medium, confinement effects do not exist and curvature effects due to non-unity Lewis number can be isolated, and (2) BOMB where the flame propagates in a closed bomb where both curvature and confinement affect the burnt and fresh gases density.

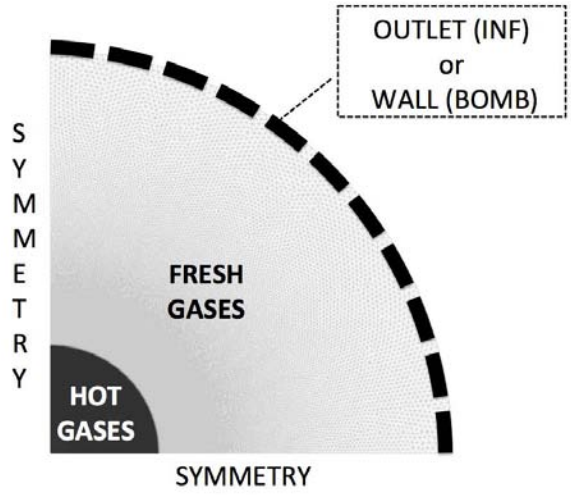

Figure 3.2: Configuration for expanding flames.

3.2 Theoretical results

Deriving an expression for flame speeds in a spherical or cylindrical flame (cf. Fig. 3.1) is a complex exercise [104, 107, 108, 109]. It is presented here without invoking an infinitely-thin-flame assumption. The formulae for the consumption flame speed presented in this work are based on the conservation equation for the species. The definition of the consumption flame speed in a spherical flame is obtained from the integral of the reaction

rate $\dot{\omega}_k$ of one species k (fuel or products for example):

$$s_c = \frac{1}{\rho_u (Y_k^b - Y_k^u) R^2} \int_0^{R_0} \dot{\omega}_k r^2 dr \tag{3.3}$$

where ρ_u is the fresh gases density, Y_k^u and Y_k^b are the mass fraction of species k in the fresh and burnt gases respectively and R_0 is the integration boundary[2] ($R_0 > R$). Since $\dot{\omega}_k$ can not be measured experimentally, other indirect expressions are required for s_c. They can be derived by starting from the conservation equation of species k (see Eq. 1.4):

$$\frac{\partial \rho Y_k}{\partial t} + \overline{\nabla} \left(\rho(\mathbf{u} + \mathbf{V_k}) Y_k\right) = \dot{\omega}_k \tag{3.4}$$

$\mathbf{V_k}$ is the diffusion velocity of species k:

$$\mathbf{V_k} = -D_k \frac{\nabla X_k}{X_k} + \mathbf{V_c} \tag{3.5}$$

where $\mathbf{V_c}$ is the correction velocity to ensure mass conservation (see Eq. 1.9). Integrating Eq. 3.4 over the control volume ($0 \leq r \leq R_0$) yields:

$$\frac{dM_k}{dt} + 4\pi R_0^2 \rho_u Y_k(r = R_0)[u_r(r = R_0) + V_{k\,r}(r = R_0)] = \int_0^{R_0} \dot{\omega}_k 4\pi r^2 dr \tag{3.6}$$

where M_k is the total mass of species k in the domain: $M_k = \int_V \rho Y_k dV$. The second left hand side term represent the flux of species k leaving the domain at $r = R_0$. Including the definition of the flame speed s_c (Eq. 3.3) in Eq. 3.6 gives:

$$\frac{dM_k}{dt} + 4\pi R_0^2 \rho_u Y_k(r = R_0)[u_r(r = R_0) + V_{k\,r}(r = R_0)] = s_c 4\pi R^2 \rho_u [Y_k^b - Y_k^u] \tag{3.7}$$

To obtain an explicit relation linking s_c to R, the second left hand side term in Eq. 3.7 must be cancelled. So the optimal choice of the species k depends on the configuration:

- In a hypothetical infinite medium (INF configuration) $u_r(r = R_0) > 0$. But if a product is used ($Y_p(r = R_0) = 0$), as long as the flame has not reached the position $r = R_0$ the second term on the LHS of Eq. 3.7 is also cancelled.
- In a closed vessel (BOMB configuration) $u_r(r = R_0) = 0$ and $V_{k\,r}(r = R_0) = 0$, so that any species can be used in Eq. 3.7.

At this point in the derivation a consumption speed has been defined but no assumptions were made. The idea is now to link M_k to the flame radius R in order to get an expression for s_c that is accessible to experimental measurements. Two cases are distinguished depending on which species k is used:

[2] R_0 goes to the infinity for the case of a flame propagating in an infinite medium.

1. **A product** ($k = p$): a flame radius R_p based on the mass of products is defined as:

$$R_p^3 = \frac{M_p}{\frac{4\pi}{3}\bar{\rho}_b Y_p^b} \tag{3.8}$$

where Y_p^b is the mass fraction of the product (*e.g.* CO_2) in the burnt gases and $\bar{\rho}_b$ is the burnt gases density (averaged spatially between $r = 0$ and $r = R_p$). Eq. 3.8 does not imply that the flame is thin: the mass of products M_p is defined unambiguously and R_p is the equivalent` radius of a sphere containing this mass. Combining Eqs. 3.7 and 3.8 to eliminate M_p yields:

$$s_c^p = \frac{\bar{\rho}_b}{\rho_u}\frac{dR_p}{dt} + \frac{R_p}{3\rho_u}\frac{d\bar{\rho}_b}{dt} \tag{3.9}$$

where the product mass fraction Y_p^b is supposed to be constant. Eq. 3.9 is derived without assumptions on the domain where the flame propagates: it can be used in a bomb of any size or in an infinite domain [110].
In a simulation Eq. 3.9 can be used directly because $\bar{\rho}_b$, ρ_u and R_p can be measured. In an experiment, however, assumptions on $\bar{\rho}_b$ and ρ_u are required. The most usual is to suppose that densities are constant (in space and time). Thus, it is generally assumed than ρ_u remains equal to its initial value (neglecting confinement effects, as expected if the bomb is sufficiently large). And $\bar{\rho}_b$ is obtained by assuming that its value does not vary with r from 0 to R_p and is equal to the burnt gases density at equilibrium ρ_b^{eq} so that Eq. 3.9 leads to:

$$s_c^{p\ expe} = \frac{\rho_b^{eq}}{\rho_u(t=0)}\frac{dR_p}{dt} \tag{3.10}$$

which is the expression used in most studies[3] .

2. **The fuel** ($k = f$): in an infinite domain, fuel can not be used in Eq. 3.7 because its flux is not zero at $r = R_0$. However, in a bomb where $\mathbf{u}(r = R_0) = 0$ and $\mathbf{V_k}(r = R_0) = 0$, fuel can be used in Eq. 3.7 leading to a formulation given by [111]. In this case, the radius of the flame based on the mass of fuel is defined by [4]:

$$R_f^3 = R_0^3 - \frac{M_f}{\frac{4\pi}{3}\rho_u Y_f^u} \tag{3.11}$$

[3]Note that an intermediate formulation could be $s_c^{p,expe,2} = \bar{\rho}_b/\rho_u dR_p/dt$ if a good approximation can be found for $\bar{\rho}_b$. We tested this solution but it shows that in Eq. 3.9 a good evaluation of both $\bar{\rho}_b$ and $d\bar{\rho}_b/dt$ is important. In practice, even if this solution had worked in the DNS where we can have access to ρ_b, it would have been difficult to use in an experiment since ρ_b is hardly measurable. $s_c^{p,expe,2}$ is not discuss anymore in this work.

[4]The present derivation is valid for lean flames and is based on the fuel balance. For rich flames, a similar derivation based on oxygen leads exactly to the same expression

where Y_f^u is the mass fraction of the fuel in the unburnt gases, which is constant. Combining Eqs. 3.7 and 3.11 yields:

$$s_c^f = \frac{dR_f}{dt} - \frac{R_0^3 - R_f^3}{3R_f^2}\frac{1}{\rho_u}\frac{d\rho_u}{dt} \tag{3.12}$$

Assuming an isentropic compression for the fresh gases which is a very reasonable approximation here, one has $(1/\rho_u)d\rho_u/dt = 1/(\gamma_u P)\ dP/dt$, where γ_u is the ratio of the heat capacities in the fresh gases. Equation 3.12 is then recast into:

$$s_c^f = \frac{dR_f}{dt} - \frac{R_0^3 - R_f^3}{3R_f^2}\frac{1}{\gamma_u P}\frac{dP}{dt} \tag{3.13}$$

Note that Eqs. 3.10 and 3.13 are very different: Eq. 3.13 includes no density ratio in front of dR_f/dt which suggests that the pressure term dP/dt is important. Both expressions use a flame radius which is defined differently. For Eq. 3.10, the flame radius R_p is defined from the mass of products while for Eq. 3.13, the flame radius R_f is obtained from the mass of fuel. In practice, experimentally, the flame fronts are thin and it is probably impossible to distinguish R_p and R_f which are both equal to the observed flame radius R. In other words, an infinite thin flame assumption is implicitly done when post processing experiments. Eq. 3.13 can be used in bombs but not in an infinite medium. It has been previously derived [108, 107, 111] but it does not seem to be used, even though it is directly accessible in an experiment because it requires only R_f and P versus time as input data. It will be shown in Sec. 3.3.2.c using DNS that Eq. 3.13 is insensitive to curvature and confinement effects, unlike Eq. 3.10.

3.3 Validation with numerical simulations

Direct Numerical Simulations are performed using the *AVBP* code [53, 112, 113] with a third-order (in space and time) scheme called TTGC [52]. Flames are ignited using the procedure presented in Sec. 1.6.2.

The definition of the true consumption speed, given in Eq. 3.3, can not be used in an experiment but can easily be computed from a DNS. Eqs. 3.9, 3.10 and 3.13 are compared here with the true consumption flame speed s_c defined by Eq. 3.3. All flame speed expressions derived in Sec. 3.2 are summarized in Tab. 3.1.

In order to address both confinement and Lewis number effects, two simulations with different fuels are conducted: a lean methane/air ($Le_{CH_4} = 0.996$, $\Phi = 0.8$) flame and a lean octane/air flame ($Le_{C_8H_{18}} = 2.78$, $\Phi = 0.8$). The Lewis number compares thermal diffusion D_{th} to the diffusion coefficient of species k, D_k (see Sec. 1.3.2). The thermodynamic conditions for all simulations presented in this chapter are $\Phi = 0.8$, $P_0 = 101325$ Pa and $T_0 = 323$ K. In these conditions, the thermal flame thickness, defined by $\delta_l^0 = (T_b - T_u)/\max(dT/dr)$ is 0.43 mm for octane and 0.51 mm for methane.

Three configurations are also compared. First, a one-dimensional configuration is computed to mimic the propagation of a planar flame in an infinite medium. Then, two

Symbol	Name	Expression	Validity
s_c	True consumption speed	$s_c = \frac{1}{\rho_u (Y_k^b - Y_k^u) R^2} \int_0^{R_0} {}_k r^2 dr$ (Eq. 3.3)	Definition
s_c^p	Speed based on conservation of burnt gases	$s_c^p = \frac{\bar{\rho_b}}{\rho_u} \frac{dR_p}{dt} + \frac{R_p}{3\rho_u} \frac{d\bar{\rho_b}}{dt}$ (Eq. 3.9)	Bombs or infinite medium
$s_c^{p\ expe}$	Speed based on conservation of burnt gases & constant densities assumption	$s_c^{p\ expe} = \frac{\rho_b^{eq}}{\rho_u(t=0)} \frac{dR_p}{dt}$ (Eq. 3.10)	Bombs of very large size or infinite medium
s_c^f	Speed based on fuel conservation	$s_c^f = \frac{dR_f}{dt} - \frac{R_0^3 - R_f^3}{3R_f^2} \frac{1}{\gamma_u P} \frac{dP}{dt}$ (Eq. 3.13)	Bombs only (of any size)

Table 3.1: Consumption flame speed expressions in laminar deflagrations. R_0 is the radius of the spherical bomb. R, R_p and R_f are evaluations of the flame radius. ρ_b^{eq} is the burnt gases density at equilibrium.

cylindrical configurations are tested: the first one mimics the propagation of cylindrical flames in an infinite medium (called INF) while the other one corresponds to ignition in a closed vessel (called BOMB).

3.3.1 One-dimensional propagation

First, a one-dimensional simulation of a laminar premixed flame is performed to study a flame propagation with no curvature and confinement effects.

3.3.1.a Numerical configuration

A one-dimensional propagating flame is considered to mimic the propagation of a planar flame. The sketch of the configuration is presented in Fig. 3.3. Only octane is used in this configuration ($Le_{C_8H_{18}} = 2.78$) and the flame propagates from left to right. The length

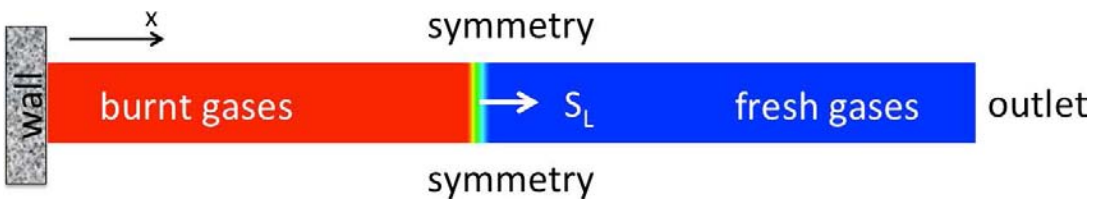

Figure 3.3: Sketch of the one-dimensional configuration.

of the domain is 4 cm and the cell size is 20 μm to ensure that the flame front is fully resolved: 20 points in the thermal flame thickness ($\delta_l^0 = 0.43$ mm for octane). The left

boundary is a wall and the right one is a non reflecting outlet [114]. This configuration looks like a spherical propagation because the velocity of the burnt gases is zero. However there is no curvature effect because the flame is flat (one-dimensional) and there is no confinement because the right boundary is an outlet which mimics an infinite domain (pressure does not go up). The flame is initialized with a burnt gases kernel (note that the velocity profile is not initialized here: it is set to zero in the whole domain). The temperature of the burnt kernel is the adiabatic flame temperature. We will see that this temperature plays an important role in turbulent case (Sec. 7). For laminar flames, its influence was not tested to avoid the introduction of an additional parameter. This simplification is justified if the spark energy remains small to avoid overdriven` flames where the initial kernel is warmer than the adiabatic flame temperature.

3.3.1.b Results

Figure 3.4 shows temperature profiles along the x-axis at several times when the flame propagates. Figure 3.4 confirms that if the flame is flat (not curved), non unity Lewis

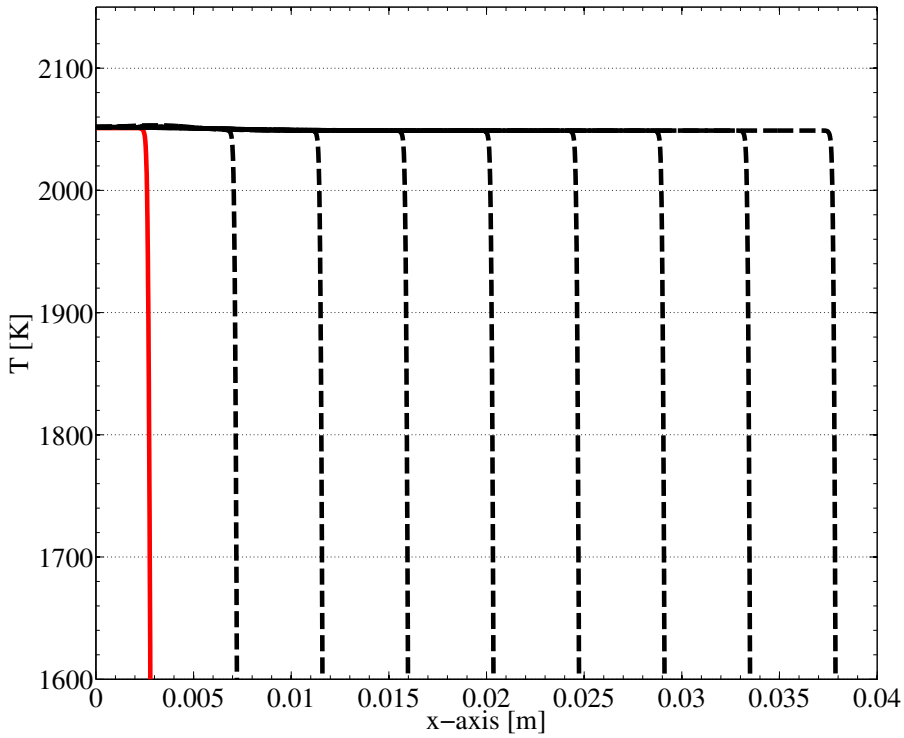

Figure 3.4: Temperature profiles versus the flame radius R when the octane / air flame propagates. —— Initial solution ($T_b = T_{ad}$) ; ---- Temporal evolution: time varies from $t = 0$ to $t = 20$ ms by step of 2 5 ms.

effects do not appear and the burnt gases temperature remains constant and equal to the adiabatic burnt gases imposed in the initial kernel.

As a result, Fig. 3.5 displays the consumption speed versus time[5]. If there is no

[5]In a one-dimensional framework, Eq. 3.3 writes $s_c = \frac{1}{\rho_u (Y_k^b - Y_k^u)} \int_{-\infty}^{-\infty} {}_k dx$ and Eq. 3.10 writes

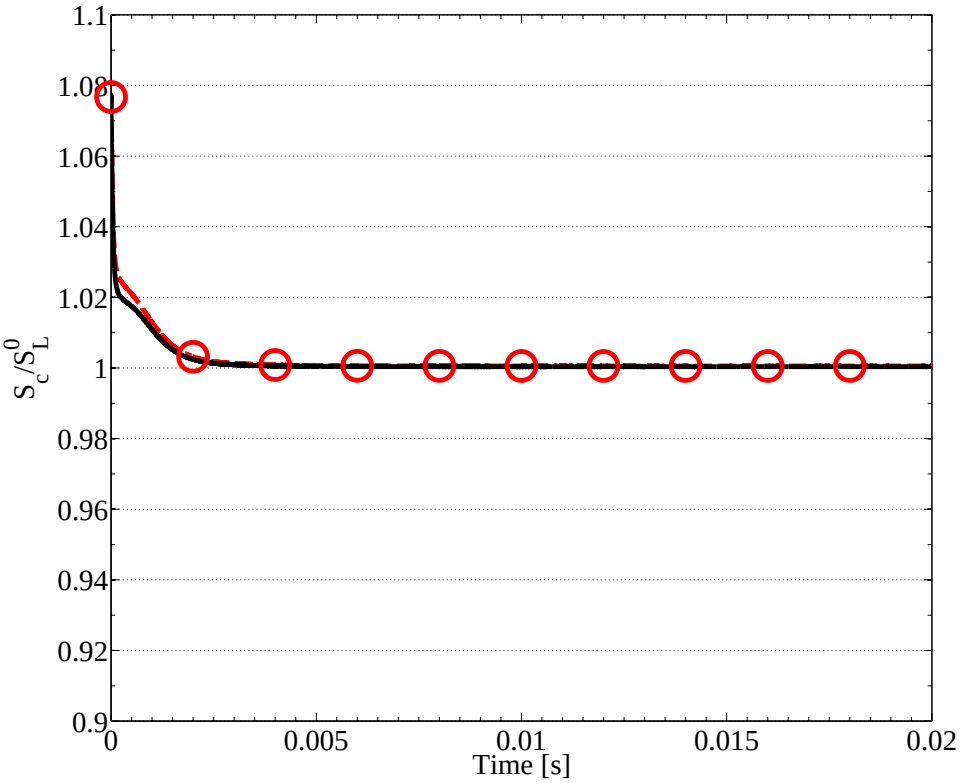

Figure 3.5: Normalized consumption speed versus time for an octane/air flame in a configuration without compression and confinement with $s_L^{0\ C8H18} = 0\ 264$ m/s. —— s_c (Eq. 3.3) ; -⊖- $s_c^{p\ expe}$ (Eq. 3.10).

confinement and curvature effects, the classical relation Eq. 3.10 predicts very well the true consumption flame speed Eq. 3.3 (even for non unity Lewis fuel).

3.3.2 Cylindrical configurations

Simulations of spherical flames are presented here. First the two numerical configurations (BOMB and INF) are presented then results are discussed.

3.3.2.a Numerical configurations

A cylindrical flame propagating in a domain of size $R_0 = 10$ cm is considered (Fig. 3.2). When non reflecting boundary conditions [114] are used at $r = R_0$, the configuration mimics an infinite medium where pressure is constant (INF configuration). If a wall is setup at $r = R_0$, the configuration corresponds to a closed vessel (BOMB configuration). Table 3.2 summarizes these two configurations. Using symmetry boundary conditions,

Case	**Boundary conditions at $r = R_0$**	**Expression**
INF	Non reflecting outlet at $P = P_0$	Infinite medium, constant pressure
BOMB	$\mathbf{u} = 0$	Bomb of radius R_0, pressure goes up

Table 3.2: Computed configurations: in real systems, only the BOMB case can be tested but in simulations both can be computed.

only a quarter of the bomb is meshed. The grid is refined within a radius $r < 30$ mm from the center with a cell size $\Delta = 25\mu$m to ensure that the flame front is fully resolved: 17 to 20 points in the thermal flame thickness ($\delta_l^0 = 0.43$ mm for octane and $\delta_l^0 = 0.51$ mm for methane). As suggested by Bradley [110], the time interval used for plots corresponds to phases where the flame has grown enough ($R > 5.5$ mm) to have forgotten initial conditions but is still small enough compared to the size of the bomb ($R < 26.5$ mm) to avoid wall effects and remain perfectly spherical. The flame is initialized by introducing a sphere of burnt gases of radius 1 mm. As presented in Sec. 1.6.2, temperature, density and species mass fractions come from a previous computation (CANTERA) and the velocity profile is initialized following the relation Eq. 1.91.

3.3.2.b Curvature effects only: cylindrical flame in an infinite medium

Numerical simulations are performed now in an idealized spherical case (INF configuration) where there is no compression in order to study the impact of the curvature effects only. This is achieved by using a non reflecting outlet boundary condition [114] (*cf.* Fig. 3.2) at $r = R_0$. Thus, pressure, fresh-gases temperature and density remain constant. In this configuration, there is a flux of fresh gases through the boundary $r = R_0$ so that Eq. 3.9, based on the conservation of the product species is used. Equation 3.13 can not be used in the INF configuration. Consequently, Fig. 3.6 presents the comparison of

$s_c^{p,expe} = \frac{\rho_b^{eq}}{\rho_u(t=0)} \frac{dX_p}{dt}$ where X_p is the position of the flame according to the mass of product.

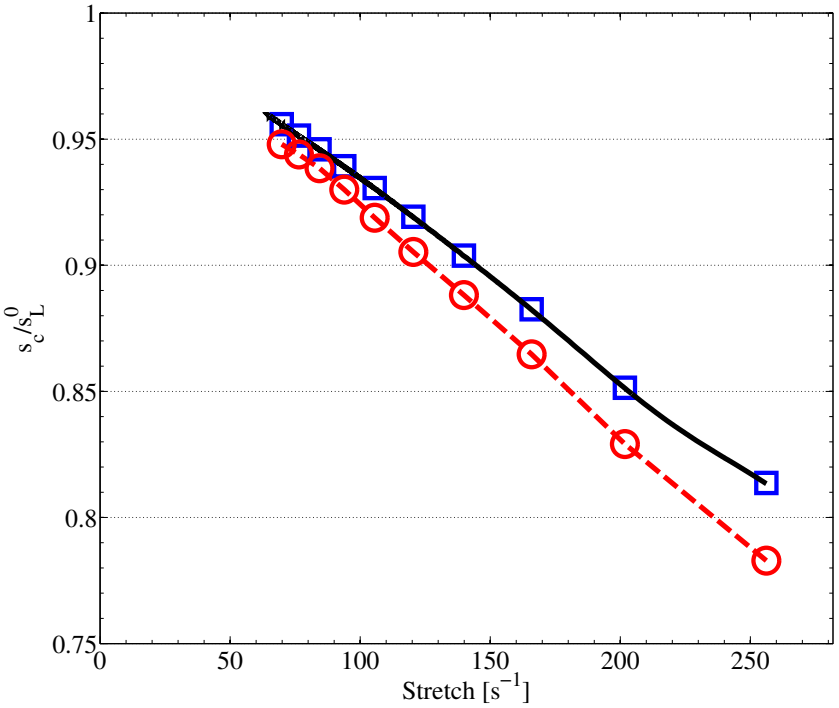

(a) Octane.

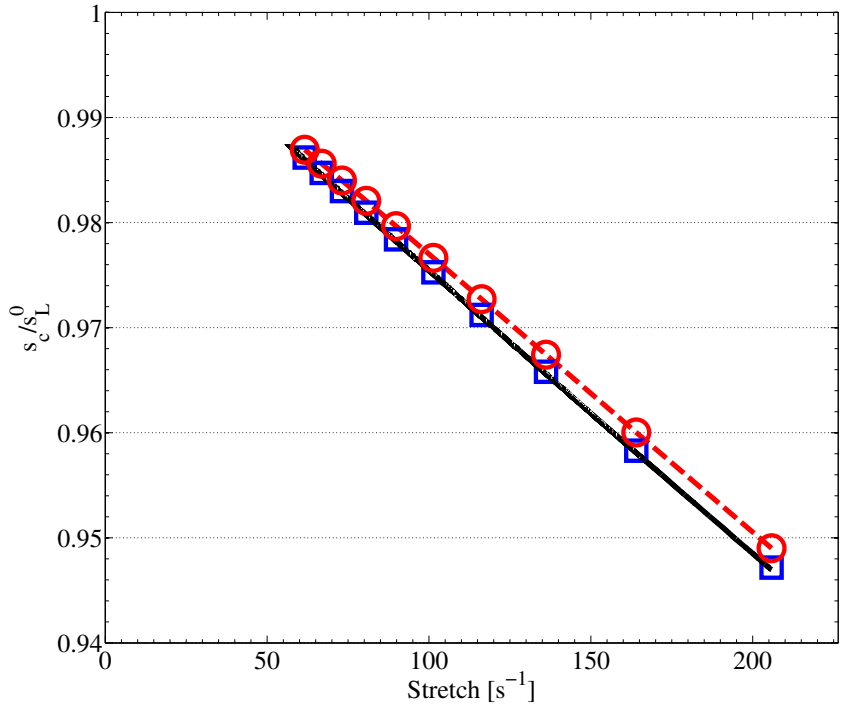

(b) Methane.

Figure 3.6: Normalized consumption speed versus stretch for a configuration without compression (INF) with $s_L^{0\,CH4} = 0\ 255$ m/s and $s_L^{0\,C8H18} = 0\ 264$ m/s : —— s_c (Eq. 3.3) ; -⊖- $s_c^{p\ expe}$ (Eq. 3.10) ; □ s_c^p (Eq. 3.9).

Eq. 3.9 and Eq. 3.10 with the true consumption flame speed s_c (Eq. 3.3) for both fuels.

Equation 3.9 matches the true consumption speed for both fuels. Moreover all curves extrapolate to s_L^0 at $\kappa = 0$. Interestingly, the simplified expression used by most authors (Eq. 3.10) shows a different behavior for the two fuels: while for methane it matches the true consumption speed, except in the very early times, for octane, there is a clear gap between the two curves. In other words, Eq. 3.10 does not predict the correct stretched flame speed for the octane / air flame. This phenomenon is due to a Lewis number effect. Unlike the planar flame of Sec. 3.3.1.b, the present flame is stretched and this affects the burnt gases temperatures. When the flame is stretched, the burnt gases temperature is not equal to the adiabatic burnt gases temperature T_{ad}. Figure 3.7 displays various temperature profiles versus radius r when the octane / air flame propagates. Shortly after ignition, the maximum temperature drops from equilibrium $T_{ad} = 2051$ K to about 1840 K. When the flame propagates, the temperature goes up again and comes back to T_{ad} at the end of the simulation. These changes are due to stretch: like the flame speed,

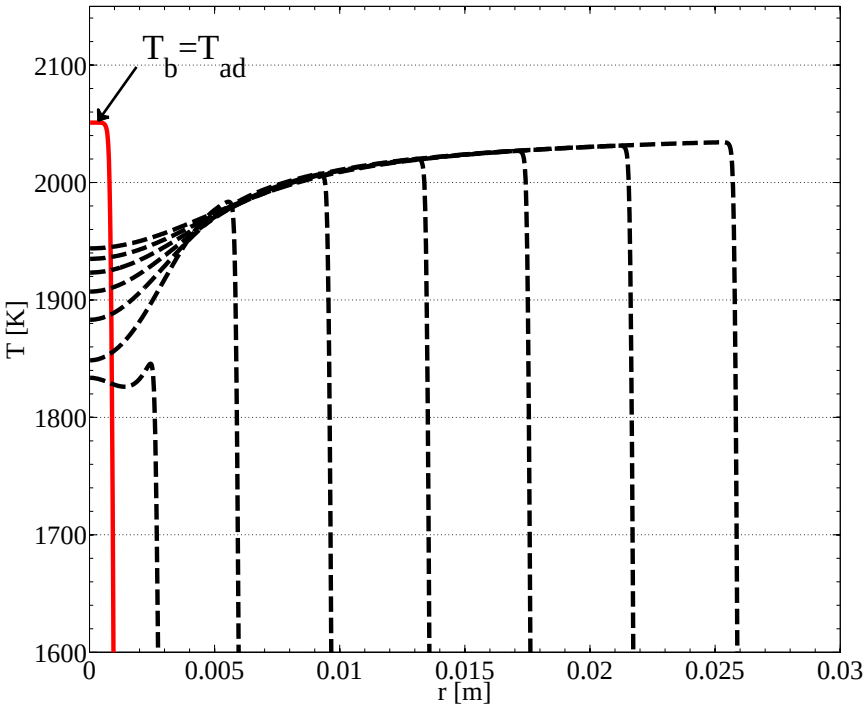

Figure 3.7: Temperature profiles versus the flame radius R when the octane / air flame propagates . —— Initial solution ($T_b = T_{ad}$) ; ---- Temporal evolution: time varies from $t = 0$ to $t = 17\ 5$ ms by step of $2\ 5$ ms.

the adiabatic flame temperature is influenced by stretch and this effect has been analyzed in the literature [115, 116]. The relation between the burnt gases temperature T_b and stretch κ is:

$$\frac{T_b - T_{ad}}{T_{ad}} = \left(\frac{1}{Le} - 1\right) \frac{D}{{s_L^0}^2} \kappa \tag{3.14}$$

where Le is the Lewis number of the limiting reactant and D a characteristic diffusivity. For the methane / air flame since $Le_{CH4} = 0.996$, T_b is almost insensitive to stretch so that $\bar{\rho}_b$ is close to its equilibrium value and Eq. 3.10 is close to the true flame speed (Fig. 3.6(b)). This result is similar to the result obtained in Sec. 3.3.1.b where the flat octane/air flame propagates (no confinement and no Lewis effect because the flame is not curved). On the other hand, for octane ($Le_{C8H18} = 2.78$), $T_b < T_{ad}$ so that $\bar{\rho}_b > \rho_b^{ad}$ leading to an underestimation of $s_c(\kappa)$ in Fig. 3.6(a) by 2 to 3 %. To compare Eq. 3.14 and simulations, a temperature that represents fairly the burnt gases temperature for a given stretch must be defined. The maximum temperature T_b^{max} seems to be reasonable, as presented by Fig. 3.8. Here, the characteristic diffusivity D used is the fuel molecular diffusivity in the fresh gases D_f^u. Figure 3.9 presents the comparison of Eq. 3.14 and results

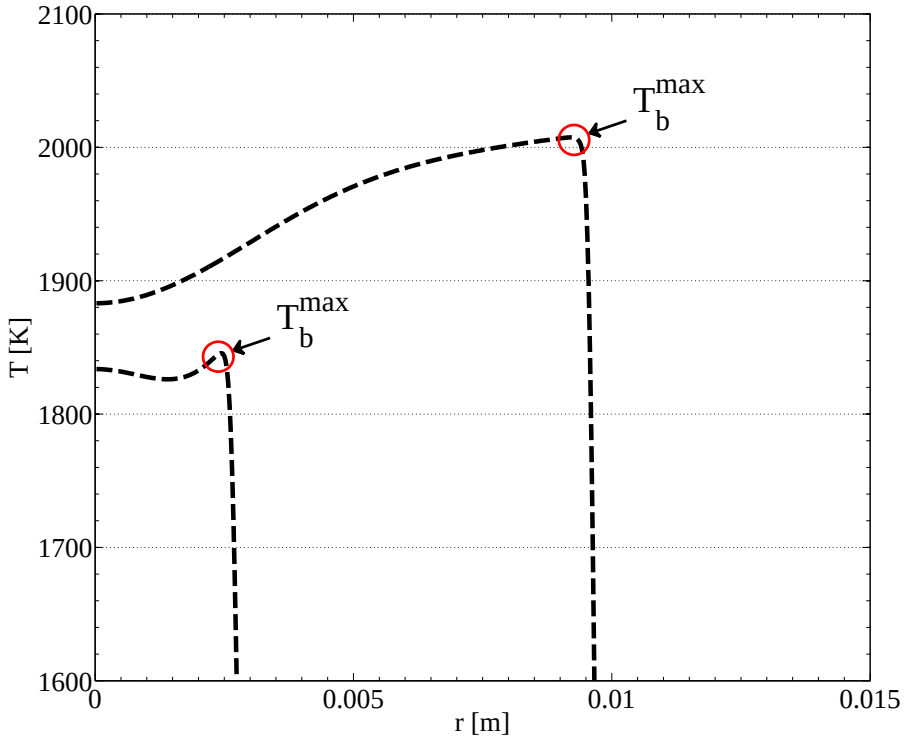

Figure 3.8: Definition of T_b^{max} using the temperature profiles versus flame radius r.

obtained in methane and octane air flame simulations. A good agreement between theory and simulation is found: it confirms that the burnt gases temperature (and therefore the burnt gases density in Eq. 3.10) is not constant and changes with stretch if the Lewis number is not equal to unity. Figure 3.9 shows that for methane, Lewis effects are negligible but not for octane. This explains why in Fig. 3.6, $s_c^{p\ expe}$ matches the true consumption flame speed s_c for methane ($Le \simeq 1$) but not for octane ($Le \simeq 2.75$).

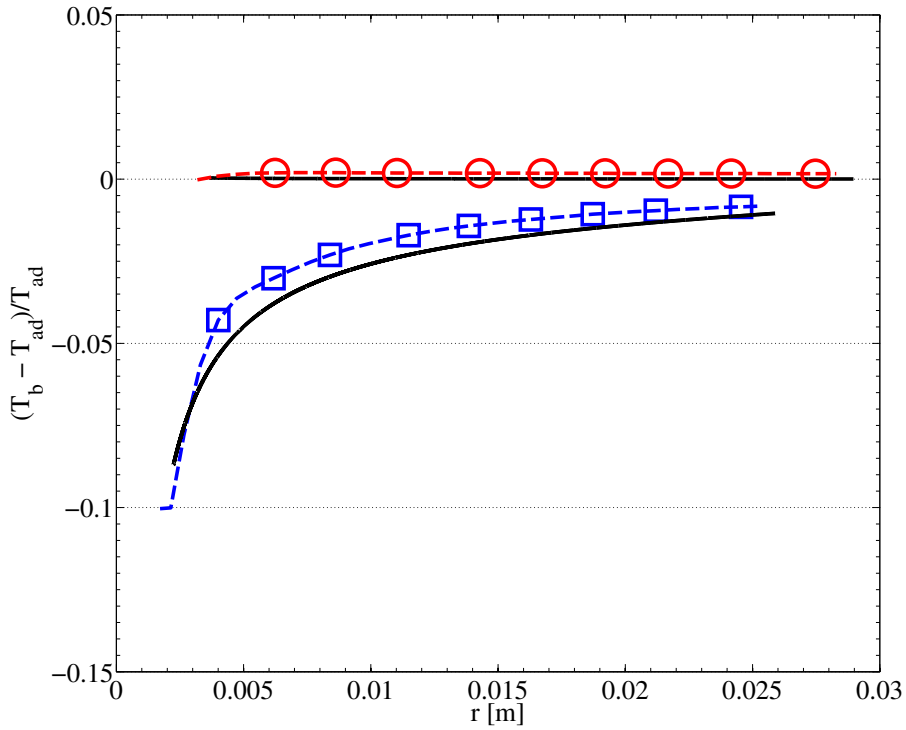

Figure 3.9: Normalized burnt gases temperature $(T_b^{max} - T_{ad})/T_{ad}$ versus the flame radius R. -□- C8H18 ; -○- CH4 ; —— Theoretical expression of Clavin and Williams (Eq. 3.14).

3.3.2.c Combined curvature and confinement effects: cylindrical flame in a closed bomb

Figure 3.10 shows the evolution of the various expressions for the consumption speed[6], normalized by the unstretched laminar flame speed s_L^0, versus stretch. Using the classical expression Eq. 3.10 (open circles) one recovers the classical shape for the flame speed: fairly linear at high stretch (small radii) but bent downward for lower stretch (large radii). However, the true consumption speed based on the integral of the fuel consumption rate (Eq. 3.3, solid line in Fig. 3.10) does not show a reduction as the flame grows. In the present configuration, for $\kappa < 150$ s^{-1}, the departure between Eq. 3.3 and Eq. 3.10 is significant ($\simeq 8$ % at low stretch).

The reason why Eq. 3.10 is not right here is that it uses the approximation $\bar{\rho}_b = \rho_{ad}$. Figure 3.11 displays the time variation of $\bar{\rho}_b$ is the BOMB case for octane and methane. As expected:

- for methane, at small times, curvature effects have no influence on $\bar{\rho}_b$. At later times, curvature effects decrease but confinement effects appear: pressure goes up and so does $\bar{\rho}_b$, an effect which is ignored by Eq. 3.10.

[6]Equations 3.9 and 3.13 are derived for a spherical flame but it is straightforward to modify them for a cylindrical flame. In this case Eq. 3.9 becomes $s_c^p = \frac{\bar{\rho}_b}{\rho_u}\frac{dR_p}{dt} + \frac{R_p}{2\rho_u}\frac{d\rho_b}{dt}$ and Eq. 3.13 becomes $s_c^f = \frac{dR_f}{dt} - \frac{R_0^2 - R_f^2}{2R_f}\frac{1}{\gamma_u P}\frac{dP}{dt}$.

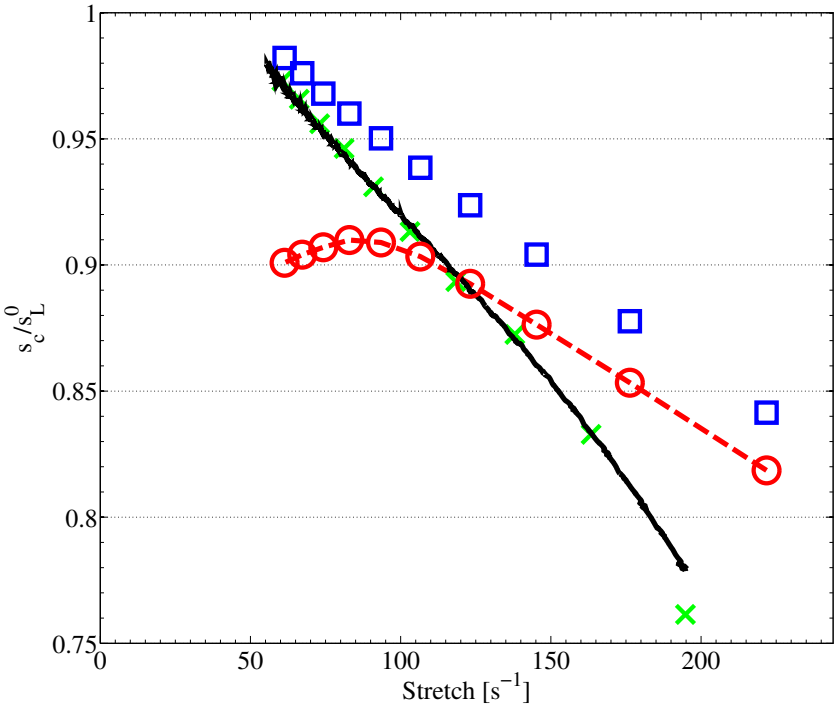

(a) Octane.

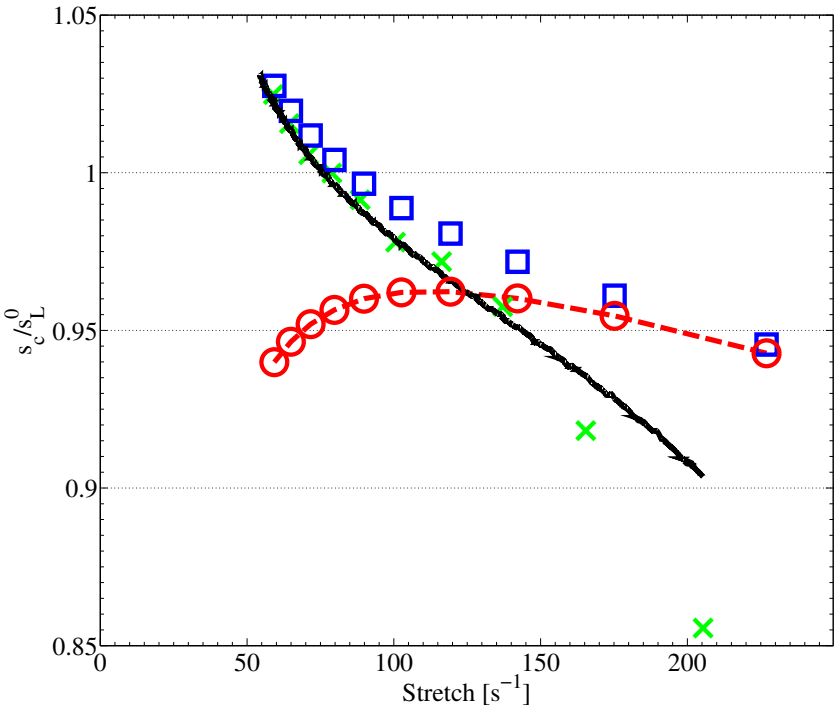

(b) Methane.

Figure 3.10: Normalized consumption speed versus stretch in a closed bomb (BOMB) with $s_L^{0\,\mathrm{CH4}} = 0\ 255$ m/s and $s_L^{0\,\mathrm{C8H18}} = 0\ 264$ m/s : —— s_c (Eq. 3.3) ; -⊖- $s_c^{p\ expe}$ (Eq. 3.10) ; □ s_c^p (Eq. 3.9) ; × s_c^f (Eq. 3.13)

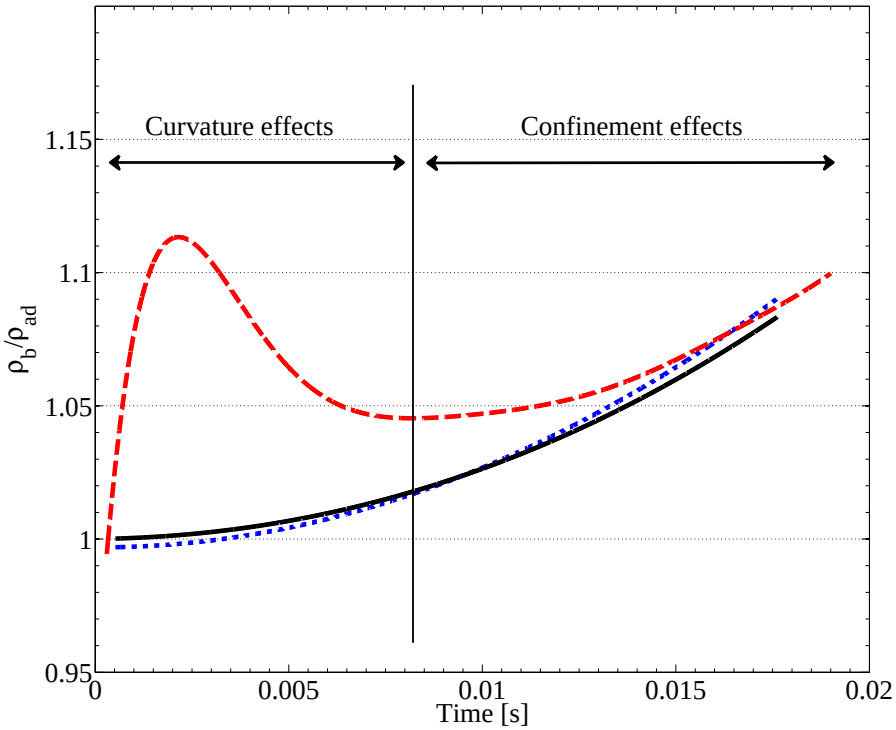

Figure 3.11: Normalized burnt gases density $\bar{\rho}_b/\rho_{ad}$ versus time. ---- C8H18 ; ····· CH4 ; —— isentropic compression ($P/\bar{\rho}_b{}^{\gamma_b}$ =cste).

- for octane flames the situation is not better: curvature effects lead to an increase of $\bar{\rho}_b$ at small times and confinement effects only make it worse at later times.

The standard procedure with such data is to extrapolate the linear portion of the curve towards $\kappa = 0$. As illustrated in [104] (their Fig. 5), the length of this linear portion is greatly influenced by the size of the apparatus, *i.e.* by confinement. This sensitivity affects the precision of the extrapolation procedure, as shown in [106] using both linear and non-linear methods. However, the consumption speed s_c^p (Eq. 3.9, open squares in Fig.3.10) does not match exactly the true consumption flame speed s_c (Eq. 3.3) at large stretch. This can be explained by the difference between R_f and R_p, especially when the flame is very small. Indeed, replacing R_p by R_f in Eq. 3.9 leads to a better result. In practice, s_c^p is not used in an experiment because $d\rho_b/dt$ is not easily accessible. Conversely, the consumption speed s_c^f based on the conservation of the fuel (Eq. 3.13) is can be measured and is unaffected by the confinement as shown in Fig. 3.10. This expression matches perfectly the true consumption flame speed s_c.

For methane, in the early development of the flame $\kappa > 150$ s^{-1}, s_c^f does not seem to match the true consumption speed because the pressure increase is very small initially. At later times (the region in which we are interested and where stretch is smaller) the accuracy of Eq. 3.13 is very good as shown in Fig. 3.10.

Note that the simulations of Sec. 3.3.2.b and 3.3.2.c were conducted in a 2D configuration. In a cylindrical flame, the pressure increase is stronger than for a spherical

flame so that confinement effects are overestimated in the present simulations. The first consequence is that for a spherical bomb with the same radius R_0, the diminution of s_L at low stretch would be less pronounced. Nevertheless, even with an exaggerated pressure increase, Eq. 3.13 is more precise than the classical formulae, which can only improve the accuracy of the extrapolation method. The second consequence is that even at moderate flame radii, the pressure and temperature increase in the fresh gases changes the flame speed. This is particularly striking for the methane flame in Fig. 3.10(b) as the normalized consumption flame speed exceeds unity at $\kappa < 70$ s^{-1} because the fresh gases are not in the nominal conditions any more. This peculiarity of the cylindrical flame does not affect the conclusion about the precision of Eq. 3.13 versus Eq. 3.10.

3.4 Conclusion

This chapter has discussed the post-processing methods of flame radii, obtained from spherical flames in bombs, to deduce laminar flame speeds and Markstein lengths. These experiments raise difficult questions [104]: when the flame is too small, it is influenced by curvature and non-unity Lewis number effects; when it is too large, it is affected by the confinement effect of the bomb. In the present work, the limitations of the classical formula used experimentally to construct flame speeds from flame radius measurements ($s_L = \rho_b/\rho_u \; dR/dt$) are discussed.

Two expressions for the consumption speed were derived from the conservation equation of the species, without the assumption of an infinitely-thin flame front. The first one:

$$s_c^p = \frac{\bar{\rho}_b}{\rho_u}\frac{dR_p}{dt} + \frac{R_p}{3\rho_u}\frac{d\bar{\rho}_b}{dt}$$

is the generalization of the classical formula that accounts for the temporal evolution of the density in the fresh and burnt gases. Because this formula requires the mean burnt gases density as an input, a quantity which can not be measured in experiments, another expression using only the flame radius and the pressure inside the bomb (two quantities which are directly measured):

$$s_c^f = \frac{dR_f}{dt} - \frac{R_0^3 - R_f^3}{3R_f^2}\frac{1}{\gamma_u P}\frac{dP}{dt}$$

is presented (existing in the literature [111] but seldom used).

A cylindrical flame computed with DNS was used to evaluate the precision of these two expressions for the consumption flame speed. In a configuration where confinement effects do not exist (propagation in an infinite medium where pressure is rigorously constant but never happens in experiments),

$$s_c^{p\ expe} = \frac{\rho_b^{eq}}{\rho_u(t=0)}\frac{dR_p}{dt}$$

incorrectly predicts the flame speeds for non-unity Lewis number (octane) but performs correctly for methane because Lewis number is close to unity in this case. In a second configuration, corresponding to a bomb, results show that $s_c^{p\,expe}$ incorrectly predicts flame speeds for both octane and methane / air flames because the burnt gases density increases with pressure (in addition to curvature effects for octane) while s_c^f captures the correct consumption speeds. Since s_c^f only requires the knowledge of $R(t)$ and $P(t)$, it is simple to use experimentally and the present work suggests that it is a good candidate for a more precise determination of the flame speeds.

The main difficulty of this method may be the measurement and treatment of the pressure signal because the pressure increase in a large bomb may be difficult to measure accurately and to post process to obtain the pressure derivative required in s_c^f. The experimental measurement of the flame radii R_f and R_p is not possible but these radii are very close, except at the very early stage of propagation. Assuming $R(t) = R_f = R_p$ should have a limited impact on flame speed definitions.

CHAPTER 4

IMPLEMENTATION OF AN IMMERSED BOUNDARIES METHOD IN *AVBP*

Contents

There have been quite a few numerical studies dedicated to turbulent flame propagation in isotropic turbulence. Such DNS or LES are usually performed in cubic boxes where turbulence is introduced at t=0 assuming a given spectrum for the fluctuations. In the ICAMDAC project, it was decided to try a more ambitious strategy where the turbulence itself would be computed and not arbitrarily imposed at the initial simulation time. In other words, the complete bomb with the fans had to be computed before ignition to propagate the flame in a realistic turbulent flow. This required a complete shift in DNS paradigms: instead of using a cubic box with high-order compact schemes [117, 118, 119] or spectral methods [120, 121] and an ad-hoc initial condition for turbulence, an unstructured mesh solver had to be used, incorporating the six fans in the bomb and therefore representing a much more difficult numerical challenge. The first step for this challenge was to identify a code and we chose to use AVBP [53, 112, 113] because it offered high-fidelity schemes together with unstructured mesh capacities. The second step was to choose a mesh movement strategy since the movement of the six fans had to be explicitly captured. At this point, the ALE (Arbitrary Lagrangian Eulerian) [78, 122, 53] strategy available in AVBP for piston engine LES [5, 74] was discarded because it was not adapted to fans and two other strategies were evaluated. The first one is based on Immersed Boundaries Methods (IBM) and is described in this chapter. First the method implemented is presented, then academic test-cases of growing complexity are performed. Finally, the method is tested on a one-fan isolated test-case where results are not satisfactory. The second strategy is called MISCOG (for Multi Instances Solver Coupled on Overlapping Grids). Initially developed at CERFACS [123, 124, 125] for turbomachinery simulations, it is the method which proved to be the most precise for our simulations and it will be discussed in Chapter 5.
I would like to acknowledge Dr. Antoine Dauptain and Dr. Olivier Vermorel from CERFACS for their help when I worked on IB. Thanks to their knowledge of the AVBP *code sources and their scientific background in the IB field, they gave me very precious advices to develop the method.*

4.1 Introduction to Immersed Boundaries Methods

In traditional CFD, a flow domain is first discretized (meshed) and boundary conditions are applied to the domain boundaries (typically inlet/outlet or walls). As long as boundaries do not move this approach is very efficient. But fluid-structure interactions, piston engine or turbomachinery computations (this list is non-exhaustive) require to deal with moving boundaries. As presented in Sec. 1.7, one approach to handle moving boundaries is to use Immersed Boundaries Methods (IBM). Meshes are generated over the whole domain and do not have to match the shape of the moving body. The body boundary conditions are introduced later into the governing equations via forcing terms. Figure 4.1 shows an example for a standard Body-Conformal (BC) mesh and an IB representation of an ellipsoidal shape.

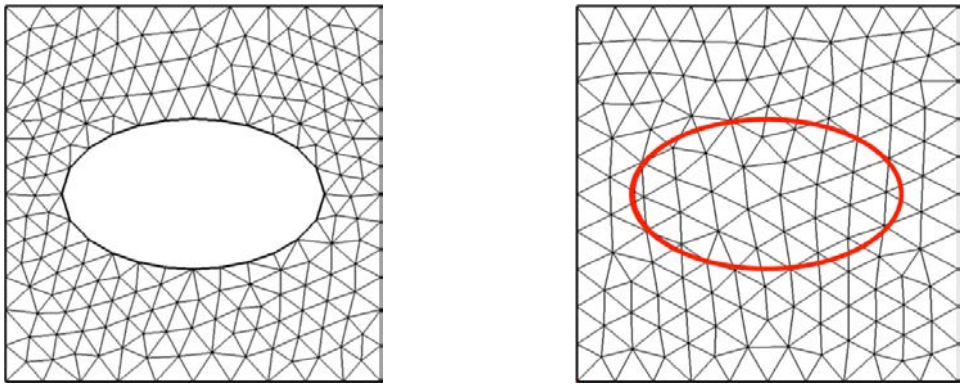

(a) Standard Body Conformal approach.

(b) Immersed Boundaries Method.

Figure 4.1: Comparison of the Immersed Boundaries Method (IBM) to the classic Body Conformal (BC) approach.

The approach which consists in decoupling the mesh generation from the body geometry makes the method particularly interesting for complex and moving geometries. Indeed, the mesh does not move nor deform and only one mesh is needed. This is a very interesting point in terms of complexity meshing time. That is why the implementation of an IBM method in the *AVBP* code seems very attractive to compute the flow generated by fans.

IBM were first introduced by Peskin in 1972 [126] to simulate the flow inside the beating human heart. So far, IBM have been applied to a wide range of applications: compressible [127, 128] particulate flows [129], micro-scale flows [130], interaction with solid bodies [131], conjugate heat transfer [132], environmental flows [133] or bio-fluids [134]. However, only a small number of studies have been published for cases with high Reynolds numbers. All these techniques differ essentially by the formulation of the forcing term. The introduction of a forcing function leads to a division of IB methods into two groups [135], namely direct (or discrete) forcing or continuous forcing.

1. **Direct forcing method:** This approach consists of an imposition of the velocity boundary conditions on the immersed surface: the forcing term is computed so that it directly compensates for the differences between the calculated velocities and the desired velocities on the IB.
2. **Continuous forcing method:** This approach consists in adding a source term in the right-hand-side term of the Navier-Stokes equation to force the fluid velocity at the boundary position to be equal to the boundary velocity.

A review on immersed boundary methods for solid surfaces can be found in [136]. In this work an IBM based on a continuous forcing method was implemented (based on the initial development of A. Dauptain and O. Vermorel at CERFACS) in the *AVBP* code. The formulation of the source term used is the one proposed by Goldstein in 1993 [137]. More recently, Saiki and Biringen [138] applied this method to simulate the flow past a

cylinder. This method is implemented on the basis of the Lagrangian module introduced by M. Garcia [46] in 2009: indeed, many features required to implement an IB technique can be obtained from the Lagrangian modules of *AVBP* initially developed for droplets and described below.

4.2 The Lagrangian module in *AVBP*

To deal with two-phase flows using a Euler-Lagrange approach, a Lagrangian module was implemented in 2009 by M. Garcia [46] in the *AVBP* code. This Lagrangian module includes:

- a specific data structure. Two arrays are dedicated to particles depending on their data type: integer or real. The integer data type contains the particle identifier, the processor number containing the particle, the cell number containing the particle and the kind of particle (solid, liquid). The real data type contains the particle position (x_p, y_p and z_p), the particle velocity (u_p, v_p and w_p), the particle temperature T_p and its radius r_p,
- an efficient algorithm to locate and track the particles (based on neighbor to neighbor approach),
- an algorithm to find gas-phase properties at the particle position (in general, the particle position does not match with a grid node). This data is obtained by interpolating the gas-phase variables at the vertices of the cell that contains the particle using Taylor series, Linear Least Square or Lagrangian polynomials.
- two-way coupling. The flow can modify the particles behavior and the particles can modify the flow.

In Lagrangian two phase flow modeling, the filtered Navier-Stokes equations (see Eqs. 1.49 - 1.52) can be modified to take into account particles and droplets mass, momentum and energy exchanges with the gas. This is done by adding to the right-hand side of gas equations, the corresponding source terms, ρ_p, $F_{p\,i}$, Q_p and $S_{p\,k}$ for mass, momentum, energy and species equations, respectively:

$$\frac{\partial \overline{\rho}}{\partial t} + \frac{\partial}{\partial x_i}(\overline{\rho} u_i) = \rho_p \tag{4.1}$$

$$\frac{\partial \overline{\rho} u_j}{\partial t} + \frac{\partial}{\partial x_j}(\overline{\rho} u_i u_j) = -\frac{\partial}{\partial x_j}(\overline{P}\delta_{ij} - \overline{\tau}_{ij} - \overline{\tau}^t_{ij}) + F_{p\,i} \tag{4.2}$$

$$\frac{\partial \overline{\rho} E}{\partial t} + \frac{\partial}{\partial x_j}(\overline{\rho} E u_j) = -\frac{\partial}{\partial x_j}[\overline{u_i(P\delta_{ij} - \tau_{ij})} + \overline{q}_j + \overline{q}^t_j] + \overline{\ }_T + \overline{Q}_r + Q_p \tag{4.3}$$

$$\frac{\partial \overline{\rho} Y_k}{\partial t} + \frac{\partial}{\partial x_j}(\overline{\rho} Y_k u_j) = -\frac{\partial}{\partial x_j}[\overline{J}_{j\,k} + \overline{J}^t_{j\,k}] + \overline{\ }_k + S_{p\,k} \tag{4.4}$$

During this thesis, the IBM has been developed to mimic adiabatic no-slip walls. Thus, all terms with variations in the particle mass are zero. This leads directly to:

$$\rho_p = 0 \qquad \text{and} \qquad S_{p\,k} = 0 \tag{4.5}$$

In two-phase flow modeling the $F_{p\,i}$ term is the fluid-particle interaction force (taken into account through drag force). But this source term can easily been modified to introduce the source term proposed by Goldstein [137]. Note that $F_{p\,i}$ is a volume force expressed in [N/m^3]. The term added in the energy equation (Eq. 4.3) Q_p writes $Q_p = F_{p\,i} u_i$.

4.3 Implementation of the Immersed Boundaries Method

The implementation of the Immersed Boundaries Method (IBM) in the *AVBP* code is based on the Lagrangian module developed by Marta Garcia [46] for the treatment of two-phase flows. Figure 4.2 shows how a wall can be modeled by Lagrangian particles on an eulerian mesh. To define a wall, each eulerian cell must have at least one particle to be airtight. In this thesis, it was decided to put Lagrangian particles only on the skin of the solid part to save Lagrangian particles (calculations with a large number of Lagrangian particles requires more memory and increases the CPU cost of the simulation) but it could also be possible to add particles within the solid part. The wall can be motionless or at a known/imposed velocity $\mathbf{u_p}$. Then the objective is to set the fluid velocity at the position of the particle $\mathbf{u_{f@p}}$ equal to $\mathbf{u_p}$. In practice, the fluid velocity is not imposed at the exact position of particles but at the grid nodes surroundings particles.

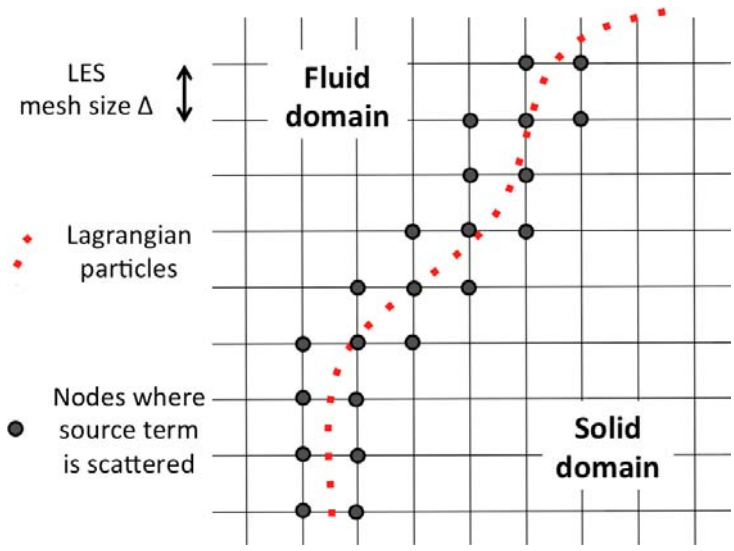

Figure 4.2: Modeling of a wall with Lagrangian particles. Particles are only located on the wall but could also be added within the solid part.

Lagrangian source term

Various formulations can be used for the fluid-particle interaction force $F_{p\,i}$. During this thesis a feedback forcing, first proposed by Goldstein et *al* [137], was implemented. The expression for the source term in the eulerian momentum equation (Eq. 4.2) at node m writes:

$$F^m_{p\,i} = \frac{1}{\sum_{n=1}^{Np} W_i(x_i^n, x_i^m)} \sum_{n=1}^{Np} f_i^n . W_i(x_i^n, x_i^m) \tag{4.6}$$

where N_p is the number of particles, f_i^n is the fluid-particle interaction force on a single particle located at x_i^n and W is the projection weight of the Lagrangian force onto the grid node m. The weights in the projection operation are constructed to be inversely proportional to the distances d_j between the particle and the nodes of the cell containing the particle:

$$W_j = \frac{1/d_j}{\sum_{k=1}^{N} 1/d_k} W_p \tag{4.7}$$

where j is the index of the cell vertex and N is the number of vertices of the cell. Figure 4.3 sketches the coupling force exerted by a particle on the fluid and its projection onto the grid nodes. The source term in the energy equation yields:

$$Q_p = \sum_i F_{p\,i} u_{p\,i} \tag{4.8}$$

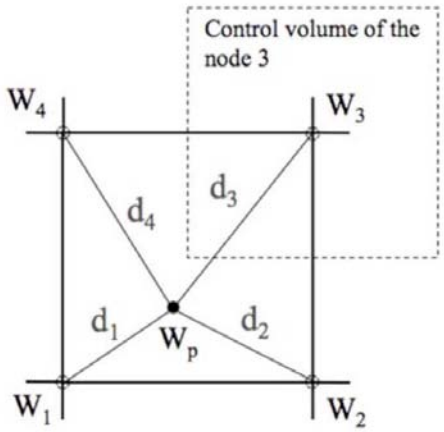

Figure 4.3: Example of projection of a particle two-way coupling contribution into the vertices of a quadrilateral cell

The formulation of the forcing term f_i^n proposed by Goldstein [137] is:

$$f_i^n = \beta \int_0^t u_{p\,i}^n - u_{f@p\,i}\, \mathrm{d}t' + \alpha(u_{p\,i}^n - u_{f@p\,i}) \tag{4.9}$$

where $u_{f@p\,i}$ is the i-component of the gas velocity at the particle position. α and β are two case-dependent parameters. This feedback forcing is a straightforward feedback of the velocity field at the particle velocity $\mathbf{u_p}$. In the framework on control systems theory, it is called a Proportional-Integral (PI) controller. One should think that using concepts from linear control theory in simulations of turbulent and highly non-linear flows would be difficult but we only need to control small regions of the flow where near-linear responses might be expected. The first term in Eq. 4.9 with integral feedback is sufficient to create a force field that will bring the flow to rest on the surface points: the force increase (or decrease) with time to oppose the flow to go through the interface. But in practice this integral controller is slow and a proportional controller (the second term in Eq. 4.9) is added to handle fast variations which could occur in a turbulent flow. A general description of possible forms for Eq. 4.9 is given below.

1. **The proportional controller (P):**

$$f_i^n = \alpha(u_{p\,i}^n - u_{f@p\,i}) \tag{4.10}$$

Equation. 4.10 is a particular case of the feedback forcing (Eq. 4.9). Considering the Navier-Stokes equation Eq. 4.2, if α 0, the forcing vanishes and Eq. 4.2 recovers the standard Navier-Stokes equation. In contrast, if α , the forcing becomes dominant in the equation yielding the solution $\mathbf{u_{f@p}} = \mathbf{u_p}$. For $0 < \alpha <$, the forcing can be modulated to provide a momentum loss in a desired region, thus simulating porous media.

2. **The integral controller (I):**

$$f_i^n = \beta \int_0^t u_{p\,i}^n - u_{f@p\,i}\ \mathrm{d}t' \tag{4.11}$$

This formulation accumulates a force from zero to the force leading to $\mathbf{u_{f@p}} = \mathbf{u_p}$. Thanks to a `system regulation analogy, this formulation is slower than the direct forcing method but it has the advantage of giving a null static error. Like in the proportional method, the forcing can be modulated for $0 < \beta <$.

The problem with these formulations is the determination of the α and β coefficients. The choice of this value is case dependent: if the values are too high, the source terms become too big and the code crashes but if the values are two low, the source terms are not sufficient and the wall is porous. So that the classical formulation of f_i^n in Eq. 4.9 is not easy to parametrize in terms of α and β and a new formulation is proposed below.

The objective is to determine a new formulation for f_i^n which is easier to use than Eq. 4.9. Typically the method should not depend on the mesh and the configuration. The intensity of the source terms could be controlled by the user only by specifying a relaxation time: the number of iterations needed to reach the equilibrium $\mathbf{u_{f@p}} = \mathbf{u_p}$. To do this normalization, a simplified analysis is necessary. The equation really solved by the code can be reduced to:

$$\rho\frac{\partial u}{\partial t} = \frac{F_p}{V_m} \tag{4.12}$$

where F_p is a force expressed in Newton and V_m is the fictitious volume surrounding each grid node m. The proportional and the integral formulation can be injected in F_p.

1. The proportional formulation (P)
   The source term is $F_p = \alpha(u_p - u)$. Injecting F_p in Eq. 4.12 yield:

   $$\rho\frac{\partial u}{\partial t} = \frac{\alpha}{V_m}(u_p - u) \tag{4.13}$$

   Equation 4.13 is a linear ordinary differential equation of first-order with constant coefficients. A trivial solution of this equation is:

   $$u - u_p = A\exp\left(-\frac{\alpha}{\rho V_m}t\right) \tag{4.14}$$

   The ratio $\rho V_m/\alpha$ is the relaxation time τ_P associated to the proportional corrector:

   $$\tau_P = \frac{\rho V_m}{\alpha} \tag{4.15}$$

   Then τ_P can be expressed as a number N of iterations : $\tau_P = N\Delta t$. Thus an expression for α can be found:

   $$\alpha = \frac{\rho V_m}{N\Delta t} \tag{4.16}$$

2. The integral formulation (I)
   The source term is $F_p = \beta\int_0^t u_p - u \, \mathrm{d}t'$. A similar derivation for the integral formulation leads to:

   $$\beta = \frac{\rho V_m}{M^2\Delta t^2} \tag{4.17}$$

   where M is the number of iterations in the relax time associated to the integral formulation $\tau_I = M\Delta t$.

Finally, the formulation for f_i^n is the following (it replaces Eq. 4.9):

$$f_i^n = \frac{\rho V_m}{N\Delta t}\left(u_{p\,i}^n - u_{f@p\,i}\right) + \frac{\rho V_m}{M^2\Delta t^2}\int_0^t u_{p\,i}^n - u_{f@p\,i}\,\mathrm{d}t' \tag{4.18}$$

where M and N are respectively the relaxation time, in number of iterations, for the integral and proportional source term. N must be higher than one (the code can not impose $\mathbf{u_{f@p}} = \mathbf{u_p}$ in less than one iteration). Typically $N \in [2; 10]$. M must be higher than one: the objective of the integral source term is to find the mean force to apply to fluid to ensure the no-slip condition and must be slower` than the proportional. Typically $M \in [100; 1000]$.

To monitor the IMB, two quantities were added in the real data type array (presented in Sec. 4.2) dedicated to particles:

- the slip velocity at the particle position $|\mathbf{u_{f@p}} - \mathbf{u_p}|$. This quantity checks the accuracy of the method and is a measure of the error since the objective is to get $\mathbf{u_{f@p}} = \mathbf{u_p}$
- the Lagrangian source term f_i^n. It is important to verify that the N and M parameters allow f_i^n to remain in a reasonable range.

4.4 Numerical strategy for the Immersed Boundaries

A robust numerical strategy to perform computations using IB is presented in this chapter. This numerical strategy is employed for all simulations (using IB) realized in this thesis. In order to evaluate the behavior of the IBM, a very simple computation with only one Lagrangian particle translating at constant velocity in a stagnant fluid is performed.

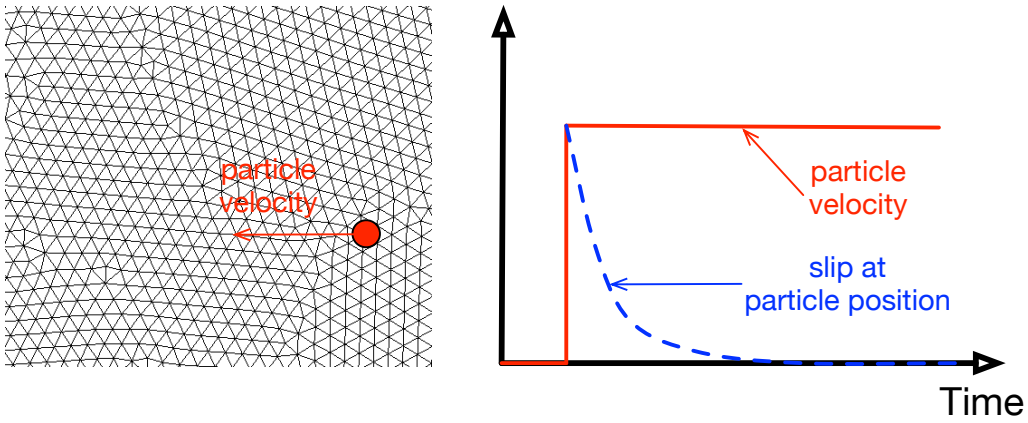

Figure 4.4: Sketch of the numerical configuration used to developed the numerical strategy to perform computations using IB.

It is expected that the slip velocity at the particle position goes to zero: the fluid velocity goes from zero (stagnant fluid) to the velocity of the particle. In control systems theory, this test characterizes the response of the fluid to a step. The response using the P controller, the I controller or a combination of both are presented in this section.

4.4.1 The proportional controller (P)

First the computation is performed using only the proportional controller (P). Three different values of N are tested: $N = 1$, $N = 10$ and $N = 100$. M is set to infinity (in practice $M = 1.10^9$) to disable the effect of the I controller. Figure 4.5 presents the results: as expected, the response time of the controller depends on the coefficient N (N controls the response time). The proper trend is recovered: when N is increased the time response of the P controller increases too. Moreover, one can see that the accuracy of the P controller depends on N. When $N = 100$ the slip at the particle position is bigger than when $N = 1$. So one would choose $N = 1$ but the problem is that when $N = 1$ the source term at the first iteration is 100 times bigger than when $N = 100$. This overshoot can lead to crash depending on the configuration. Moreover setting $N = 1$ always leads to large oscillations of the source term because the history of the source term is not taken into account when using a P controller.

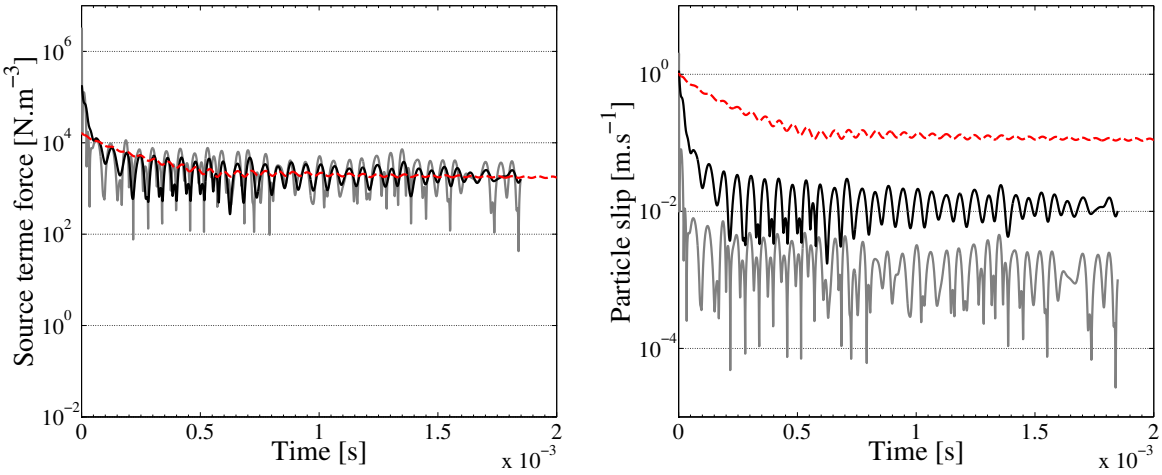

(a) Lagrangian source term f_i^n.

(b) Slip at the particle position $|\mathbf{u_{f@p}} - \mathbf{u_p}|$.

Figure 4.5: Lagrangian source term and slip at the particle position when using P controller ($M =$). —— $N = 1$; —— $N = 10$; ---- $N = 100$

4.4.2 The integral controller (I)

The computation is now performed using only the integral controller (I). Three different values of M are tested: $M = 10$, $M = 50$ and $M = 100$. N is set to infinity (in practice $N = 1.10^9$) to disable the effect of the P controller. Figure 4.6 presents the results obtained. Once again, the response time depends on the coefficient M. But in this case,

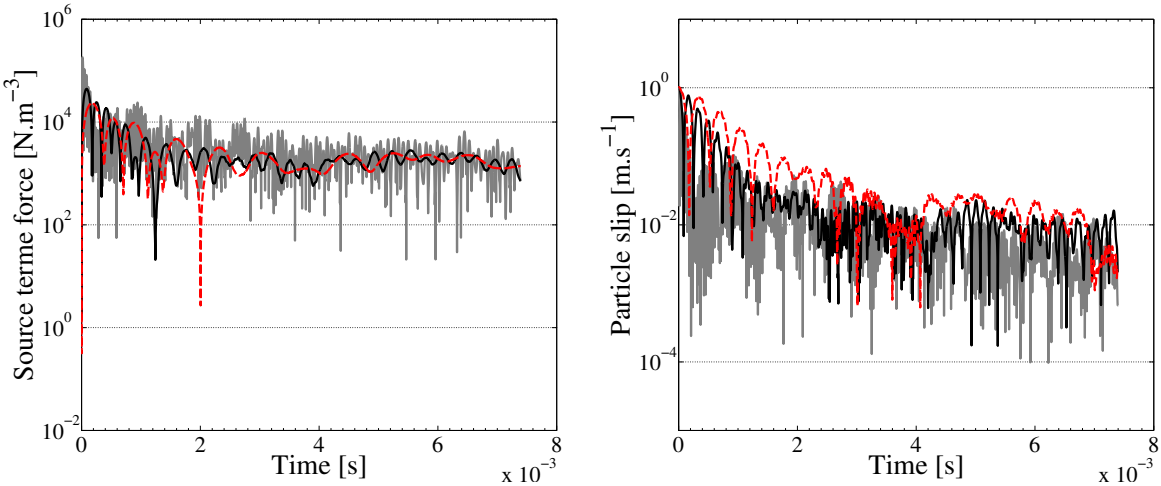

(a) Lagrangian source term f_i^n.

(b) Slip at the particle position $|\mathbf{u_{f@p}} - \mathbf{u_p}|$.

Figure 4.6: Lagrangian source term and slip at the particle position when using I controller ($N =$). —— $M = 10$; —— $M = 50$; ---- $M = 100$

the slip at the particle position does not depend on the value of M. This is a typical behavior for an integral controller. The source term is continuously adapted (thanks to the integral formulation) to reduce the error between the instantaneous value of the fluid velocity and the target. This controller is slower than the proportional controller but it always reaches the target.

4.4.3 The proportional-integral controller (PI)

When using the PI controller, the computation is performed in two steps. First the I controller is used to find the steady value of the source term needed to get $\mathbf{u_{f@p}} = \mathbf{u_p}$ without overshoot on the source term at the beginning of the simulation. Then the PI controller is turned on with an infinite response time for the I controller ($M =$) and a very strong P controller ($N = 1$). Figure 4.7 presents the results. This methodology is

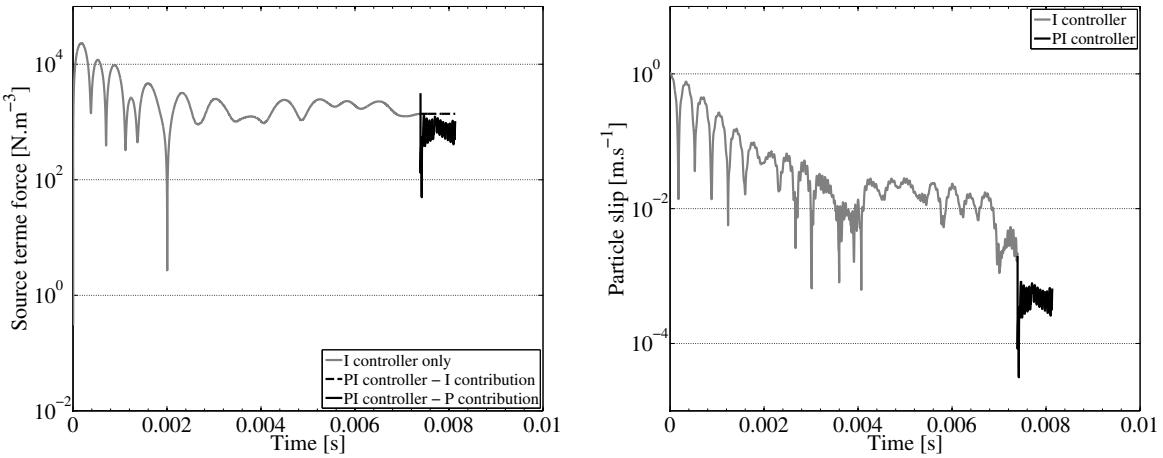

(a) Lagrangian source term f_i^n.

(b) Slip at the particle position $|\mathbf{u_{f@p}} - \mathbf{u_p}|$.

Figure 4.7: Lagrangian source term and slip at the particle position when using I ($N =$ and $M = 100$) then PI ($M =$ and $N = 1$) controller.

very robust and can be applied to a wide range of applications (all further cases presented later are performed using this methodology): there never are overshoots on the source term. It combines the integral controller which finds the good steady state value at the beginning of the simulation (in practice about 1,000 iterations are enough) then the PI controller is turned on. The P controller is turned on with a response time equal to one iteration $N = 1$ and the I controller is turned on with an infinite response time (the objective is just to store the steady state value). The P controller can be set with $N = 1$ because it just needs to add a `small contribution since the mean value is added by the I controller. In other words, in a turbulent flow, the I controller get the mean value of the source term (at the beginning of the simulation) and the P controller handles fluctuations to ensure the no-slip condition at the particle position.

4.5 Validation test-cases of the Immersed Boundaries Method

Various academic test-cases were performed to validate the IBM implemented in *AVBP*. These test-cases are of growing complexity and the solutions obtained are compared to analytical solutions or/and solutions obtained with the classic Body Conformal (BC) approach.

4.5.1 Two-dimensional Poiseuille flow

The first test-case computed is a 2-dimensional Poiseuille flow. Lagrangian particles mimic the channel walls. These two walls do not move. The flow goes from left to right. To be able to compare the solution found to an analytic one, the flow remains laminar. The sketch of the configuration is presented in Fig. 4.8. There are several particles in each cell to ensure that no cell is empty which can lead to a leak through the wall. The main characteristics of the configuration are summarized in Tab. 4.1. With a ratio

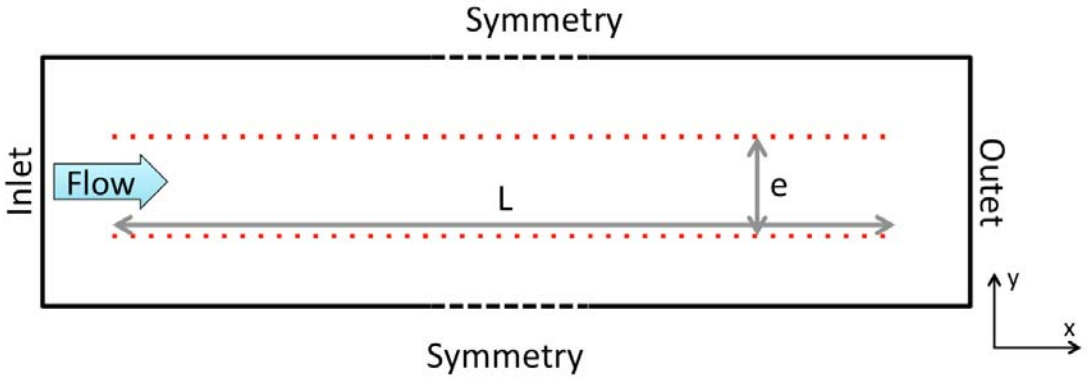

Figure 4.8: Sketch of the 2-dimensional Poiseuille flow configuration: within the domain delimited by the Lagrangian particles a classical Poiseuille flow is expected. □ Computational domain ; ····· Lagrangian particles.

$e/L \simeq 100$, the channel can be considered as an infinitely channel. With a Reynolds number $Re = 130$, the flow remains laminar. Table 4.1 summarizes the flow conditions.

e	$1\,\mathrm{mm}$
U_{inlet}	$2\,\mathrm{m{\cdot}s^{-1}}$
L	$93.4\,\mathrm{mm}$
μ	$1.807 \times 10^{-5}\,\mathrm{kg{\cdot}m^{-1}{\cdot}s^{-1}}$
Re	130

Table 4.1: Main characteristics for the 2-dimensional Poiseuille flow.

Figure 4.9 presents a magnitude velocity field with a vector velocity field. Before the inlet of the channel, the flow is uniform with an inlet velocity $U_{inlet} = 2$ m/s and

a pressure $P_{inlet} = 101372$ Pa. In the channel, at the Lagrangian particles position the velocity is expected to be zero and maximum at the center. The analytical solution of

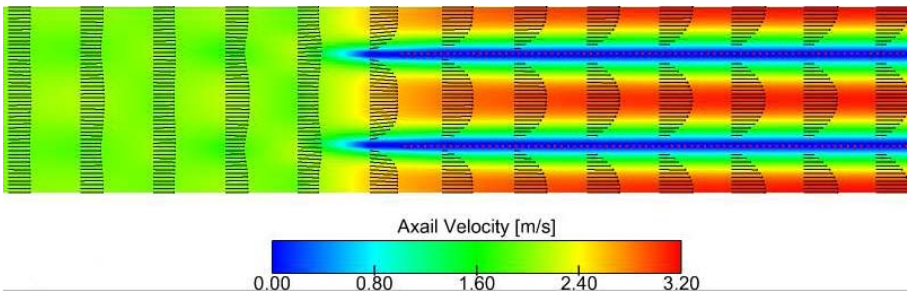

Figure 4.9: Steady state velocity field: zoom at the inlet of the channel.

the axial velocity in a Poiseuille flow is well-known and can be expressed as:

$$u(y) = 4U_{max}\frac{y}{e}\left(1 - \frac{y}{e}\right) \tag{4.19}$$

where U_{max} is the maximum velocity reach at the center of the channel. U_{max} writes:

$$U_{max} = \frac{3}{2e}Q_v = \frac{3}{2e}\int_0^e \vec{u}.\vec{x}\ \mathrm{d}y \tag{4.20}$$

Q_v is the flow rate calculated with the velocity found in the simulation. An analytical expression can also be derived for the pressure gradient [139] along the x-axis:

$$\frac{\partial P}{\partial x} = -\frac{3}{2}\mu\frac{Qv}{(e/2)^3} \tag{4.21}$$

Figure 4.10 plots analytical velocity and pressure profiles. A very good agreement is found between the analytical and the IBM velocity profiles. The velocity at the Lagrangian particles is zero as expected (the mean value over all particles is 7.10^{-4} m/s and the maximum value is $6.5.10^{-3}$ m/s during all the simulation), the maximum of velocity is recovered as well as the shape of the curve. The pressure drop is slightly overestimated using IBM however the agreement is reasonnable.

4.5.2 Two-dimensional Couette flow

The second test-case is a 2-dimensional Couette flow. This configuration is based on two co-axial cylinders. The inner-one rotates while the other remains fixed. Figure 4.11 presents the sketch of the configuration. This test-case is more complicated than the Poiseuille flow because the particles of the inner cylinder move: they rotate. However, this test-case is still laminar and steady. The main characteristics of the configuration are summarized in Tab. 4.2. At this operating point, no Taylor-Couettte instabilities are expected (the Taylor number is lower than 1700). The grid contains 18532 cells (triangles). The analytical solution of this flow is known. The radial velocity u_r is zero

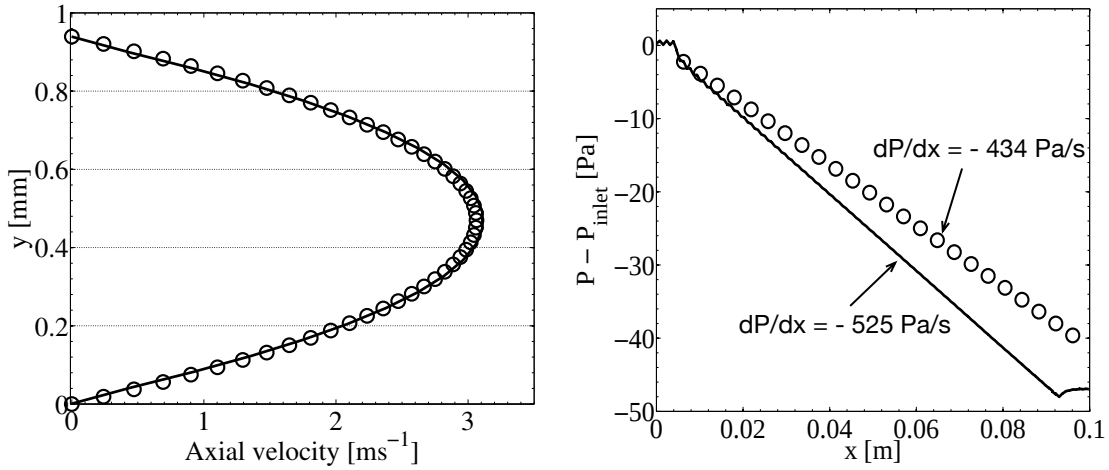

(a) Velocity profile.

(b) Pressure profile.

Figure 4.10: Velocity profile. ◯ Theoretical profile ; —— Immersed Boundaries Method

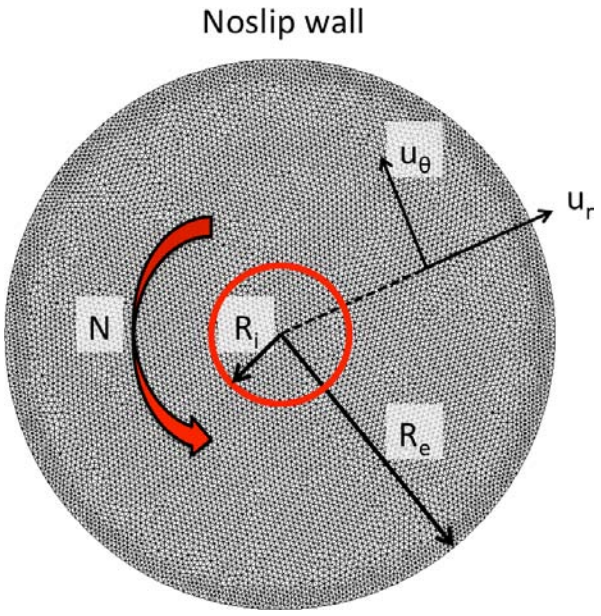

Figure 4.11: Sketch of the 2-dimensional Couette flow configuration. —— Computational domain, —— Lagrangian particles (to mimic a wall)

R_e	20 mm
R_i	5 mm
N	1500 rpm
μ	1.54×10^{-3} kg·m^{-1}·s^{-1}

Table 4.2: Main characteristics for the 2-dimensional Couette flow

and the tangential velocity u_θ is function of the radius r:

$$u_\theta = \begin{array}{ll} \frac{2\pi}{60} N r & \text{if } r \in [0, R_i] \\ \frac{2\pi}{60} N \frac{R_i^2}{R_e^2 - R_i^2} \left(\frac{R_e^2}{r} - r \right) & \text{if } r \in [R_i, R_e] \end{array} \tag{4.22}$$

Figure 4.12 shows the comparison between the analytical velocity profile and the results obtained with the IBM. A very good agreement between theoretical and numerical so-

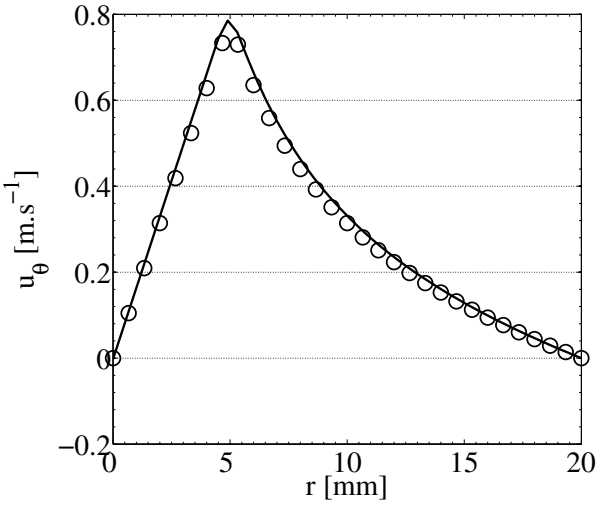

Figure 4.12: Tangential velocity profile. ◯ Theoretical profile ; —— Immersed Boundaries Method

lutions is found. The shape of the curve is retrieved: from $r = 0$ to $r = R_i$ the curve is linear then from $r = R_i$ to $r = R_e$, the curve is non-linear. Over all the particles, the mean slip value is $5.5.10^{-3}$ m/s and the maximum value is $1.4.10^{-3}$ m/s during the simulation.

4.5.3 Cylinder in a flow

A classical validation test-case performed to evaluate numerical methods is the cylinder in a free stream. This configuration is widely studied experimentally and numerically in the literature [138, 140, 141, 142, 143, 144, 145, 146, 147]. In this test-case the cylinder of diameter D is fixed and a flow coming from left to right. Figure 4.13 presents the sketch of the configuration. The results obtained with IB are compared both to the literature

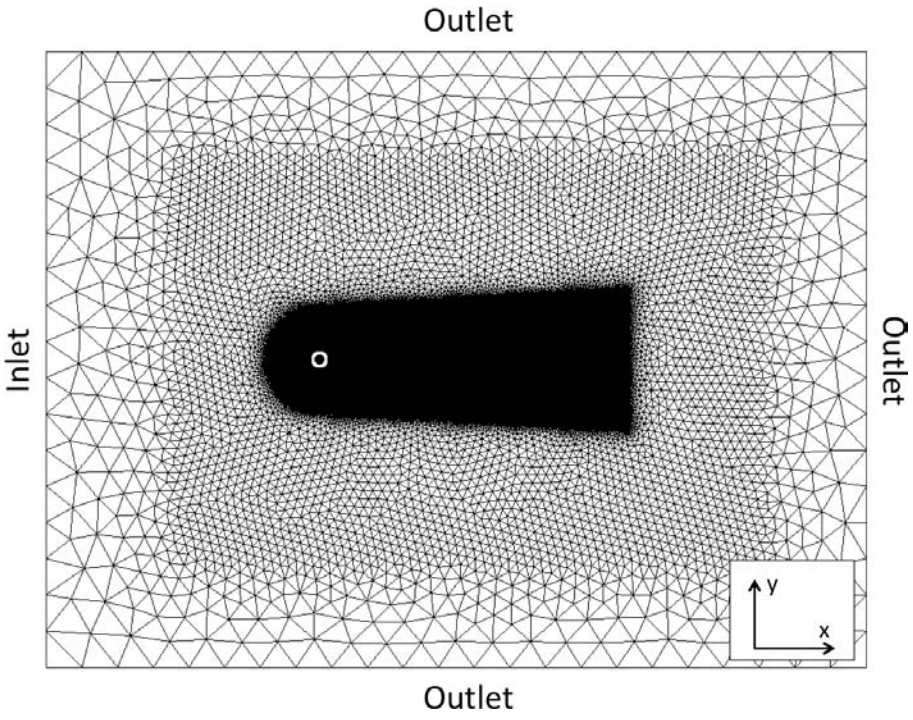

Figure 4.13: Sketch of the configuration computed

and to a classical` computation called Body Conformal (BC). In the Body Conformal approach the cylinder is meshed and a no-slip boundary condition is applied. Figure 4.14 shows the two different approaches. With the IBM, the flow inside the cylinder is resolved too. This test-case is conducted at two operating points. First it is computed in laminar

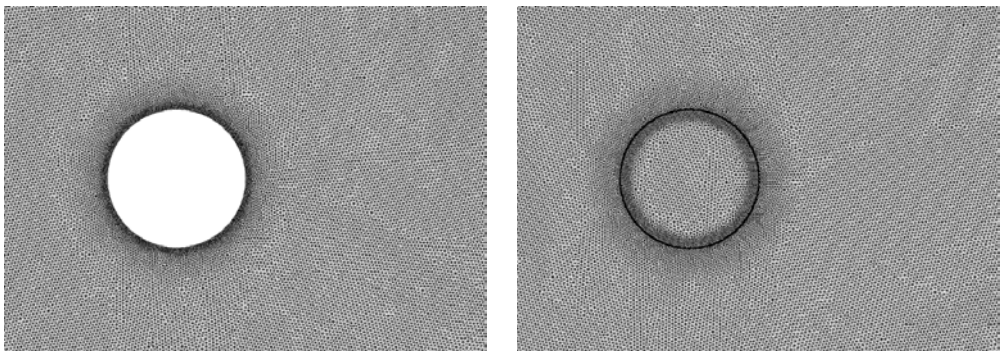

(a) Body Conformal (b) Immersed Boundaries Method

Figure 4.14: Zoom on the mesh closed to the cylinder

regime at $Re = 20$ then it is computed at a transitional regime (where vortices start to appear) at $Re = 100$. The main characteristics of the configuration are summarized in Tab. 4.3. For practical reasons the Reynolds number is changed by modifying the fluid

	Re = 20	**Re = 100**
D	2 mm	2 mm
P_0	101325 Pa	101325 Pa
T_0	300 K	300 K
U_{inlet}	$10\,\mathrm{m{\cdot}s^{-1}}$	$10\,\mathrm{m{\cdot}s^{-1}}$
μ	$1.17 \times 10^{-3}\,\mathrm{kg{\cdot}m^{-1}{\cdot}s^{-1}}$	$2.34 \times 10^{-4}\,\mathrm{kg{\cdot}m^{-1}{\cdot}s^{-1}}$

Table 4.3: Main characteristics for cylinder case at $Re = 100$

viscosity rather than the inlet velocity.

4.5.3.a Laminar regime $Re = 20$

First a comparison between the Body Conformal approach and the Immersed Boundaries Method is done in a laminar regime (at $Re = 20$). At this regime no vortex appears and it is easy to compare velocity profiles. Table 4.4 compares the computational costs for BC and IBM. The time step in BC is smaller than in IBM because the mesh is refined near the wall but the computational times are almost the same. Figure 4.15 presents

	Body Conformal	**Immersed Boundaries Method**
Cells (triangles)	521558	525392
Time step	$\simeq 0.18 \times 10^{-7}\,\mathrm{s}$	$\simeq 0.26 \times 10^{-7}\,\mathrm{s}$
CPU-time	17900 s	15000 s
Nb. CPU	128	128

Table 4.4: Main characteristics for cylinder case at $Re = 100$

the velocity fields obtained with both BC and IB methods. Qualitatively a very good agreement is observed. Getting the good velocity field is one important thing but a more difficult task is to get the good pressure field. Figure 4.16 shows the pressure fields obtained with both methods. Even the pressure fields are qualitatively in good agreement. To compare qualitatively the velocity and pressure fields between the BC approach and the IBM vertical cuts are performed upstream, at $x_1 = -D$, and downstream of the cylinder at $x_2 = D$, $x_3 = 2D$ and $x_4 = 3D$ ($x = 0$ is located at the center of the cylinder). Figure 4.17 presents the axial velocity u, Fig. 4.18 the transversal velocity v and Fig. 4.19 the pressure P. The velocity and the pressure are well predicted by the Immersed Boundaries Method in a laminar regime. Finally, to compare the BC approach to the IBM, the recirculation zone can be observed. Figure 4.20 displays streamlines around the cylinder. As expected, the shape and the length of this recirculation zone downstream of the cylinder is well predicted too by the IBM.

4.5.3.b Transitional regime $Re = 100$

Since the flow around the cylinder in a laminar regime in Sec. 4.5.3.a was validated, the IB method can be tested in a transient regime where vortices appear. At $Re = 100$ a

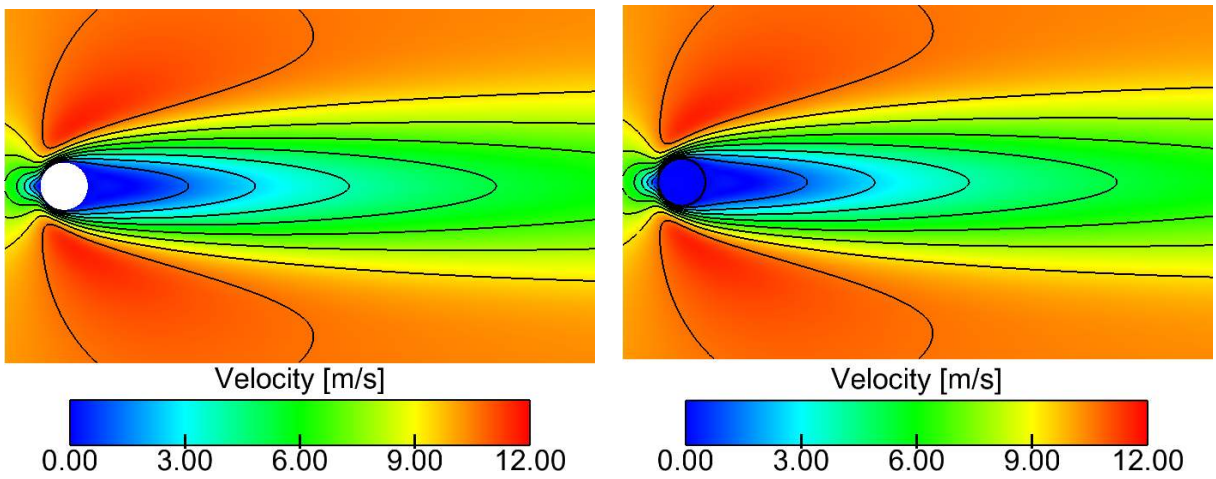

(a) Body Conformal (b) Immersed Boundaries Method

Figure 4.15: Velocity fields at $Re = 20$ with iso-lines

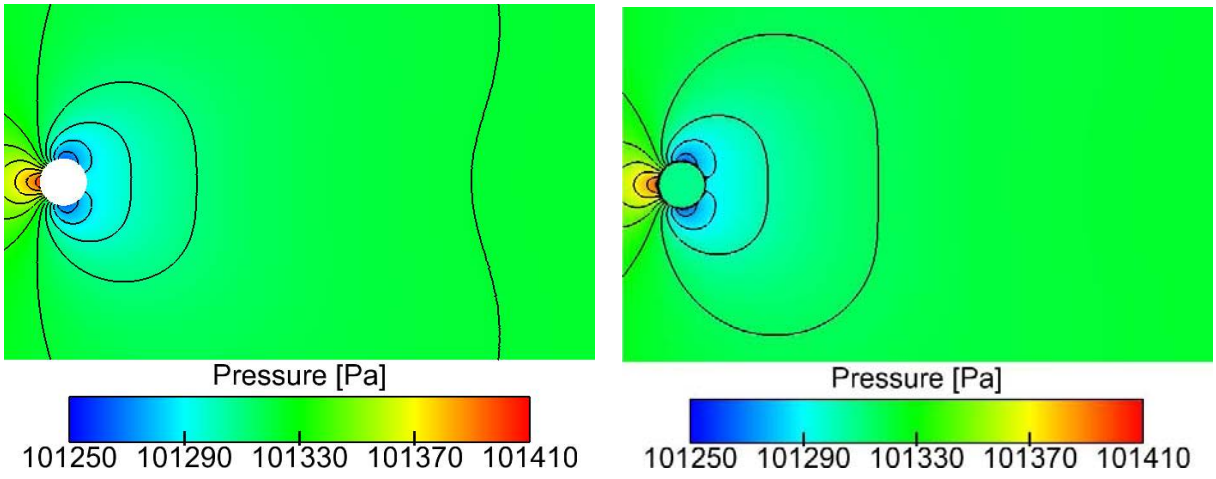

(a) Body Conformal (b) Immersed Boundaries Method

Figure 4.16: Pressure field at $Re = 20$ with iso-lines

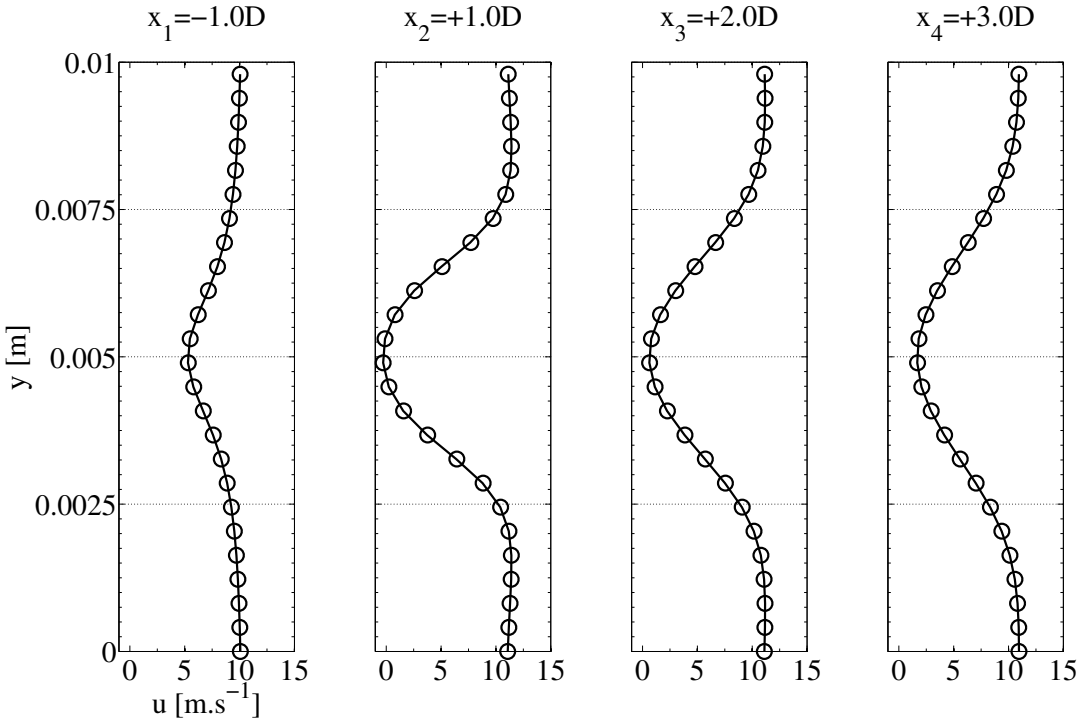

Figure 4.17: Axial velocity u. ◯ Body Conformal ; —— Immersed boundaries Method

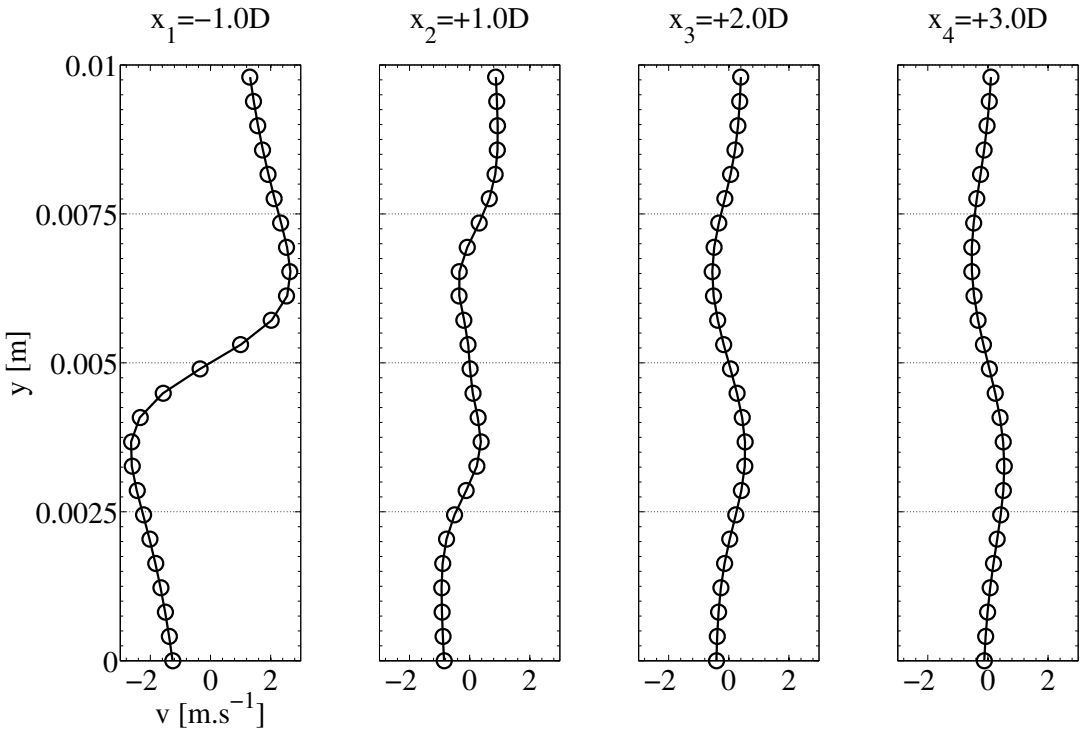

Figure 4.18: Transversal velocity v. ◯ Body Conformal ; —— Immersed boundaries Method

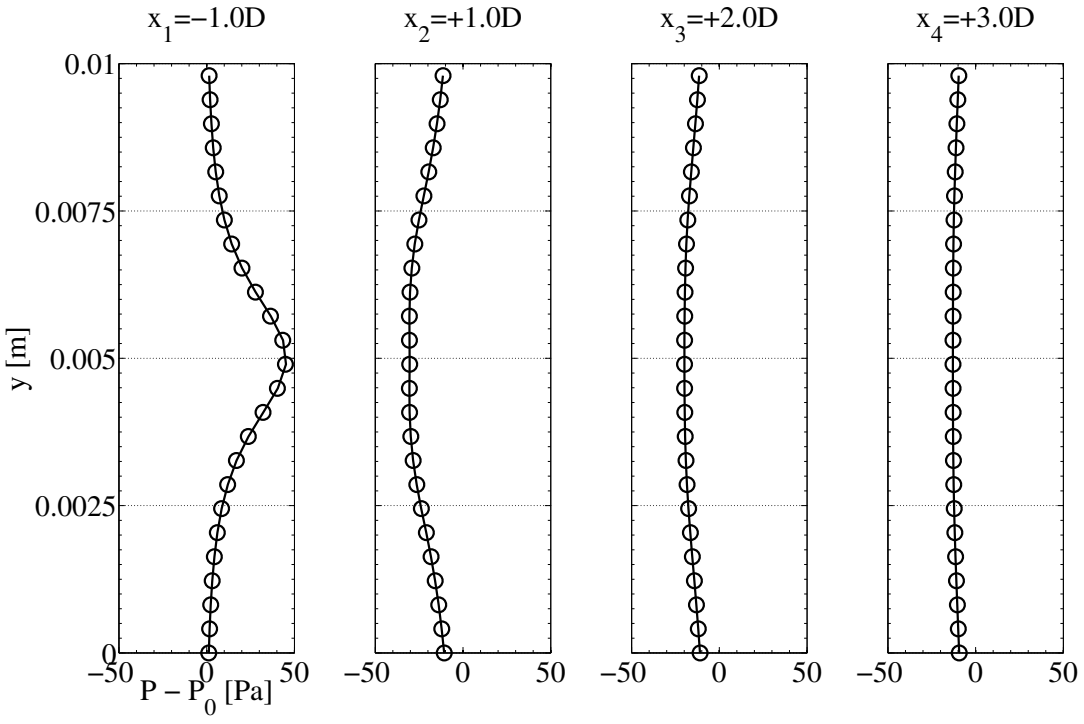

Figure 4.19: Pressure P. ◯ Body Conformal ; —— Immersed boundaries Method

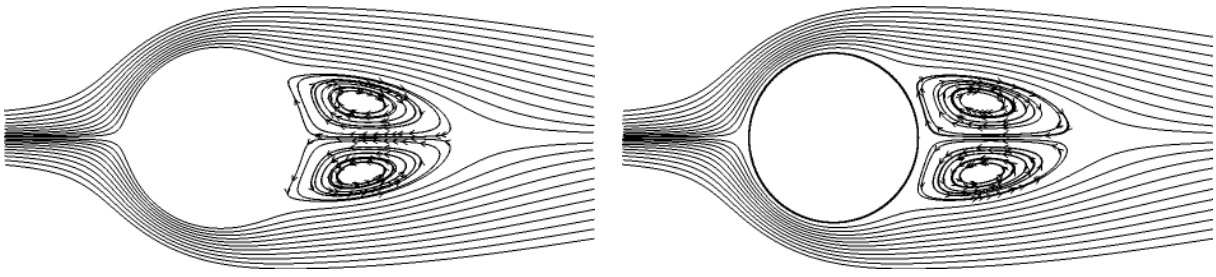

(a) Body Conformal (b) Immersed Boundaries Method

Figure 4.20: Streamline around a cylinder at $Re = 20$

Kármán vortex street appears downstream of the cylinder. This test-case is computed both with the BC approach and with the IBM. Figure 4.21 presents vorticity fields to compare vortex shedding with the two methods. Six solutions are displayed during one period of the vortex shedding (the period of the vortex shedding is known a posteriori). The structure of the vortex is well predicted by the IBM.

To validate the IBM, three coefficients are checked:

1. the Strouhal number St which is the dimensionless frequency of the vortex shedding: $St = f * D/U_{inlet}$,
2. the drag coefficient C_D,
3. the lift coefficient C_L.

To find the Strouhal number of the vortex shedding, a probe is placed downstream of the cylinder to record the transversal velocity v. The signal recorded with IBM is displayed in Fig. 4.22 and a Fast Fourier Transform of the signal is performed to exhibit its spectral content. With the IBM the first mode is found at $f_{IBM} = 827$ Hz. The same treatment is done for the BC approach and the frequency found is $f_{BC} = 821$ Hz. The Strouhal number associated for both approaches is about 0.16 as expected at $Re = 120$ [141, 142, 143].

Because it is based on forces, the drag and lift coefficients can easily be found with the IBM. The principle of the IBM is to apply the force needed to ensure the no slip condition. Integrating this force over the computational domain gives the drag force F_x. Then the expression of the drag coefficient is:

$$C_D = \frac{F_x}{\frac{1}{2}\rho D U_{inlet}^2} \tag{4.23}$$

where F_x writes:

$$F_x = \iiint_V F_{p\,x}\ \mathrm{d}V \tag{4.24}$$

$F_{p\,x}$ is the eulerian force applied to the fluid (see Eq. 4.2). The lift coefficient writes:

$$C_L = \frac{F_y}{\frac{1}{2}\rho D U_{inlet}^2} \tag{4.25}$$

where F_y writes:

$$F_y = \iiint_V F_{p\,y}\ \mathrm{d}V \tag{4.26}$$

Figure 4.23 displays a field of $F_{p\,x}$ on the grid mesh. As expected, the force is applied only on the grid nodes surrounding the Lagrangian particles. The major part of the force is applied in the frontside of the cylinder (at the stagnation point). When the boundary layer detaches, the force needed to stop the flow decreases. Figure 4.24 presents the drag and lift coefficients calculated with the IBM and compare these results to those obtained by other authors. These results are presented as a function of a dimensionless time $t^* = tU_{inlet}/D$. An acceptable agreement is found for the mean steady state value

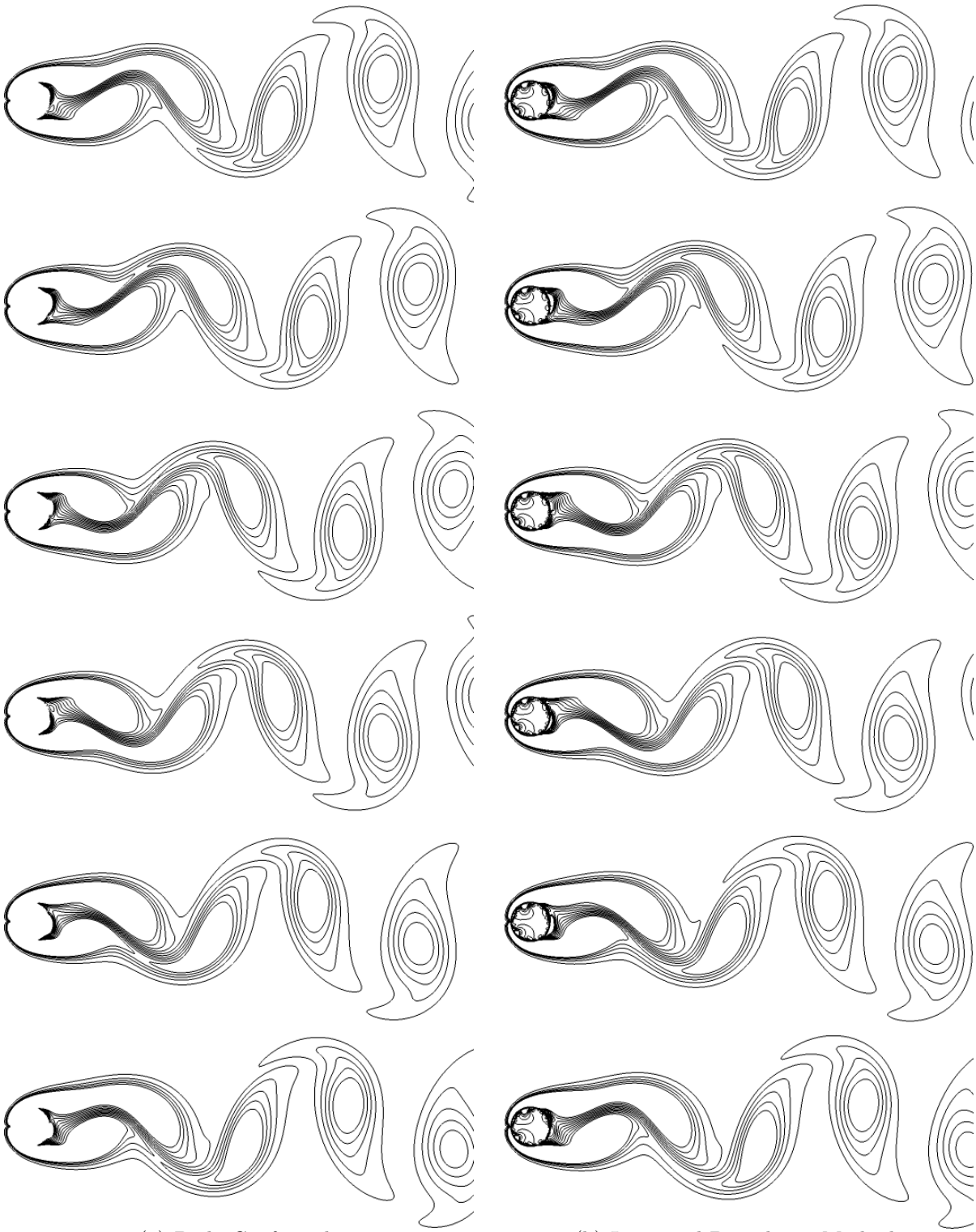

(a) Body Conformal (b) Immersed Boundaries Method

Figure 4.21: Vortex shedding at $Re = 100$. Isolines of vorticity. Temporal evolution from top to bottom. Time step between to filed is $2\ 01 \times 10^{-4}$ s

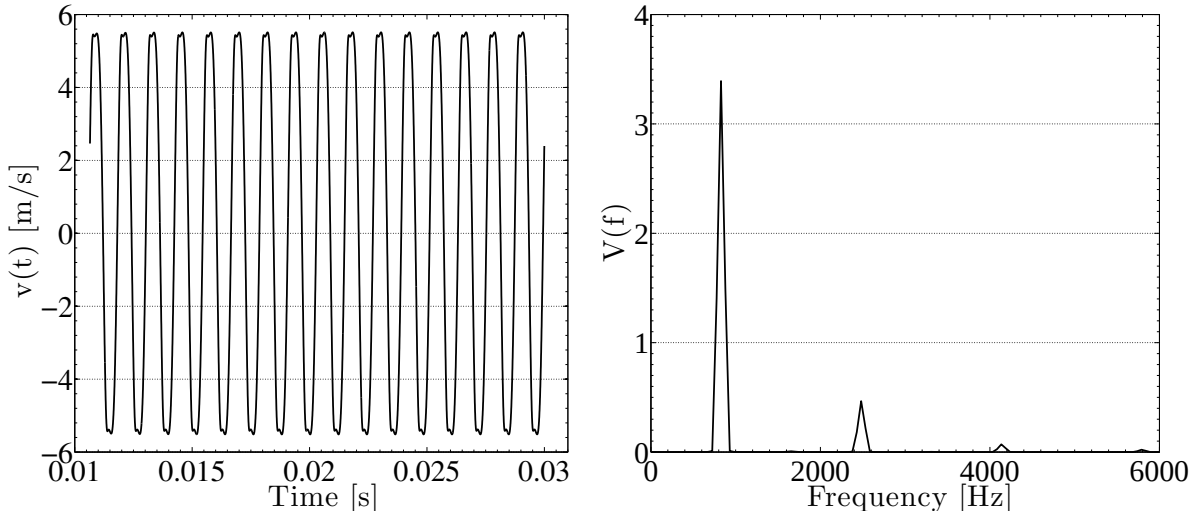

(a) Temporal signal.

(b) Fast Fourier Transform.

Figure 4.22: Vortex shedding. Signal recorded by a probe downstream the cylinder at $x = 3\ 75D$

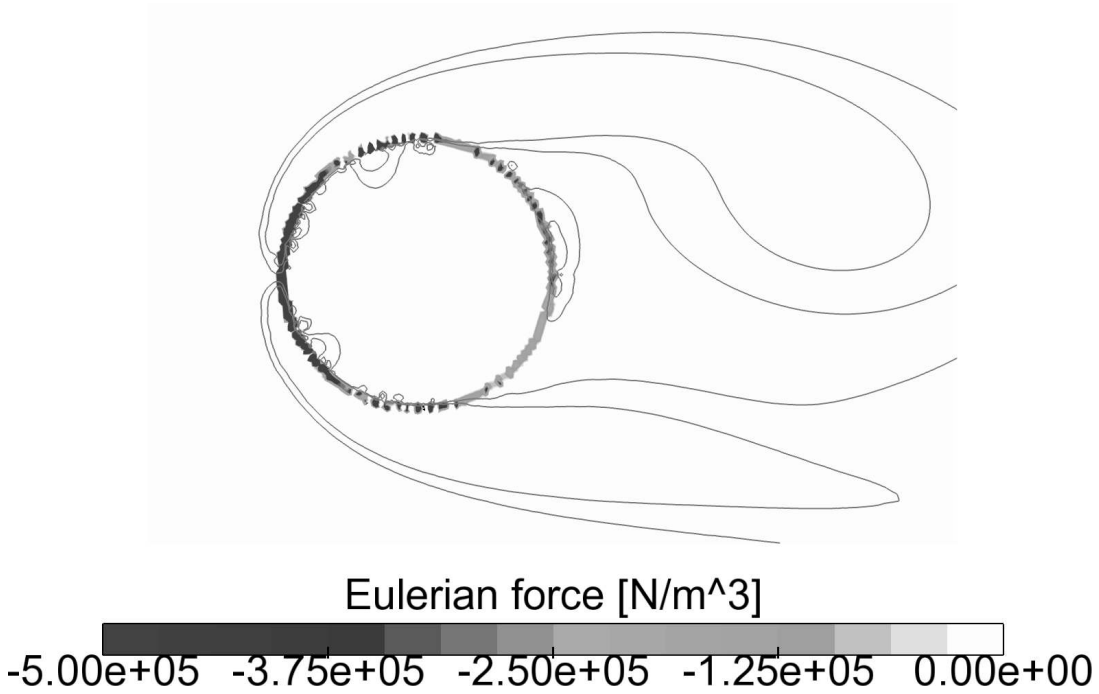

Figure 4.23: Eulerian force $F_{p\,x}$ applied to the fluid with iso-lines of vorticity.

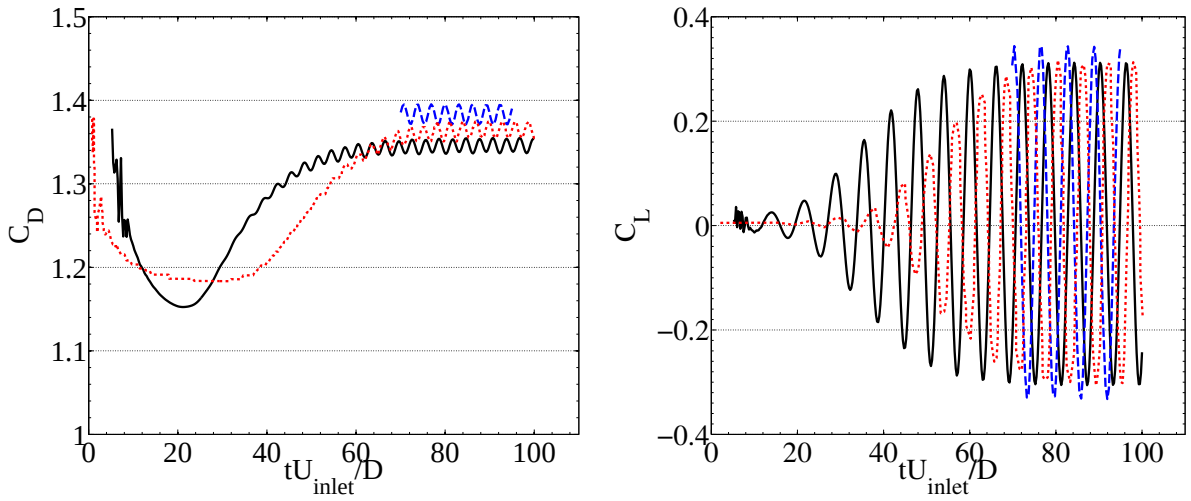

(a) Drag coefficient

(b) Lift coefficient

Figure 4.24: Drag and lift coefficient of a cylinder in a flow at $Re = 100$. —— Present work ; - - - - Shu et al. [141] ; ····· Haeri et al. [148]

even if there are discrepancies for the growth rate for drag and lift coefficients. The lift coefficient oscillates at a frequency equal to the frequency of the vortex shedding while the drag coefficients varies two times faster. Table 4.5 summarizes the results obtained in this work and those obtained by other authors. Authors do not agree on exact values for the Strouhal number and the drag coefficient and a clear variability can be found in the literature.

Case	$\mathbf{f_d}$ **[Hz]**	**St**	$\overline{\mathbf{C_D}}$
Present work - Body Conformal	821	0.164	-
Present work - IBM	827	0.165	1.35
Saiki et al. [138]	-	0.171	1.26
Joran & Fromm [140]	-	0.16	1.28
Shu et .al [141]	-	0.16	1.38
Tseng & Ferzieger [142]	-	0.164	1.42
Braza et al. [143]	-	0.16	1.28

Table 4.5: Reference results

Figure 4.25 shows the probability density function of the velocity slip at the particle position (at the end of the simulation). For both laminar and transient regimes, the slip velocity at the particle position is very low compared to the flow velocity (less than 1% in transient regime). However one can show that the IBM is more efficient when the Reynolds number is low.

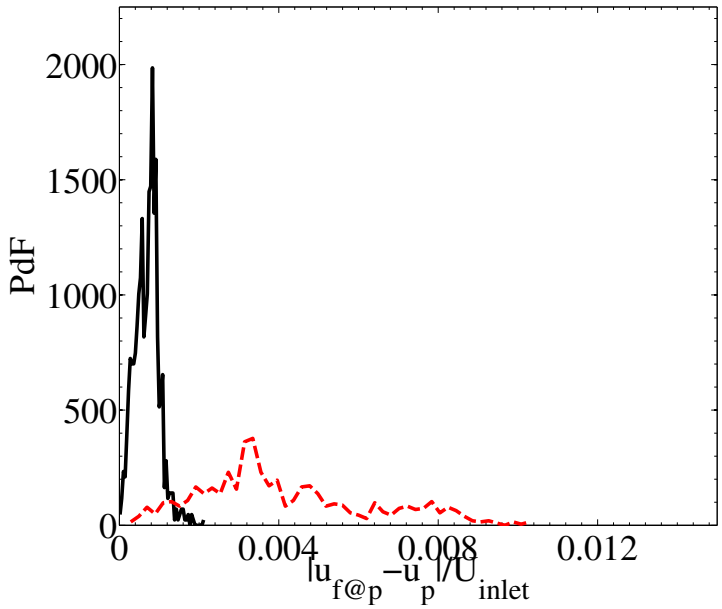

Figure 4.25: Probability Density Function of the slip at the Lagrangian particles. —— $Re = 20$ (laminar regime) ; ---- $Re = 100$ (transient regime)

4.5.4 Translating inclined plate

In this test-case, the IBM is tested with a translating inclined plate. The sketch of the configuration is presented in Fig. 4.26. The aim of this test-case is to mimic the movement of a blade of a rotating-fan. The plate thickness is $e = 1$ mm, the height of the front surface is $h = 1.2$ cm and the laminar viscosity is $\mu = 1.807.10^{-2}\ kg.m^{-1}.s^{-1}$. This test-case is computed in a laminar regime. The reference computation is performed

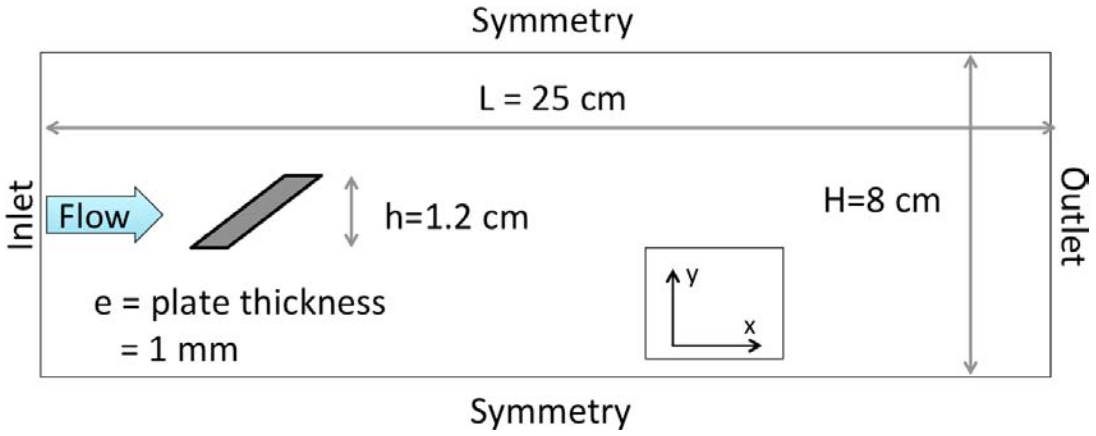

Figure 4.26: Sketch of the configuration: inclined plate.

with the Body Conformal approach where a no-slip boundary condition is applied on the plate. The flows comes from left to right at a velocity $U_{inlet} = 20$ m/s. On this

reference computation, the plate does not move. Then the same computation is done with the IBM. Finally, to test the IBM when the wall are moving, the plate translates from left to right at a velocity $u_p = -10$ m/s and the flow velocity coming from the inlet is decreased at $U_{inlet} = 10$ m/s. Thus, the difference $U_{inlet} - u_p$ remains constant and the Reynolds number is unchanged for the three computations. The Reynolds number is $Re = \rho\,(U_{inlet} - u_p)\,h/\mu \simeq 16$. Figure 4.27 illustrates the moving and non-moving cases. The simulations are performed on the same physical time $T = 18$ ms. The initial position

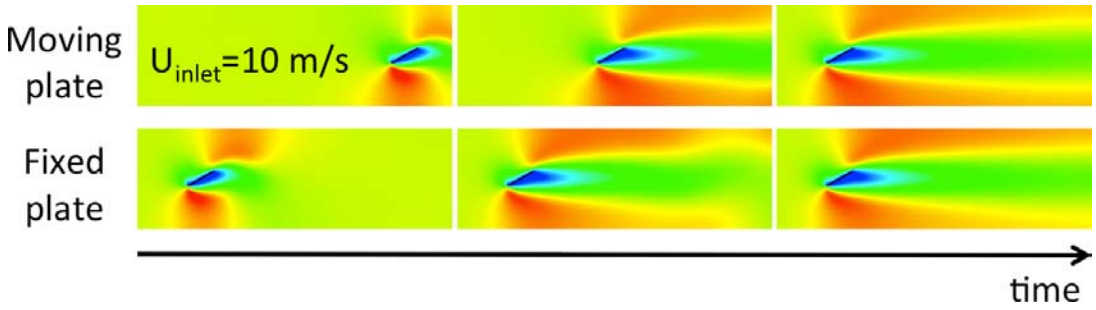

Figure 4.27: Inclined plate: moving and fixed configuration

of the translating plate is chosen so that at the end of the simulation, the plate reaches the position of the non-moving plate. To compare the results, Figure 4.28 and Fig. 4.29 shows the axial and transversal velocities. Once again, the agreement between the BC approach and the IBM is very good. However, in the configuration where the plate is moving, results are worse than when the plate is non-moving. Severals tests have been conducted to explain this. The temporal convergence was tested (the physical time of the simulation was doubled), the mesh grid was refined (8 points in the plate thickness instead of 4) but this phenomenon is not explained yet.

4.6 One-fan validation test case: failure

All academic test-cases previously presented in Sec. 4.5 give very encouraging results: all the comparisons between results obtained with the IBM and references solutions (analytical solutions and/or body conformal solutions) match very well.

Before computing the full configuration (the spherical vessel stirred by six fans), an experiment with only one fan (Fig. 2.2 in Sec. 2) in a rectangular box was setup in the PRISME laboratory in Orléans. Figure 4.30 shows a picture of the experimental setup and Fig. 4.31 presents the sketch of the configuration. The length of the box is 40 cm, the height and the width are 20 cm. The fan is located in the middle left hand side of the box. The back side of the fan is at 11 mm of the backside of the box. The rectangular box has two large windows to do PIV measurements in the axial direction. The box is closed so that the flow recirculates. This setup aims to validate the IBM implemented in a complex configuration (high Reynolds number, complex geometry): numerical and experimental solutions are compared to check if the IBM is able to predict the flow generated by a

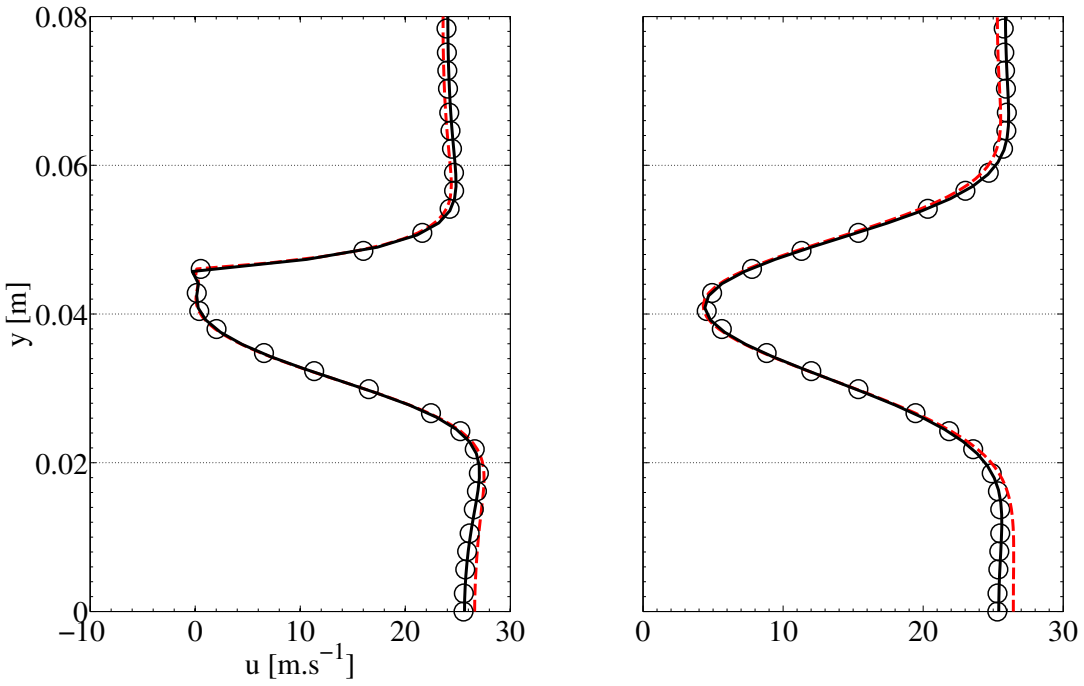

Figure 4.28: Axial velocity u. ◯ Body Conformal ; —— IBM with $u_p = 0$; ---- IBM with $u_p = -10$ m/s.

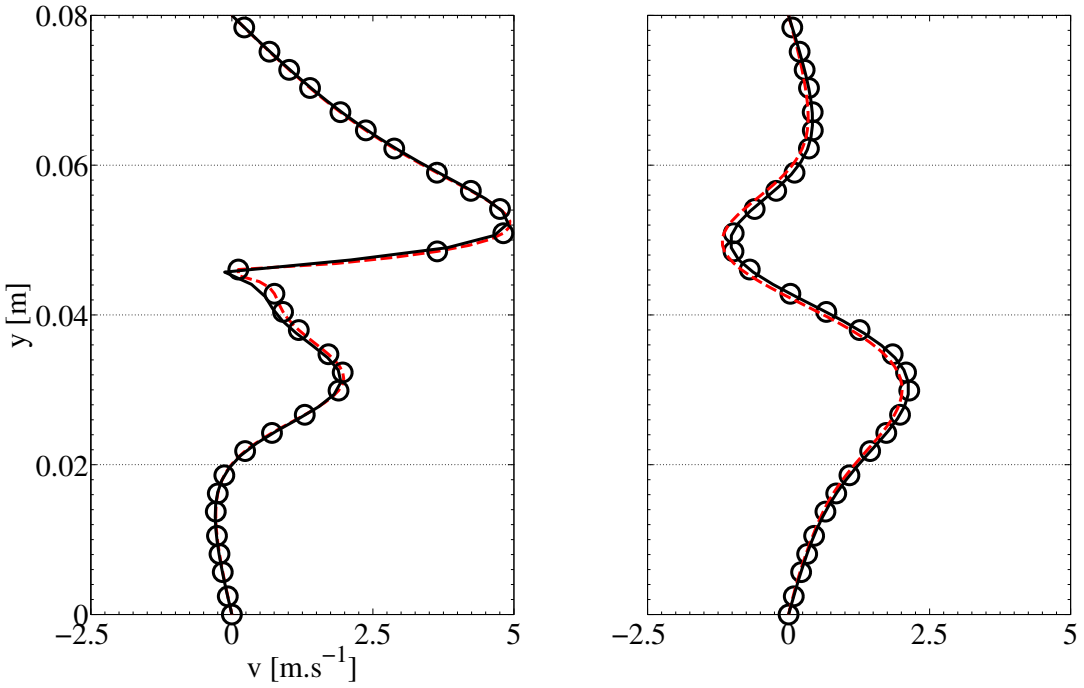

Figure 4.29: Axial velocity v. ◯ Body Conformal ; —— IBM with $u_p = 0$; ---- IBM with $u_p = -10$ m/s.

Figure 4.30: One-fan experiment setup in the PRISME laboratory in Orléans.

single axial fan. The experiment is conducted in ambient conditions and the fan rotation speed is $N_{fan} = 10,000$ tr/mn (the Reynolds number, based on tip radius (30 mm) and rotor tip speed (31.5 m/s) is about 60,000). The procedure to go from the fan geometry (coming from a CAD software) to an immersed boundary is the following. First the interior domain of the fan is meshed. Then a specific tool was developed to find all nodes on the skin of the fan and particles are generated at these points. Thus the number of particle can be easily changed by controlling the mesh resolution at the beginning of the procedure. Figure 4.32 displays the cloud of particles to mimic the fan boundaries. Here 93180 particles are generated with a resolution of about 4 particles in the blade thickness.

Figure 4.33 presents the experimental results obtained with PIV. Figure 4.33 shows average fields of axial u and transversal velocity v over 200 instantaneous fields. The convergence is ensured.

The computation with the IBM method is performed with the Lax-Wendroff scheme and the WALE subgrid scale (SGS) model. The grid is presented in Fig. 4.34. 13.7 millions of tetrahedra are used. The entire zone spanned by the fan is meshed with a fine cell size of the order of 0.5 mm (2 points in the plate thickness). This is the minimum cell size acceptable (the computation of the whole bomb with six fans would become impossible if the method requires more points to work). In the region surrounding the fan, the mesh size is 1 mm (about 30 points in the fan radius). Since the zone spanned by fans is meshed with only two points in the blade thickness, the real geometry of the fan is simplified in this computation: the geometry of the leading and trailing edges are originally curved but here they are replaced by flat leading and trailing edges (see 4.35). This simplification is then discussed in Sec. 5.2.2.

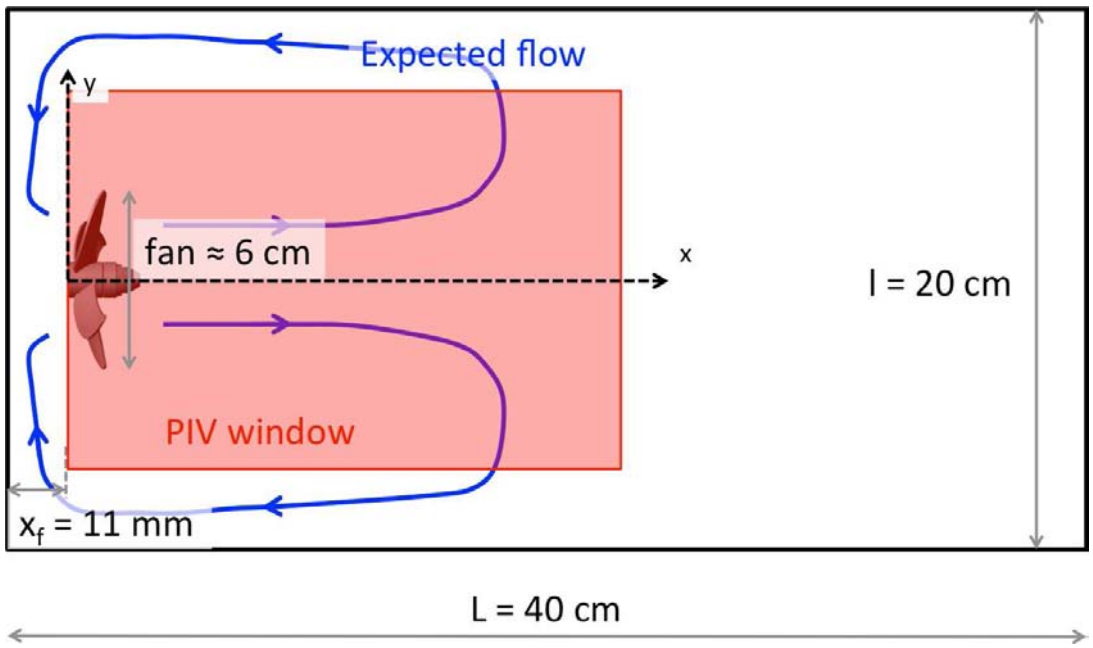

Figure 4.31: Sketch of the one-fan experiment conducted in the PRISME laboratory in Orléans.

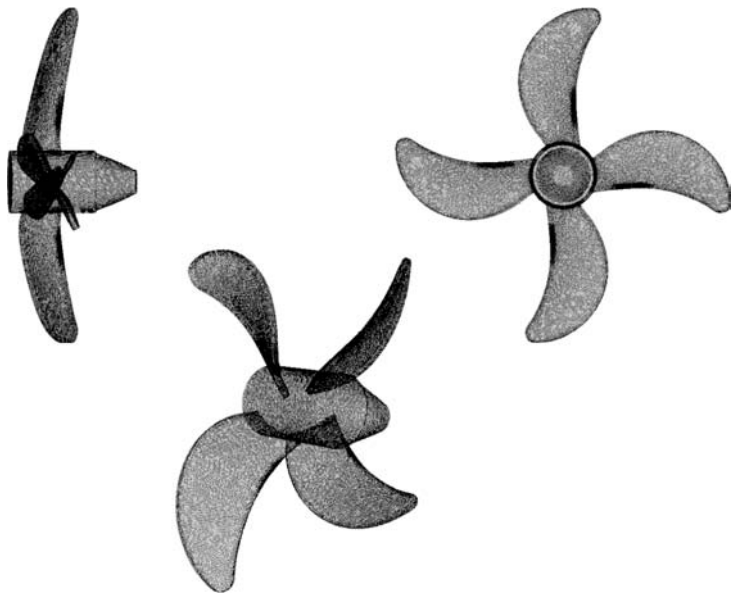

Figure 4.32: Cloud of particles to mimic the fan boundaries (walls). 93180 particles are disposed on the skin of the fan.

The procedure to compute this configuration is the same as the one described in Sec. 4.4. First, the computation is started using only the I controller to find the mean value of the source term. In this case, this value varies with the fan radius. Then the PI

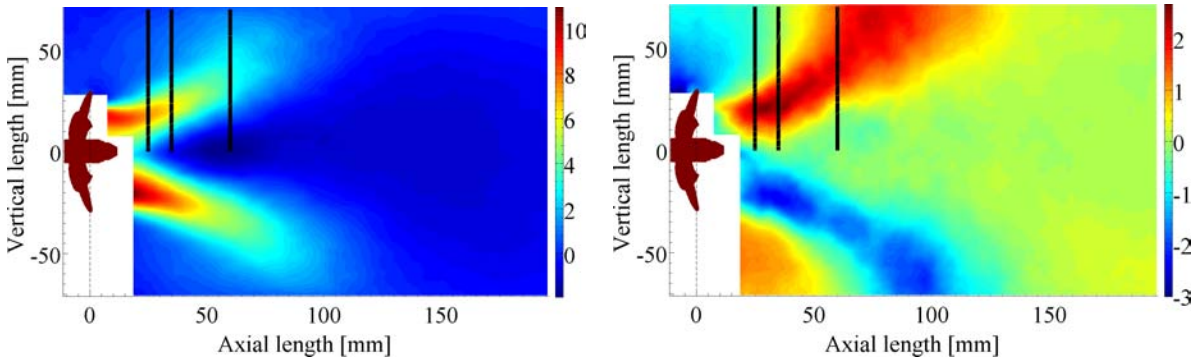

(a) Average axial velocity u.

(b) Average vertical velocity v.

Figure 4.33: Average velocities measured experimentally with PIV over 200 instantaneous solutions (black lines display the cuts position).

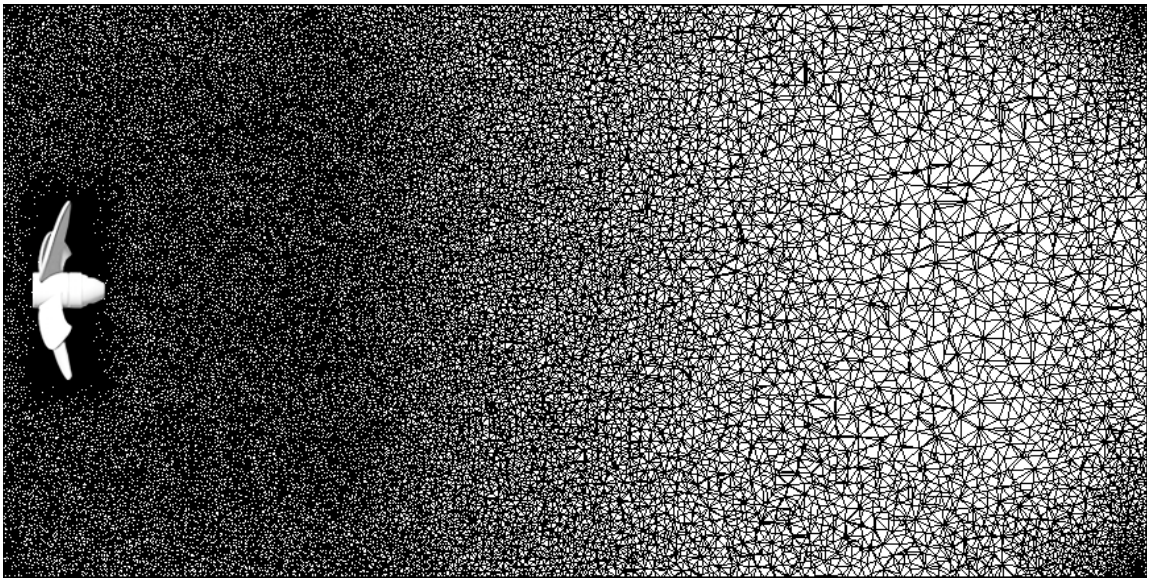

Figure 4.34: One-fan experiment mesh. 13.7 millions of tetrahedra.

controller is turned on. After that, several fan revolutions are computed to reach steady state. Figure 4.36 displays the mean flow computed with the IBM over 20 fan revolutions (which is enough to ensure fan convergence). Figure 4.33 and Fig. 4.36 show qualitative differences. The typology of the flow is not the same. One can see that the penetration of the air blast computed with the IBM is widely under estimated. The radial component of the flow at the fan outlet is over estimated with the IBM. To get more quantitative comparisons, Fig. 4.37 plots axial and vertical velocities cut downstream of the fan (see black lines in Fig. 4.36 to locate cuts position). Figure 4.37 confirms the previous observations: profiles obtained using the IB method do not match the experimental measurements.

To check the accuracy of the IBM in this test case, Fig. 4.38 shows the slip velocities at the immersed boundary position. The cumulative probability density function shows

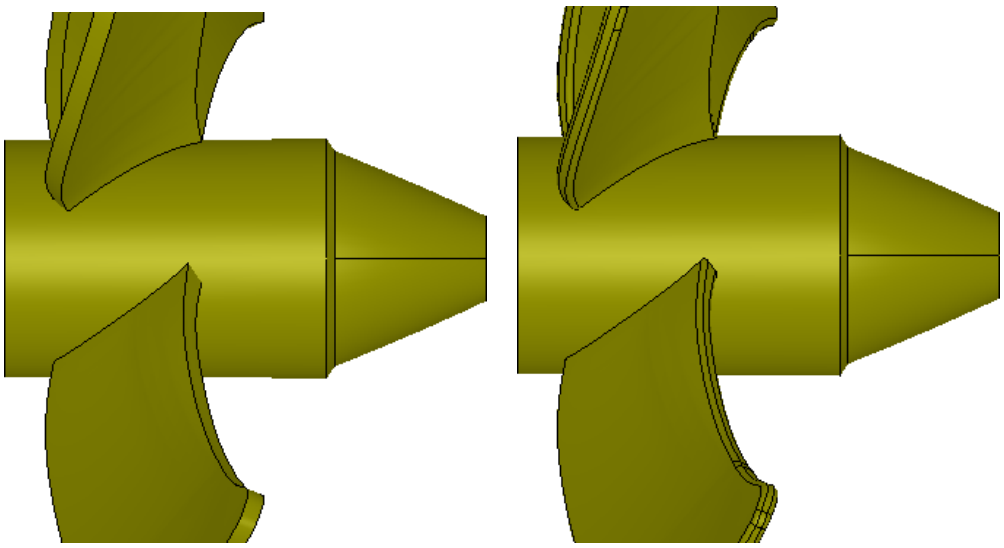

(a) Flat (b) Curved

Figure 4.35: Geometries of the leading and trailing edges of fan blades.

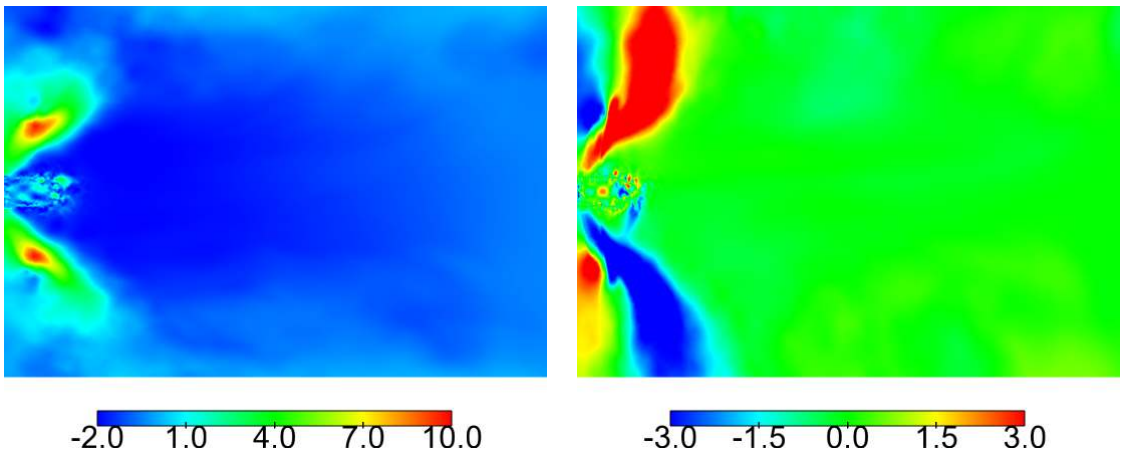

(a) Mean axial velocity u. (b) Mean vertical velocity v.

Figure 4.36: Average velocities computed with IBM.

that 90% of the Lagrangian particles have a slip inferior at 0.5 m/s. The maximum slip velocity is about 3 m/s and is located on the tip of the leading edge. At this place, the blade velocity is 31.5 m/s. This indicates that the maximum slip is about 10% of the boundary velocity which is acceptable confirming that the method gives reasonable results in term of no-slip boundary condition.

This test case is not widely described but many tests were performed to try to increase the accuracy of the method on this configuration. Several numerical setups were tested (TTGC scheme, Smagorinsky SGS etc.). Many grids have been tested but this one is the

finest and the one which gives the best results. This failure can be explained by the lack of resolution in the region spanned by the blades. Indeed, the resolution in this region is only of the order of two points in the plate thickness. So the shape of the blade seen by the fluid is not the expected shape (see Fig. 4.39). Even if the intensity of the source term scatter on node m depends on the distance between the node m and the Lagrangian particles, the shape seen by the fluid is not the original shape of the blade. That is why the flow generated is not the good one. The reason of this failure will be confirmed further in Chapter 5 where both geometries (flat and curved) will be computed and compared (flow structure, mean velocity).

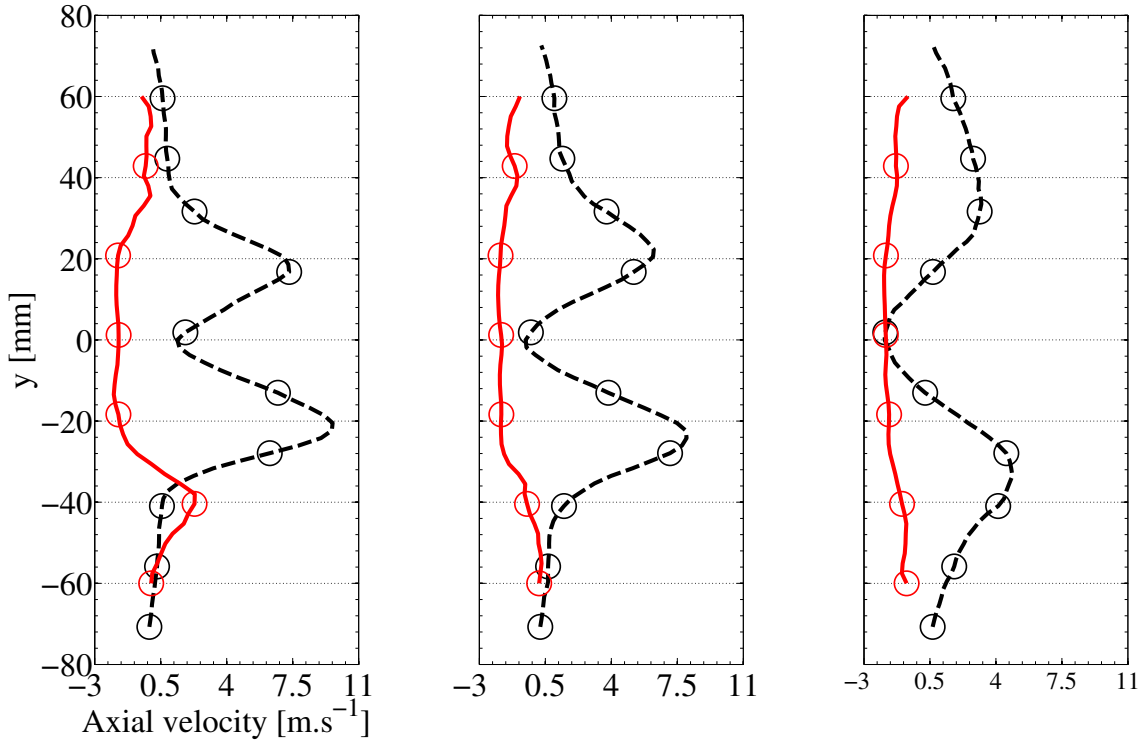

(a) Mean axial velocity u.

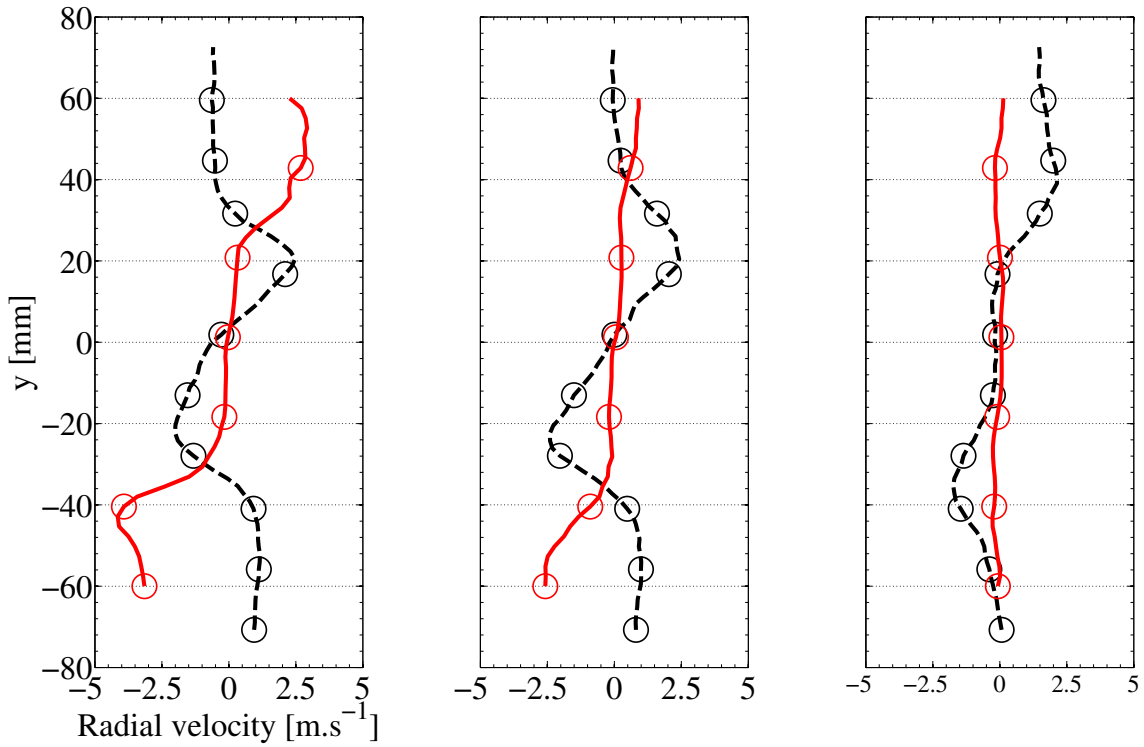

(b) Mean vertical velocity v.

Figure 4.37: Mean axial and radial velocities. -⊖- : PIV measurements ; —⊖— : IBM computation

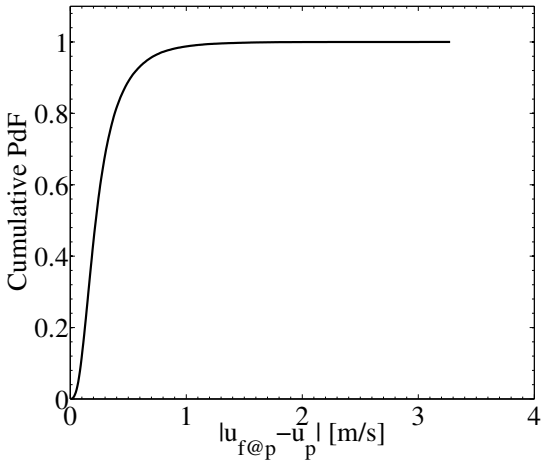

Figure 4.38: Slip at the particle position.

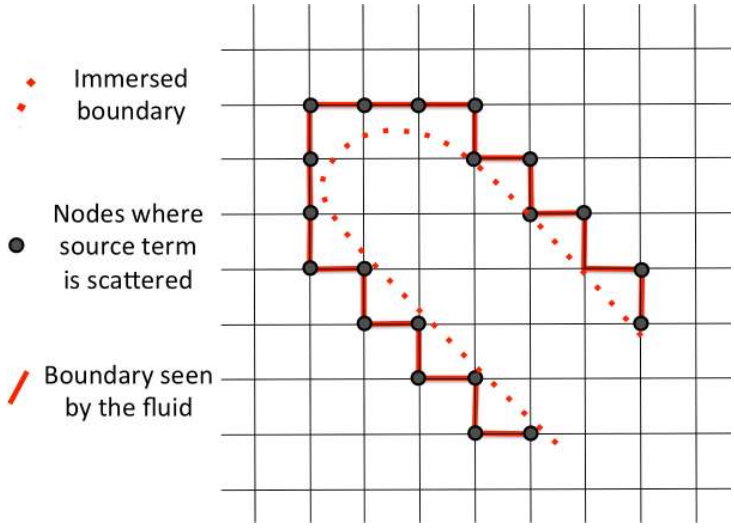

Figure 4.39: Blade shape seen by the Eulerian mesh.

4.7 Conclusion

An Immersed Boundaries Method was implemented in the AVBP code. This method is based on a continuous forcing approach using a source term in the RHS term in the momentum equation. The formulation of the source term used is the one proposed by Goldstein in 1993 [137].

Various academic test cases were performed such as a Poiseuille flow, a Couette flow, the flow around a cylinder or the flow around an inclined plate. Very good agreements were found between IBM computations and reference solutions for all these simple cases.

Finally, the method was used to compute the flow generated by one isolated fan in a simple configuration. Comparisons between computations and experimental data (obtained using PIV) in terms of mean and fluctuating flow gave bad results showing that the IBM method implemented can not be used to simulate the flow in the fan-stirred bomb.

CHAPTER 5

PRESENTATION AND VALIDATION OF THE MISCOG APPROACH

Contents

An Immersed Boundary Method was implemented in the AVBP *code and tested (see Chapter 4). Even though it gave good results on academic test cases, it was shown that the IB method is not able to predict correctly the flow generated by one isolated fan, that is why this approach can not be used to compute the full geometry of the fan-stirred bomb. After this partial failure, a new method had to be used in this PhD work to reach our objectives. Therefore, an approach based on the simultaneous execution of multiple instances of the same solver, called MISCOG for Multi Instances Solver Coupled on Overlapping Grids, first developed for turbomachinery [123, 124, 125] calculations was adapted to handle rotating parts. A three-dimensional vortex case was performed to check the ability of MISCOG to convect vortices, then the one-fan validation test case was performed.*

5.1 The MISCOG approach

The objective of this section is to show how the turbulent flow in a fan-stirred bomb can be studied today using high-resolution LES to complement experimental diagnostics. To reach this objective, the simulation code must satisfy three criteria:

1. Considering the complexity of the objects to mesh, the need to correctly capture the blade geometry and the necessity to handle moving objects, unstructured meshes are required so that classical DNS codes used for HIT (spectral methods [120, 121], high-order compact schemes [117, 118, 119]) cannot be used.
2. The method must be able to accommodate a large number of moving objects (the fans) close to each other. Classical techniques such as ALE [78, 122, 53] are difficult to implement for a flow with multiple fans because of meshing issues. Immersed Boundary methods [75, 76, 135] are easier to develop for moving objects but the method implemented in *AVBP* was shown to be unable to predict correctly the flow generated by one isolated fan. Here a new multidomain high-order LES technique with mesh overlapping (called MISCOG for Multi Instances Solver Coupled on Overlapping Grids) developed by Wang et *al.* [123, 124, 125] is used on a real bomb.
3. To capture turbulent structures explicitly, a high fidelity LES solver is needed and the corresponding CPU cost is expected to be large so that the implementation of the multidomain method must be fully parallel.

The MISCOG approach, initially developed for turbomachinery [123, 124, 125], was extended to bomb configurations. In MISCOG, two or more instances of the same LES solver (namely AVBP), each with their own computational domain, are coupled through the parallel coupler OpenPALM [149, 150]. For the bomb case, the whole flow domain is initially divided into 7 parts: the bomb itself has a static mesh (AVBP01) while each fan is computing in a moving framework (AVBP0i, $i \in [2; 7]$). For moving parts, the code uses the ALE block rotation approach [77, 79, 53]: the grid is rotated without deformation. The remaining unit AVBP01 simulates the flow in the static part of the bomb in the same coordinate system. The solution retained to handle interfaces between the units involving

rotating and non-rotating parts consists in reconstructing the residuals using an overset grid method and exchanging by interpolation the multi-domain conservative variables wherever needed. To do so an efficient distributed search algorithm is implemented in the OpenPALM coupler to locate the points in parallel partitioned mesh blocks and a linear method is used to interpolate residuals (the interpolation is of 2^{nd} order). This coupling phase is implemented outside the CFD instances in conjunction with second order interpolation.

The domains used for the Orléans bomb configuration are displayed in Fig. 5.1: six cylindrical rotating domains ($i = 2$ to 7) are used for each fan zone while AVBP01 is used for the rest of the bomb. In general, the number of cells used for each domain

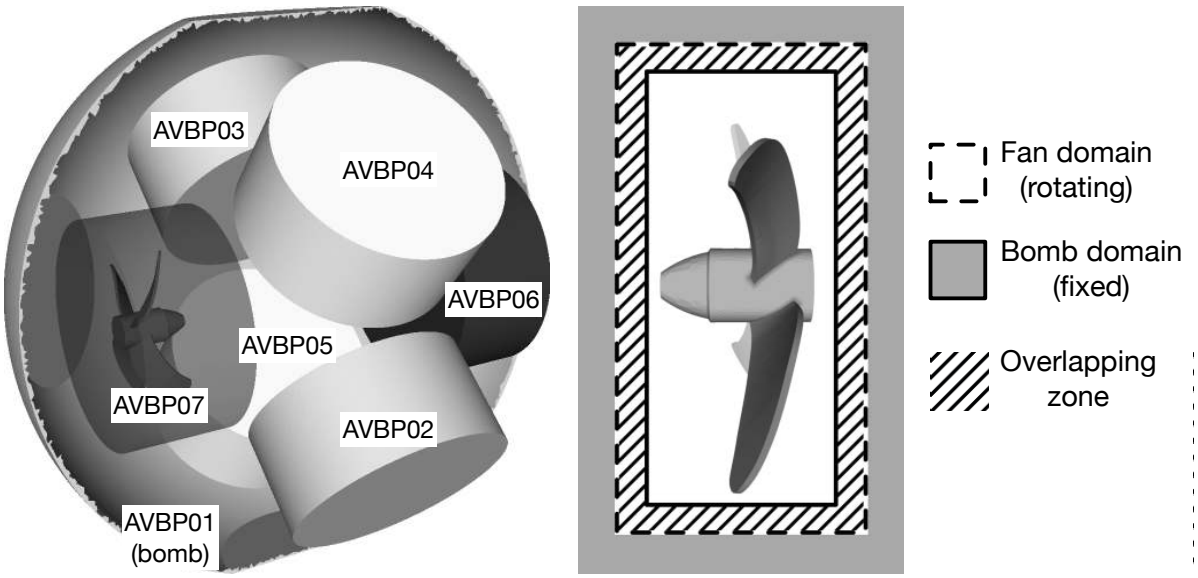

Figure 5.1: Domain decomposition in the Orleans bomb configuration. Six cylindrical rotating domains (AVBP02 to AVBP07) containing each fan and one fixed domain (AVBP01) for the rest of the bomb.

can be different. Here the grids for the six fans (AVBP02 to AVBP07) have the same number of cells but the bomb grid (AVBP01) is different so that load balancing becomes immediately an issue which will be discussed in Sec. 6.2. The timetable used in the MISCOG approach for each iteration is the following:

1. All AVP0i ($i \in [1; N]$) entities run.
2. When AVBP01 and AVBP02 have computed one iteration, they exchange conservative variables in the buffer zone of regions 1 and 2. After this exchange, AVBP02 starts to compute the next iteration.
3. When AVBP03 finishes its iteration and AVBP01 is done exchanging, AVBP01 and AVBP03 start to exchange, otherwise AVBP01 waits. This is repeated for all AVBP0i instances ($i \in [2; N]$).

Note that AVBP01 starts to compute the next iteration as soon as it has exchanged residuals with the last instance AVBP0N.

5.2 Validation test cases

Many academic test cases have been performed by CERFACS and University of Sherbrooke to validate the MISCOG approach in cases where a single mesh or an analytical solution can be used as a reference solution. For example, acoustic wave and two-dimensional vortex propagation cases were tested successfully using MISCOG by Wang et *al.* [123, 124, 125]. Rotor/stator computations with ALE and MISCOG were compared by Duran during its PhD. These results show good performances of the MISCOG approach and a negligible loss of precision through the overlapping zone thanks to the second order interpolation. Here, two test-cases are performed:

- a three-dimensional vortex case through a rotating domain closer to the Orléans bomb geometry was tested by propagating a vortex with the TTGC scheme
- the one-fan validation test case, previously presented in Sec. 4.6, is performed to check the ability of MISCOG to predict the flow generated by one isolated fan.

5.2.1 Convection of a vortex

A first good test case is to compute a flow which can be computed on a fixed grid (for reference) but is computed using a moving part to verify that MISCOG remains accurate when the meshes move. Here a simple vortex convection case was tested in a box where the grid contains a rotating cylinder part (Fig. 5.2). The computational domain is a tri-periodic cubic box where the cylindrical grid is inserted. The cylinder rotates at $10,000$ rpm corresponding to the rotation speed of the fans in the real bomb. The mean flow goes from left to right at $U_0 = 50$ m/s. In this test case, the vortex must travel through interfaces without being affected by the inner rotating mesh so that the exact solution is simple to derive as a reference. Indeed, the analytical solution of this case can be derived easily: the velocity field $u(X,t)$ at a given time t is the initial velocity field $u(X,t_0)$ translated at the convection velocity: $u(X,t) = u(X - U_0(t-t_0),t)$ This test case is representative of the target configuration where fans are encapsulated in finite cylinders: vortices created by the fan blades must travel through the coupling interface. This case is simulated both with the MISCOG approach and with a single domain (fixed grid) AVBP computation with the TTGC scheme (LW was successfully tested but results are not shown here). Figure 5.3 shows a qualitative comparison of the velocity field with both methods after two convection times through the full domain. Figure 5.4(a) presents the time evolution of the axial velocity at the center of the rotating cylinder while Fig. 5.4(b) shows a cut of the pressure field after two convection times. A very good agreement is found between the analytical solution, the single domain computation and the MISCOG approach. The vortex is convected at the expected speed U_0 (no dispersion) and its structure is preserved (no dissipation). Note that formally, when the vortex goes through the overlapping zone, the third order of the TTGC scheme is lost since the current interpolation is of 2^{nd} order. However, the pressure and the velocity profiles are both well convected.

This test case demonstrates the ability of the MISCOG approach to convect a 3D vortex through different interfaces and confirms the accuracy of this approach for coupled

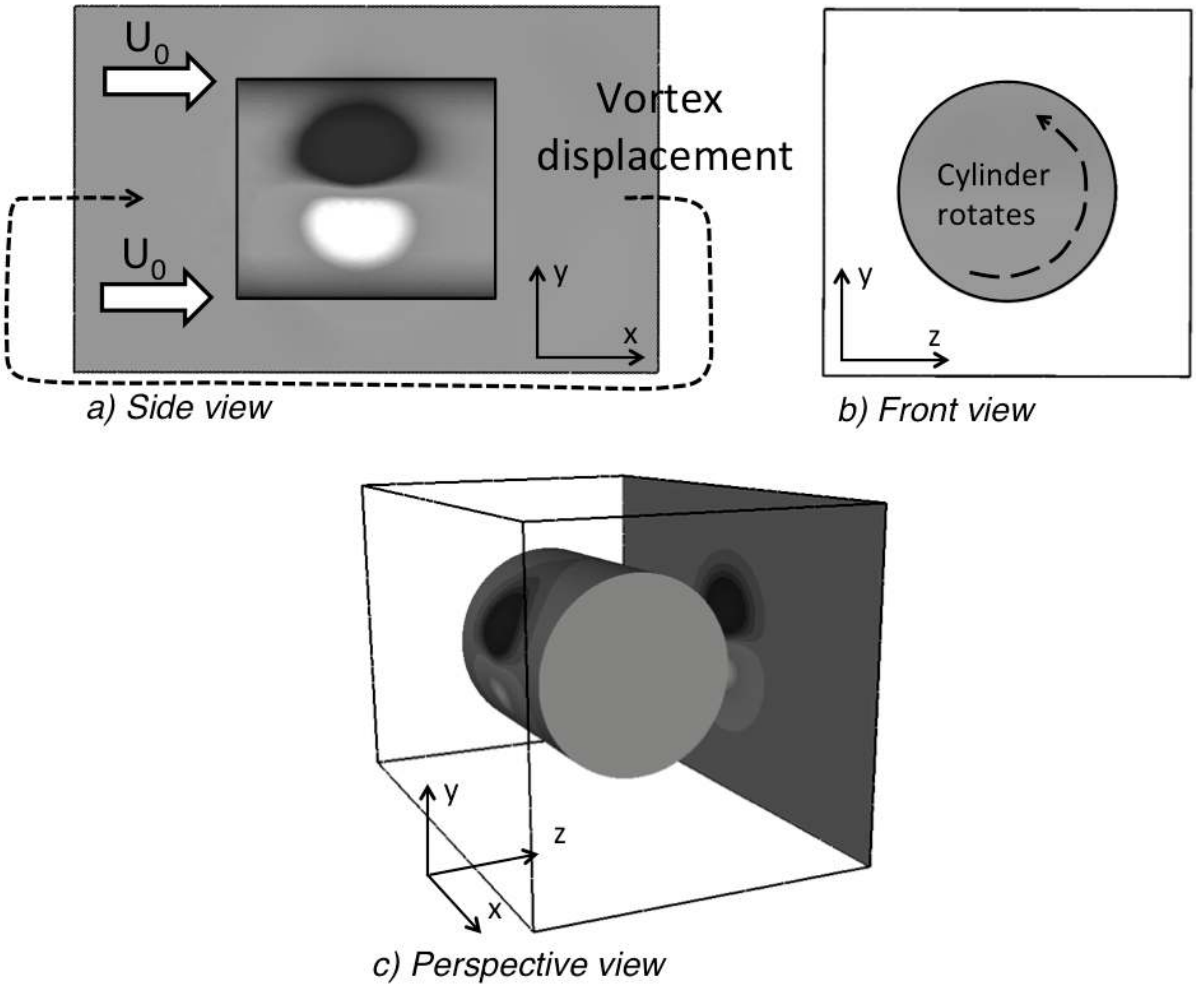

Figure 5.2: Sketch of the 3D convection vortex test case: a rotating cylinder (AVBP02) is placed inside a tri-periodic box (AVBP01). Views are colored by the velocity field.

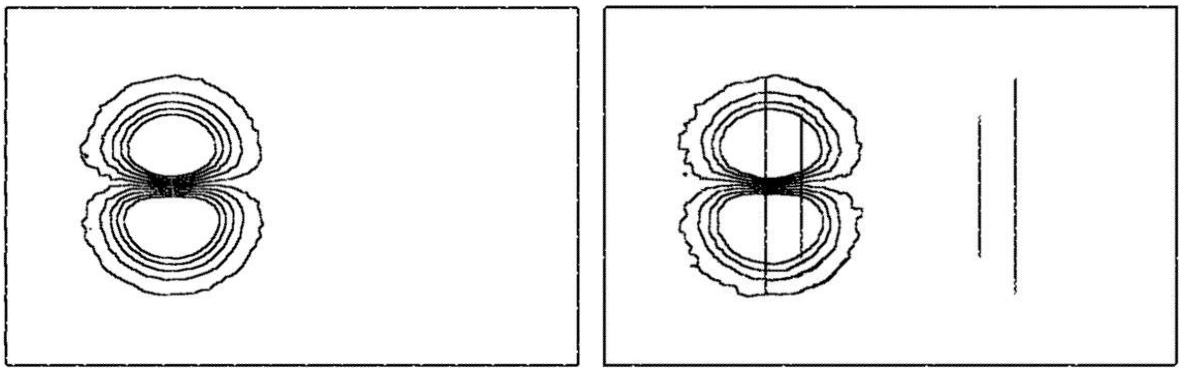

(a) Single instance computation. (b) MISCOG computation.

Figure 5.3: Comparison between a classic` single mesh AVBP computation and the MISCOG approach. Isolines of velocity after two convection times (the vertical lines in Fig. 5.3(b) indicate the position of the rotating cylinder and of the overlapping zone).

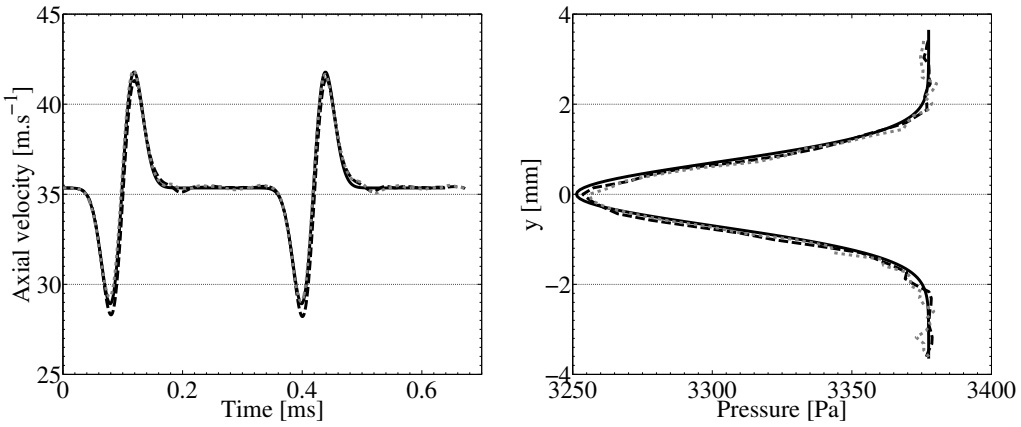

(a) Axial velocity at center of the cylinder versus time.

(b) Pressure along y-axis after two convection times.

Figure 5.4: Comparison between a classic` single mesh AVBP computation and the MISCOG approach. —— : analytical solution ; ---- : single mesh approach ; ····· : MISCOG.

LES. On the long term, it is clear that the interpolation method used in the overlapping zone combined with the numerical scheme in each domain leads to global dispersion and dissipation properties which would require a much more precise analysis. This is left for further studies because it would require much more numerical analysis work. Here we will concentrate on the fan-stirred bomb simulations using the existing MISCOG method.

5.2.2 One-fan validation test case

The one-fan validation test case is performed now to check if the MISCOG approach is able to give better results than the IB method (presented in Sec. 4) to predict the flow generated by one isolated fan. The configuration is presented in Sec. 4.6. The operating point computed is the same: ambient air conditions and the fan rotation speed is $N_{fan} = 10,000$ tr/mn.

The computational domain is decomposed into two instances (see Fig. 5.5):

- the box which is fixed (AVBP01),
- a rotating domain which contains the fan geometry (AVBP02).

All boundary conditions are no-slip walls. Prism layers are added on all blade-walls to describe the boundary layer [151]. The typical thickness of the prism layers is about 0.04 mm, so that the maximum wall $y+$[1] on the first grid point near the blade wall is about 7 and is located at the leading edge of the blade. All around the fan, the mesh size is about 1.5 mm then the cell size is increased until the end of the box. This leads to grid of about 16 millions of tetrahedra. Computations are performed using LW scheme and WALE as SGS model.

[1]The non-dimensional wall distance y^+ is defined by $u^+ = yu_\tau/\nu$ where u_τ is the friction velocity. u_τ is defined by $u_\tau = \sqrt{\tau_{wall}/\rho}$

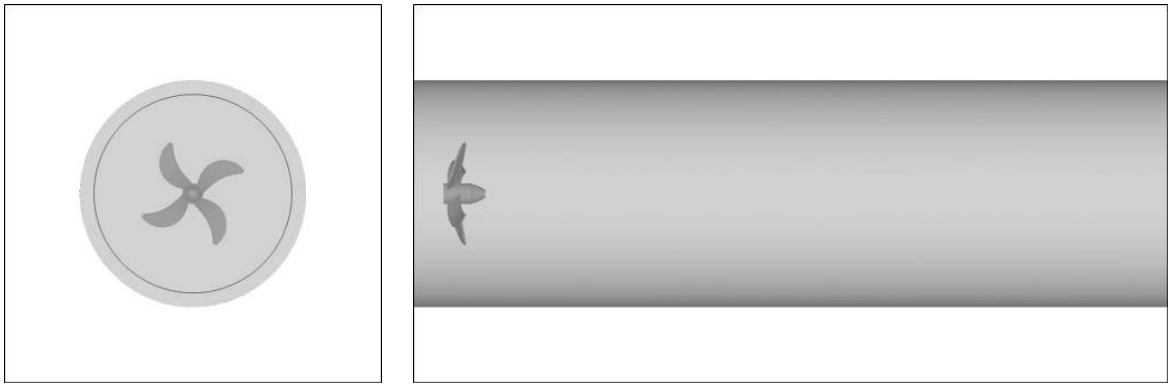

(a) Front view (b) Side view

Figure 5.5: Domain decomposition in the one-fan configuration. Gray: rotating cylindrical domain ; Gray : fix domain.

Thanks to the MISCOG approach, both geometries of blades (curved and flat leading and trailing edges) presented in Sec. 4.6 (see Fig. 4.35) can be computed and compared. Specialists of turbomachinery CFD insist on the necessity of properly resolving the blade geometrical details, at leading and trailing edges. With the IB method this was difficult (because the shape must be resolved on a mesh which is not body fitted) but the MISCOG technique allows to resolve these details because the mesh rotates with the blade and can capture the exact geometry. This will also allows us to evaluate the impact of any approximations on the results, for example, when leading and trailing edges are assumed to be flat. Here, the curved shape of leading and trailing edges is discretized using 6 points in the blade thickness for the MISCOG computations.

Figure 5.6 compares average axial velocity fields using flat or curved edges. These fields show qualitative differences. The penetration length of the air blast is much more important when the real leading and trailing edges are considered: assuming that they are flat leads to erroneous results.

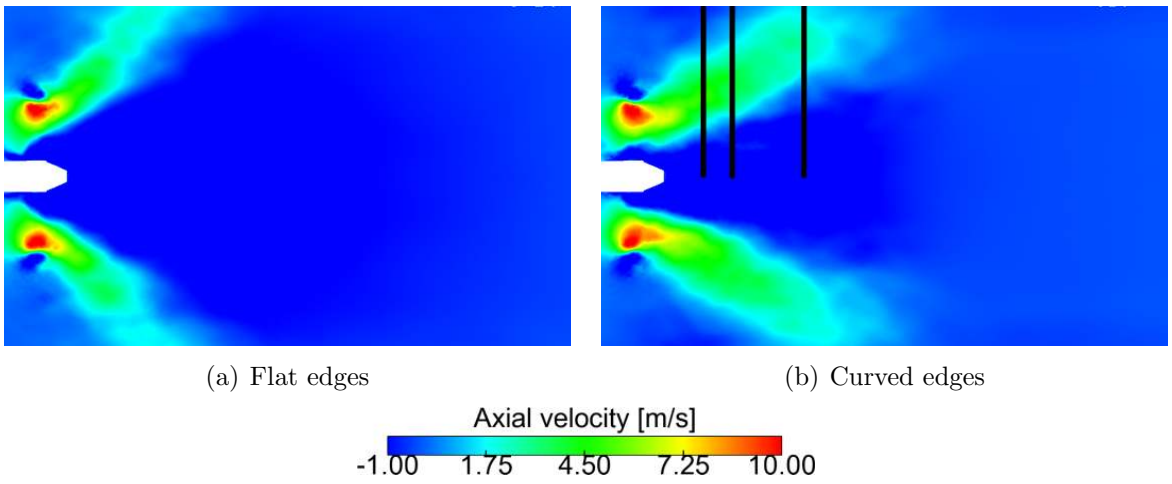

(a) Flat edges (b) Curved edges

Figure 5.6: Mean axial velocity comparison between flat and curved leading and trailing edges (black lines in display the cuts position).

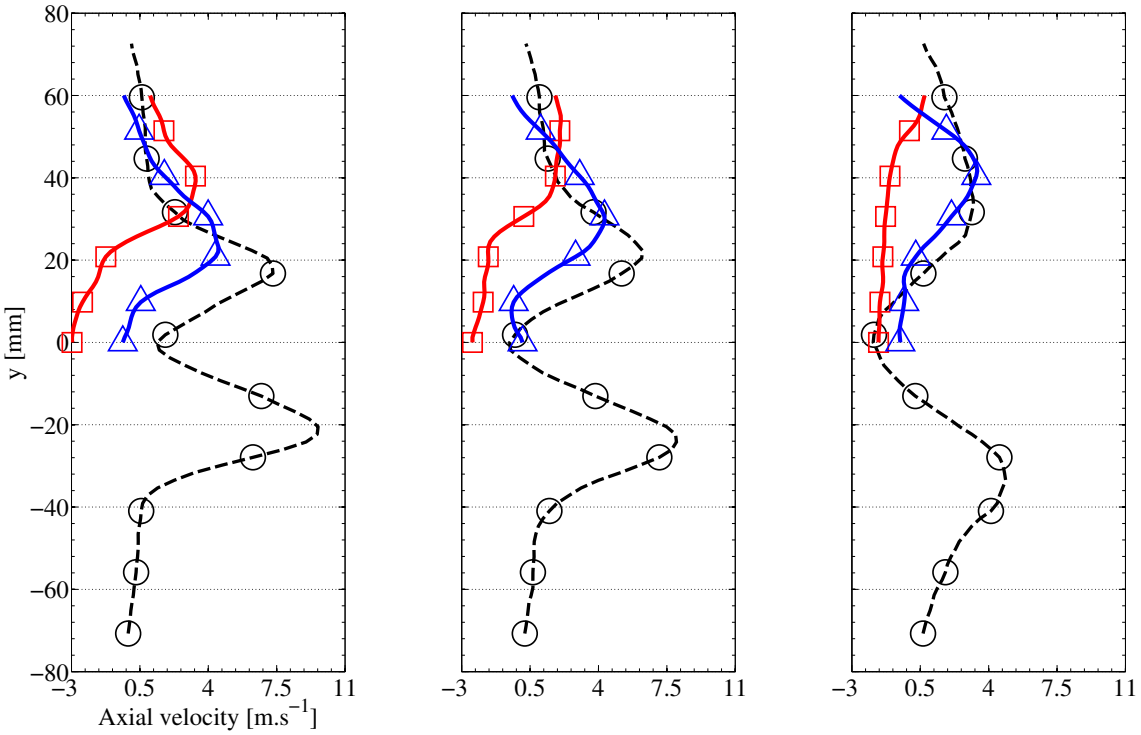

(a) Axial velocity

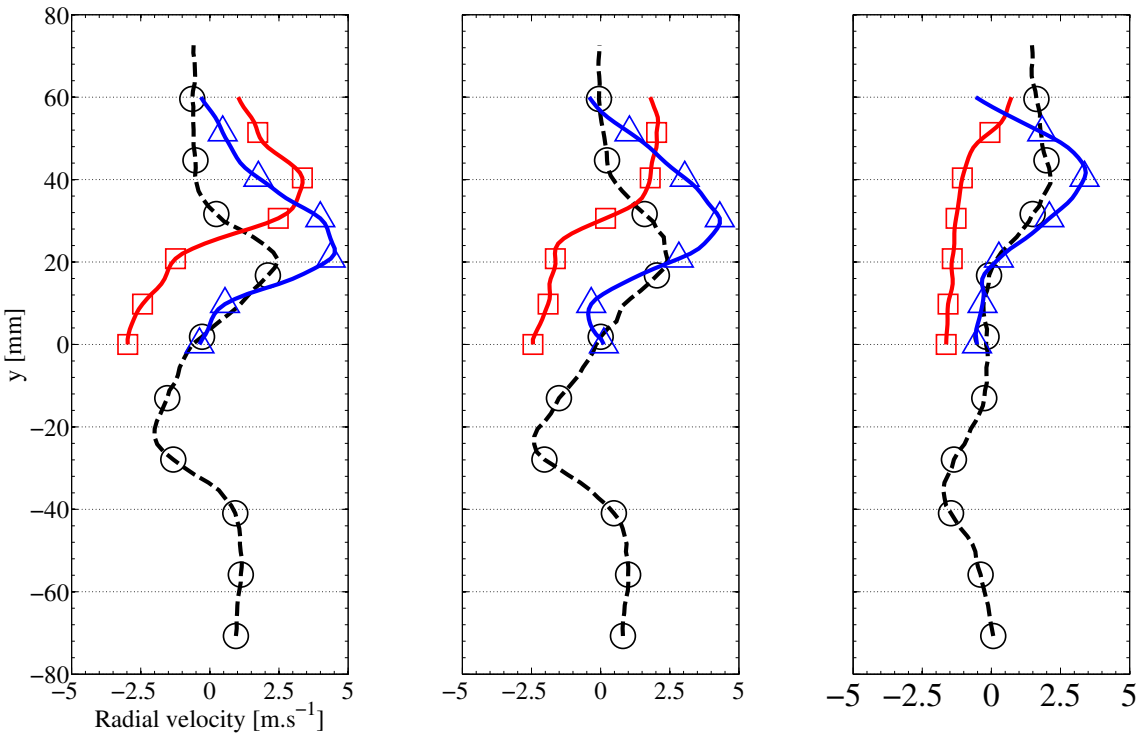

(b) Radial velocity

Figure 5.7: Mean axial and radial velocities. -⊖-: PIV measurements ; —□—: Flat leading and trailing edges ; —△—: Curved leading and trailing edges.

Figure 5.7 shows mean axial and radial velocity cuts downstream of the fan (black lines in Fig. 5.6 display the cuts position). Results are compared to PIV measurements. In all cases, results obtained using the MISCOG approach are much better than results obtained using IB method (Fig. 4.37). Moreover, a significant improvement is obtained when the real geometry of edges (curved) is considered: the airflow opening is narrow and the penetration length is longer. For axial and radial velocities, the position and the magnitude of the maximum of velocity are displaced in the right direction compared to experimental data. In the far field the agreement is good.

Taking into account curved edges leads to important variations in the blade boundary layer (see Fig. 5.8). When flat edges are considered, the leading edge acts like a step and

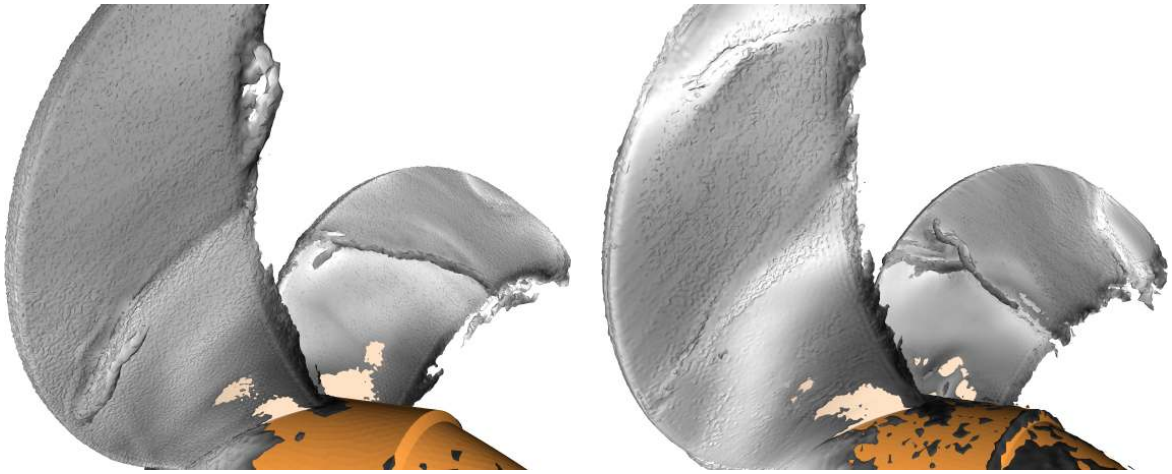

(a) Flat edges (b) Curved edges

Figure 5.8: Laminar to turbulent boundary layer transition. Isosurface of vorticity colored by the velocity.

the boundary layer is turbulent all along the blade: from the leading to the trailing edge. On the contrary, when curved edges are considered, the boundary lawyer is first laminar then becomes turbulent. This small` geometric variation leads to important variations, not only at the boundary layer scale but even at large scales (the mean flow is completely different).

As a conclusion, the MISCOG approach is able to predict the flow generated by an axial fan provided that the exact geometry of blades is computed: even minor simplifications of the fan geometry (at the leading and trailing edges) leads to large errors. This result explains why the IBM is not able to do the job: the mesh resolution required, in the region spanned by the fan, to capture the exact shape of the blade is prohibitive in terms of CPU cost. Indeed, at least 6 points in the blade thickness will be necessary leading to a cell size of 150 μm, which is not realizable especially with the objective of computing the six-fan-stirred vessel. For all result described now, the MISCOG approach will be used. The next chapter describes how it was applied to the full six-fan bomb.

5.3 Conclusion

In order to compute the full geometry of the Orléans closed vessel, an approach coming from turbomachinery calculations was adapted to handle rotating parts. This method couples multiple instances of the same code, exchanging residuals on small overlapping zones. A first test case shows that the MISCOG approach is able to convect vortices with limited dispersion and dissipation effects. The second test case shows that the method is able to predict the flow generated by one isolated fan.

CHAPTER 6

AERODYNAMICAL STUDY OF A SPHERICAL BOMB STIRRED BY SIX FANS

Contents

The MISCOG approach, presented in Chapter 5, has demonstrated its ability to simulate the flow generated by one isolated fan. First, the parallel efficiency of MISCOG technique applied to the bomb configuration (closed vessel with six fans) is discussed. Then, this chapter discusses non-reacting flow results in the full closed vessel with six rotating fans: quantities that can be obtained both from LES and PIV are first compared (using mean flow fields and RMS values for all three velocity components). LES results are used to analyze quantities which can not be experimentally obtained such as the velocity tensor to identify the structure of the turbulence or the budget of turbulent kinetic energy in order to understand how turbulence reaches the center of the vessel.

6.1 Numerical setup

Simulations used to gather statistics are performed with the TTGC scheme. The subgrid scale (SGS) model is WALE [48] which was developed for wall bounded flows. All boundary conditions are no-slip and adiabatic walls (fans and closed vessel).

Experimental results obtained in the PRISME laboratory, give values for the RMS velocity $\mathbf{u_{rms\ exp}}$ and the integral length scale $L_{\tau\ exp}$ at the bomb center: $\mathbf{u_{rms\ exp}} \simeq 3$ m/s and $L_{\tau\ exp} \simeq 3$ mm. The time scale associated to the integral length scale τ is $\tau = L_{\tau\ exp}/\mathbf{u_{rms\ exp}} \simeq 1$ ms. Knowing the viscosity $\nu = 1.78.10^{-5}$ m^2.s^{-1} the turbulent Reynolds number can be evaluated $Re_{t\ exp} = \mathbf{u_{rms\ exp}} L_{\tau\ exp}/\nu \simeq 600$. The experimental Kolmogorov length scale η_{exp} can be estimated with the relation:

$$\eta_{exp} = L_{\tau\ exp}/Re_{t\ exp}^{3/4} \tag{6.1}$$

giving a value of the order of $\eta_{exp} \simeq 40\ \mu m$. Theses information are summarized in Tab. 6.1. The computation with a constant mesh size in the whole bomb of $\Delta x = 1$ mm

$\mathbf{u_{rms\ exp}}$	3 m/s
$L_{\tau\ exp}$	3 mm
τ	1 ms
$Re_{t\ exp}$	600
η_{exp}	40 μm

Table 6.1: Experimental data about the flow at the bomb center.

in the closed vessel gives a ratio $\Delta x/\eta_{exp} \simeq 25$ corresponding to a mesh of 21 million of cells for AVBP01. For the mesh of the fan, a fine discretization at the blade-walls is used to capture the flow generated by fans (Fig. 6.1): four prism layers are added on all blade-walls to describe the boundary layer [151]. The typical thickness of the prism layers is about 0.05 mm, so that the maximum wall $y+$[1] on the first grid point near the

[1]The normalized wall distance y^+ is defined by $u^+ = yu_\tau/\nu$ where u_τ is the friction velocity. u_τ is defined by $u_\tau = \sqrt{\tau_{wall}/\rho}$

blade wall is 10 and is located at the leading edge of the blade (see Fig. 6.2). The mesh size around the fan (away from the walls) is 1 mm leading to a mesh of 3.3 million cells for each fan instance AVBP02 to AVBP07. Thus the full mesh including the bomb-mesh and the six fan-meshes contains 41 million cells.

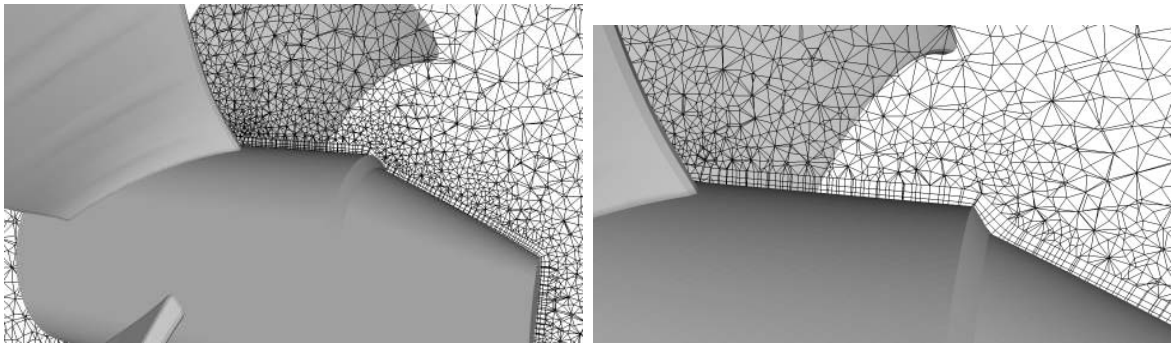

Figure 6.1: Mesh of the fan. Four prism layers were added near blade-walls.

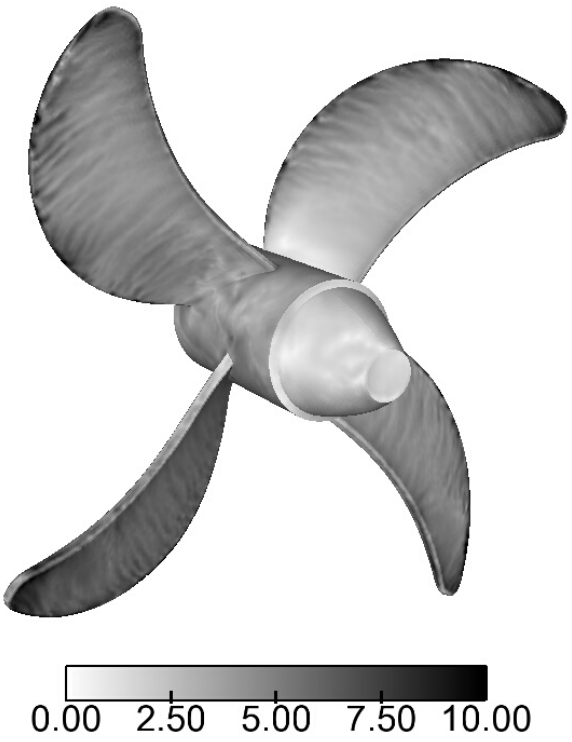

Figure 6.2: y^+ field on the fan walls.

6.2 Efficiency of the MISCOG approach in the bomb configuration

The load balancing of the MISCOG approach strategy raises much more questions than the usual optimization of single instance codes on parallel systems: the present configuration requires the coupling of 7 AVBP entities (one for the bomb and 6 six for the fans). Timers were added to measure the times needed for (1) computation, T_c, (2) exchange, T_e and (3) waiting, T_w.

Defining a waiting time T_w in a multiple instances run requires caution. Here we define T_w using the following convention: T_w is negative when fans (AVBP02 to AVBP07) wait while it is positive if the bomb (AVBP01) waits. Note that T_e corresponds to exchanges between AVBP01 and individual fans: communication times between cores inside each instance are included in the computation time. Two computation times are defined: T_c^f and T_c^b, the fan and the bomb standalone computational times, respectively.

A theoretical model of performance for MISCOG can be derived using simple relations. Two limit cases are considered. The bomb-limited case (BL) where fans have to wait - corresponding to $T_w < 0$ - and the fan-limited case (FL) where the bomb has to wait - corresponding to $T_w > 0$. Timetables of BL and FL cases are displayed in Figs. 6.3 and 6.4, respectively. According to timetables presented in Figs. 6.3 and 6.4 and using the

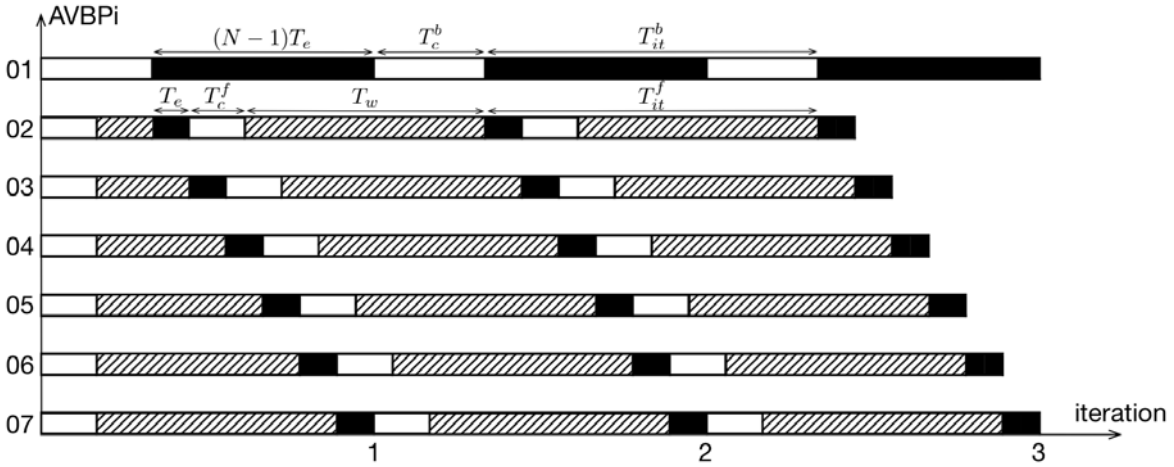

Figure 6.3: Timetable of the operations performed in the MISCOG approach for the BL case (only fans wait). ▭ : Computing ; ▨ : waiting ; ■ : exchanging

convention previously proposed for the waiting time, leads to an expression for T_w, which is valid for all cases:

$$T_w = (T_c^f - T_c^b) - (N-2)T_e \tag{6.2}$$

The exchange time, T_e, can not be estimated simply (its dependance on load balancing is not easy to evaluate) and it was measured in the solver. The total time for one iteration T_{it} can be expressed using two relations: communications between instances in MISCOG

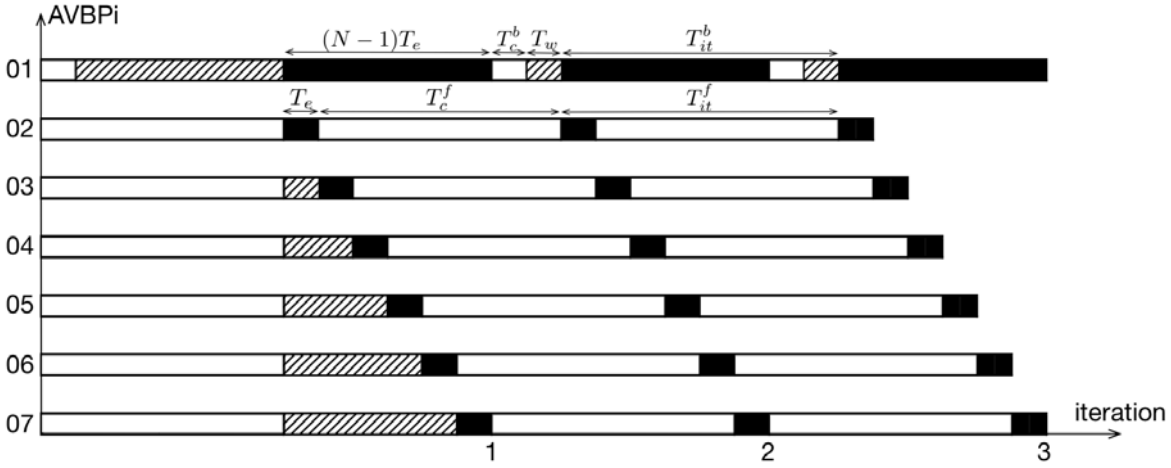

Figure 6.4: Timetable of the operations performed in the MISCOG approach for the FL case (only bomb waits). ▭ : Computing ; ▨ : waiting ; ■ : exchanging

approach are sequential so that (except for the first iteration) the time needed by the bomb (AVBP01) to compute one iteration T_{it}^b is equal to the time needed by each fan (AVBP02 to AVBP07) to compute one iteration T_{it}^f (Figs. 6.3 and 6.4). This leads to two expressions for T_{it}:

$$T_{it} = \underbrace{(N-1)T_e + T_c^b}_{T_{it}^b} + \max(0, T_w) = \underbrace{T_e + T_c^f}_{T_{it}^f} - \min(0, T_w) \tag{6.3}$$

To validate this model, computations were performed where the total number of cores was fixed (400 on SGI Altix ICE 8200) and the ratio $R_c = N_c^b/N_c^f$ of the number of cores allocated to the bomb instance AVBP01 (N_c^b) to the number of cores allocated to fan instances AVBP02 to AVBP07 (N_c^f) was varied (all fan instances have the same number of cores). Table 6.2 summarizes the computations performed to evaluate the performance of MISCOG. Figure 6.5 compares the model (Eqs. 6.2 and 6.3) to waiting and total times

Name	R_c	T_e	T_w	T_{it}
MISCOG 1	2	0.593	-4.35	6.19
MISCOG 2	4.5	0.345	-2.42	4.37
MISCOG 3	9.9	0.347	-1.28	3.93
MISCOG 4	19	0.423	-0.34	4.03
MISCOG 5	34	0.606	-0.25	7.84

Table 6.2: Simulations performed to evaluate the performance of MISCOG. The ratio R_c is increased for MISCOG 1 to 5. All times are given in seconds per iteration.

measured in simulations. Figure 6.5(a) shows the waiting times. When Rc is increased (more cores are allocated to the bomb instance AVBP01), the waiting time is expected to go from negative (fans wait) to positive (bomb waits) values as shown by Eq. 6.2.

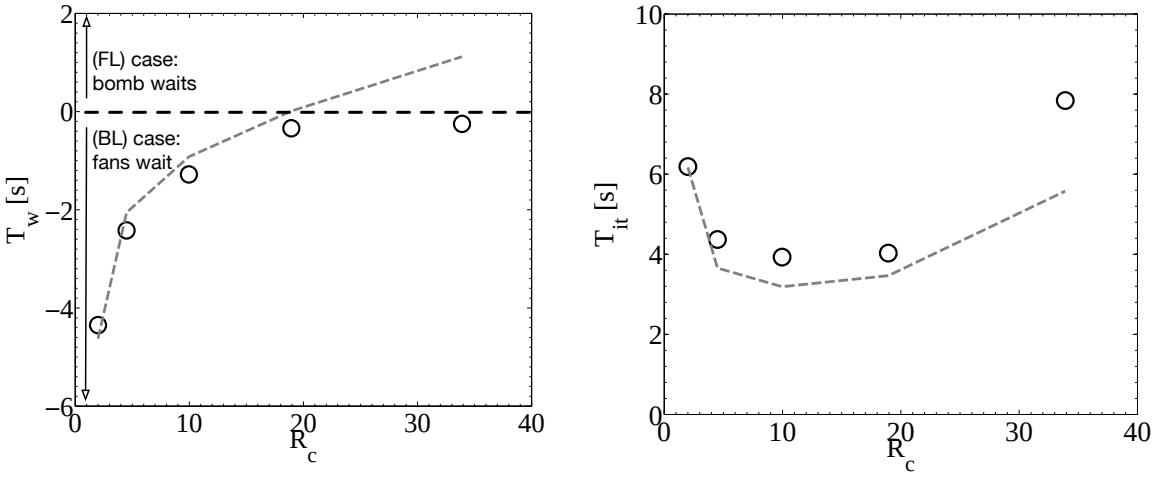

(a) Waiting time T_w.

(b) Total time for one iteration T_{it}.

Figure 6.5: Performance of MISCOG. ∘ : Computations ; ---- : model.

A good agreement is found while Rc is less than 20. For large Rc values, the trend is good but values differ slightly: in simulations the waiting time goes to zero but remains negative. When there are extreme differences in load balancing between AVBP01 and AVBP02 ($R_c > 20$) the behavior of MISCOG is not well understood yet. According to Eq. 6.2, in order to cancel the waiting time ($T_w = 0$), the load balancing must be chosen such as $T_c^f = T_c^b + (N-2)T_e$. This leads here to a ratio $R_c \simeq 19$, where 303 cores are allocated to AVBP01 (the bomb) and 16 cores are used for each fan domain. Figure 6.5(b) displays the absolute execution time of the code for one time-iteration. The agreement with Eq. 6.3 is reasonable.

In an ideal computation, the minimum computing cost of such a simulation is obtained when $T_w = 0$. In practice, the R_c range which minimizes the total time for one iteration is $R_c \in [10; 20]$ showing that the MISCOG efficiency is weakly dependent on this ratio. In this range, T_w is close to zero but can be negative showing that the optimal performance of MISCOG can be obtained in a situation where fans wait.

6.3 Characterization of the flow inside the vessel

The LES computation of the spherical bomb is performed using the same operating procedure than the one following experimentally: fans rotate until steady state is reached. Only one operating point is studied numerically: $P_0 = 101325$ Pa and $T_0 = 323$ K.

6.3.1 Velocity at the bomb center

Figure 6.6 presents the temporal evolution of the three velocity components $\mathbf{u} = (u, v, w)$ at the center of the vessel. The signal recorded by the probe is zero until $t^* = 6$. This time represents the time needed by large turbulent scales generated by fans to reach the

center of the vessel. The distance between the fan blades to the center of the vessel is $L_{fv} = 65$ mm. A velocity V_s can be estimated by the relation $V_s = L_{fv}/t^* \simeq 2$ m/s. This velocity is very small compared to the flow velocity at the blade tip $V_{bt} \simeq 30$ m/s, suggesting that turbulence is not convected` from the fan region to the bomb center. The mechanism by which turbulence goes from fan regions to the bomb center will be described in Sec. 6.3.4.

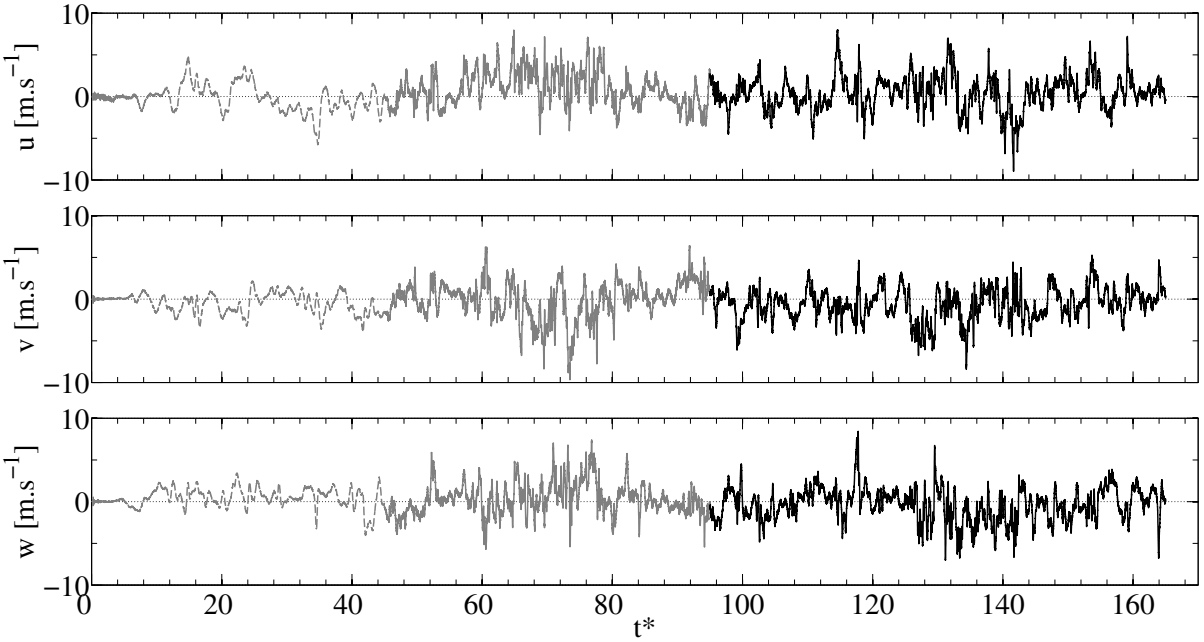

Figure 6.6: Velocity components versus number of fan rotations t^* at the center of the vessel. - - - - : coarse grid LW ; —— : coarse grid TTGC ; —— : fine grid TTGC.

The RMS velocity values[2] at the center of the vessel are respectively 2.3, 2.0 and 2.1 m/s. Probability density functions of the velocity fluctuations components $\mathbf{u}'$ are plotted on Fig. 6.7. The pdf s of u', v' and w' are compared to a Gaussian distribution which characterizes random processes. A good agreement is found between a Gaussian distribution and the distribution of the velocity components at the bomb center. These first results suggest that turbulence at the center is close to HIT which is the objective of this experimental set-up.

6.3.2 Mean and RMS velocities in the closed vessel

A second diagnostic is to compare average $\bar{\mathbf{u}}$ and fluctuating $\mathbf{u_{rms}}$ velocities measured experimentally to those computed by LES. These statistics are performed oven 60 fan rotations ($t^* \in [105; 165]$). Figure 6.8 shows fields of the magnitude of the average and fluctuating velocities in the closed vessel. As expected, the average velocity is close to

[2]RMS values are defined as $u_{rms} = \overline{\sum_{n=1}^{Ns} u_n'^2/N_s}$ where N_s is the number of samples and $u' = u - \bar{u}$. They do not include the SGS contribution.

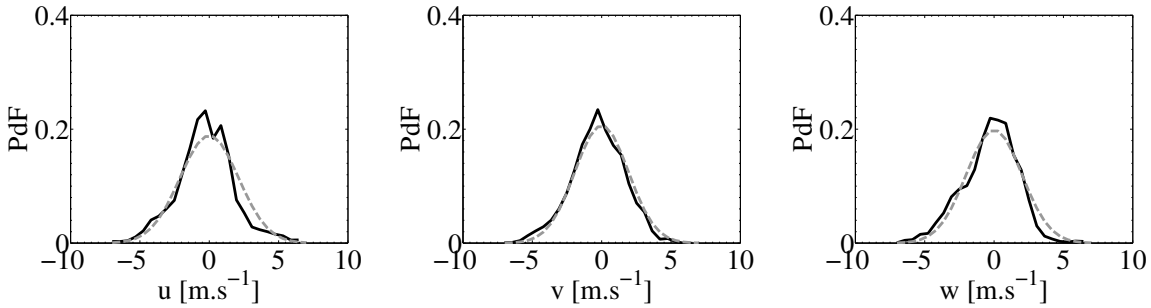

(a) PdF of u'. (b) PdF of v'. (c) PdF of w'.

Figure 6.7: Local velocity fluctuations distributions at the bomb center. ---- : Gaussian distribution ; —— : LES.

zero at the bomb center. To compare these results to experimental data, Fig. 6.9 presents

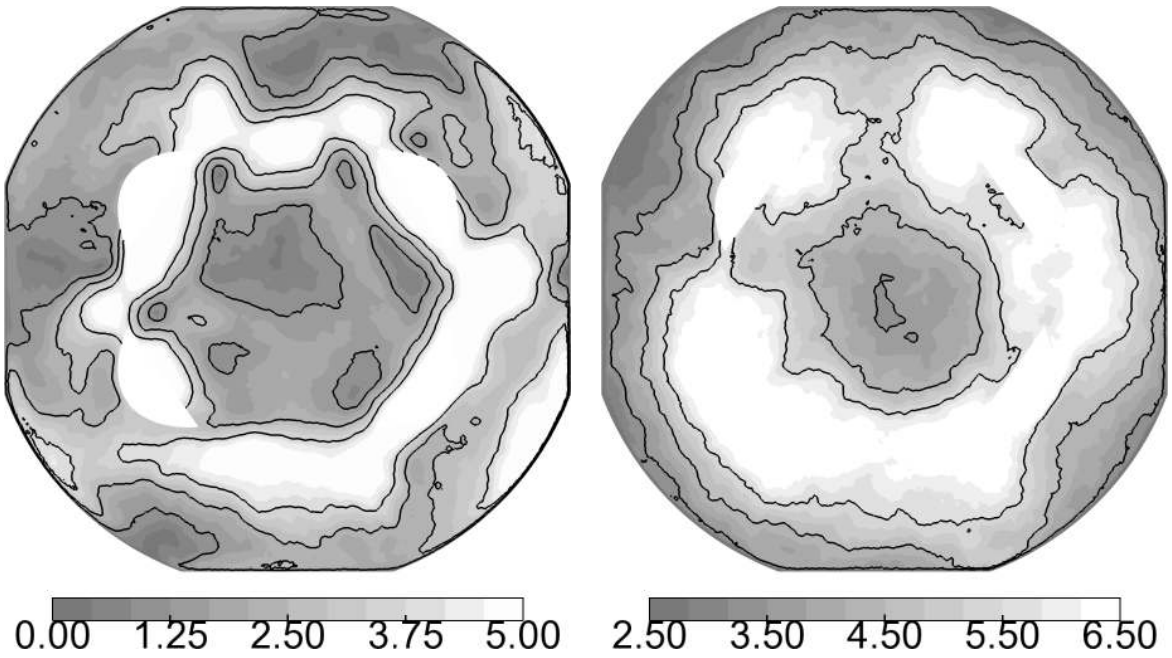

(a) Average velocity (modulus). (b) RMS velocity (modulus).

Figure 6.8: Average and RMS velocity fields. Statistics performed on 60 fan rotations ($t^* \in [105; 165]$).

x-axis cuts of average velocity components. As previously observed on Fig. 6.8, average velocities are near zero at the bomb center. The agreement between experimental data and LES calculation is good. Moreover the `S shape of the $\bar{u}$ and $\bar{v}$ curves observed experimentally is well predicted by the computation. The domain where the average velocity is near zero is a sphere with a radius of about 3 cm. Figure 6.10 presents x-axis cuts of fluctuating velocities components. Once again the agreement between experimental data and LES is good. The u_{rms} and v_{rms} profiles are well captured. The LES results

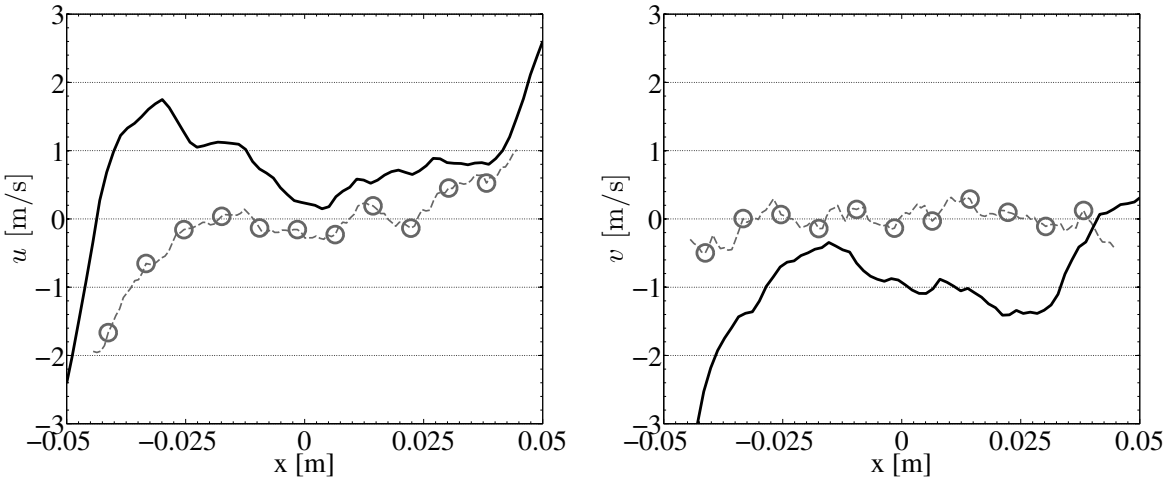

(a) $\bar{u}$. (b) $\bar{v}$.

Figure 6.9: Comparison of the average velocities $\bar{u}$ and $\bar{v}$ along the x-axis. -⊖-: experimental data (PIV) ; —— : LES. (Statistics performed on 60 fan rotations)

slightly under-estimate the velocity fluctuations since only the resolved fluctuations are plotted. Note that RMS velocities (Fig. 6.10) are actually better predicted than the mean

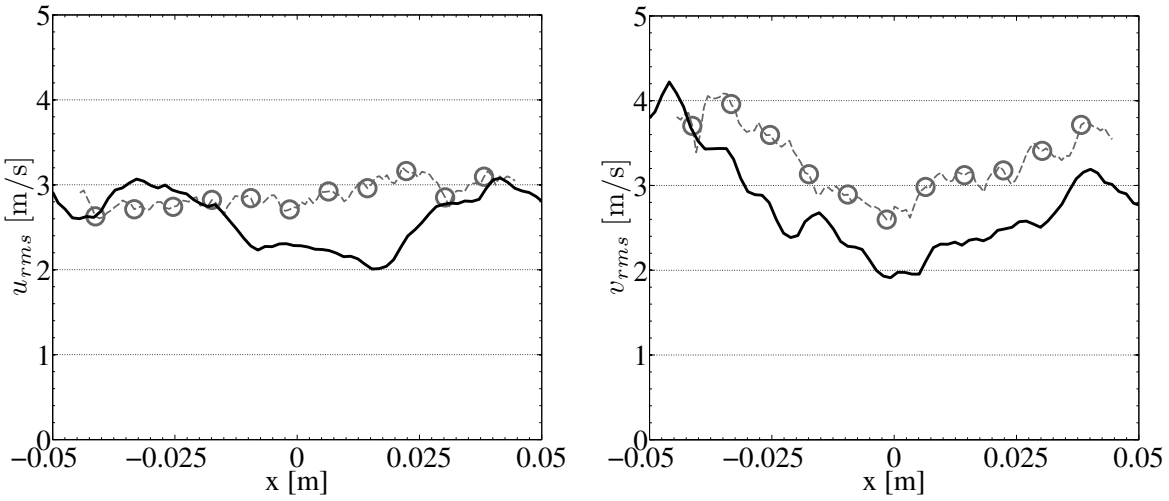

(a) u_{rms}. (b) v_{rms}.

Figure 6.10: Comparison of the fluctuating velocities u_{rms} and v_{rms} along the x-axis. -⊖-: experimental data (PIV) ; —— : LES. (Statistics performed on 60 fan rotations)

velocities (Fig. 6.9). This is unusual and certainly due to the fact that mean velocities are close to zero.

To check the flow structure, streamlines of the average velocity are displayed in Fig. 6.11. Streamlines are colored by the average velocity modulus. These streamlines are plotted for only two fans to simplify the visualization. The fans are opposite to one

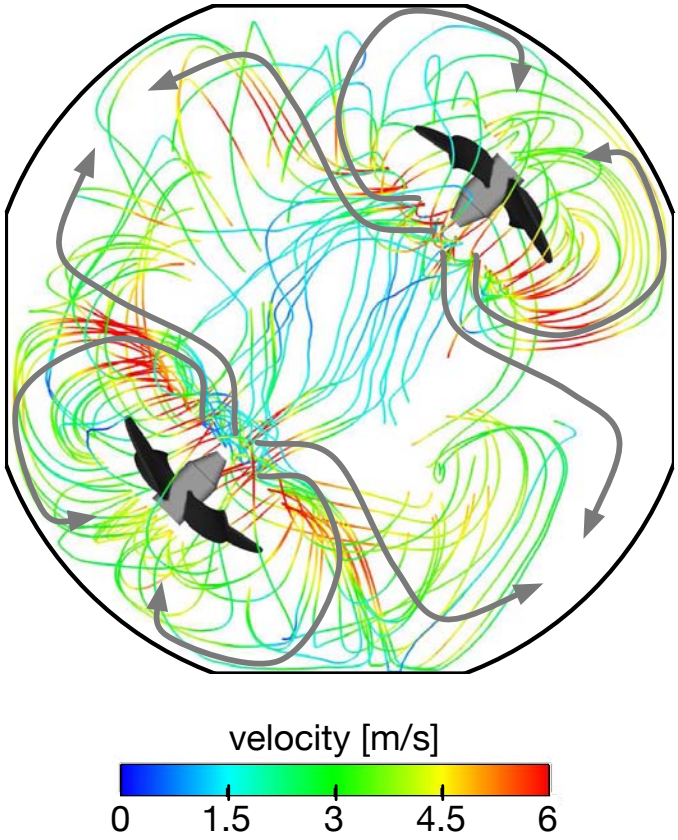

Figure 6.11: Streamlines colored by the magnitude of the average velocity modulus. Gray arrows summarize the flow direction.

another so that they generate two counterflowing streams. The stream generated by each fan separates into two streams: one which recirculates directly back to the fan and an other which go along the vessel boundary. Only few streamlines go from fans region to the bomb center which is in agreement with Fig. 6.9 showing that the average velocity at the bomb center is near zero.

6.3.3 Turbulence structure

This subsection presents the turbulence structure inside the closed vessel. Integral length and time scales and isotropy are measured.

6.3.3.a Integral length and time scales

Integral length scales are interesting values to analyze the turbulence in the spherical vessel. The following relations [11, 152] are used to measured the integral length scales and integral timescales in the bomb LES computation. The autocorrelation of a signal $s(t)$ is defined by:

$$Ac_s(\tau) = \frac{\overline{s(t)s(t+\tau)}}{\overline{s(t)^2}} \tag{6.4}$$

An integral timescale τ_t can be deduced by integrating the autocorrelation functions:

$$\tau_t = \int_0 \quad Ac_s(\tau)\ \mathrm{d}\tau \tag{6.5}$$

The velocity fluctuations cross correlations are defined by:

$$Q_{ij}(A,B) = \overline{u_i'(A)u_j'(B)} \tag{6.6}$$

Then correlation coefficients are:

$$R_{ij}(A,B) = \frac{Q_{ij}(A,B)}{\overline{\overline{u_i'(A)^2}}\ \overline{\overline{u_j'(B)^2}}} \tag{6.7}$$

Finally, the integral length scales are defined by:

$$L_{ij}^l = \int_0 \quad R_{ij}(x_l,0,0)\ \mathrm{d}x_l \tag{6.8}$$

If the turbulence is homogeneous and isotropic then $\overline{u_i'u_j'} = 0$ $(i=j)$ so that only L_{jj}^k are not zero. Moreover all L_{ii}^i are equals $(L_{11}^1 = L_{22}^2 = L_{33}^3)$ and according to the Karman and Howarth relation [153]:

$$L_{ii}^j = \frac{L_{ii}^i}{2} \tag{6.9}$$

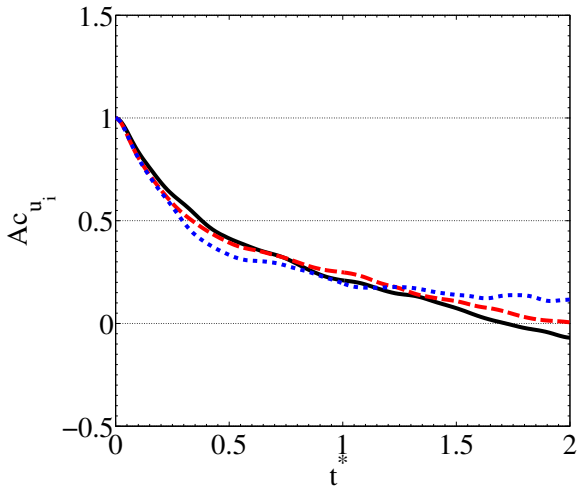

Figure 6.12: Autocorrelations functions of the velocity components versus the number of fan rotations. ——: u ; - - - -: v ; ·····: w.

Figure 6.12 presents autocorrelations of the velocity fluctuations components at the bomb center as a function of the number of fan rotations t . Autocorrelations are similar for the three components and after two fan rotations ($t = 2$), fluctuations are no more correlated. Here the integral timescale found is $\tau_t = 3.5$ ms and is almost the same for the three velocity fluctuations components.

Figure 6.13 presents the velocity fluctuations cross correlations R_{ij} along the bomb axis. R_{ij} functions obtained in LES does not seem to be well converged so that the determination of the integral length scales by integrating these R_{ij} functions would not be precise. However, one can see, for example in Fig. 6.13(a), that the uu correlation along the x-axis L^x_{11} is bigger than the two others (L^x_{22} and L^x_{33}). The integral length scales have been calculated by integrating the $R_{ij}(B_0, x_k)$ function along the x_k-axis from the bomb center B_0 ($x = 0$) to the first zero of the function. Integral length scales are summarize in Eq. 6.10.

$$L^j_{ii}\ [\text{mm}] = \begin{matrix} 13.48 & 7.90 & 10.05 \\ 7.61 & 9.81 & 8.05 \\ 9.14 & 10.52 & 11.65 \end{matrix} \tag{6.10}$$

The 0.5 expected factor (Eq. 6.9) is not clearly found but the integral length scale in the LES computation $L_{\tau\,LES}$ can be estimated at $L_{\tau\,LES} \simeq 11.5$ mm. This value is larger than the integral length scale $L_{\tau\,exp}$ measured experimentally. This is probably due to a lack of resolution in the LES computation. Indeed, the mesh resolution in the vessel is $\Delta x = 1$ mm. With such a grid, it is not possible to find an integral length scale of 3 mm: at least 10 points are needed to described the integral length scale which explains the difference between $L_{\tau\,LES}$ and $L_{\tau\,exp}$.

The common way to estimate the integral length-scale was to use Taylor s hypothesis of isotropic turbulence (Kostiuk et *al.* [154]): $L_{\tau\,LES} = \tau_t|\bar{\mathbf{u}}|$. Clearly, this estimation is not valid for the zero-mean-velocity turbulence, as in our case. For the turbulence

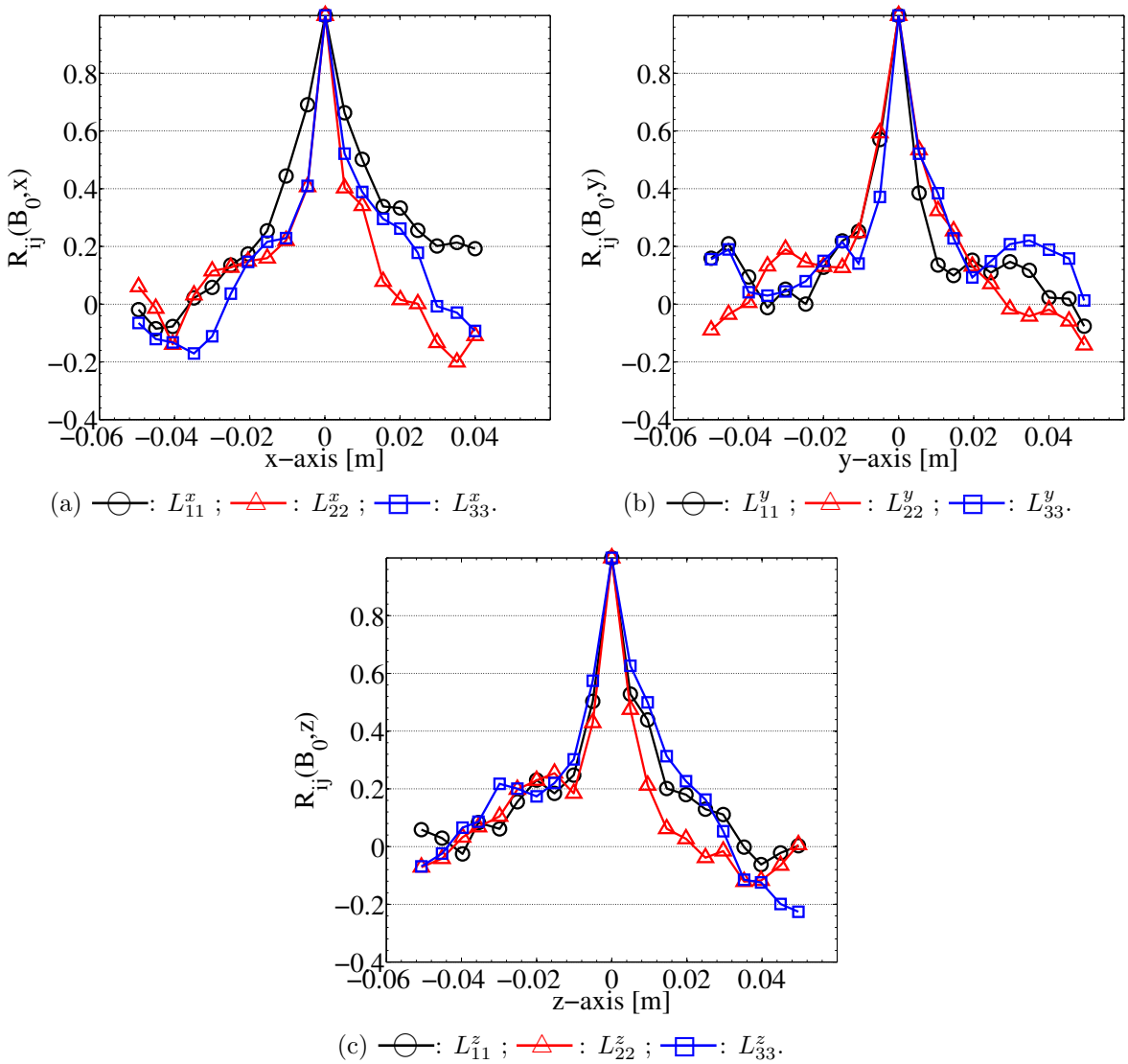

Figure 6.13: Velocity fluctuations cross correlations versus the number of fan rotations.

without mean flow velocities, the relation of $L_{\tau\,LES} = \sqrt{8/\pi}|\mathbf{u_{rms}}|\tau_t$ can used (Abdel-Gayed et *al.* [155]). According to this relation, with $\tau_t = 3.5$ ms, and $|\mathbf{u_{rms}}| = 2.5$ m.s^{-1}, $L_{\tau\,LES} \simeq 13$ mm which is very close to the first estimation of the integral length-scale founded using cross-correlations. Note that using experimental values for $\tau = 1$ ms and $|\mathbf{u_{rms\ expe}}| = 2.5$ m.s^{-1} gives $L_{\tau\,exp} = 3.7$ mm which is very close of the integral length scale computed using autocorrelations of the velocity fluctuations components.

6.3.3.b Isotropy

To study the structure of the turbulence, the time average invariants defined by Lumley [156, 157] are an useful tool. According to this theory an anisotropy invariant map within which all realizable Reynolds stress invariants must lie can be defined. The borders of this domain describe different states of the turbulence. This theory is based on the analysis of the non-dimensional form of the anisotropy tensor given by:

$$b_{ij} = \frac{\overline{\tau_{ij}}}{\overline{\tau_{kk}}} - \frac{1}{3}\delta_{ij} \tag{6.11}$$

with $\overline{\tau_{ij}} = \overline{u_i' u_j'}$ the average Reynolds stress tensor. The principal components of the anisotropy tensor may be found by solving the relation:

$$\det\left[b_{ij} - \sigma\delta_{ij}\right] = 0. \tag{6.12}$$

where σ are the eigenvalues (*i.e.* the principal stresses) of $\mathbf{b}$. Equation 6.12 expands to the following third-order equation for :

$$\sigma^3 - I_1\sigma^2 + I_2\sigma - I_3 = 0 \tag{6.13}$$

where I_1, I_2 and I_3 are respectively the first, second, and third invariants of the tensor b_{ij}. These invariants are related to the tensor terms according to the relations:

$$\begin{aligned} I_1 &= \mathrm{trace}(\mathbf{b}) = b_{kk} \\ I_2 &= \frac{1}{2}\left([\mathrm{trace}(\mathbf{b})]^2 - \mathrm{trace}(\mathbf{b^2})\right) = -\frac{1}{2}b_{ij}b_{ji} \\ I_3 &= \det(\mathbf{b}) \end{aligned} \tag{6.14}$$

I_1 is zero for incompressible flows and is not used here. The anisotropy invariant map is constructed by plotting $-I_2$ versus I_3. Isotropic turbulence is found at the origin ($\mathrm{I}_2 = I_3 = 0$). When I_2 or I_3 differ from zero, they quantify the type of turbulence which is found locally (1, 2 or 3 components, axi-symmetry, etc.). The I_2 and I_3 invariants were computed locally (which means that the $\bar{.}$ operator in Eq. 6.11 is a temporal averaging operator) in the LES on the fine mesh during the established phase ($t^* > 105$). This analysis has been done on the x, y and z-axis (20 points in each direction) of the closed vessel and results are reported in Fig. 6.14. Each point is colored by its distance r to the center of the bomb.

Figure 6.14 shows that at the bomb center ($x \in [-30; +30]$ mm), turbulence can be assumed to be isotropic. In this spherical domain all structures generated by the

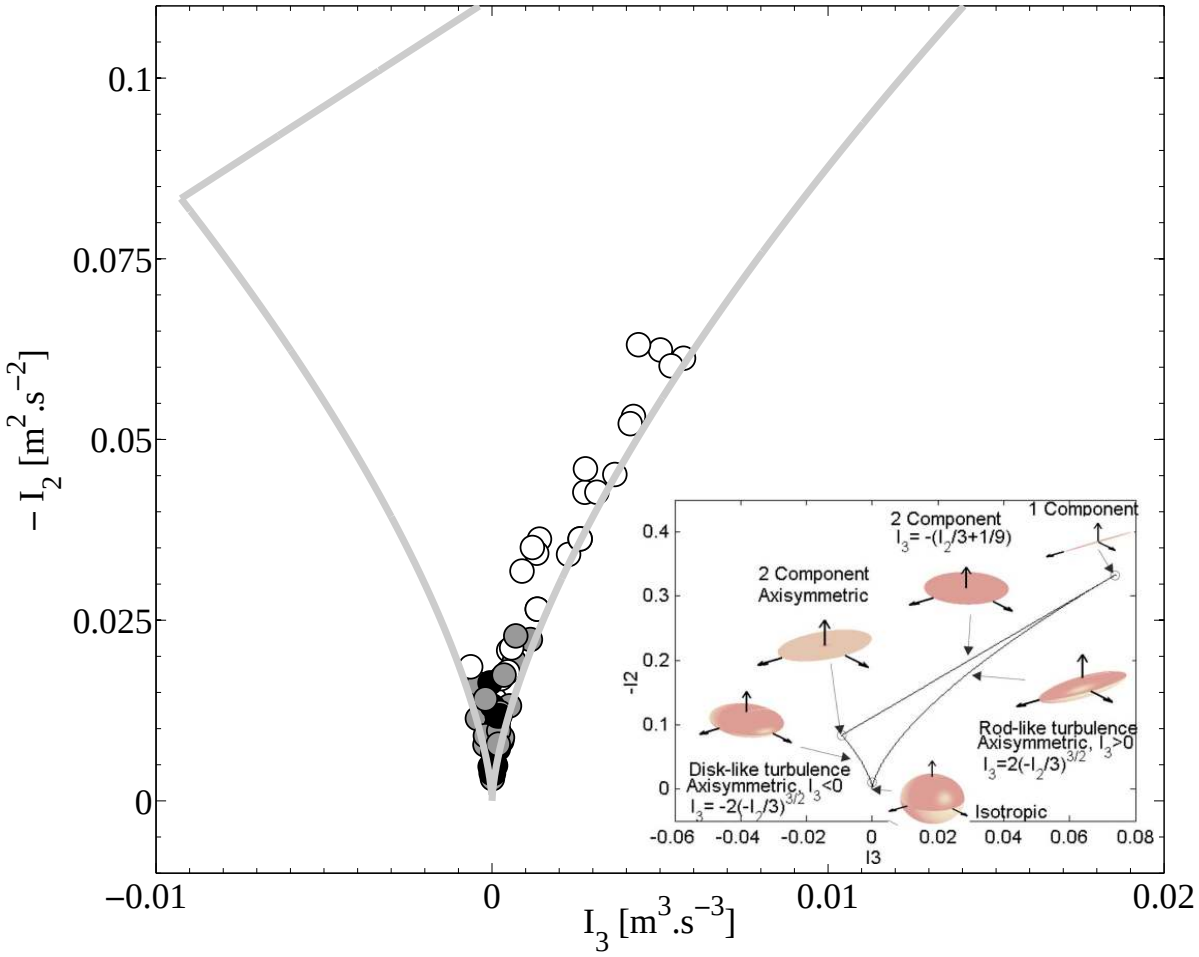

Figure 6.14: Anisotropy invariant map (Lumley triangle). Each point is colored by its distance r to the center of the bomb. ■ :$r < 15$ mm ; ● :$r \in [15;30]$ mm ; — :$r > 30$ mm. The figure in the bottom-right hand side is taken from [157].

six fans impact and mix (by diffusion) leading to an homogenous turbulence. Outside this spherical domain where turbulence is isotropic, the presence of the fans affects the structure of the turbulence: at a distance of more than 35 mm of the bomb center, turbulence becomes rod-like . This loss of isotropy is confirmed by results obtained experimentally. Figure 6.15 presents the evolution of the ratio u_{rms}/v_{rms} versus the x-axis. Figure 6.15 shows that turbulence is isotropic at the bomb center. The agreement between LES and experimental measurements is good.

6.3.3.c Spectra

The flow generated by fans is, by nature, a pulsating flow. Because fans have four blades, this flow is expected to exhibit a mode at a frequency f_p equal to four times the fan rotation frequency ($f_p = 4/T_{fan}$). To check if turbulence at the center of the bomb

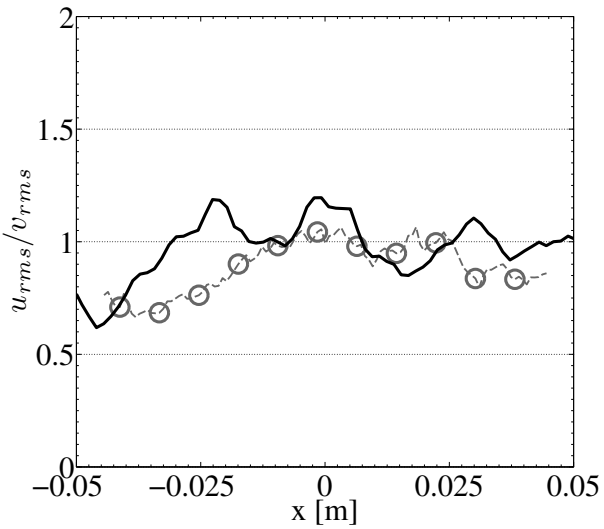

Figure 6.15: Isotropy along the x-axis. -⊖-: experimental data (PIV) ; —— : LES.

is affected by the pulsated flow created by the blades rotation, Power Spectral Density[3] (PSD) of the velocity $v(t)$ can be computed to track the existence of harmonic oscillations at f_p. Moreover, the Reynolds number at the bomb center is small (of the order of 600) and it is interesting to know if the Kolmogorov cascade can develop. To compute PSD, velocity signals (see Fig. 6.6) are sampled at a frequency $f_s = 5000$ Hz. This cut-off frequency corresponds to a Strouhal number St based on the mesh size and the RMS velocity equal to unity $St = f_s \mathbf{u_{rms}}/\Delta x \simeq 1$: beyond this cut-off frequency, only noise is recorded and must not appear in the spectral analysis.

Figure 6.16 shows the bomb configuration and the position where PSD are performed. Two points in the domain are analyzed: close to a fan (point P0) and at the bomb center (point P1). At P0, the PSD exhibits a mode at a frequency exactly equal to four times the frequency of the fan rotation as expected. On the other hand, at the bomb center (P1), this mode vanishes and the spectrum follows the Kolmogorov theory [35]. Here the slope of the spectrum is near the -5/3 theoretical slope. This confirms that turbulence at the bomb center is not affected by the periodicity of the unsteady flow generated by fans. Moreover, PSD results show that more energy is contained in the spectrum at point P0 than at point P1 (showing that turbulence decays between these two points as expected).

6.3.4 Mean turbulent kinetic energy balance

The objective in this section is to show how turbulence is transferred from the fans regions to the bomb center. A relevant quantity to characterize the turbulence inside the vessel in terms of production, dissipation and transport is the mean turbulent kinetic energy

[3]If $S(\omega)$ is the Discrete Fourier Transform (DFT) of the temporal signal $s(t)$, the PSD of $s(t)$ is $S(\omega)S^{\star}(\omega)$ where $S^{\star}(\omega)$ is the conjugate of $S(\omega)$.

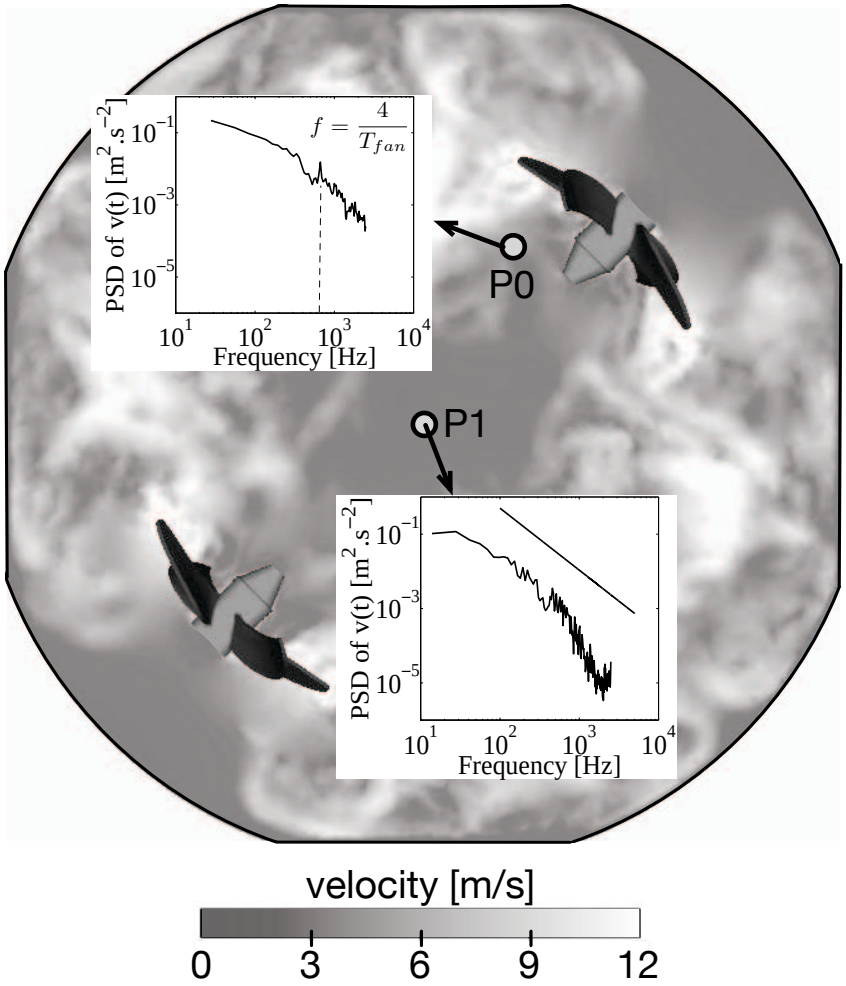

Figure 6.16: Velocity spectra close to a fan and at the bomb center.

(TKE) $\bar{e} = 1/2\overline{u_i' u_i'}$. The budget of $\bar{e}$ is given by Hinze [9]:

$$\underbrace{-\overline{u_i}\frac{\partial \bar{e}}{\partial x_i}}_{\text{Convection}} \underbrace{-\frac{\partial}{\partial x_i}\left(\overline{p' u_i'}\right)}_{\text{Pressure diffusion}} \underbrace{-\frac{\partial}{\partial x_i}\left(\overline{e u_i'}\right)}_{\text{Turbulent diffusion}}$$
$$\underbrace{+\frac{\partial}{\partial x_j}\left(2\overline{(\nu+\nu_t) s_{ij}' u_i'}\right)}_{\text{Viscous diffusion}} \underbrace{-2\overline{(\nu+\nu_t) s_{ij}' s_{ij}'}}_{\text{Dissipation}} \underbrace{-\overline{u_i' u_j'}\frac{\partial \overline{u_i}}{\partial x_j}}_{\text{Production}} = 0 \tag{6.15}$$

where p' is the pressure fluctuation, e is the instantaneous turbulent kinetic energy $e = 1/2 u_i' u_i'$ and $s_{ij}' = 1/2\left(\partial u_i'/\partial x_j + \partial u_j'/\partial x_i\right)$ is the deformation tensor [158, 10, 159, 160]. Terms in Eq. 6.15 are calculated over 60 solutions: 1 solution is stored at each fan rotation from $t* = 105$ to $t* = 165$. These solutions are uncorrelated since the time between two solutions is 6 ms and the time scale associated to the integral length scale τ is around 1 ms (convergence was checked).

The procedure to compute terms in Eq. 6.15 is presented here. First, mean pressure $\overline{p}$ and mean velocity $\overline{\mathbf{u}}$ are computed over the 60 instantaneous solutions. Then for each solution, the fluctuating quantities are computed: $\mathbf{u}' = \mathbf{u} - \overline{\mathbf{u}}$, $p' = p - \overline{p}$ and $e = 1/2 u_i' u_i'$. With these fluctuating and mean quantities, each instantaneous term in Eq. 6.15 are computed for each solution. After that, these instantaneous terms are averaged over the 60 solutions to get mean values. As an example, the mean convection term $\overline{C_{TKE}}$ in Eq. 6.15 is computed as follow. The convection term is computed for the 60 instantaneous solutions (thanks to mean and fluctuating quantities previously computed):

$$C_{TKE} = \overline{u_i}\frac{\partial e}{\partial x_i} \tag{6.16}$$

Then C_{TKE} is averaged over the 60 solutions so that the mean convection term $\overline{C_{TKE}}$ is:

$$\overline{C_{TKE}} = \overline{\overline{u_i}\frac{\partial e}{\partial x_i}} = \overline{u_i}\frac{\partial \bar{e}}{\partial x_i} \tag{6.17}$$

Finally, all terms are spatially averaged assuming spherical symmetry so that they are plotted as a function of the bomb radius r_b ($r_b = 0$ at the bomb center). To spatially average these terms, the bomb is divided into 50 concentric spherical caps and terms are averaged in each cap.

Only terms of interest are plotted here: Fig. 6.17 displays the convection, turbulent diffusion, dissipation and the production terms (resolved quantities). A fan is superimposed to the graph to show its position in the bomb. The dissipation rate found in this work is about 100 $\mathrm{m^2/s^3}$ in the region of the bomb center. This value is in agreement with the dissipation rate measured experimentally by De Jong et *al.* [161] in an eight-fan cubic turbulence box. The production term is maximum at $r_b/R_0 \simeq 0.5$: the turbulent kinetic energy is produced by fans which are located at this position. Finally, over a central region of diameter 30 mm, turbulent diffusion dominates convection as expected: the mean flow is around zero in this region (see Fig. 6.9), confirming that turbulence is not convected but diffused towards the bomb center from the fan regions.

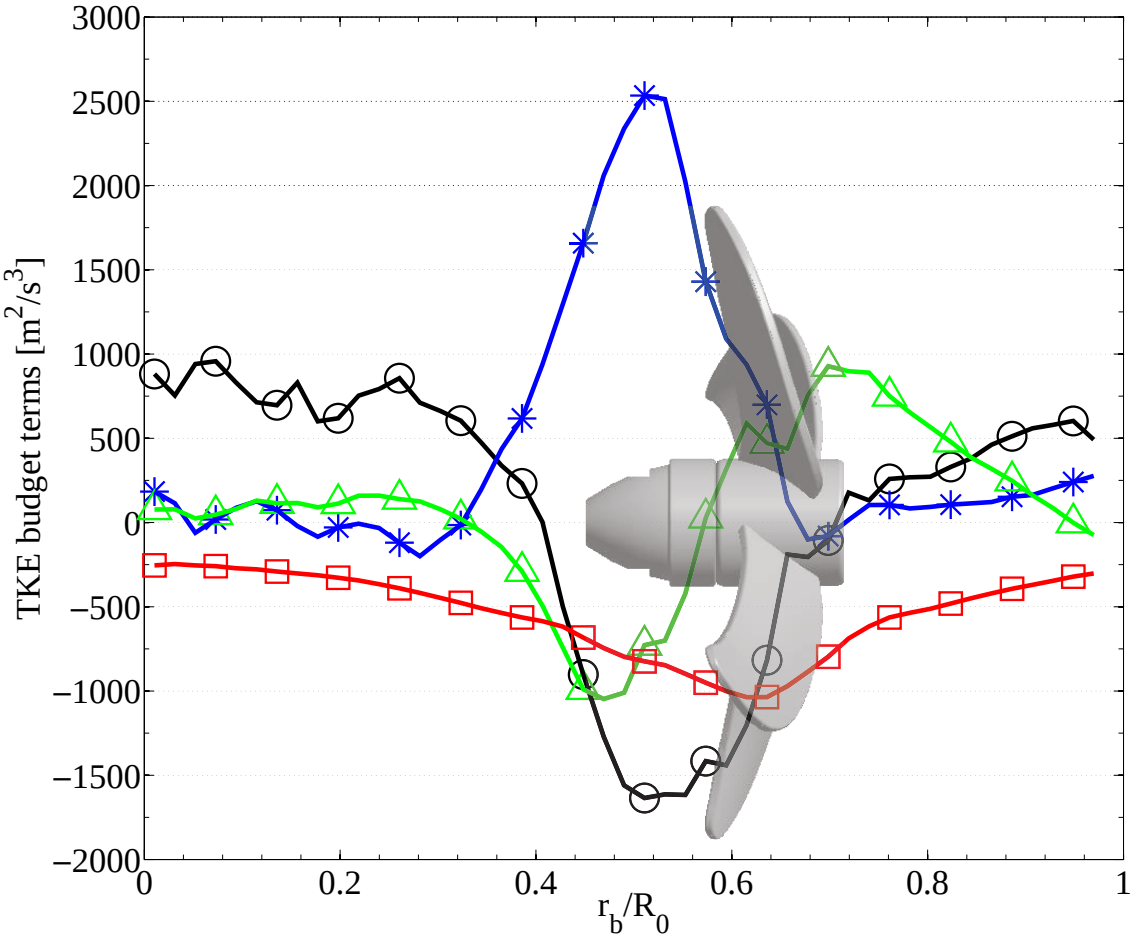

Figure 6.17: Budget of resolved TKE terms versus the normalized bomb radius r_b/R_0. △: Convection ; ○: turbulent diffusion ; □ : dissipation ; ✳ : production.

6.4 Conclusion

This chapter presented a computation of a spherical vessel stirred by six fans. This configuration corresponds to an experiment conducted at the PRISME laboratory in Orléans to study the propagation of turbulent premixed flames in homogeneous isotropic turbulence. Non-reacting flow was studied in this chapter, just before ignition. At this instant, the Reynolds number associated to the fans is 60,000 while the Reynolds number based on the integral length and RMS speed is of the order of 600 at the bomb center.

A well resolved LES of the full geometry was performed. Average and fluctuating fields match experimental data reasonably well. The structure of turbulence was studied as a function from the distance to the bomb center assuming spherical symmetry, and it was shown that turbulence is almost homogeneous and isotropic at the bomb center in a region of around 6 cm of diameter. The budget of mean turbulent kinetic energy was performed too and showed that turbulence is not convected from fans to the bomb center but diffused since the average velocities are near zero at this location. The trace of the blade passage frequency disappears near the bomb center.

CHAPTER 7

TURBULENT FLAME PROPAGATING IN A SPHERICAL BOMB STIRRED BY SIX FANS

Contents

The non-reacting flow inside the closed vessel was studied is Chapter 6. It was shown that turbulence at the bomb center is homogeneous and isotropic in a sphere of approximately 6 cm of diameter before ignition takes place. Turbulent flame propagation is now studied in this chapter. In the present simulations, flames propagate in the experimental fan-stirred configuration and not in a synthetic homogeneous and isotropic turbulence: its is the originality of this work. LES is used here to compare turbulent and laminar flame propagation in the closed vessel. A very fine mesh in the central zone of the spherical vessel is used to reach a DNS-like computation for combustion. This makes the present simulation an 'embedded DNS' where LES is active everywhere in the bomb except in the flame zone where a DNS is used.

7.1 Flame speeds in turbulent premixed flames

This chapter presents simulations of laminar and turbulent premixed flames. Before analyzing them, this section discusses how to utilize the results of these simulations in terms of flame surface density Σ, flame stretch κ and flame speeds.

For premixed flames, it is usual to define a progress variable c which goes from 0 in fresh gases to 1 in burnt gases. Here it was decided to define a progress variable based on the fuel mass fraction:

$$c = 1 - \frac{Y_f}{Y_f^u} \tag{7.1}$$

From the progress variable, the flame surface density Σ can be defined. The flame surface density measures the flame area per unit of volume: $\Sigma = |\nabla c|$. One must paid attention for the post-processing of a LES to measure the flame surface: in a LES, only the Favre filtered progress variable c is computed. To take into account the subgrid scale wrinkling, the efficiency function Ξ is introduced in the flame surface density definition:

$$\Sigma = \Xi |\nabla c| \tag{7.2}$$

The total flame surface surface S is:

$$S = \int_V \Sigma \, \mathrm{d}V = \int_V \Xi |\nabla c| \, \mathrm{d}V \tag{7.3}$$

A flame front propagating in a non-uniform flow is subject to strain and curvature effects which leads to changes in flame area S. These changes are measured by the flame stretch which is defined by:

$$\kappa_S = \frac{1}{S}\frac{dS}{dt} \tag{7.4}$$

A general expression of stretch may be derived from purely kinematic considerations for a thin flame sheet [93]:

$$\kappa = -\vec{\mathbf{n}}\vec{\mathbf{n}} : \nabla\vec{\mathbf{u}} + \nabla.\vec{\mathbf{u}} + s_d \left(\nabla.\vec{\mathbf{n}}\right) = \left(\delta_{ij} - n_i n_j\right) \frac{\partial u_i}{\partial x_j} + s_d \frac{\partial n_i}{\partial x_i} \tag{7.5}$$

where $\vec{\mathbf{n}}$ is the unit vector normal to the flame surface pointing towards the fresh gases:

$$\vec{\mathbf{n}} = -\frac{\nabla c}{|\nabla c|} \tag{7.6}$$

The first two terms on the RHS of Eq. 7.5 ($-\vec{\mathbf{n}}\vec{\mathbf{n}} : \nabla\vec{\mathbf{u}} + \nabla.\vec{\mathbf{u}}$) represent the tangential strain and $\nabla.\vec{\mathbf{n}}$ is the curvature of the flame front. Equation 7.5 gives a local value of the stretch κ. To compare this relation to the stretch definition (Eq. 7.4) which is global, the local stretch must be averaged on the flame surface and the following relation is used:

$$< \kappa >= \frac{1}{S}\int_V \kappa\Sigma \, \mathrm{d}V \tag{7.7}$$

It is easy to show that Eq. 7.4 leads to:

$$\kappa_R = \frac{2}{R}\frac{dR}{dt} \tag{7.8}$$

for a perfectly spherical flame of radius R. S. Richard [162] shows that the definition Eq. 7.7 is fully consistent with the relation Eq. 7.8 for an infinitely thin perfectly spherical flame. Whether Eq. 7.7 should also be used in turbulent cases is an open issue which will be tested here.

The `speed of a flame is a central element in combustion theory. It is also the source of many difficulties because there are multiple definitions for flame speeds. Three flame speeds are introduced (see Fig. 7.1) and are summarized in Tab. 7.1. This section provides a general framework to define flame speeds.

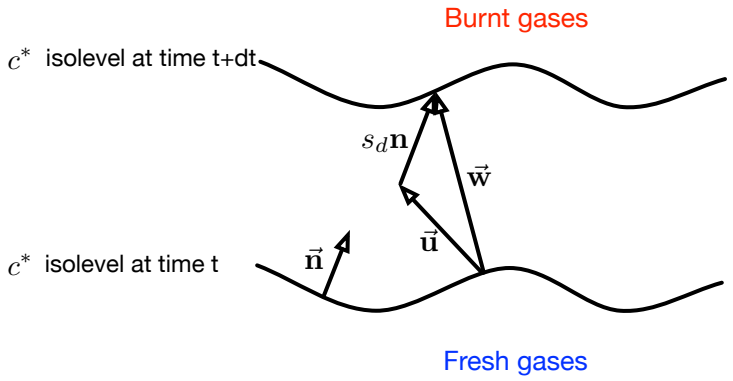

Figure 7.1: Notations for flame speed definitions

7.1.1 Mean consumption speed

First, a mean consumption speed s_c based on the fuel consumption can be derived [20]:

$$s_c = \frac{m_f}{\rho_u(Y_f^b - Y_f^u)S} = \frac{1}{\rho_u(Y_f^b - Y_f^u)S}\int_V {}_F \, \mathrm{d}V \tag{7.9}$$

Identification	Symbols	Definition
Consumption	s_c	Speed at which reactants are consumed
Absolute	s_a	Flame front speed relative to a fixed reference flame
Displacement	s_d	Flame front speed relative to the flow

Table 7.1: Classification of flame speeds.

Here, $_F$ is the D-TFLES fuel consumption term and is equal to the laminar fuel consumption term (Eq. 1.32) multiplied by Ξ/F. This speed is a spatially averaged velocity and can be computed from a LES calculation easily and it characterizes the speed at which reactants are consumed.

7.1.2 Absolute speed

Then speeds based on kinematics considerations can also be derived. Let us consider a point on an isosurface $c = c^*$. The velocity $\vec{\mathbf{w}}$ at which this point must move to remain on the surface is given by:

$$\frac{\partial \Theta}{\partial t} + \vec{\mathbf{w}}.\nabla\Theta = 0 \tag{7.10}$$

The velocity component normal to the flame front $s_a = \vec{\mathbf{w}}.\vec{\mathbf{n}}$ is the absolute speed at which an isolevel of c^* moves relative to the laboratory frame. Combining Eqs. 7.6 and 7.11 gives:

$$s_a = \vec{\mathbf{w}}.\vec{\mathbf{n}} = \frac{1}{|\nabla\Theta|}\frac{\partial\Theta}{\partial t} \tag{7.11}$$

All Θ-isolevels move at the same speed if the flame thickness remains constant.

7.1.3 Displacement speed

The displacement speed measures the front speed relative to the flow *ie.* the difference between the flow speed $\vec{\mathbf{u}}$ and the front speed $\vec{\mathbf{w}}$:

$$s_d = (\vec{\mathbf{w}} - \vec{\mathbf{u}}).\vec{\mathbf{n}} = \frac{1}{|\nabla\Theta|}\frac{\partial\Theta}{\partial t} + \vec{\mathbf{u}}.\frac{\vec{\nabla}\Theta}{|\vec{\nabla}\Theta|} = \frac{1}{|\nabla\Theta|}\frac{D\Theta}{Dt} \tag{7.12}$$

Using the energy equation Eq. 1.3 and the definition for the displacement speed given by Eq. 7.12 yields the following expression for s_d where all terms can be obtained in a simulation:

$$s_d = \frac{1}{\rho C_p|\nabla\theta|} \quad {}'_T + \frac{\partial}{\partial x_i}\left(\lambda\frac{\partial T}{\partial x_i}\right) - \frac{\partial T}{\partial x_i} \quad \rho \sum_{k=1}^{N} C_{p\,k} Y_k V_{k\,i} \tag{7.13}$$

Using Eq. 7.12, the displacement speed can easily be computed in simulations. However, the displacement speed is difficult to use. Since the flow accelerates through the flame

front, s_d changes too and depends on the position where it is measured. It can vary from negative values (on Θ-isolevels where the flame thickness changes) to values of the order of $\rho_u/\rho_b s_L^0$ in the burnt gases.

7.2 Combustion regimes

The flame/turbulence interaction is characterized by two dimensionless numbers. The Damköhler number D_a compares turbulent τ_t to chemical τ_c time scales (see Eq. 1.83). The Karlovitz number K_a corresponds to the smallest eddies and is the ratio of the chemical time scale τ_c to the Kolmogorov time τ_{η_k}:

$$K_a = \frac{\tau_c}{\tau_{\eta_k}} = \left(\frac{l_t}{\delta_L^0}\right)^{-1/2} \left(\frac{u'}{s_L^0}\right)^{3/2} \tag{7.14}$$

According to these numbers, turbulent combustion regimes can be identified and are reported in a diagram proposed by Peters in 1999 [163] presented here in Fig. 7.2.

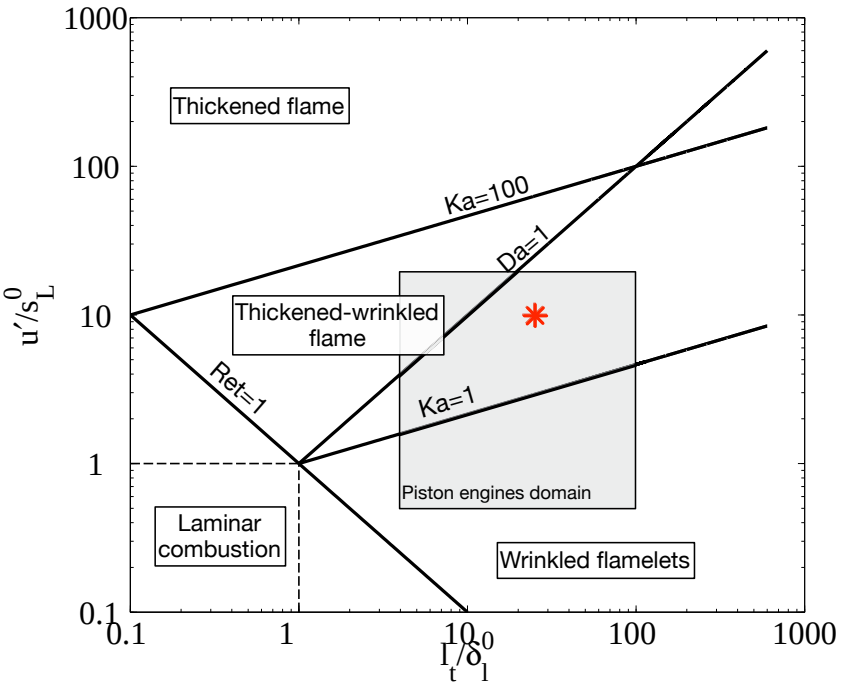

Figure 7.2: Turbulent combustion diagram proposed by Peters [163]: combustion regimes are identified in terms of length (l_t/δ_L^0) and velocity (u'/s_L^0) ratios. $*$: operating point.

Here, the dimensionless numbers associated to the operating point which is simulated are: $u'/s_L^0 \simeq 10$, $l_t/\delta_l^0 \simeq 25$ which gives a Karlovitz number $K_a \simeq 7$. The expected regime is the thickened-wrinkled flame regime: turbulent motions are able to enter and modify the flame preheat zone but not the reaction zone. An illustration of this regime was proposed by Borghi and Destriau in 1998 [164]. This regime is representative of piston engine operating points where $l_t/\delta_L^0 \in [5; 100]$ and $u'/s_L^0 \in [0.5; 20]$.

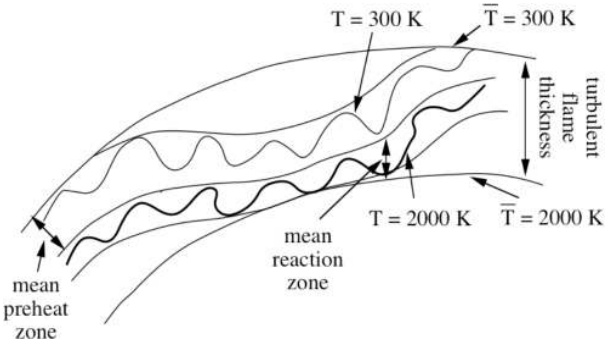

Figure 7.3: Illustration of the thickened-wrinkled flame regime proposed by Borghi and Destriau [164].

7.3 Numerical set-up

The numerical setup used here is the one used to compute the non reacting flow in Chapter 6: the numerical scheme is TTGC and the subgrid scale model is WALE. Kinetics are described with the 2S_C8H18_AB reduced mechanism presented in Sec. 1.4.1 and previously used for laminar computations in Sec. 3.3. Two simulations are performed: a laminar flame (where the fans are not rotating) and a turbulent flame where the fans rotate at 10,000 rpm (Fig. 7.4). The laminar flame results will be helpful to understand

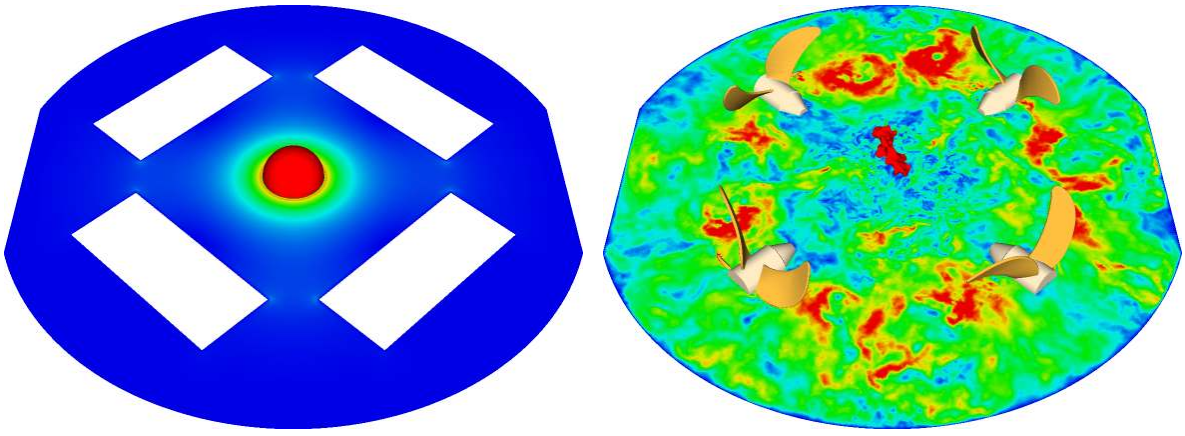

(a) Laminar flame. (b) Turbulent flame.

Figure 7.4: 3-dimensional laminar and turbulent flame propagation. Instantaneous velocity field. A red isosurface of temperature at T=1500 K shows the flame.

and compare to results coming from the turbulent flame propagation. It is also a good method to make sure that results for the turbulent case can be fully compared to a reference laminar case.

7.3.1 Mesh resolution

To compute the non-reacting flow inside the spherical vessel (see Chapter 6) a grid with a constant mesh size (except on fans blades) $\Delta x = 1$ mm has been used. For reacting cases, grid must now be refined in the region where flames are ignited and propagate to minimize the combustion modeling effect. The mesh has been refined in a spherical domain of 50 mm of diameter at the bomb center. Elsewhere the mesh is unchanged compared to the mesh used to compute the non-reacting flow. The mesh size in the refined zone at the bomb center is 0.2 mm. The laminar flame thickness for octane is $\delta_L^0 = 0.43$ mm: imposing 5 points in the flame thickness (D-TFLES model is used in this chapter with $N_c = 5$, see Sec. 1.6.1), the dynamic thickening factor F is expected to be of the order of 2 showing that a DNS-like computation is performed which minimizes the effect of the turbulent combustion model. This resolution leads to a grid of 75 millions of tetrahedra for the AVBP01 instance. Fan grids are unchanged (3.3 millions of cells) so that the whole computational grid is composed of about 95 millions of cells.

To monitor the influence of the turbulent combustion model, Fig. 7.5 plots pdf s of the thickening factor F and the efficiency function Ξ for the turbulent propagation (which is the worst case). The maximum values for F and Ξ are respectively 1.4 and 1.3 showing

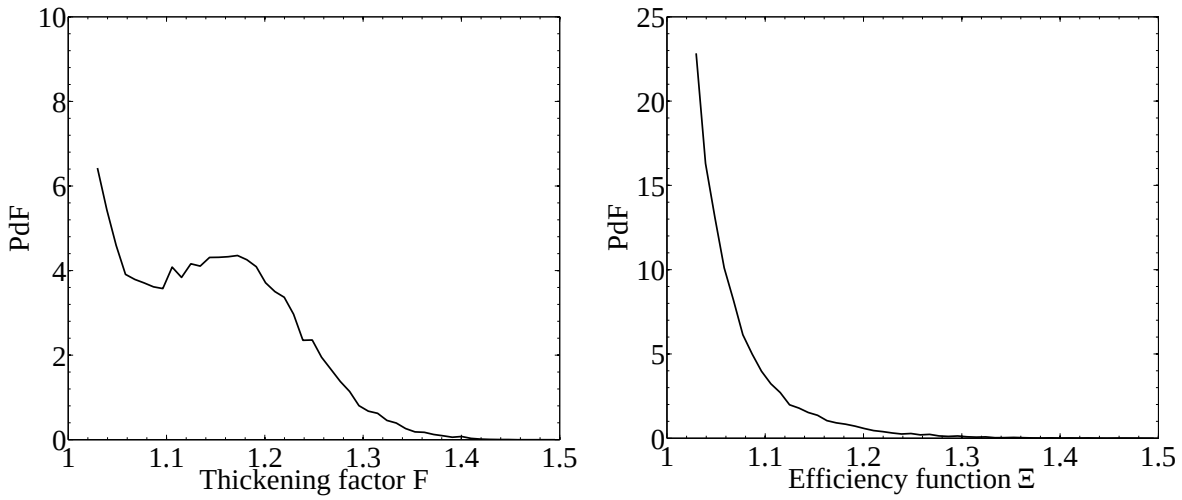

(a) Thickening factor F.

(b) Efficiency function Ξ.

Figure 7.5: Efficiency function Ξ and thickening factor F for the turbulent propagation 4.5 ms after ignition.

that a wide part of the reaction rate is resolved on the grid mesh since the turbulent combustion model parameters (F and Ξ) are close to unity. The impact of the turbulent combustion model on the flame propagation is small which confirms that a DNS like computation of the flame is computed.

7.3.2 Ignition phase

To ignite flames at the bomb center a kernel of burnt gases is deposited. Temperature, density and species profiles come from of a one-dimensional flame previously computed with CANTERA (see Sec. 1.6.2). For the velocity field at the ignition time for turbulent cases, it was decided that the turbulence inside the kernel, at the initial time, was not affected by the flame so that the velocity field is not modified, even inside the flame kernel (this hypothesis is checked in Sec. 7.5.1). For laminar cases (some of them are repeated here in the bomb geometry for reference and verification purposes), the turbulent velocity field is set to zero and initialized using Eq. 1.92. The flame kernel is a sphere of radius R_f^0 of 4 mm. The energy deposited E_d can be estimated using Eq. 7.15:

$$E_d = \frac{4}{3}\pi {R_f^0}^3 \rho_b C_{p\,b}(T_b^0 - T_u) \tag{7.15}$$

where $C_{p\,b}$ is the heat capacity in burnt gases and T_b^0 is the temperature inside the burnt gases kernel. With $R_f^0 = 4$ mm, the energy deposited is $E_d \simeq 100$ mJ. This energy is sufficient to ignite the flame. However with an initial flame kernel of radius R_f^0 of 3 mm, the energy deposited is of the order of 40 mJ and is not sufficient and computations show that the flame is subject to blow-off. This means that the amount of energy deposited is close to the critical energy.

For the turbulent propagation, 2.7 fan rotations are performed[1] on the new mesh so that turbulence develops before ignition. Figure 7.6 displays the 3 velocity components at the bomb center. The ignition time t_{ig} is highlighted by the red star. Note that at the ignition time, the velocity at the bomb center is not zero for this realization: $u = 1.7$ m/s, $v = 2.8$ m/s and $w = -0.2$ m/s^2. To give an illustration of the new structures created when using a finer mesh, Fig. 7.7 compares two instantaneous vorticity fields when using the cold` coarse flow mesh and the finer mesh used to compute combustion. Figure 7.8 displays instantaneous isosurfaces of vorticity at the bomb center colored by the velocity magnitude. This mesh ensures a ratio $\Delta x/\eta_{exp} = 5$ in the central zone of the closed vessel which allows very small resolved structures to appear.

7.4 Turbulent flame diagnostics

This section presents diagnostics performed on the octane-air flame propagating in the full closed vessel. Some comparisons with laminar flames are drawn.

Figure 7.9 proposes a visualization of the flame propagation inside the closed vessel. The flame is visualized by an isosurface of temperature at $T = 1500$ K and the velocity field is colored in gray scale. Only two fans are shown to simplify the visualization. As expected (the Karlovitz number K_a is near 7), the flame is very wrinkled and does not

[1] 2.7 fan rotations represent about 16 ms or 4.5 times the integral time scale τ_t measured in Sec. 6.3.3.a.

[2] Spatially averaged velocities over the whole burnt gases kernel at ignition time are $\overline{u^{BG}_{t=t_{ig}}} = 1\ 4$ m.s^{-1}, $\overline{v^{BG}_{t=t_{ig}}} = 2\ 24$ m.s^{-1} and $\overline{w^{BG}_{t=t_{ig}}} = -1\ 39$ m.s^{-1} confirming that the velocities at the ignition location differ from zero at a given time even if the turbulence is homogeneous and isotropic.

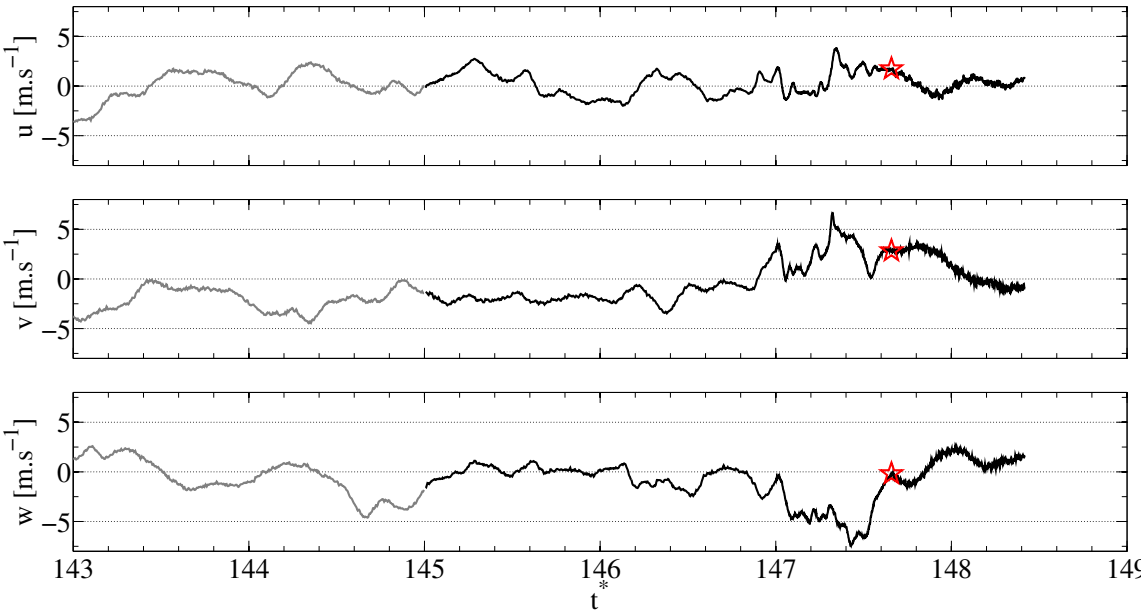

Figure 7.6: Velocity at the bomb center: ignition time is highlighted by the red star. —— : non reacting flow mesh ; —— : reacting flow mesh

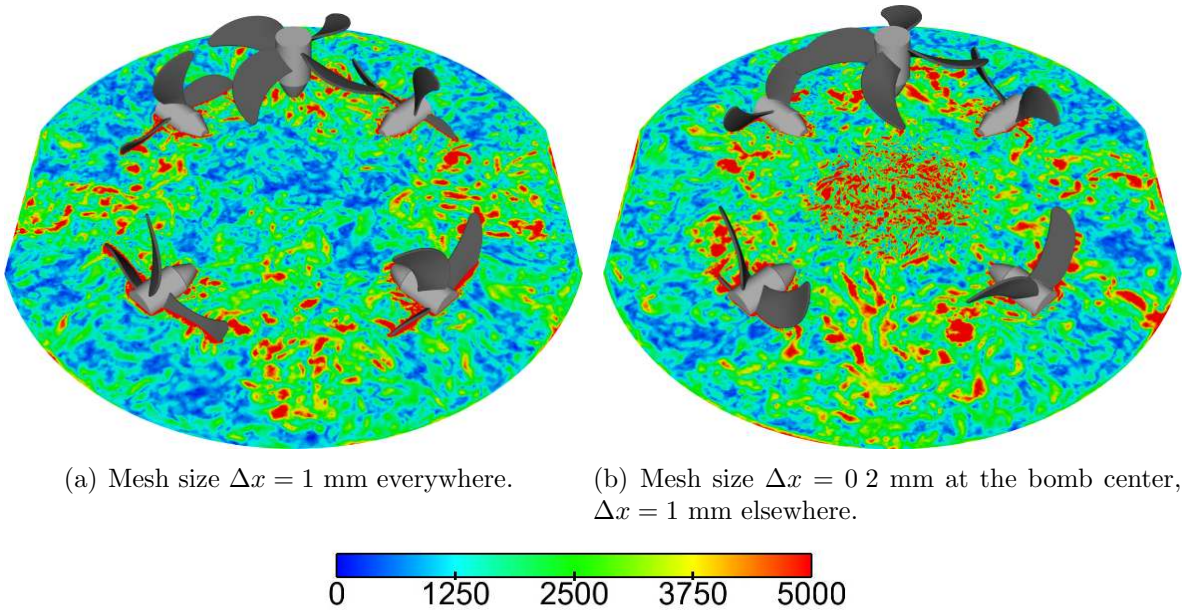

(a) Mesh size $\Delta x = 1$ mm everywhere.

(b) Mesh size $\Delta x = 0\,2$ mm at the bomb center, $\Delta x = 1$ mm elsewhere.

Figure 7.7: Instantaneous vorticity field in the bomb before ignition.

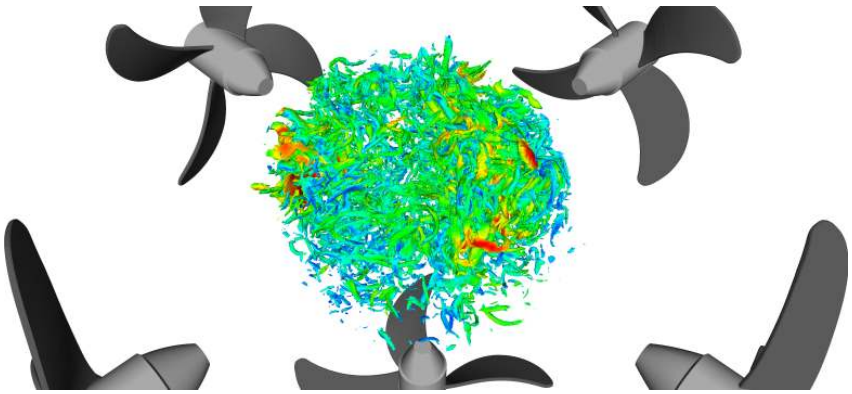

Figure 7.8: Instantaneous isosurfaces of vorticity at the bomb center colored by the velocity magnitude.

remain spherical. The flame surface is teared up into two pieces. However, the flame is ignited everywhere and keeps growing in this highly turbulent flow. The flame does not remain at the bomb center.

7.4.1 Flame surface measurement

Defining the flame surface for a turbulent premixed flame is not an easy task. Assuming that the flame front is infinitely thin (as done in multiple theoretical approaches or in the G-equation formulation) gives only one unambiguous flame surface. But in practice, the flame front is not infinitely thin and exhibits many different flame surfaces depending on the c-level where it is defined. The flame area can be measured using the area of an isosurface of the progress variable:

$$S_{c^*} = \int_S \delta(c - c^*)\ \mathrm{d}S \tag{7.16}$$

where δ is the Dirac function. Figure 7.10 shows flame surfaces obtained using different values for c^* in both laminar and turbulent flames. The flame surface definition based on the flame surface density (Eq. 7.3) is presented too. Turbulent simulations are stopped as soon as the flame leaves the central refined zone and this explains why turbulent simulations are shorter than laminar ones. For the laminar flame, all definitions give almost the same surface. Indeed, the flame front remains thin during the flame propagation. However for the turbulent flame, at the end of the simulation ($t = 4.5$ ms), a factor of the order of 3 can be found between the area of a Θ-isolevel in the fresh gases ($\Theta = 0.1$) and an isolvel in the burnt gases ($\Theta = 0.9$). Figure 7.11 shows a slice of heat release through the flame to confirm this fact. Two isolines at $c = 0.1$ and $c = 0.9$ are plotted to show the corresponding flame surface. The flame surface $S_{c^*=0.1}$ clearly overestimates the flame surface where most of the heat release takes place. Most reaction takes place near the $c^* = 0.9$ surface but there is no clear reason to argue that the surface should be measured on $c^* = 0.7$ or $c^* = 0.9$ while Fig. 7.10(b) shows that the corresponding surfaces can differ significantly.

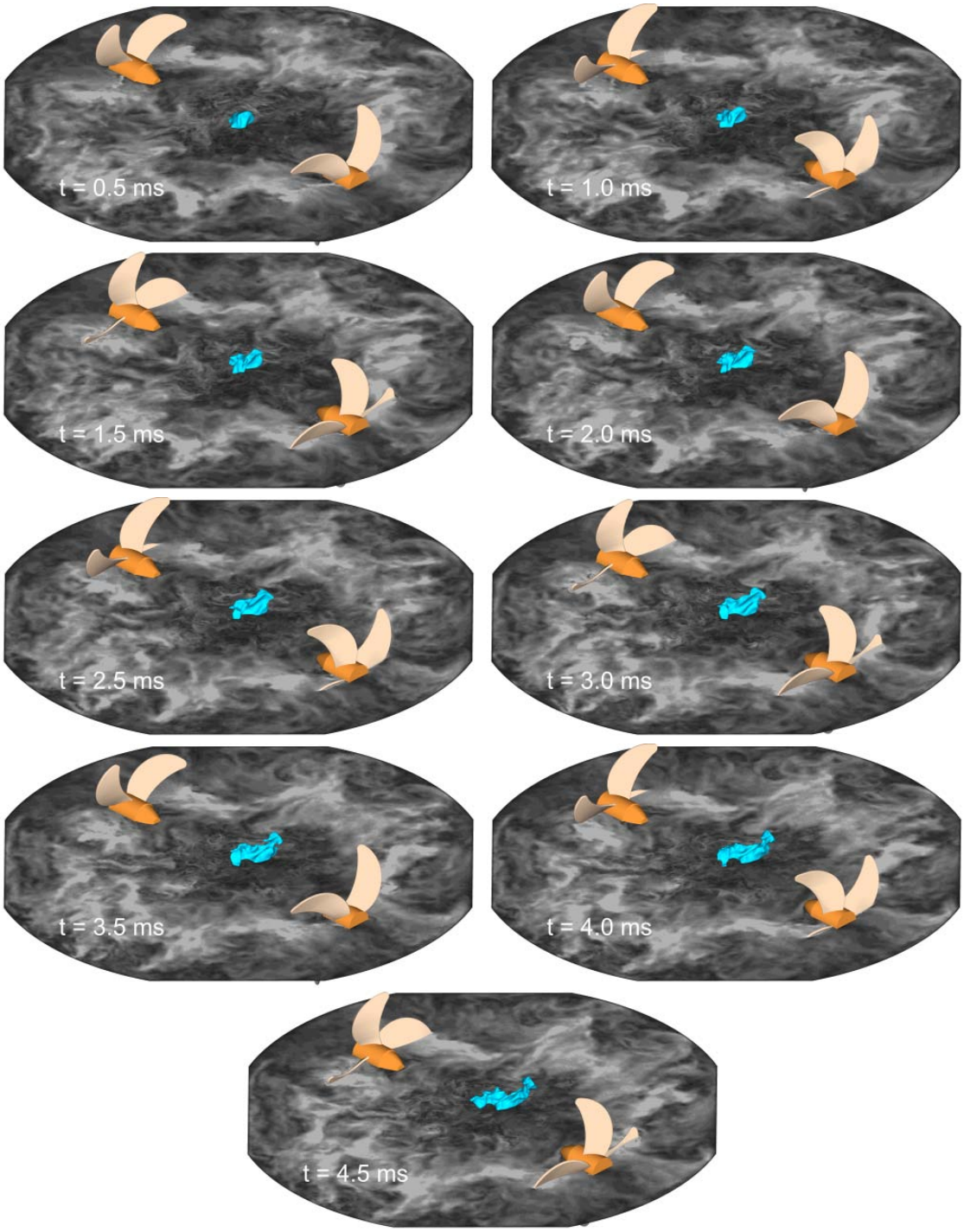

Figure 7.9: Visualization of the flame propagation in the turbulent flow. Flame is visualized by an isosurface of temperature at T=1500 K. The velocity field is colored in black and white.

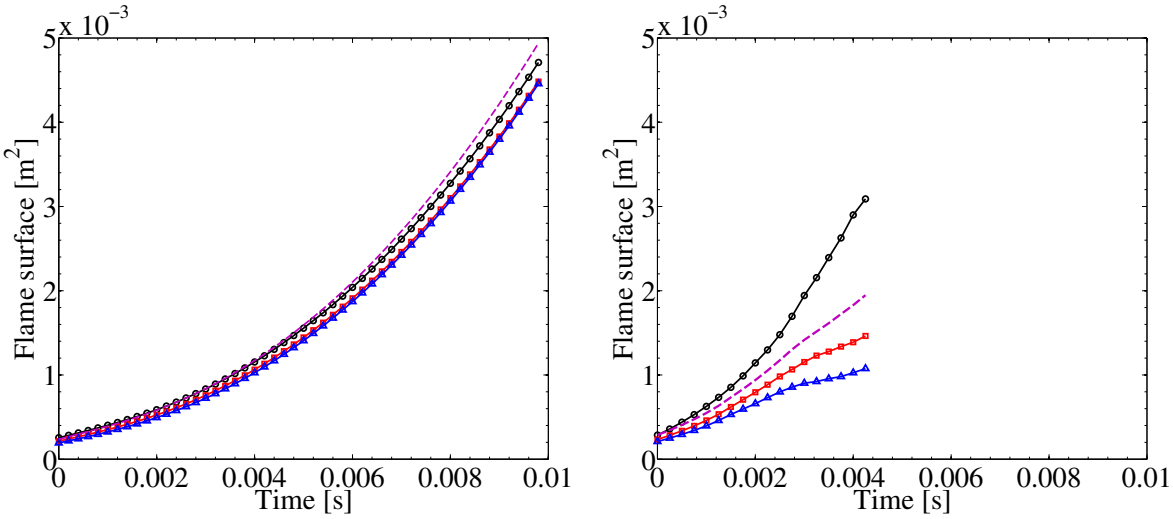

(a) Laminar flame. (b) Turbulent flame.

Figure 7.10: Flame surface. —○—: c^*=0.1 ; —□—: c^*=0.5 ; —△—: c^*=0.9 ; - - - -: $\int_V \Xi|\nabla c|\ \mathrm{d}V$

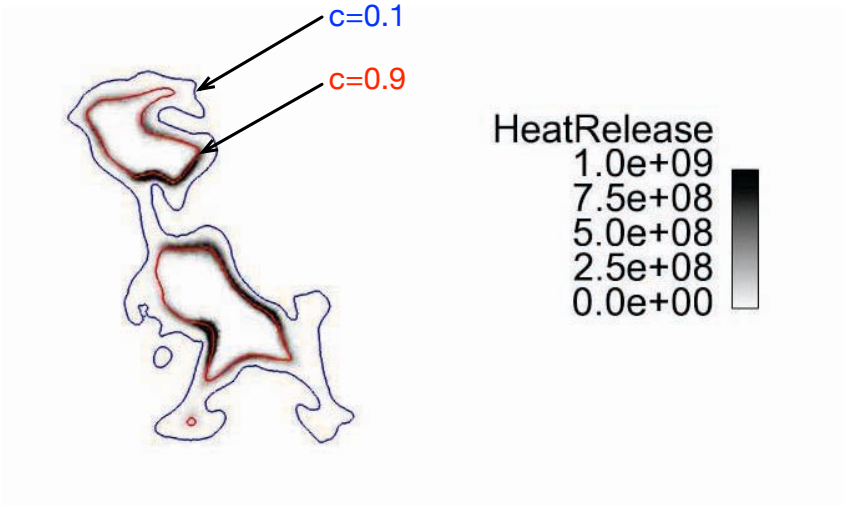

Figure 7.11: Instantaneous heat release field with two isolines: c=0.1 and c=0.9.

7.4.2 Stretch and curvature effects on combustion

Laminar and turbulent spherical flames are all subject to stretch. For laminar spherical flames, stretch is only due to the flame expansion and can be written analytically as $\kappa_R = (2/R)dR/dt$ where R is the flame radius. Turbulent flames are also wrinkled by turbulence which leads to additional stretch.

Figure 7.12(a) presents the temporal evolution of stretch and curvature for the laminar flame. Equations 7.4, 7.7 and 7.8 are compared. To compute Eq. 7.8, the flame radius is determined using the isosurface of $c^* = 0.9$: $R = \sqrt{S_{c^*=0.9}/(4\pi)}$. Equations 7.4 and

7.8 give same stretch values since all flame surfaces are almost the same (Fig. 7.10(a)), as expected for a perfectly spherical flame. However, Eq. 7.7 underestimates the stretch. This result is unexpected since Eq. 7.7 gives the same result as 7.4 for an infinitely thin flame as shown by S. Richard [162]. The discrepancy observed here can be due to the fact that the flame is not infinitely thin as assumed in the derivation of S. Richard [162].

For turbulent flames, stretch definitions differ since the flame surface is not easy to measure. To illustrate the dispersion of stretch and curvature in the flame front, Fig. 7.13

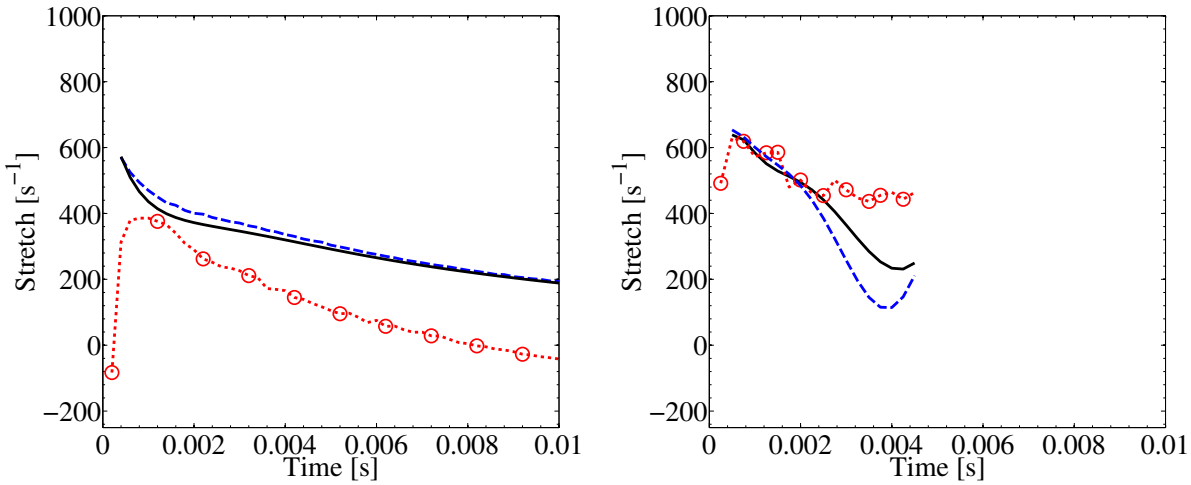

(a) Laminar flame.

(b) Turbulent flame.

Figure 7.12: Evolution of stretch and curvature during the propagation phase. —— : κ_Σ (Eq. 7.4) ; ···⊙··· : $<\kappa>$ (Eq. 7.7) ; - - - - : κ (Eq. 7.8)

displays pdf s function of these quantities. For laminar flames, pdf are sharp since all points in the flame front are subject to the same stretch and curvature, only induced by the flame geometry. For turbulent flames, pdf s are wider and negative values appear. Turbulence wrinkles the flame and very high (positive and negative) values for stretch and curvature can be generated. Mean values of stretch are positive (pdf s function are centered on value greater than zero) which is consistent with the fact that the flame is growing.

7.4.3 Consumption flame speed s_c

The response of the consumption flame speed s_c to stretch κ is usually based on a Markstein-type correlation [98, 101, 102] $s_c(\kappa) = s_L^0 - \mathcal{L}\kappa$ where $\mathcal{L}$ is the Markstein length. The Markstein length is a quantity which essentially depends on the fuel and is classically determined using laminar flame (spherical propagating flames are one of the methods available to measure $\mathcal{L}$ [98, 100, 165]). This quantity can be positive or negative, depending on the fuel. The mean consumption flame speed is obtained using Eq. 7.9.

A two-step chemical mechanism is used to describe kinetics (see Eq. 1.44). In this context, the combustion intensity (and thereby the total reaction rate) can be evaluated

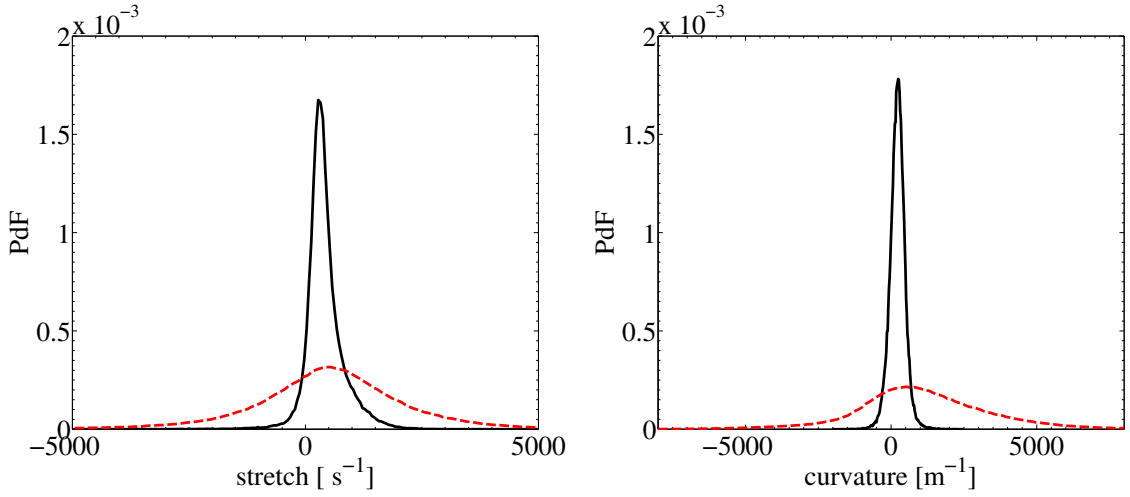

(a) Stretch. (b) Curvature.

Figure 7.13: Pdf s function of local stretch and curvature during the propagation phase 4 ms after ignition. —— : laminar flame ; - - - - : turbulent flame.

by the rate of progress of the first reaction (fuel oxidation) $q_1 = q_1^f + q_1^r$ where q_1^f and q_1^r are the forward and reverse rates of the reaction (here q_1^r is zero since the first reaction is irreversible). Figure 7.14 plots a scatterplot of q_1^f as a function of the variable progress during the propagation phase at $t = 4$ ms. Figure 7.14(a) compares q_1^f for the laminar and

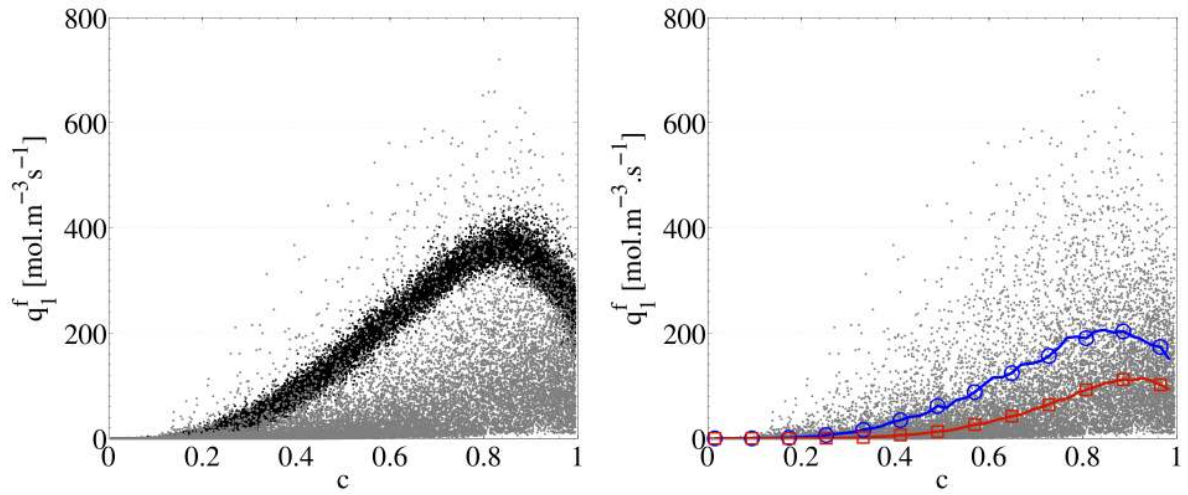

(a) Scatterplot of combustion intensity for laminar and turbulent flame. • : laminar flame ; • : turbulent flame.

(b) Scatterplot of combustion intensity for turbulent flame conditioned by curvature values. • : all points in the flame front ; —○—: average scatterplot conditioned by negative curvature ; —□—: average scatterplot conditioned by positive curvature.

Figure 7.14: Scatterplot of the rate of progress of the first kinetic reaction 4 ms after ignition.

turbulent flames. All values of q_1^f in the flame front ($0 < c < 1$) are reported in the plot. For the laminar flame, all points are contained in a narrow envelope as expected [20]. For the turbulent flame, the scatterplot of combustion intensity shows a dispersion of the values of q_1^f in the flame front. Even if some higher values are reached in the turbulent flame, most of them are below the envelope of the laminar flame. The scatterplots of q_1^f have been averaged on isosurfaces of the progress variable c in order to get a curve of q_1^f as a function of c. The values of q_1^f have been conditioned by the sign of the curvature leading to two curves $q_1^f(c)$: one for positive curvature and one for negative curvature (Fig. 7.14(b)). This diagnostic shows that the combustion intensity is higher in regions of negative curvature. This result is typical of heavy fuel with a Lewis number greater than unity[3].

The response of the turbulent consumption flame speed s_c to stretch is presented and compared to the response of the consumption speed for a laminar flame in Fig. 7.15(a)[4]. For the laminar flame, a classical behavior is found: close to the ignition time, the flame

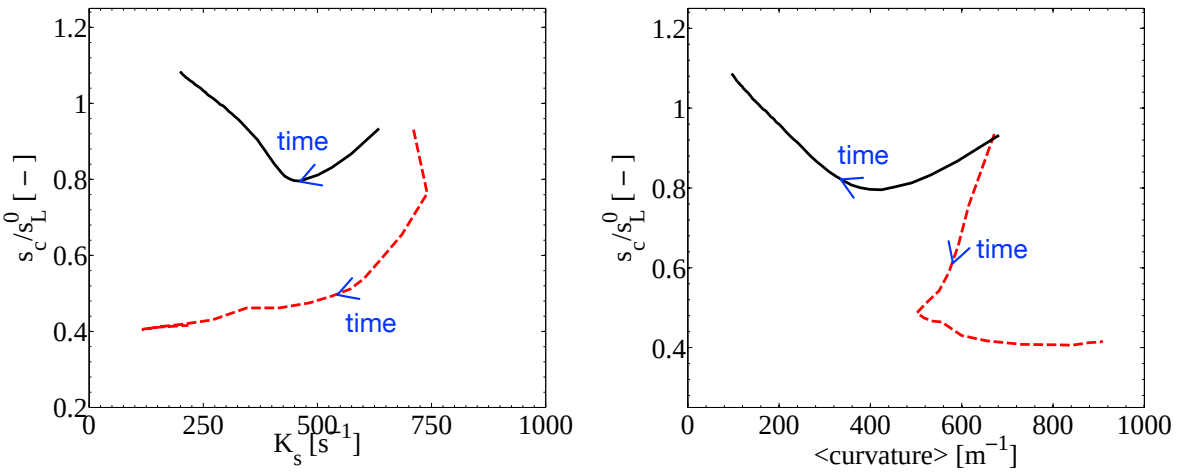

(a) Stretch. (b) Curvature.

Figure 7.15: Response of the consumption flame speed s_c (Eq. 7.9) to stretch $\kappa_{S_{c^*=0.9}}$ (Eq. 7.4) and curvature. —— : laminar flame ; - - - - : turbulent flame.

is sensitive to the ignition procedure (the velocity decrease) [110]. After that, for $\kappa < 300$, the flame speed varies linearly with stretch as predicted by the Markstein-type correlation. As previously observed in Chapter 3 on laminar spherical flames, the extrapolation of $s_c(\kappa)$ to zero stretch overestimates the unstretched laminar flame speed for confined flames (Fig. 3.10). Close to the ignition time, turbulent and laminar flames have the same consumption speeds and are subject to the same stretch[5] since turbulence has not started to wrinkle the flame. During the propagation phase, the turbulent flame behaves differently. When it propagates, turbulence wrinkles the flame and the consumption speed

[3]The Lewis number Le of the octane is $Le_{C8H18} = 2\ 78$

[4]When spherical flames propagate, the global stretch decrease.

[5]The ignition procedure for laminar and turbulent flame is the same: a kernel of burnt gases of 4 mm of radius in adiabatic conditions is deposited at the bomb center.

goes down even if the flame is not going to quench. Figure 7.15(b) plots the response to s_c to curvature. For a laminar flame, the response of s_c to curvature is very similar to its response to stretch since curvature and stretch play similar roles on s_c. For turbulent flames, when the flame propagates, first, curvature decreases slightly then it increases due to strong flame/turbulence interactions which generates high curvature zone locally in the flame front, especially when pockets of burnt gases are created.

7.4.4 Displacement flame speed s_d

To understand the flame propagation mechanism, the displacement speed (Eq. 7.17) can be split into two main terms: $s_d = s_{reac} + s_{diff}$. These terms can be extracted from a simulation by:

$$s_d = \underbrace{\frac{1}{\rho C_p |\nabla\theta|}}_{s_{reac}} \overset{\prime}{T} + \underbrace{\frac{1}{\rho C_p |\nabla\theta|} \frac{\partial}{\partial x_i}\left(\lambda \frac{\partial T}{\partial x_i}\right) - \frac{\partial T}{\partial x_i} \rho \sum_{k=1}^{N} C_{p\,k} Y_k V_{k\,i}}_{s_{diff}} \tag{7.17}$$

The speed s_d is a local quantity which is governed by the local balance between molecular diffusion and reaction rate, which together determine its direction and magnitude.

Figure 7.16 displays the flame speed s_d and the two terms s_{reac} and s_{diff}. Equation 7.17 gives local values of s_{reac} and s_{diff}. To obtain statistical values, these local values are averaged on isosurfaces of the progress variable c and plotted as a function of c. These terms are compared for laminar and turbulent flames at two different times: just after ignition and during the propagation phase. For laminar flames, s_{reac} and s_{diff} are the same at the ignition time and during the propagation phase. In the fresh gases $0.1 < c < 0.3$, the displacement speed s_d is dominated by the diffusion term s_{diff} and the reaction term s_{reac} is nil. For $c > 0.5$, s_{reac} is positive and counterbalance s_{diff} which is negative. Globally, the displacement speed is positive and the flame grows up.

Turbulent flames exhibit a different behavior (Figs. 7.16(c) and 7.16(d)). Just after ignition, the displacement speed terms are very similar to those obtained for laminar flame. But when the turbulent flame propagates ($t = 4.0$ ms), turbulence wrinkles the flame and modify the local (and thereby the global) reaction and diffusion term. Turbulence modifies the diffusion term in the fresh gases and the reaction term for $c > 0.5$. In fresh gases, the diffusion term s_{diff} becomes nil which leads to a displacement speed close to zero. For $c > 0.5$, the reaction term is decreased which decreases the flame speed displacement in the burnt gases too.

Turbulence wrinkles the flame surface and induces high curvatures. Locally the flame front is thickened and can make the local displacement speed negative. Figure 7.17 plots pdf s function of the displacement flame speed s_d. For laminar flames, the displacement speed is always positive while the pdf is centered on zero and almost symmetrical for the turbulent flame.

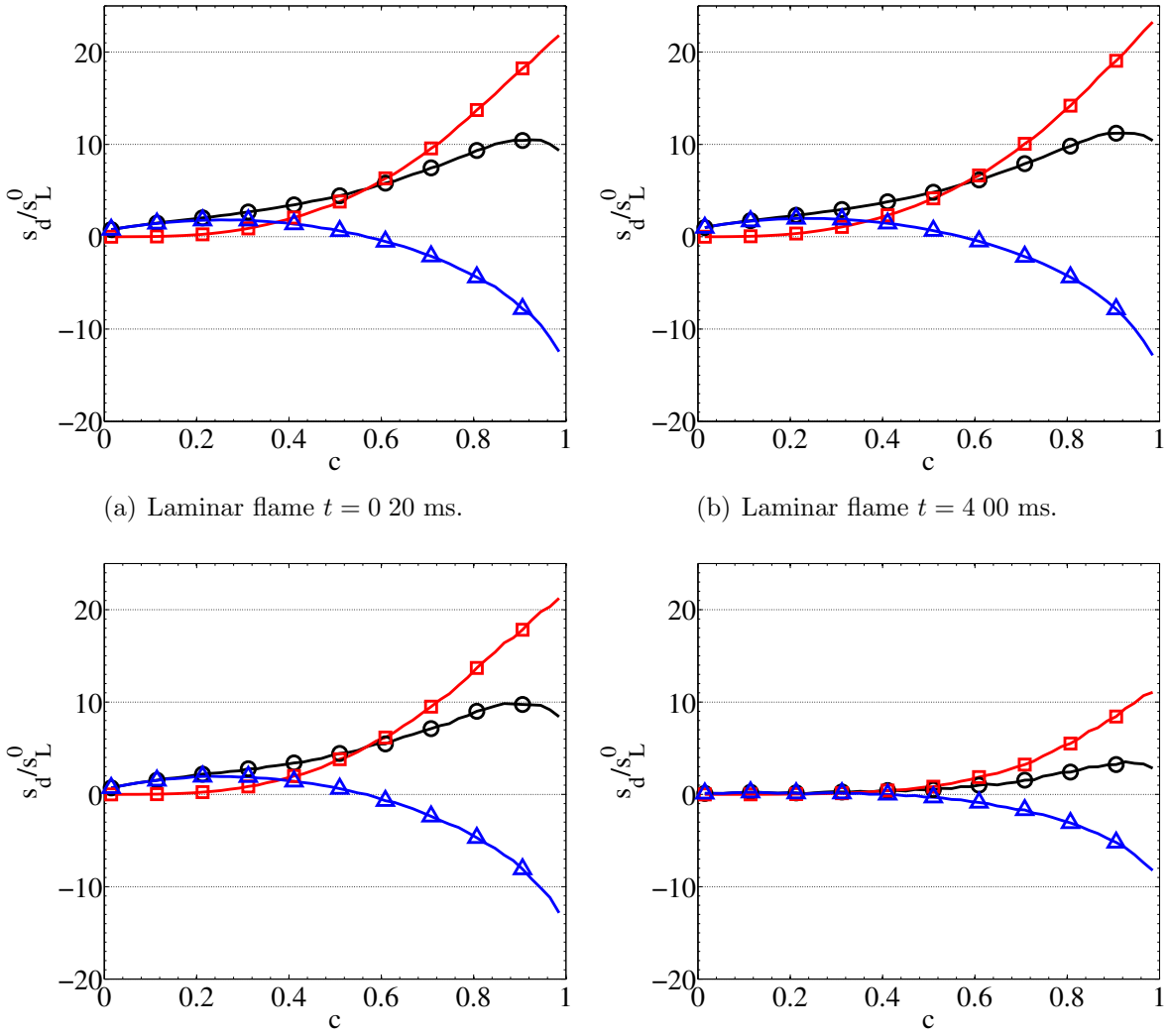

(a) Laminar flame $t = 0\ 20$ ms.

(b) Laminar flame $t = 4\ 00$ ms.

(c) Turbulent flame $t = 0\ 25$ ms.

(d) Turbulent flame $t = 4\ 00$ ms.

Figure 7.16: Displacement flame speed analysis (Eq. 7.17) for laminar and turbulent flames just after the ignition time and 4 ms after ignition. Local values of flame speeds are averaged on isosurfaces of c. ◯: s_d ; □: s_{reac} ; △: s_{diff}.

7.5 Influence of the burnt gases kernel characteristics imposed at ignition on the flame propagation

Computing the exact flow field and the composition a few microseconds after a sparking event is beyond the capabilities of present solvers: the plasma phase and the high temperature reached in the gas make such a simulation impossible today in a turbulent flow (see Sec. 1.6.2). Therefore all DNS of turbulent flames begin after this plasma phase and use an ad-hoc initialization. In this thesis, flames are ignited using a kernel of burnt gases where the shape of the profiles of composition, temperature and velocity are imposed.

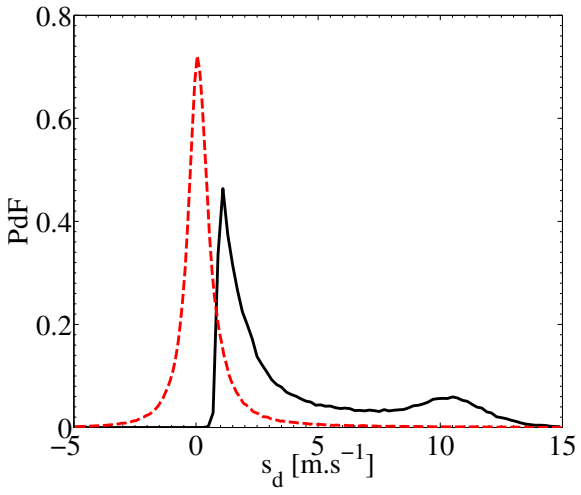

Figure 7.17: Comparison of pdf s function of the displacement speed s_d in laminar and turbulent flame. —— : laminar flame ; - - - -: turbulent flame.

This choice is an arbitrary one and it is usually assumed that it plays a limited role on the following flame growth so that initial conditions are forgotten after a few flame times. As done before in this thesis, we tried to revisit usual assumptions used in most DNS. We test here the effect of two important parameters on the initialization of a flame kernel in turbulent flow:

- the velocity field in the burnt kernel and,
- the temperature field imposed for the gas inside the burnt gas kernel.

Both fields are unknown in the real world but have to be specified for the DNS. The composition (species profile) is always extracted from a previous CANTERA computation (at equilibrium).

7.5.1 Influence of the velocity field

What is the influence of the velocity field inside the burnt gases on the flame propagation? Due to the viscosity increase in the burnt gases, the velocity field is smoother in burnt gases than in the fresh gases. Two extreme options are possible to initialize the velocity field inside the burnt gases kernel: (1) it can be set to zero to mimic the viscosity increase (Fig. 7.18(a)) or (2), it can be unchanged and turbulence inside the kernel is conserved (7.18(b)) from the non-reacting flow computation just before ignition. All other parameters are the same for the two computations: the burnt gases temperature is the adiabatic flame temperature.

Figure 7.19 compares the flame propagation in both cases: the flame is represented by an isoline of progress variable at $c^* = 0.9$. The flame propagation is very similar and does not seem to be affected by the velocity field inside the burnt gases kernel at ignition. The flame surface deformation is comparable in both cases. Here, the flow is highly turbulent and structures go into the flame quickly. Thereby the ignition condition, without

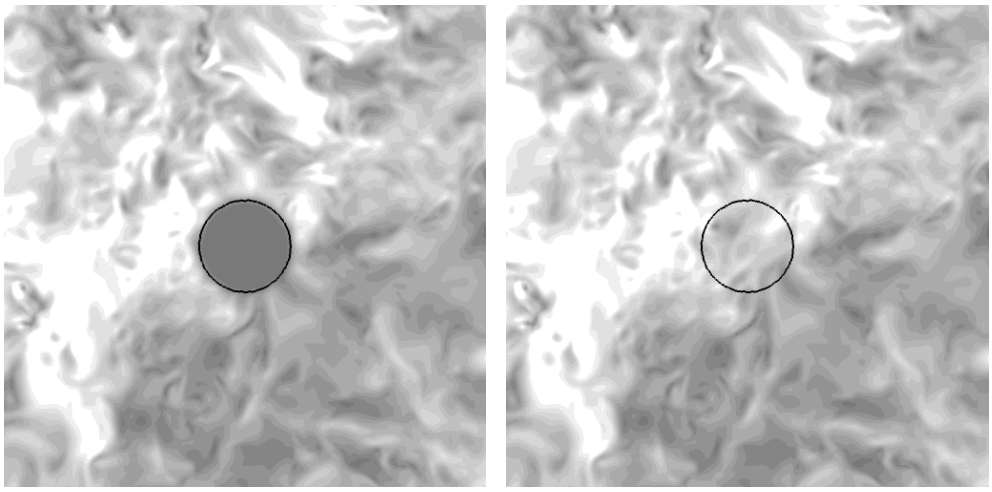

(a) Velocity field set to zero inside the burnt gases kernel.

(b) Velocity field unchanged inside the burnt gases kernel.

Figure 7.18: Velocity modulus fields at ignition. Flame is represented by an isoline progress variable at $c^* = 0\ 9$.

Figure 7.19: Flame propagation illustrated by instantaneous isolines at $c^* = 0\ 9$. —— : velocity field unchanged (Fig. 7.18(a)) ; —— : velocity field set to zero (Fig. 7.18(b)).

turbulence inside the flame kernel, is forgotten rapidly leading to similar propagations.

Finally, Fig. 7.20 compares the flame surfaces. Figure 7.20 confirms the previous

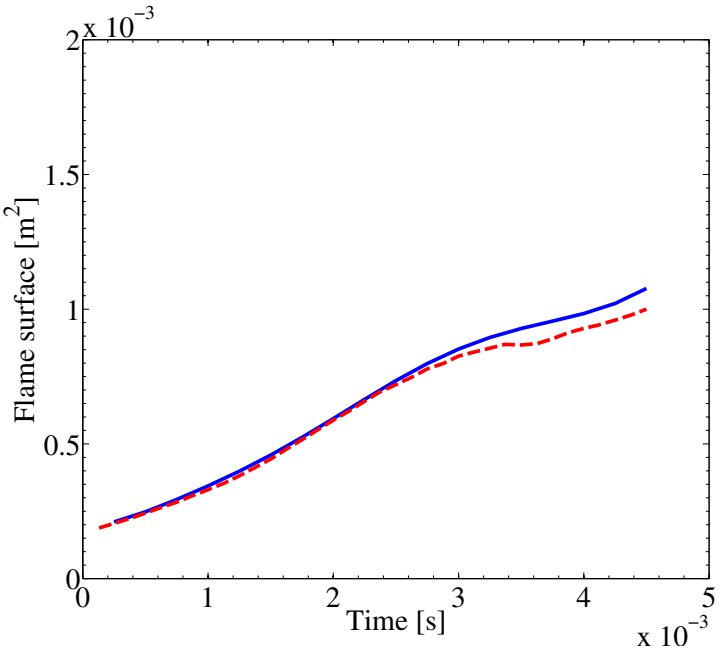

Figure 7.20: Temporal evolution of the flame surface. —— : velocity field unchanged in the burnt gases kernel ; ---- : velocity field set to zero in the burnt gases kernel.

observation: flame surfaces match very well which means that the flame propagation is not affected by the velocity field inside the burnt gases kernel at ignition.

7.5.2 Influence of the temperature

Minimum Ignition Energy (MIE) is a critical property for safety standards as well as for the fundamental understandings of the ignition process of combustible mixtures. In particular, it is known that for a given mixture, MIE increases with the ratio u'/s_L^0 [166]. In this thesis, MIE is not studied but the influence of the burnt gases temperature imposed at ignition time on the propagation phase is investigated. Obviously, the spark can create a kernel of hot gases of arbitrary temperature. Often, this kernel is super-adiabatic: the temperature can be larger than the adiabatic flame temperature. It is important to investigate the effects of this parameter. Up to now we have used an initial temperature of kernel equal to the adiabatic flame temperature. Here we test higher temperatures.

Two computations are compared: the first one where the flame is ignited with an adiabatic hot gases kernel (procedure described in Sec. 1.6.2) and another one with a temperature inside the burnt gases kernel larger than the adiabatic flame temperature: the initial temperature profile imposed in the burnt kernel is increased to reach 200 K more than the adiabatic temperature (Fig. 7.21). The kernel size is kept constant ($R_f^0 = 4$ mm).

Even if the burnt gases temperature is raised, the energy deposited is almost constant since the product $\rho_b T_b$ is constant: the energy increase is only due to the variation of $C_{p\,b}$ with the temperature which is very small.

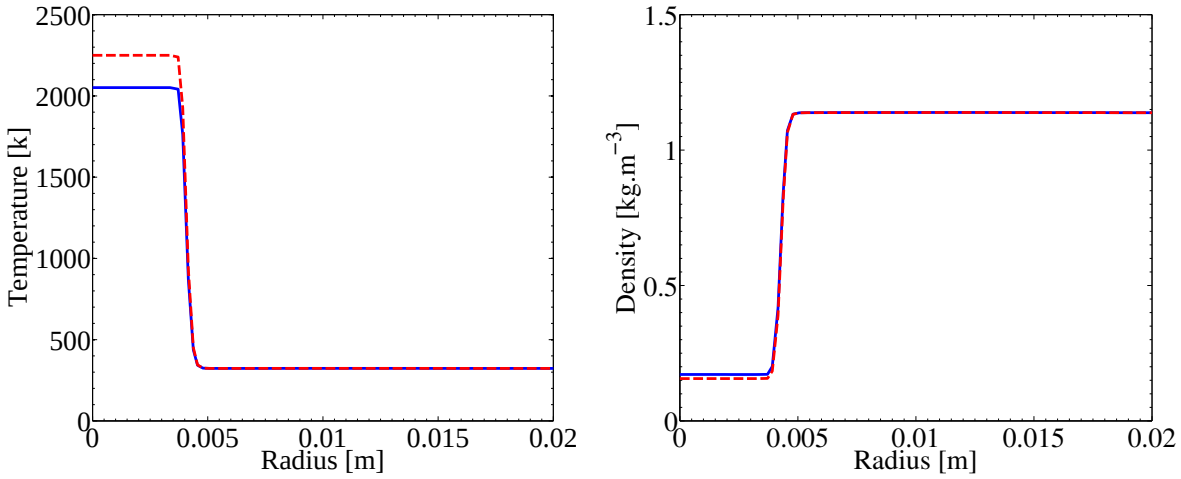

(a) Temperature profiles. (b) Density profiles.

Figure 7.21: Temperature and density profiles to compare flame kernel at ignition time. ——— : adiabatic flame kernel ($T_b^0 = T_{ad}$ and $\rho_b^0 = \rho_{ad}$) ; ---- : over adiabatic flame kernel ($T_b^0 = T_{ad} + 200 = 2250$ K).

Figure 7.22 compares the propagation phase for the two ignition conditions. When

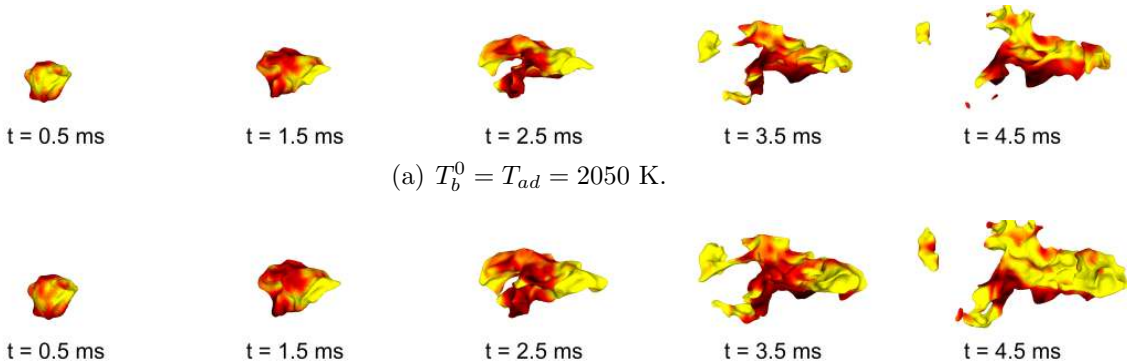

(a) $T_b^0 = T_{ad} = 2050$ K.

(b) $T_b^0 = T_{ad} + 200 = 2250$ K.

Figure 7.22: Flame propagation illustrated by instantaneous isosurfaces of $c^* = 0\,9$ colored by the velocity magnitude.

the burnt gases kernel is overheated, the flame develops faster, is more robust and is less affected by velocity fluctuations and stretch. For example, 3.5 ms after ignition, the flame surface is teared in two pieces when the burnt gases temperature is equal to the adiabatic flame temperature while it still is in one piece otherwise.

The flame propagation can be compared using isolines of $c^* = 0.9$ for the two ignition

configurations (Fig. 7.23): using this visualization, flame surfaces can be superimposed to give a more quantitative comparison.

Figure 7.23: Flame propagation illustrated by instantaneous isolines of $c^* = 0.9$. —— : $T_b^0 = T_{ad} = 2050$ K ; —— : $T_b^0 = T_{ad} + 200 = 2250$ K.

Figure 7.24(a) compares the flame surfaces for the two ignition conditions. As previously observed on Figs. 7.22 and 7.23, when the burnt gases temperature is upper than the adiabatic flame temperature, the flame grows up faster. Increasing the burnt gases temperature of 10% can lead to large discrepancies in the flame surface: 4.5 ms after ignition, the flame surface is 60% bigger when the burnt gases temperature is larger than the adiabatic temperature. Finally, Fig. 7.24(b) compares the temporal evolution of the mean consumption flame speed s_c (Eq. 7.9) for two ignition conditions. The mean consumption flame speed of the flame ignited with a burnt gases temperature $T_b^0 = T_{ad} + 200 = 2250$ K has a consumption speed slightly larger than the flame ignited with a burnt gases temperature equal to the adiabatic flame temperature. However, the two curves have a similar trend and reach an asymptotic value $s_c/s_L^0 \simeq 50\%$.

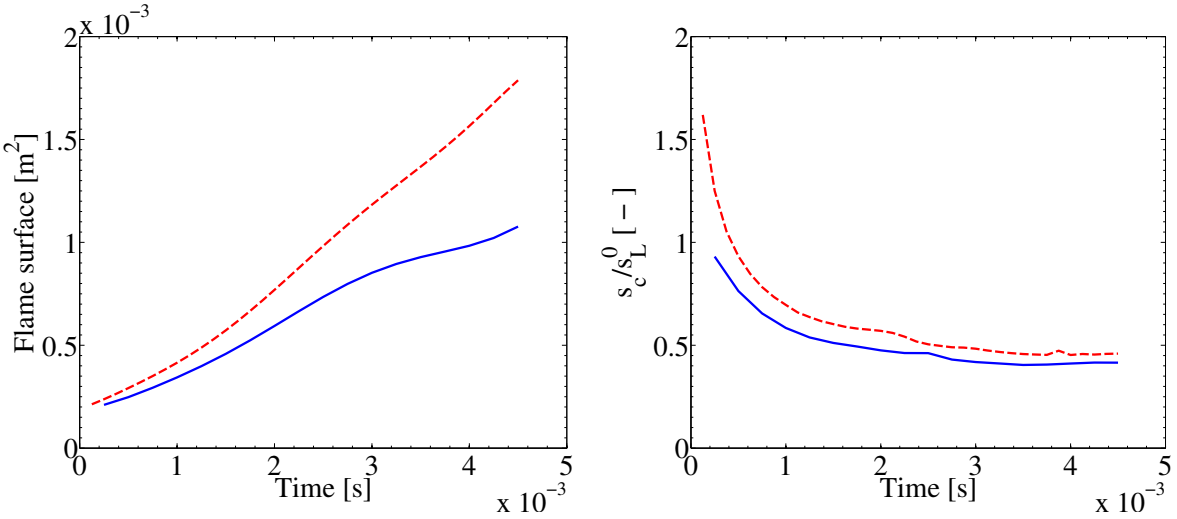

(a) Flame surface $S_{c^*=0.9}$ (Eq. 7.16) versus time. (b) Mean consumption flame speed s_c (Eq. 7.9) versus time.

Figure 7.24: Influence of the burnt gases temperature imposed at ignition. —— : $T_b^0 = T_{ad} = 2050$ K ; ---- : $T_b^0 = T_{ad} + 200 = 2250$ K.

This demonstrates that in all these DNS, there is a hidden parameter in the initialization phase: the temperature of the initial kernel. Since this temperature results from the

plasma phase which is never computed, it is difficult to specify. Unfortunately, it seems to play a strong role. Note that this probably does not affect statistics gathered at later times. It changes the combustion timing but not the flame/turbulence interaction.

7.6 Conclusion

This chapter presents well resolved LES of turbulent premixed flames propagating in the spherical vessel stirred by six fans. The mesh grid used leads to DNS like computations at the bomb center to resolve the flame. First a laminar (fans are stopped) and a turbulent flame propagation are compared. The difficulty of measuring the flame surface in a highly turbulent flow is highlighted and it is shown that the turbulent consumption flame speed is lower than the laminar flame speed. Finally, the influence of the velocity field and the temperature inside the burnt gases kernel imposed at ignition is evaluated. It is shown that the temperature of the burnt gases kernel imposed at ignition is an important parameter controlling the propagation phase. On the other hand, the velocity field (turbulence removed or not) imposed within the initial burnt gases kernel does not modify the flame propagation.

CONCLUSIONS & PERSPECTIVES

The context of this PhD was the understanding of abnormal combustions in spark-ignition piston engines. This project was funded by the French Research National Agency through the ICAMDAC project. To increase the engine fuel efficiency and decrease pollutant emissions, engine manufacturers decrease the size of engines (downsizing`). To keep the engine power constant, the trapped mass inside the combustion chamber is increased using turbochargers. However, due to in-cylinder pressure increase, this may lead to abnormal combustions (knocking or rumble).

Large Eddy Simulation has proved its ability to predict these abnormal combustions [5, 6] in piston engines. In a spark-ignition engine, the premixed flame is ignited by the energy deposited by the spark plug. Then the flame must propagate in the turbulent premixed flow. This propagation phase is critical and its simulation the heart of this PhD. A better understanding of premixed turbulent flame propagation properties is necessary to improve turbulent combustion models used in full engine computations.

To focus on laminar and turbulent flame propagation, an experiment was setup at the PRISME laboratory (Orléans): it consists in a closed spherical vessel fed with premixed gases. To generate turbulence, six fans are placed in the vessel. A spark-plug located at the vessel center is used to ignite premixed gases. The objective of this work was twofold:

- characterize the turbulence generated inside the vessel to check wether it is homogeneous and isotropic or not,
- finely characterize laminar and turbulent combustion cases in order to increase the knowledge in this field, and thereby improve models used.

Conclusions are drawn below:

- **Reduced kinetic scheme for octane:** First, a reduced kinetic scheme, called 2S_C8H18_AB, has been developed and validated using the reference Jerzembeck scheme [43]. Laminar flame speed and adiabatic flame temperature have been validated for lean mixture by comparison with a detailed scheme.
- **Stretch and confinement effect on laminar flame speed:** Post-processing methods of flame radii for laminar spherical flame to deduce laminar flame speeds and Markstein lengths were discussed. It was shown that the classical relation

based on time evolution of the flame radius only:

$$s_c^{p\,expe} = \frac{\rho_b^{eq}}{\rho_u(t=0)} \frac{dR_p}{dt}$$

is not adequate to predict the true consumption speed based on the fuel consumption. An expression using only the flame radius and the pressure inside the bomb (two quantities which are directly measured) [111]:

$$s_c^f = \frac{dR_f}{dt} - \frac{R_0^3 - R_f^3}{3R_f^2} \frac{1}{\gamma_u P} \frac{dP}{dt}$$

gives better results than $s_c^{p\,expe}$ and captures reasonably well the evolution of the consumption speed versus flame stretch. Since s_c^f only requires the knowledge of $R(t)$ and $P(t)$, it is simple to use experimentally. The present work suggests however that this equation is a good candidate for a more precise determination of the flame speeds. Results of this study have been published in Combustion and Flame [81].

- **Immersed Boundary Method in *AVBP*:** To compute the turbulence generated by fans inside the spherical vessel, two numerical strategies have been tested. Fans rotate so that all strategies involving mesh deformations are proscribed due to complexity and meshing time. First, an Immersed Boundary Method (IBM) was implemented in the *AVBP* code. It is based on continuous forcing method. To impose a velocity at the immersed boundary, a source term is added in the momentum equation: a feedback scheme [137] was implemented. A procedure was set-up to optimize the IB method efficiency. Various test cases were performed and a very good agreement with reference solutions in simple cases was found. However, the IB method was tested on a one-fan validation test case and very large differences were found between experimental and numerical results. A lack of resolution in the zone spanned by the blades is probably the reason of this failure.
- **MISCOG approach:** To reach our objective, an other numerical strategy was developed. The method comes from turbomachinery calculations: multiple instances of the same solver run simultaneously and these instances are coupled on a small overlapping zone (the method is called MISCOG, for Multi Instances Solver Coupled on Overlapping Grids). A convection vortex test case was performed and showed very good results. Then the method was validated on the one-fan validation test case. First the computation was performed assuming flat leading and trailing edges for the fan blades to save mesh points. Compared to PIV measurements, the computation leads to large errors on the velocity fields. An other computation with the real (curved) leading and trailing edges was performed and gives better results demonstrating the impact of the blade shape on the average flow: taking into account the real blade shape geometry is essential to predict the flow generated by the fan.
- **Non-reacting flow in the fan-stirred vessel:** Using the MISCOG approach, the closed vessel stirred by the six fans was computed. The flow inside the vessel

was studied using a well resolved LES of the full geometry. Average and fluctuating fields match experimental data reasonably well. The structure of the turbulence was studied and it was shown that turbulence is almost homogeneous and isotropic at the bomb center in a region of around 6 cm of diameter. The budget of mean turbulent kinetic energy was evaluated and showed that turbulence is not convected from fans to the bomb center but diffused since the average velocities are near zero at this location. The trace of the blade passage frequency disappears near the bomb center.

- **Reacting flow in the fan-stirred vessel:** Well resolved LES of turbulent premixed flames propagating in the spherical vessel stirred by six fans have been performed. The grid used here leads to DNS-like` computation at the bomb center to resolve the flame. Laminar and turbulent flames propagation have been compared in condition of intense turbulence ($u'/s_L^0 \simeq 10$). The difficulty of measuring the flame surface in a highly turbulent flow is highlighted and it is shown that the turbulent consumption flame speed is lower than the laminar flame speed for this case, an uncommon result in DNS. Finally, the influence of the velocity field and the temperature inside the burnt gases kernel imposed at ignition is evaluated. It is shown that the temperature of the burnt gases kernel imposed at ignition is an important parameter controlling the propagation phase. On the other hand, the velocity field (turbulence removed or not) within this hot initial kernel does not modify the flame propagation.

More generally, even tough this work has not tried to analyze all DNS results, it has demonstrated that usual DNS could be improved by explicitly computing the flow in turbulent bombs (and not assuming it is homogeneous and isotropic) and that the temperature of the initial kernel was a problem. It is actually the whole plasma phase which is neglected in most DNS and this may have an important effect on all conclusions. Moreover, the grid resolution at the surface of fan blades was clearly shown as a key parameter to get reliable results (in terms of turbulence inside the vessel) since the flow is only piloted by the fans.

Further investigations will be necessary to complete the numerical study in order to compare numerical results to the experimental database. In this PhD, only one fan rotation speed ($N_{fan} = 10,000$ rpm) was considered but it was shown experimentally (in the Orléans bomb [80] and in similar configurations [167, 30]) that a linear relation links the fans rotation speed and the velocity fluctuations at the bomb center. It will be interesting to see if LES is able to retrieve this property. Moreover, computing other fan rotation speeds will enable to study turbulent combustion in regimes where turbulence is less energetic (in order to decrease the ratio u'/s_L^0). Finally, this work could be completed by changing the thermodynamic conditions (pressure and temperature) and the equivalence ratio in the spherical bomb before ignition as it was done experimentally.

An important part of this PhD was devoted to develop numerical methods (Immersed Boundaries and MISCOG). These numerical methods are not specific to computations performed during this work but can be applied to a wide range of applications such as piston engine or turbomachinery calculations.

BIBLIOGRAPHY

[1] R. Sawyer. Science based policy for addressing energy and environmental problems. *Proc. Combust. Inst.*, 32(1):45 56, 2009. (Cited on page 1.)

[2] M.C. Drake and D.C. Haworth. Advanced gasoline engine development using optical diagnostics and numerical modeling. *Proc. Combust. Inst.*, 31(1):99 124, January 2007. (Cited on page 4.)

[3] P. Leduc, B. Dubar, A. Ranini, and G. Monnier. Downsizing of Gasoline Engine : an Efficient Way to Reduce CO2 Emissions. *Oil & Gas Science and Technology*, 58(1):115 127, 2003. (Cited on page 5.)

[4] L. Thobois. *Intérêt et faisabilité de la Simulation aux Grandes Echelles dans les moteurs automobiles*. PhD thesis, INP Toulouse, 2006. (Cited on page 5.)

[5] B. Enaux. *Simulation aux Grandes Échelles d'un moteur à allumage commandé - Évaluations des variabilités cycliques*. PhD thesis, INP Toulouse, 2010. (Cited on pages 5, 70, and 161.)

[6] V. Granet. *La Simulation aux Grandes Echelles : un outil pour la prédiction des variabilités cycliques dans les moteurs à allumage commandé ?* PhD thesis, INP Toulouse, 2011. (Cited on pages 5 and 161.)

[7] H. Tennekes. Simple model for the small scale structure of turbulence. *Phys. Fluids*, 11(3):669 670, 1968. (Cited on page 5.)

[8] H. Tennekes and J. L. Lumley. *A first course in turbulence*. M.I.T. Press, Cambridge, 1972. (Cited on page 5.)

[9] J. O. Hinze. *Turbulence*. McGraw-Hill, New-York, 1975. (Cited on pages 5 and 134.)

[10] F. Risso and J. Fabre. Diffusive turbulence in a confined jet experiment. *J. Fluid Mech.*, 337:233 261, 1997. (Cited on pages 5 and 134.)

[11] S. B. Pope. *Turbulent flows*. Cambridge University Press, 2000. (Cited on pages 5 and 127.)

[12] P. Sagaut. *Large eddy simulation for incompressible flows*. Springer, 2002. (Cited on pages 5 and 31.)

[13] E. Garnier, M. Mossi, P. Sagaut, P. Comte, and M. Deville. On the use of shock-capturing schemes for large-eddy simulation. *J. Comput. Phys.* , 153(2):273 311, 1999. (Cited on page 5.)

[14] E. Lenormand, P. Sagaut, L. Ta Phuoc, and P. Comte. Subgrid-scale models for large-eddy simulations of compressible wall bounded flows. *AIAA Journal* , 41(6), 2000. (Cited on page 5.)

[15] P. Moin, K. D. Squires, W. Cabot, and S. Lee. A dynamic subgrid-scale model for compressible turbulence and scalar transport. *Phys. Fluids* , A 3(11):2746 2757, 1991. (Cited on page 5.)

[16] F. Mashayek, F. A. Jaberi, R. S. Miller, and P. Givi. Dispersion and polydispersity of droplets in stationary isotropic turbulence. *Int. J. Multiphase Flow* , 23(2):337 355, 1997. (Cited on page 5.)

[17] A. Aliseda, A. Cartellier, F. Hainaux, and J. C. Lasheras. Effect of preferential concentration on the settling velocity of heavy particles in homogeneous isotropic turbulence. *J. Fluid Mech.*, 468:77 105, October 2002. (Cited on page 5.)

[18] J. P. L. C. Salazar, J. De Jong, L. Cao, S. H. Woodward, H. Meng, and L. R. Collins. Experimental and numerical investigation of inertial particle clustering in isotropic turbulence. *J. Fluid Mech.*, 600:245 256, March 2008. (Cited on page 5.)

[19] M. Birouk and I. Gokalp. Current status of droplet evaporation in turbulent flows. *Prog. Energy Comb. Sci.*, 32(4):408 423, 2006. (Cited on page 5.)

[20] T. Poinsot and D. Veynante. *Theoretical and Numerical Combustion*. Third Edition (www.cerfacs.fr/elearning), 2011. (Cited on pages 5, 6, 17, 25, 34, 37, 50, 52, 139, and 151.)

[21] N. Peters. *Turbulent combustion*. Cambridge University Press, 2001. (Cited on pages 5 and 50.)

[22] S. S. Girimaji and S. B. Pope. Propagating surfaces in isotropic turbulence. *J. Fluid Mech.* , 234:247 277, 1992. (Cited on page 5.)

[23] P. Laffitte. *La propagation des flammes dans les mélanges gazeux*. Hermann et Cie, Actualités scientifiques et industrielles, PARIS, 1939. (Cited on pages 5 and 50.)

[24] E. S. Semenov. Measurement of turbulence characteristics in a closed volume with artificial turbulence. *Combustion, explosion and shock waves*, 1(2):57 62, 1965. (Cited on pages 5 and 6.)

[25] R. G. Abdel-Gayed, D. Bradley, M. N. Hamid, and M. Lawes. Lewis number effects on turbulent burning velocity. *Proc. Combust. Inst.* , 20:505 512, 1984. (Cited on page 6.)

[26] O. Gulder. Turbulent premixed flame propagation models for different combustion regimes. *23rd Symp. (Int.) on Combustion*, 23(1):743 750, 1991. (Cited on page 6.)

[27] J. H. Chen and H. G. Im. Correlation of flame speed with stretch in turbulent premixed methane/air flames. *27th Symp. (Int.) on Combustion*, (1):819 826, January 1998. (Cited on page 6.)

[28] S. S. Shy, W. J. Lin, and J. C. Wei. An experimental correlation of turbulent burning velocities for premixed turbulent methane-air combustion. *Proc. R. Soc. Lond. A*, 456(2000):1997 2019, August 2000. (Cited on page 6.)

[29] S. Y. Liao, D. M. Jiang, Z. H. Huang, K. Zeng, and Q. Cheng. Determination of the laminar burning velocities for mixtures of ethanol and air at elevated temperatures. *Applied Thermal Engineering*, 27(2-3):374 380, February 2007. (Cited on page 6.)

[30] M. Birouk, B. Sarh, and I. Gökalp. An attempt to realize experimental isotropic turbulence at low Reynolds number. *Flow, Turbulence and Combustion*, 70(1-4):325 348, 2003. (Cited on pages 6 and 163.)

[31] W. Hwang and J. K. Eaton. Creating homogeneous and isotropic turbulence without a mean flow. *Exp. Fluids*, 36(3):444 454, March 2004. (Cited on page 6.)

[32] M. E. Brachet, M. D. Bustamante, G. Krstulovic, P. D. Mininni, A. Pouquet, and D. Rosenberg. Ideal evolution of MHD turbulence when imposing Taylor-Green symmetries. *Phys. Rev. E*, 87:1 16, 2013. (Cited on page 6.)

[33] J. Boussinesq. Essai sur la théorie des eaux courantes. *26ème édn. Acad. Sci. Paris*, 1877. (Cited on pages 14 and 30.)

[34] J. O. Hirschfelder, C. F. Curtiss, and R. B. Bird. *Molecular theory of gases and liquids*. John Wiley & Sons, New York, 1969. (Cited on page 14.)

[35] A. N. Kolmogorov. The local structure of turbulence in incompressible viscous fluid for very large reynolds numbers. *C. R. Acad. Sci. , USSR*, 30:301, 1941. (Cited on pages 15, 31, and 132.)

[36] W. Rodi. Comparison of LES and RANS calculations of the flow around bluff bodies. *J. Wind Engineering and Industrial Aerodynamics*, 69-71:55 75, July 1997. (Cited on page 18.)

[37] H. Lübcke, S. Schmidt, T. Rung, and F. Thiele. Comparison of LES and RANS in bluff-body flows. *J. Wind Engineering and Industrial Aerodynamics*, 89(14-15):1471 1485, December 2001. (Cited on page 18.)

[38] Y. Cheng, F. S. Lien, E. Yee, and R. Sinclair. A comparison of large Eddy simulations with a standard k ϵ Reynolds-averaged Navier Stokes model for the prediction of a fully developed turbulent flow over a matrix of cubes. *J. Wind Engineering and Industrial Aerodynamics*, 91(11):1301 1328, November 2003. (Cited on page 18.)

[39] S. M. Salim, K. C. Ong, and S. C. Cheah. Comparison of RANS , URANS and LES in the Prediction of Airflow and Pollutant Dispersion. *Proceedings of the World Congress on Engineering and Computer Science*, II, 2011. (Cited on page 18.)

[40] D. G. Goodwin. Cantera C++ User s Guide. Technical report, 2002. (Cited on page 20.)

[41] D. R. Stull and H. Prophet. JANAF thermochemical tables, 2nd Edition. Technical Report NSRDS-NBS 37, US National Bureau of Standards, 1971. (Cited on page 23.)

[42] L. Selle, G. Lartigue, T. Poinsot, R. Koch, K.-U. Schildmacher, W. Krebs, B. Prade, P. Kaufmann, and D. Veynante. Compressible large-eddy simulation of turbulent combustion in complex geometry on unstructured meshes. *Combust. Flame* , 137(4):489 505, 2004. (Cited on pages 25, 26, and 35.)

[43] S. Jerzembeck, N. Peters, P. Pepiot-Desjardins, and H. Pitsch. Laminar burning velocities at high pressure for primary reference fuels and gasoline: Experimental and numerical investigation. *Combust. Flame*, 156(2):292 301, February 2009. (Cited on pages 26, 27, and 161.)

[44] B. Franzelli, E. Riber, M. Sanjosé, and T. Poinsot. A two-step chemical scheme for kerosene air premixed flames. *Combust. Flame*, 157(7):1364 1373, July 2010. (Cited on page 26.)

[45] J. Boussinesq. Théorie de l écoulement tourbillant. *Mém. Présentés par Divers Savants. Acad. Sci. Inst. Fr.*, 23:46 50, 1877. (Cited on page 31.)

[46] M. Garcia. *Développement et validation du formalisme Euler-Lagrange dans un solveur parallèle et non-structuré pour la simulation aux grandes échelles.* PhD thesis, 2009. (Cited on pages 31, 72, and 73.)

[47] J. Smagorinsky. General circulation experiments with the primitive equations: 1. the basic experiment. *Mon. Weather Rev.* , 91:99 164, 1963. (Cited on page 31.)

[48] F. Ducros, F. Nicoud, and T. Poinsot. Wall-adapating local eddy-viscosity models for simulations in complex geometries. In *ICFD*, pages 293 300. Baines M. J., 1998. (Cited on pages 31 and 118.)

[49] C. Hirsch. Finite volume method and conservative discretization with an introduction to finite element method. In *Numerical Computation of internal & external flows: Fundamentals of Computational Fluid Dynamics, second edition*, chapter 5, pages 203 248. John Wiley & Sons, New York, 2007. (Cited on page 31.)

[50] N. Lamarque. *Schémas numériques et conditions limites pour la simulation aux grandes échelles de la combustion diphasique dans les foyers d'hélicoptère.* Phd thesis, INP Toulouse, 2007. (Cited on page 31.)

[51] P. D. Lax and B. Wendroff. Systems of conservation laws. *Commun. Pure Appl. Math.* , 13:217 237, 1960. (Cited on page 32.)

[52] O. Colin and M. Rudgyard. Development of high-order taylor-galerkin schemes for unsteady calculations. *J. Comput. Phys.* , 162(2):338 371, 2000. (Cited on pages 32 and 55.)

[53] V. Moureau, G. Lartigue, Y. Sommerer, C. Angelberger, O. Colin, and T. Poinsot. Numerical methods for unsteady compressible multi-component reacting flows on fixed and moving grids. *J. Comput. Phys.* , 202(2):710 736, 2005. (Cited on pages 32, 55, 70, and 106.)

[54] K. N. C. Bray and J. B. Moss. A closure model for the turbulent premixed flame with sequential chemistry. *Combust. Flame* , 30:125 131, 1977. (Cited on page 33.)

[55] E. R. Hawkes and S. R. Cant. A flame surface density approach to large eddy simulation of premixed turbulent combustion. In *28th Symp. (Int.) on Combustion*, pages 51 58. The Combustion Institute, Pittsburgh, 2000. (Cited on page 33.)

[56] H. Pitsch. A consistent level set formulation for large-eddy simulation of premixed turbulent combustion. *Combustion and Flame*, 143(4):587 598, 2005. Special Issue to Honor Professor Robert W. Bilger on the Occasion of His Seventieth Birthday /ce:title . (Cited on page 33.)

[57] V. Moureau, B. Fiorina, and H. Pitsch. A level set formulation for premixed combustion LES considering the turbulent flame structure. *Combust. Flame* , 156(4):801 812, 2009. (Cited on page 33.)

[58] M.S. Anand and S.B. Pope. Calculations of premixed turbulent flames by pdf methods. *Combustion and Flame*, 67(2):127 142, 1987. (Cited on page 33.)

[59] C. Dopazo. Recent developments in pdf methods. In P. A. Libby and F. A. Williams, editors, *Turbulent Reacting Flows*, pages 375 474. Academic, London, 1994. (Cited on page 33.)

[60] B. Fiorina, R. Vicquelin, P. Auzillon, N. Darabiha, O. Gicquel, and D. Veynante. A filtered tabulated chemistry model for les of premixed combustion. *Combustion and Flame*, 157(3):465 475, 2010. (Cited on page 33.)

[61] O. Colin, F. Ducros, D. Veynante, and T. Poinsot. A thickened flame model for large eddy simulations of turbulent premixed combustion. *Phys. Fluids* , 12(7):1843 1863, 2000. (Cited on pages 33, 34, and 35.)

[62] J.-Ph. Légier, T. Poinsot, and D. Veynante. Dynamically thickened flame LES model for premixed and non-premixed turbulent combustion. In *Proc. of the Summer Program* , pages 157 168. Center for Turbulence Research, NASA Ames/Stanford Univ., 2000. (Cited on pages 33 and 35.)

[63] T. D. Butler and P. J. O Rourke. A numerical method for two-dimensional unsteady reacting flows. *Proc. Combust. Inst.* , 16(1):1503 1515, 1977. (Cited on page 33.)

[64] F. A. Williams. *Combustion Theory*. Benjamin Cummings, Menlo Park, CA, 1985. (Cited on pages 33 and 50.)

[65] K. K. Kuo. *Principles of combustion*. John Wiley & Sons, Inc., Hoboken, New Jersey, 2005 Second Edition. (Cited on page 33.)

[66] C. Angelberger, D. Veynante, F. Egolfopoulos, and T. Poinsot. Large eddy simulations of combustion instabilities in premixed flames. In *Proc. of the Summer Program* , pages 61 82. Center for Turbulence Research, NASA Ames/Stanford Univ., 1998. (Cited on page 34.)

[67] J.-Ph. Légier, B. Varoquié, F. Lacas, T. Poinsot, and D. Veynante. Large eddy simulation of a non-premixed turbulent burner using a dynamically thickened flame model. In A. Pollard Eds and S. Candel, editors, *IUTAM Symposium on Turbulent Mixing and Combustion*, pages 315 326. Kluwer Academic Publishers, 2002. (Cited on page 35.)

[68] P. Wolf, G. Staffelbach, R. Balakrishnan, A. Roux, and T. Poinsot. Azimuthal instabilities in annular combustion chambers. In NASA Ames/Stanford Univ. Center for Turbulence Research, editor, *Proc. of the Summer Program* , pages 259 269, 2010. (Cited on page 35.)

[69] B. Enaux, V. Granet, O. Vermorel, C. Lacour, C. Pera, C. Angelberger, and T. Poinsot. Les and experimental study of cycle-to-cycle variations in a spark ignition engine. *Proc. Combust. Inst.* , 33:3115 3122, 2011. (Cited on page 35.)

[70] R. Maly and M. Vogel. Initiation and propagation of flame fronts in lean ch4-air mixtures by the threemodes of the ignition spark. In *17th Symp. (Int.) on Combustion*, pages 821 831. The Combustion Institute, Pittsburgh, 1978. (Cited on page 36.)

[71] H. G. Adelman. A time dependent theory of spark ignition. *18th Symp. (Int.) on Combustion*, 18(1):1333 1342, 1981. (Cited on page 36.)

[72] D. Bradley and K. K. Lung. Spark ignition and the early stages of turbulent flame propagation. *Combust. Flame*, 69:71 93, 1987. (Cited on page 36.)

[73] K. Eisazadeh-Far, F. Parsinejad, H. Metghalchi, and J. C. Keck. On flame kernel formation and propagation in premixed gases. *Combust. Flame*, 157(12):2211 2221, December 2010. (Cited on page 36.)

[74] L. Thobois. *Intérêt et faisabilité de la simulation aux grandes échelles dans les moteurs automobiles*. Phd thesis, INP Toulouse, 2006. (Cited on pages 36 and 70.)

[75] C. S. Peskin. The Immersed Boundary Method. *Acta Numerica*, pages 479 517, July 2002. (Cited on pages 37 and 106.)

[76] R. Verzicco, J. Mohd-Yusof, P. Orlandi, and D. Haworth. Large eddy simulation in complex geometric configurations using boundary body forces. *AIAA Journal* , 38(3):427 433, March 2000. (Cited on pages 37 and 106.)

[77] C. W. Hirt, A.A. Amsden, and J. L. Cook. An arbitrary lagrangian-eulerian computing method for all flow speeds. *J. Comput. Phys.* , 131(4):371 385, 1974. (Cited on pages 37 and 106.)

[78] V. Moureau. *Simulation aux grandes échelles de l'aérodynamique interne des moteurs à piston*. Phd thesis, Ecole Centrale Paris, 2004. (Cited on pages 37, 39, 70, and 106.)

[79] V. Moureau, O. Vasilyev, C. Angelberger, and T. Poinsot. Commutation errors in Large Eddy Simulations on moving grids: Application to piston engine flows. In *Proc. of the Summer Program* , pages 157 168, Center for Turbulence Research, NASA AMES/Stanford University, USA, 2004. (Cited on pages 37 and 106.)

[80] B. Galmiche, F. Halter, N. Mazellier, and F. Foucher. Turbulent flow field measurements in a fan-stirred combustion vessel. In *European Turbulence Conference*, 2013. (Cited on pages 42 and 163.)

[81] A. Bonhomme, L. Selle, and T. Poinsot. Curvature and confinement effects for flame speed measurements in laminar spherical and cylindrical flames. *Combust. Flame*, 160(7):1208 1214, 2013. (Cited on pages 50 and 162.)

[82] E. Ranzi, A. Frassoldati, R. Grana, A. Cuoci, T. Faravelli, A. P. Kelley, and C. K. Law. Hierarchical and comparative kinetic modeling of laminar flame speeds of hydrocarbon and oxygenated fuels. *Prog. Energy Comb. Sci.*, 38(4):468 501, April 2012. (Cited on page 50.)

[83] K. N. C. Bray, M. Champion, and P. A. Libby. The interaction between turbulence and chemistry in premixed turbulent flames. In R. Borghi and S.N.B. Murthy, editors, *Turbulent Reactive Flows*, volume 40, pages 541 563. Lecture notes in engineering, Springer Verlag, 1989. (Cited on page 50.)

[84] S. B. Pope. Lagrangian PDF methods for turbulent flows. *Ann. Rev. Fluid Mech.* , pages 23 63, 1994. (Cited on page 50.)

[85] D. Veynante and L. Vervisch. Turbulent combustion modeling. *Prog. Energy Comb. Sci.* , 28:193 266, 2002. (Cited on page 50.)

[86] E. Mallard and H. Le Chatelier. Sur la vitesse de propagation de l inflamation dans les mélanges explosifs. *C. R. Acad. Sci. , Paris*, 93:145, 1881. (Cited on page 50.)

[87] E. Mallard and H. Le Chatelier. *Ann. Min.*, 4:274, 1883. (Cited on page 50.)

[88] H. Le Chatelier. *Lecons sur le carbone, la combustion, les lois chimiques*. Hermann, 1907. (Cited on page 50.)

[89] R. V. Wheeler. The inflammation of mixtures of ethane and air in a closed vessel - the effects of turbulence. *J. Chem. Soc.*, 115:81 94, 1919. (Cited on page 50.)

[90] G. I. Sivashinsky. Diffusional-thermal theory of cellular flames. *Combust. Sci. Tech.* , 15:137 146, 1977. (Cited on page 50.)

[91] P. Clavin. Dynamics of combustion fronts in premixed gases: from flames to detonations. *Proc. Combust. Inst.* , 28:569 586, 2000. (Cited on page 50.)

[92] R. A. Strehlow and L. D. Savage. The concept of flame stretch. *Combust. Flame* , 31:209, 1978. (Cited on page 50.)

[93] S. M. Candel and T. Poinsot. Flame stretch and the balance equation for the flame surface area. *Combust. Sci. Tech.* , 70:1 15, 1990. (Cited on pages 50 and 138.)

[94] L. Selle, T. Poinsot, and B. Ferret. Experimental and numerical study of the accuracy of flame-speed measurements for methane/air combustion in a slot burner. *Combust. Flame*, 158(1):146 154, January 2011. (Cited on page 50.)

[95] M. I. Hassan, K. T. Aung, and G. M. Faeth. Measured and predicted properties of laminar premixed methane/air flames at various pressures. *Combust. Flame* , 115(4):539 550, 1998. (Cited on page 50.)

[96] D. R. Dowdy, D. B. Smith, and S. C. Taylor. The use of expanding spherical flames to determine burning velocities and stretch effects in hydrogen/air mixtures. In *23rd Symp. (Int.) on Combustion*, pages 325 332. The Combustion Institute, Pittsburgh, 1990. (Cited on page 50.)

[97] T. Poinsot. Comments on flame stretch interactions of laminar premixed hydrogen air flames at normal temperature and pressure by Aung et al. *Combust. Flame* , 113:279 284, 1998. (Cited on page 50.)

[98] F. Halter, T. Tahtouh, and C. Mounaïm-Rousselle. Nonlinear effects of stretch on the flame front propagation. *Combust. Flame*, 157(10):1825 1832, October 2010. (Cited on pages 50, 51, and 149.)

[99] K. Eisazadeh-Far, A. Moghaddas, J. Al-Mulki, and H. Metghalchi. Laminar burning speeds of ethanol/air/diluent mixtures. *Proc. Combust. Inst.*, 33(1):1021 1027, 2011. (Cited on page 50.)

[100] E. Varea, V. Modica, A. Vandel, and B. Renou. Measurement of laminar burning velocity and Markstein length relative to fresh gases using a new postprocessing procedure: Application to laminar spherical flames for methane, ethanol and isooctane/air mixtures. *Combust. Flame*, 159:577 590, October 2012. (Cited on pages 50 and 149.)

[101] J. Tien and M. Matalon. On the burning velocity of stretched flames. *Combust. Flame*, 84(3-4):238 248, April 1991. (Cited on pages 51 and 149.)

[102] J. K. Bechtold and M Matalon. The dependence of the Markstein length on stoichiometry. *Combust. Flame*, 127(1-2):1906 1913, October 2001. (Cited on pages 51 and 149.)

[103] H. G. Im and J. H. Chen. Effects of flow transients on the burning velocity of laminar hydrogen/air premixed flames. *Proc. Combust. Inst.*, 28:1833 1840, 2000. (Cited on page 51.)

[104] A. P Kelley and C. K. Law. Nonlinear effects in the extraction of laminar flame speeds from expanding spherical flames. *Combust. Flame*, 156(9):1844 1851, September 2009. (Cited on pages 51, 52, 65, and 66.)

[105] Z. Chen. Effects of radiation and compression on propagating spherical flames of methane/air mixtures near the lean flammability limit. *Combust. Flame*, 157(12):2267 2276, December 2010. (Cited on page 51.)

[106] Z. Chen. On the extraction of laminar flame speed and Markstein length from outwardly propagating spherical flames. *Combust. Flame*, 158(2):291 300, February 2011. (Cited on pages 51 and 65.)

[107] D. Bradley and A. Mitcheson. The venting of gaseous explosions in spherical vessels. I - Theory. *Combust. Flame*, 32:221 236, January 1978. (Cited on pages 52 and 55.)

[108] D. Bradley and A. Mitcheson. The venting of gaseous explosions in spherical vessels. II - Theory and experiment. *Combust. Flame*, 32:237 255, January 1978. (Cited on pages 52 and 55.)

[109] A. P. Kelley, J. K. Bechtold, and C. K. Law. Propagation of confined premixed flames. In *7th US National Technical Meeting of the Combustion Institute*, pages 1 24, 2011. (Cited on page 52.)

[110] D. Bradley, P. H. Gaskell, and X. J. Gu. Burning velocities, markstein lengths, and flame quenching for spherical methane-air flames: A computational study. *Combust. Flame*, 104(1-2):176 198, January 1996. (Cited on pages 54, 59, and 151.)

[111] D. Bradley and A. Mitcheson. Mathematical solutions for explosions in spherical vessels. *Combust. Flame*, 26:201 217, February 1976. (Cited on pages 54, 55, 66, and 162.)

[112] P. Schmitt, T. Poinsot, B. Schuermans, and K. P. Geigle. Large-eddy simulation and experimental study of heat transfer, nitric oxide emissions and combustion instability in a swirled turbulent high-pressure burner. *J. Fluid Mech.* , 570:17 46, 2007. (Cited on pages 55 and 70.)

[113] N. Gourdain, L. Gicquel, G. Staffelbach, O. Vermorel, F. Duchaine, J. F. Boussuge, and T. Poinsot. High performance parallel computing of flows in complex geometries: II. Applications. *Computational Science and Discovery*, 2(1):015004, November 2009. (Cited on pages 55 and 70.)

[114] T. Poinsot and S. Lele. Boundary conditions for direct simulations of compressible viscous flows. *J. Comput. Phys.* , 101(1):104 129, 1992. (Cited on pages 57 and 59.)

[115] C. K. Law and P. Cho. Flame curvature and preferential diffusion in the burning intensity of bunsen flames. *21st Symp. (Int.) on Combustion*, pages 1803 1809, 1986. (Cited on page 61.)

[116] P. Clavin and F. A. Williams. Effects of molecular diffusion and of thermal expansion on the structure and dynamics of premixed flames in turbulent. *J. Fluid Mech.*, 116:251 282, 1982. (Cited on page 61.)

[117] S.K. Lele. Compact finite difference schemes with spectral like resolution. *J. Comput. Phys.* , 103:16 42, 1992. (Cited on pages 70 and 106.)

[118] J. Berland, C. Bogey, O. Marsden, and C. Bailly. High-order, low dispersive and low dissipative explicit schemes for multiple-scale and boundary problems. *J. Comput. Phys.*, 224(2):637 662, June 2007. (Cited on pages 70 and 106.)

[119] S. Marié, D. Ricot, and P. Sagaut. Comparison between lattice Boltzmann method and Navier Stokes high order schemes for computational aeroacoustics. *J. Comput. Phys.*, 228(4):1056 1070, March 2009. (Cited on pages 70 and 106.)

[120] P. R. Spalart, R. D. Moser, and M. M. Rogers. Spectral methods for the Navier-Stokes equations with one infinite and two periodic directions. *J. Comput. Phys.*, 96(2):297 324, 1991. (Cited on pages 70 and 106.)

[121] R. D. Moser, P. Moin, and A. Leonard. A spectral numerical method for the Navier-Stokes equations with applications to Taylor-Couette flow. *J. Comput. Phys.*, 52(3):524 544, 1983. (Cited on pages 70 and 106.)

[122] V. Moureau, I. Barton, C. Angelberger, and T. Poinsot. Towards large eddy simulation in internal-combustion engines: simulation of a compressed tumble flow. *SAE*, (2004-01-1995), 2004. (Cited on pages 70 and 106.)

[123] G. Wang, DD Papadogiannis, F. Duchaine, N. Gourdain, and L. Gicquel. Towards Massively Parallel Large Eddy Simulation of Turbine Stages. In *ASME Turbo Expo 2013*, San Antonio, Texas, USA, 2013. (Cited on pages 70, 106, and 108.)

[124] G. Wang, S. Moreau, F. Duchaine, N. Gourdain, and L. Gicquel. Large Eddy Simulations of the MT1 high-pressure turbine using TurboAVBP. In *Proceeding of 21st Annual Conference of the CFD Society of Canada*, Sherbrooke, Quebec, Canada, 2013. (Cited on pages 70, 106, and 108.)

[125] Gaofeng Wang, Florent Duchaine, Dimitrios Papadogiannis, Ignacio Duran, Stéphane Moreau, and Laurent Y.M. Gicquel. An overset grid method for large eddy simulation of turbomachinery stages. *J. Comput. Phys.*, 274:333 355, October 2014. (Cited on pages 70, 106, and 108.)

[126] C. S. Peskin. Flow patterns around heart valves: A numerical method. *J. Comput. Phys.*, 10(2):252 271, 1972. (Cited on page 71.)

[127] R. Ghias, R. Mittal, and H. Dong. A sharp interface immersed boundary method for compressible viscous flows. *J. Comput. Phys.*, 225(1):528 553, July 2007. (Cited on page 71.)

[128] Q. Liu and O. V. Vasilyev. A Brinkman penalization method for compressible flows in complex geometries. *J. Comput. Phys.*, 227(2):946 966, December 2007. (Cited on page 71.)

[129] M. Uhlmann. An immersed boundary method with direct forcing for the simulation of particulate flows. *J. Comput. Phys.*, 209(2):448 476, November 2005. (Cited on page 71.)

[130] P. J. Atzberger, P. R. Kramer, and C. S. Peskin. A stochastic immersed boundary method for fluid-structure dynamics at microscopic length scales. *J. Comput. Phys.*, 224(2):1255 1292, June 2007. (Cited on page 71.)

[131] A. Gilmanov and F. Sotiropoulos. A hybrid cartesian/immersed boundary method for simulating flows with 3D, geometrically complex, moving bodies. *J. Comput. Phys.*, 207(2):457 492, August 2005. (Cited on page 71.)

[132] G. Iaccarino and S. Moreau. Natural and forced conjugate heat transfer in complex geometries on cartesian adapted grids. *J. Fluids Eng.*, 128(4):838, 2006. (Cited on page 71.)

[133] P. K. Smolarkiewicz, R. Sharman, J. Weil, S. G. Perry, D. Heist, and G. Bowker. Building resolving large-eddy simulations and comparison with wind tunnel experiments. *J. Comput. Phys.*, 227(1):633 653, November 2007. (Cited on page 71.)

[134] L. J. Fauci and R. Dillon. Biofluidmechanics of reproduction. *Ann. Rev. Fluid Mech.*, 38(1):371 394, January 2006. (Cited on page 71.)

[135] R. Mittal and G. Iaccarino. Immersed Boundary Methods. *Ann. Rev. Fluid Mech.*, 37(1):239 261, January 2005. (Cited on pages 71 and 106.)

[136] G. Iaccarino and R. Verzicco. Immersed boundary technique for turbulent flow simulations. *Applied Mechanics Reviews*, 56(3):331, 2003. (Cited on page 71.)

[137] D. Goldstein, R. Handler, and L. Sirovich. Modeling a no-slip flow boundary with an external force field. *J. Comput. Phys.*, 105:354 366, 1993. (Cited on pages 71, 73, 74, 103, and 162.)

[138] E. M. Saiki and S. Biringen. Numerical Simulation of a Cylinder in Uniform Flow : Application of a Virtual Boundary Method. *J. Comput. Phys.*, 123:450 465, 1996. (Cited on pages 71, 83, and 92.)

[139] H. Schlichting. *Boundary layer theory*. McGraw-Hill, New York, 1955. (Cited on page 81.)

[140] S. K. Jordan and J. E. Fromm. Oscillatory drag, lift, and torque on a circular cylinder in a uniform flow. *Phys. Fluids*, 15(3):371, 1972. (Cited on pages 83 and 92.)

[141] C. Shu, N. Liu, and Y. T. Chew. A novel immersed boundary velocity correction lattice Boltzmann method and its application to simulate flow past a circular cylinder. *J. Comput. Phys.*, 226(2):1607 1622, October 2007. (Cited on pages 83, 89, and 92.)

[142] Y. Tseng and J. H. Ferziger. A ghost-cell immersed boundary method for flow in complex geometry. *J. Comput. Phys.*, 192(2):593 623, December 2003. (Cited on pages 83, 89, and 92.)

[143] M. Braza, P. Chassaing, and H. H. Minh. Numerical study and physical analysis of the pressure and velocity fields in the near wake of a circular cylinder. *J. Fluid Mech.*, 165:79 130, April 1986. (Cited on pages 83, 89, and 92.)

[144] W. H. Graf and B. Yulistiyanto. Experiments on flow around a cylinder; the velocity and vorticity fields. *J. of Hydraulic Research*, 36(4):637 654, July 1998. (Cited on page 83.)

[145] C. Norberg. An experimental investigation of the flow around a circular cylinder : influence of aspect ratio. *J. Fluid Mech.*, 258:287 316, 1994. (Cited on page 83.)

[146] A. G. Kravchenko and P. Moin. Numerical studies of flow over a circular cylinder at Re=3900. *Phys. Fluids*, 12(2):403, 2000. (Cited on page 83.)

[147] A. Roshko. Experiments on the flow past a circular cylinder at very high Reynolds number. *J. Fluid Mech.*, 10(3):345 356, 1961. (Cited on page 83.)

[148] S. Haeri and J. S. Shrimpton. On the application of immersed boundary, fictitious domain and body-conformal mesh methods to many particle multiphase flows. *Int. J. Multiphase Flow*, 40:38 55, April 2012. (Cited on page 92.)

[149] A. Piacentini, T. Morel, A. Thévenin, and F. Duchaine. Open-palm an open source dynamic parallel coupler. In *IV International Conference on Computational Methods for Coupled Problems in Science and Engineering*, 2011. (Cited on page 106.)

[150] F. Duchaine, S. Jauré, D. Poitou, E. Quémerais, G. Staffelbach, T. Morel, and L. Gicquel. High performance conjugate heat transfer with the OpenPALM coupler. In *V International Conference on Coupled Problems in Science and Engineering - Coupled Problems*, Ibiza, Spain, 2013. (Cited on page 106.)

[151] M. Boileau, F. Duchaine, J.-C. Jouhaud, and Y. Sommerer. Large-Eddy Simulation of heat transfer around a square cylinder using unstructured grids. *AIAA Journal*, 51(2):372 385, February 2013. (Cited on pages 110 and 118.)

[152] H. Boughanem and A. Trouvé. Validation du code de simulation directe NTMIX3D pour le calcul des écoulements turbulents réactifs. Technical Report 42907, Institut Français du Pétrole, 1996. (Cited on page 127.)

[153] H. De Karman and L. Howarth. On the statistical theory of isotropic turbulence. *Proc. R. Soc. Lond. A*, 164(917):192 215, 1938. (Cited on page 127.)

[154] L. W. Kostiuk, K. N. C. Bray, and T. C. Chew. Premixed turbulent combustion in counterflowing streams. *Combust. Sci. Tech.*, 64(4-6), 1987. (Cited on page 128.)

[155] R. G. Abdel-Gayed, D. Bradley, and M. Lawes. Turbulent burning velocities: a general correlation in terms of straining rates. *Proc. R. Soc. Lond. A*, 414(1847):389 413, December 1987. (Cited on page 130.)

[156] J. Lumley. Computational modelling of turbulent flows. *Adv. Appl. Mech.*, 18:123 176, 1978. (Cited on page 130.)

[157] J. A. Simonsen and P. A. Krogstad. Turbulent stress invariant analysis: Clarification of existing terminology. *Phys. Fluids*, 17(8):088103, 2005. (Cited on pages 130 and 131.)

[158] M. J. Dwyer, E. G. Patton, and R. H. Shaw. Turbulent kinetic energy budgets from a large-eddy simulation of airflow above and within a forest canopy. *Boundary-Layer Meteorology*, 84(1):23 43, 1997. (Cited on page 134.)

[159] X. Liu and F. O. Thomas. Measurement of the turbulent kinetic energy budget of a planar wake flow in pressure gradients. *Exp. Fluids*, 37(4):469 482, July 2004. (Cited on page 134.)

[160] A. Sideridis, K. Yakinthos, and A. Goulas. Turbulent kinetic energy balance measurements in the wake of a low-pressure turbine blade. *Int. J. Heat Fluid Flow*, 32(1):212 225, February 2011. (Cited on page 134.)

[161] J. De Jong, L. Cao, S. H. Woodward, J. P. L. C. Salazar, L. R. Collins, and H. Meng. Dissipation rate estimation from PIV in zero-mean isotropic turbulence. *Exp. Fluids*, 46(3):499 515, October 2008. (Cited on page 134.)

[162] S. Richard. *Simulation aux grandes échelles de la combustion dans les moteurs à allumage commandé*. Phd thesis, Ecole Centrale Paris, 2005. (Cited on pages 139 and 149.)

[163] N. Peters. The turbulent burning velocity for large-scale and small-scale turbulence. *J. Fluid Mech.* , 384:107 132, 1999. (Cited on page 141.)

[164] R. Borghi and M. Destriau. *Combustion and Flames, chemical and physical principles*. Editions TECHNIP, 1998. (Cited on pages 141 and 142.)

[165] S. Kwon, L. Tseng, and G. M. Faeth. Laminar burning velocities and transition to unstable flames in H2/O2/N 2 and C3H 8/02/N2 Mixtures. *Combust. Flame*, 246:230 246, 1992. (Cited on page 149.)

[166] C. C. Huang, S. S. Shy, C. C. Liu, and Y. Y. Yan. A transition on minimum ignition energy for lean turbulent methane combustion in flamelet and distributed regimes. *Proc. Combust. Inst.*, 31(1):1401 1409, January 2007. (Cited on page 156.)

[167] V. Sick, M. R. Hartman, V. S. Arpaci, and R. W. Anderson. Turbulent scales in a fan-stirred combustion bomb. *Combust. Flame*, 127:2119 2123, November 2001. (Cited on page 163.)

APPENDIX A

COMBUSTION AND FLAME, VOL. 160, N^O 7 ,PP. 1208-1214 (2013)

Combustion and Flame 160 (2013) 1208–1214

Contents lists available at SciVerse ScienceDirect

Combustion and Flame

journal homepage: www.elsevier.com/locate/combustflame

Curvature and confinement effects for flame speed measurements in laminar spherical and cylindrical flames

Adrien Bonhomme [a,*], Laurent Selle [a,b], Thierry Poinsot [a,b]

[a] Université de Toulouse, INPT, UPS, IMFT (Institut de Mécanique des Fluides de Toulouse), Allée Camille Soula, F-31400 Toulouse, France
[b] CNRS, IMFT, F-31400 Toulouse, France

ARTICLE INFO

Article history:
Received 19 June 2012
Received in revised form 19 December 2012
Accepted 6 February 2013
Available online 30 March 2013

Keywords:
Flame speed
Curvature
Confinement

ABSTRACT

This paper discusses methods used to obtain laminar flame speeds in spherical laminar premixed flames. Most recent studies express the laminar flame consumption speed as $\rho_b/\rho_u\, dR/dt$, where R is the flame radius and ρ_b/ρ_u is the ratio of the burnt to the fresh gas density (ρ_b is evaluated at chemical equilibrium and supposed to be constant). This paper investigates the validity of this assumption by reconsidering it in a more general framework. Other formulae are derived and tested on a DNS of cylindrical flames (methane/air and octane/air). Results show that curvature and confinement effects lead to variations of ρ_b and ρ_u and to significant errors on the flame speed. Another expression (first proposed by Bradley and Mitcheson in 1976) is derived where no density evaluation is required and only pressure and flame radius evolution are used. It is shown to provide more precise results for the consumption speed than $\rho_b/\rho_u\, dR/dt$ because it takes into account curvature and confinement of the flame in the closed bomb.

1. Introduction

The experimental determination of the laminar consumption flame speed, s_L^0, is an overarching problem in combustion [1]. Indeed the knowledge of the rate at which the fresh gases are consumed is instrumental in the study of flame dynamics as well as the development of kinetic schemes. For modeling purposes, the laminar flame speed is the central ingredient of most turbulent-combustion models [2–6].

Despite the apparent simplicity in the formulation of the problem, measuring accurately s_L^0 is a delicate task. Since the early attempts, which date as far back as a hundred and fifty years ago [7–11], a variety of methods have been devised. These methods find their roots in analytical solutions of reacting fluid mechanics but most of them suffer from approximations or experimental difficulties that strongly affect their precision. For example, the flat flame propagating in a tube is strongly perturbed by instabilities or the presence of walls [12,13]. Other techniques require extrapolation or correcting factors in order to account for the effects of curvature or strain [14–17].

In the present paper, we revisit the classical technique of the '*spherical flame in a bomb*' (Fig. 1a): in a closed vessel, a mixture of fresh gases is ignited, a spherical flame develops and its radius, $R(t)$, is measured vs. time using simple optical methods.

Such experiments are fairly easy to conduct. Moreover initial conditions (temperature, pressure, composition, etc.) are well controlled and can be extended to high temperatures and pressures.

However, extracting flame speed values from spherical flames is a much more difficult exercise which has lead to multiple controversies in the past [18–22]. Two quantities can be measured experimentally to construct a flame speed in a bomb: (1) the flame radius evolution $R(t)$ and (2) the bomb pressure $P(t)$. Most existing methods use one of these two quantities (or the two) to deduce flame speeds.[1]

Assuming that $R(t)$ and/or $P(t)$ are available, two independent steps are then required to obtain flame speeds:

- STEP I: the instantaneous flame speed must be obtained from $R(t)$ and/or $P(t)$.
- STEP II: since a spherical flame is a stretched flame, the speed which is measured in STEP I is not the unstretched laminar flame speed s_L^0 but a stretched flame speed $s_L(\kappa)$ where $\kappa = 2/R\, dR/dt$ is the instantaneous flame stretch. Therefore a model for $s_L(\kappa)$ is needed to obtain s_L^0. This model is usually based on a Markstein-type correlation [21,24,25], for example the linear expression:

$$s_L(\kappa) = s_L^0 - \mathcal{L}\kappa \tag{1}$$

* Corresponding author.
E-mail addresses: adrien.bonhomme@imft.fr (A. Bonhomme), laurent.selle@imft.fr (L. Selle), thierry.poinsot@imft.fr (T. Poinsot).

[1] Recent methods using direct flow and front speed measurements have begun in the last two years [23] but they are not discussed here.

0010-2180/$ - see front matter © 2013 The Combustion Institute. Published by Elsevier Inc. All rights reserved.
http://dx.doi.org/10.1016/j.combustflame.2013.02.003

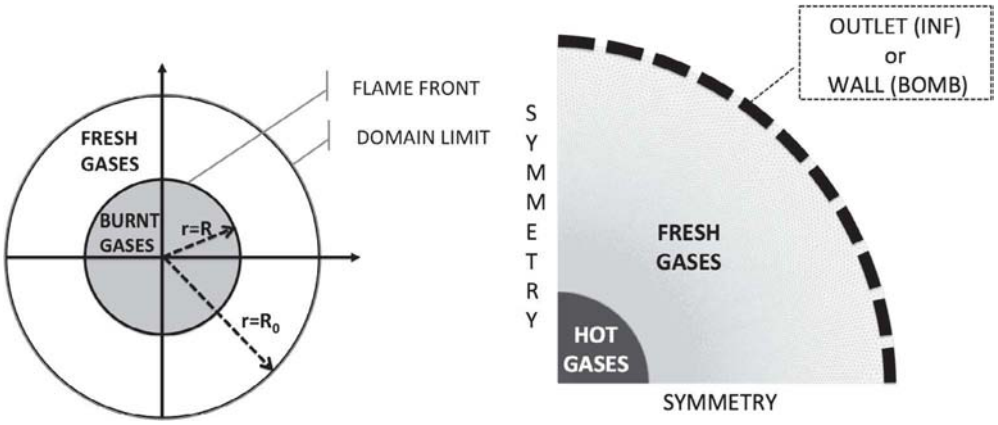

(a) Generic configuration for a spherical flame in a bomb.

(b) Computational domain for the cylindrical flame.

Fig. 1. Configuration for expanding flames.

where $\mathcal{L}$ is the Markstein length which becomes an additional unknown quantity to determine [26]. In the past five years, other expressions have also been proposed to replace Eq. (1) (mostly based on the non-linear form of s_b [27,21]).

This paper does not discuss STEP II and focuses on STEP I. During this step, approximations between the various flame speeds characterizing a front are utilized and the present work shows that they can have a direct impact on the result. Indeed, the only speed which is unambiguously measured in a bomb is the flame speed of the front relative to the burnt gases $s_b(\kappa) = dR/dt$ because the burned gases do not move.

Obtaining a relation between $s_b(\kappa)$ and $s_L(\kappa)$ is a delicate task because it requires well chosen assumptions. A classical, albeit approximate, relation used in multiple recent studies is:

$$s_L(\kappa) = \frac{\rho_b}{\rho_u} s_b(\kappa) \tag{2}$$

where ρ_b is the density of the burnt gases and ρ_u that of the unburnt gases.

In addition to stretch, other factors modify the flame speed in a spherical explosion [27,21,28,29]:

1. In the early stages, the energy of the spark modifies the burnt gases temperature as well as the flame speed.
2. Curvature effects and preferential diffusion (for non-unity Lewis number) also influence the evolution of the flame and the burnt gases temperature. In Eq. (2), most authors recognize that s_b depends on stretch but neglect the influence of stretch on ρ_b. However, the burnt gases density, like the burnt gases temperature, is affected by stretch too. And even if this effect is smaller than the effect of κ on s_L it must be taken into account.
3. For large radii, the confinement of the flame in a closed vessel influences ρ_u and ρ_b and therefore changes the flame speed.

The objective of the present work is to revisit the formulation of Eq. (2) and to propose theoretical expressions for the consumption flame speed that alleviate the problems of Eq. (2). The derivations are presented in Section 2 and Direct Numerical Simulations (DNS) are conducted in Section 3 where the formulae can be compared to the true consumption speed based on the integral of the reaction rate [6] in the case of a cylindrical flame. All derivations are performed in two cases: (1) INF where the flame propagates in an infinite medium, confinement effects do not exist and curvature effects due to non-unity Lewis number can be isolated, and (2) BOMB where the flame propagates in a closed bomb where both curvature and confinement affect the burnt and fresh gases density.

2. Theoretical results

Deriving an expression for flame speeds in a spherical or cylindrical flame (cf. Fig. 1a) is a complex exercise [27,30–32]. It is presented here without invoking an infinitely-thin-flame assumption. The formulae for the consumption flame speed presented in this paper are based on the conservation equation for the species. The definition of the consumption flame speed in a spherical flame is obtained from the integral of the reaction rate $\dot{\omega}_k$ of one specie k (fuel or products for example):

$$s_c = \frac{1}{\rho_u \left(Y_k^b - Y_k^u\right) R^2} \int_0^{R_0} \dot{\omega}_k r^2 dr \tag{3}$$

where ρ_u is the fresh gases density, Y_k^u and Y_k^b are the mass fraction of specie k in the fresh and burnt gases respectively and R_0 is the integration boundary[2] ($R_0 > R$). Since $\dot{\omega}_k$ cannot be measured experimentally, other indirect expressions are required for s_c. They can be derived by starting from the conservation equation of specie k [6]:

$$\frac{\partial \rho Y_k}{\partial t} + \vec{\nabla}(\rho(\mathbf{u} + \mathbf{V_k})Y_k) = \dot{\omega}_k \tag{4}$$

where Y_k is the mass fraction and $\mathbf{V_k}$ is the diffusion velocity of specie k. Integrating Eq. (4) over the control volume ($0 \leqslant r \leqslant R_0$) yields:

$$\frac{dM_k}{dt} + 4\pi R_0^2 \rho_u Y_k(r = R_0)[u_r(r = R_0) + V_{k,r}(r = R_0)] = \int_0^{R_0} \dot{\omega}_k 4\pi r^2 dr \tag{5}$$

where M_k is the total mass of specie k in the domain: $M_k = \int_V \rho Y_k dV$. The second left hand side term represent the flux of specie k leaving the domain at $r = R_0$. Including the definition of the flame speed s_c (Eq. (3)) in Eq. (5) gives:

$$\frac{dM_k}{dt} + 4\pi R_0^2 \rho_u Y_k(r = R_0)[u_r(r = R_0) + V_{k,r}(r = R_0)] = s_c 4\pi R^2 \rho_u \left[Y_k^b - Y_k^u\right] \tag{6}$$

[2] R_0 goes to the infinity for the case of a flame propagating in an infinte medium.

To obtain an explicit relation linking s_c to R, the second left hand side term in Eq. (6) must be canceled. So the optimal choice of the specie k depends on the configuration:

- In a hypothetical infinite medium (INF configuration) $u_r(r = R_0) > 0$. But if a product is used ($Y_p(r = R_0) = 0$), as long as the flame has not reached the position $r = R_0$ the second term on the LHS of Eq. (6) is also canceled.
- In a closed vessel (BOMB configuration) $u_r(r = R_0) = 0$ and $V_{k,r}(r = R_0) = 0$, so that any species can be used in Eq. (6).

At this point in the derivation a consumption speed has been defined but no assumptions were made. The idea is now to link M_k to the flame radius R in order to get an expression for s_c that is accessible to experimental measurements. Two cases are distinguished depending on which species k is used:

1. **A product** ($k = p$): a flame radius R_p based on the mass of products is defined as:

$$R_p^3 = \frac{M_p}{\frac{4\pi}{3}\overline{\rho_b} Y_{p,b}} \tag{7}$$

where $Y_{p,b}$ is the mass fraction of the product (e.g. CO_2) in the burnt gases and $\overline{\rho_b}$ is the burnt gases density (averaged spatially between $r = 0$ and $r = R_p$). Eq. (7) does not imply that the flame is thin: the mass of products M_p is defined unambiguously and R_p is the 'equivalent' radius of a sphere containing this mass. Combining Eqs. (6) and (7) to eliminate M_p yields:

$$s_c^p = \frac{\overline{\rho_b}}{\rho_u}\frac{dR_p}{dt} + \frac{R_p}{3\rho_u}\frac{d\overline{\rho_b}}{dt} \tag{8}$$

where the product mass fraction $Y_{p,b}$ is supposed to be constant. Eq. (8) is derived without assumptions on the domain where the flame propagates: it can be used in a bomb of any size or in an infinite domain [33].
In a simulation Eq. (8) can be used directly because $\overline{\rho_b}$, ρ_u and R_p can be measured. In an experiment, however, assumptions on $\overline{\rho_b}$ and ρ_u are required. The most usual is to suppose that densities are constant (in space and time). Thus, it is generally assumed than ρ_u remains equal to its initial value (neglecting confinement effects, as expected if the bomb is sufficiently large). And $\overline{\rho_b}$ is obtained by assuming that its value does not vary with r from 0 to R_p and is equal to the burnt gases density at equilibrium ρ_b^{eq} so that Eq. (8) leads to:

$$s_c^{p,expe} = \frac{\rho_b^{eq}}{\rho_u(t=0)}\frac{dR_p}{dt} \tag{9}$$

which is the expression used in most studies.[3]

2. **The fuel** ($k = f$): in an infinite domain, fuel cannot be used in Eq. (6) because its flux is not zero at $r = R_0$. However, in a bomb where $\mathbf{u}(r = R_0) = 0$ and $\mathbf{V_k}(r = R_0) = 0$, fuel can be used in Eq. (6) leading to a formulation given by [34]. In this case, the radius of the flame based on the mass of fuel is defined by[4]:

$$R_f^3 = R_0^3 - \frac{M_f}{\frac{4\pi}{3}\rho_u Y_{f,u}} \tag{10}$$

where $Y_{f,u}$ is the mass fraction of the fuel in the unburnt gases, which is constant. Combining Eqs. (6) and (10) yields:

$$s_c^f = \frac{dR_f}{dt} - \frac{R_0^3 - R_f^3}{3R_f^2}\frac{1}{\rho_u}\frac{d\rho_u}{dt} \tag{11}$$

Assuming an isentropic compression for the fresh gases which is a very reasonable approximation here, one has $(1/\rho_u)\, d\rho_u/dt = 1/(\gamma_u P)\, dP/dt$, where γ_u is the ratio of the heat capacities in the fresh gases. Eq. (11) is then recast into:

$$s_c^f = \frac{dR_f}{dt} - \frac{R_0^3 - R_f^3}{3R_f^2}\frac{1}{\gamma_u P}\frac{dP}{dt} \tag{12}$$

Note that Eqs. (9) and (12) are very different: Eq. (12) includes no density ratio in front of dR_f/dt which suggests that the pressure term dP/dt is important. Both expressions use a flame radius which is defined differently. For Eq. (9), the flame radius R_p is defined from the mass of products while for Eq. (12), the flame radius R_f is obtained from the mass of fuel. In practice, experimentally, the flame fronts are thin and it is probably impossible to distinguish R_p and R_f which are both equal to the observed flame radius R. In other words, an infinite thin flame assumption is implicitly done when post processing experiments. Eq. (12) can be used in bombs but not in an infinite medium. It has been previously derived [31,30,34] but it does not seem to be used, even though it is directly accessible in an experiment because it requires only R_f and P vs. time as input data. It will be shown in Section 3.4 using DNS that Eq. (12) is insensitive to curvature and confinement effects, unlike Eq. (9).

3. Validation with numerical simulations

All flame speed expressions derived in Section 2 are summarized in Table 1. To check their accuracy, Eqs. (8), (9) and (12) are compared here in a simulation of cylindrical flames with the true consumption flame speed s_c defined by Eq. (3).

Direct Numerical Simulations of cylindrical flames are performed using the AVBP code [35]. AVBP is an unsteady compressible Navier–Stokes solver. The present simulations are performed with a third-order (in space and time) scheme called TTGC [36]. In order to address both confinement and Lewis number effects, two simulations with different fuels in air are conducted: a lean methane/air ($Le_{CH_4} = 0.996,\ \Phi = 0.8$) flame and a lean octane/air flame ($Le_{C_8H_{18}} = 2.78,\ \Phi = 0.8$). The Lewis number is defined by $Le_k = D_{th}/D_k$, where $D_{th} = \lambda/(\rho c_p)$ is the heat diffusivity coefficient and D_k is the diffusion coefficient of specie k in the mixture. Moreover two geometrical cases are also compared (configuration INF and BOMB).

3.1. Kinetic schemes

Reduced two-step mechanisms are used for this work:

1. For methane a scheme [37] called 2S_CH4_CM2 is employed.

$$CH_4 + \frac{3}{2}\ O_2 \rightarrow CO + 2\ H_2O \tag{13}$$

$$CO + \frac{1}{2}\ O_2 \leftrightarrow CO_2 \tag{14}$$

2. For octane, a scheme called 2S_C8H18_AB was developed following the same methodology.

$$C_8H_{18} + \frac{17}{2}\ O_2 \rightarrow 8\ CO + 9\ H_2O \tag{15}$$

$$CO + \frac{1}{2}\ O_2 \leftrightarrow CO_2 \tag{16}$$

[3] Note that an intermediate formulation could be $s_c^{p,expe,2} = \overline{\rho_b}/\rho_u dR_p/dt$ if a good approximation can be found for $\overline{\rho_b}$. We tested this solution but it shows that in Eq. (8) a good evaluation of both $\overline{\rho_b}$ and $d\overline{\rho_b}/dt$ is important. In practice, even if this solution had worked in the DNS where we can have access to ρ_b, it would have been difficult to use in an experiment since ρ_b is hardly measurable. $s_c^{p,expe,2}$ is not discuss anymore in this work.

[4] The present derivation is valid for lean flames and is based on the fuel balance. For rich flames, a similar derivation based on oxygen leads exactly to the same expression.

Table 1
Consumption flame speed expressions in laminar deflagrations. R_0 is the radius of the spherical bomb. R, R_p and R_f are evaluations of the flame radius. ρ_b^{eq} is the burnt gases density at equilibrium.

Symbol	Name	Expression	Validity
s_c	True consumption speed	$s_c = \frac{1}{\rho_u (Y_k^b - Y_k^u) R^2} \int_0^{R_0} \dot{\omega}_k r^2 dr$	Definition
s_c^p	Speed based on conservation of burnt gases	$s_c^p = \frac{\overline{\rho_b}}{\rho_u}\frac{dR_p}{dt} + \frac{R_p}{3\rho_u}\frac{d\overline{\rho_b}}{dt}$	Bombs or infinite medium
$s_c^{p,expe}$	Speed based on conservation of burnt gases & constant densities assumption	$s_c^{p,expe} = \frac{\rho_b^{eq}}{\rho_u(t=0)}\frac{dR_p}{dt}$	Bombs of very large size or infinite medium
s_c^f	Speed based on fuel conservation	$s_c^f = \frac{dR_f}{dt} - \frac{R_0^3 - R_f^3}{3R_f^2}\frac{1}{\gamma_u P}\frac{dP}{dt}$	Bombs only (of any size)

Both schemes account for the oxidation of the fuel through an irreversible reaction at a rate q_1 while a second reaction accounts for the equilibrium between CO and CO_2 with a rate q_2:

$$q_1 = A_1 \left(\frac{\rho Y_F}{W_F}\right)^{n_1^F} \left(\frac{\rho Y_{O_2}}{W_{O_2}}\right)^{n_1^{O_2}} exp\left(\frac{E_{a,1}}{RT}\right) \tag{17}$$

$$q_2 = A_2 \left[\left(\frac{\rho Y_{CO}}{W_{CO}}\right)^{n_2^{CO}} \left(\frac{\rho Y_{O_2}}{W_{O_2}}\right)^{n_2^{O_2}} - \frac{1}{K_e}\left(\frac{\rho Y_{CO_2}}{W_{CO_2}}\right)^{n_2^{CO_2}}\right] exp\left(\frac{E_{a2}}{RT}\right) \tag{18}$$

where K_e is the equilibrium constant for the CO/CO_2 equilibrium and R the perfect-gas constant. The coefficients for the two schemes are recalled in Table 2.

While the reduced scheme for methane has already been validated [37], the validation of the 2S_C8H18_AB scheme for octane vs. a detailed scheme [38] is presented in Fig. 2.

For a one-dimensional planar flame at $P_0 = 101{,}325$ Pa and $T_0 = 323$ K, the reduced scheme reproduces accurately the laminar flame speed and burnt gases adiabatic temperature, for equivalence ratios up $\Phi = 1.2$.

3.2. Numerical set-up

The definition of the consumption speed, given in Eq. (3), cannot be measured in an experiment but it can easily be computed from a DNS: this is how the formulae proposed in this paper (Eqs. (8) and (12)) as well as the approximation of Eq. (9) are validated. A cylindrical flame propagating in a domain of size $R_0 = 10$ cm is considered (Fig. 1b). When non-reflecting boundary conditions [39] are used at $r = R_0$, the configuration mimics an infinite medium where pressure is constant (INF configuration). If a wall is setup at $r = R_0$, the configuration corresponds to a closed vessel (BOMB configuration). Table 3 summarizes these two configurations.

Using symmetry boundary conditions, only a quarter of the bomb is meshed. The grid is refined within a radius $r < 30$ mm from the center with a cell size $\Delta = 25$ μm to ensure that the flame front is fully resolved: 17–20 points in the thermal flame thickness, defined by $\delta_l^0 = (T_b - T_u)/\max dT/dr$ ($\delta_l^0 = 0.43$ mm for octane and 0.51 mm for methane). The thermodynamic conditions for all simulations presented in this paper are $\Phi = 0.8$, $P_0 = 101{,}325$ Pa and $T_0 = 323$ K. As suggested by Bradley [33], the time interval used for plots corresponds to phases where the flame has grown enough ($R > 5.5$ mm) to have forgotten initial conditions but is still small enough compared to the size of the bomb ($R < 26.5$ mm) to avoid wall effects and remain perfectly spherical. The flame is initialized by introducing a sphere of burnt gases of radius 1 mm, at temperature, density and species mass fractions corresponding to the equilibrium conditions. This avoids to considers the details of the ignition phase and corresponds to the assumptions required for Eq. (9).

Table 2
Coefficients for the reduced kinetic schemes. Activation energies are in [cal mol^{-1}] and pre-exponential constants in [cgs] units

q_1	A_1	$E_{a,1}$	n_1^F	$n_1^{O_2}$	
methane	2.00×10^{15}	35,000	0.9	1.1	
octane	6.05×10^{11}	41,500	0.55	0.9	
q_2	A_2	$E_{a,2}$	n_2^{CO}	$n_2^{O_2}$	$n_2^{CO_2}$
methane	2.00×10^{9}	12,000	1.0	0.5	1.0
octane	4.50×10^{10}	20,000	1.0	0.5	1.0

3.3. Curvature effects only: cylindrical flame in an infinite medium

First, numerical simulations are performed in an idealized case (INF configuration) where there is no compression to study the impact of the curvature effects only. This is achieved by using a non-reflecting outlet boundary condition (cf. Fig. 1b) at $r = R_0$. Thus, pressure, fresh-gases temperature and density remain constant. In this configuration, there is a flux of fresh gases through the boundary $r = R_0$ so that Eq. (8), based on the conservation of the product species is used. Eq. (12) cannot be used in the INF configuration.

Consequently, Fig. 3 presents the comparison of Eqs. (8) and (9) with the true consumption flame speed s_c (Eq. (3)) for both fuels.

Eq. (8) matches the true consumption speed for both fuels. Moreover all curves extrapolate to s_L^0 at $\kappa = 0$. Interestingly, Eq. (9) shows a different behavior for the two fuels: while for methane it matches the true consumption speed, except in the very early times, for octane, there is a clear gap between the two curves. In other words, Eq. (9) does not predict the correct stretched flame speed for the octane/air flame. This phenomenon is due to a Lewis number effect. When the flame is stretched, the burnt gases temperature is not equal to the adiabatic burnt gases temperature T_{ad}. Figure 4 displays various temperature profiles vs. radius r when the octane/air flame propagates. Shortly after the ignition, the maximum temperature drops from the equilibrium $T_{ad} = 2051$ - K to about 1840 K. When the flame propagates, the temperature goes up again and comes back to T_{ad} at the end of the simulation.

These changes are due to stretch: like the flame speed, the adiabatic flame temperature is influenced by stretch and this effect has been analyzed in the literature [40,41]. The relation between the burnt gases temperature T_b and stretch κ is:

$$\frac{T_b - T_{ad}}{T_{ad}} = \left(\frac{1}{Le} - 1\right)\frac{D}{s_L^{0^2}}\kappa \tag{19}$$

where Le is the Lewis number of the limiting reactant and D a characteristic diffusivity. For the methane/air flame since $Le_{CH4} = 0.996$, T_b is almost insensitive to stretch so that $\overline{\rho_b}$ is close to its equilibrium value and Eq. (9) is close to the true flame speed (Fig. 3b). On the other hand, for octane ($Le_{C8H18} = 2.78$), $T_b < T_{ad}$ so that $\overline{\rho_b} > \rho_b^{ad}$ leading to an underestimation of $s_c(\kappa)$ in Fig. 3a by 2–3%. To compare Eq. (19) and simulations, a temperature that represents

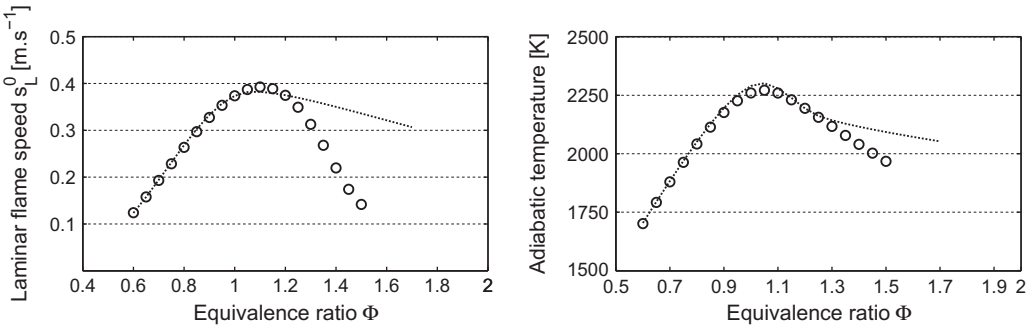

(a) Laminar flame speed. (b) Adiabatic temperature.

Fig. 2. Validation of the reduced scheme for octane/air flames at P_0 = 101,325 Pa and T_0 = 323 K. ○ Jerzembeck et al. [38], ……, 2S_C8H18_AB.

Table 3
Details on INF and BOMB configurations.

Case	Boundary conditions at $r = R_0$	Expression
INF	Non-reflecting	Infinite medium, constant pressure
BOMB	$\mathbf{u} = 0$	bomb of radius R_0, pressure goes up

fairly the burnt gases temperature for a given stretch must be defined. The maximum of temperature T_b^{max} seems to be reasonable here, as presented by Fig. 5. In this paper, the characteristic diffusivity D used is the fuel molecular diffusivity in the fresh gases D_f^u.

Figure 6 presents the comparison of Eq. (19) and results obtained in methane and octane air flame simulations.

A good agreement between theory and simulation is found: it confirms that the burnt gases temperature (and therefore the burnt gases density in Eq. (9)) are not constant and change with stretch if the Lewis number is not equal to unity. Figure 6 shows that for methane, Lewis effects are neglectible but not for octane. This explains why in Fig. 3, $s_c^{p,expe}$ matches the true consumption flame speed s_c for the methane but not for the octane.

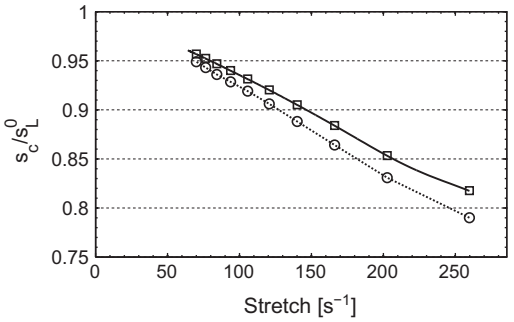

(a) Octane.

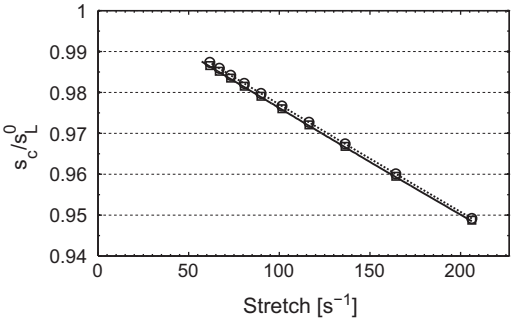

(b) Methane.

Fig. 3. Normalized consumption speed vs. stretch for a configuration without compression (INF) with $s_L^{0,CH4} = 0.255$ m/s and $s_L^{0,C8H18} = 0.264$ m/s: — s_c (Eq. (3)); -⊖- $s_c^{p,expe}$ (Eq. (9)); □ s_c^p (Eq. (8)).

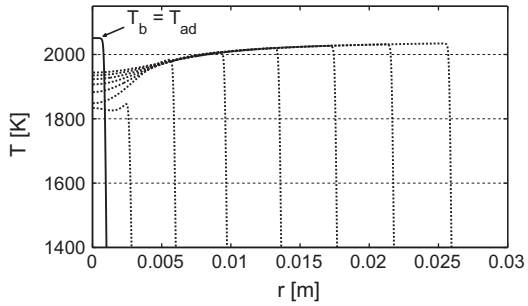

Fig. 4. Temperature profiles vs. the flame radius R when the octane/air flame propagates. — Initial solution ($T_b = T_{ad}$); ---- Temporal evolution: time varies from $t = 0$ to $t = 17.5$ ms by step of 2.5 ms.

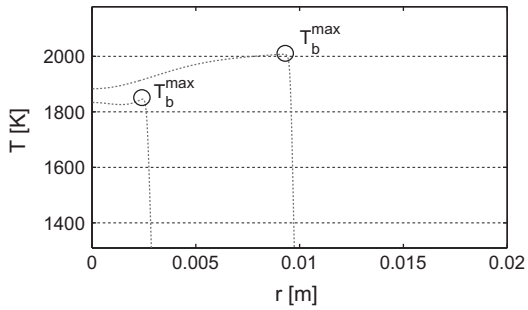

Fig. 5. Definition of T_b^{max} with the temperature profiles vs. the flame radius r.

3.4. Combined curvature and confinement effects: cylindrical flame in a closed bomb

Figure 7 shows the evolution of the various expressions for the consumption speed,[5] normalized by the unstretched laminar flame speed s_L^0, vs. stretch. Using Eq. (9) (open circles) one recovers the classical shape for the flame speed: fairly linear at high stretch (small radii) but bent downward for lower stretch (large radii). However, the true consumption speed based on the integral of the fuel

[5] Eqs. (8) and (12) are derived for a spherical flame but it is straightforward to modify them for a cylindrical flame. In this case Eq. (8) becomes $s_c^p = \frac{\overline{\rho_b}}{\rho_u}\frac{dR_p}{dt} + \frac{R_p}{2\overline{\rho_u}}\frac{d\overline{\rho_b}}{dt}$ and Eq. (12) becomes $s_c^f = \frac{dR_f}{dt} - \frac{R_0^2 - R_f^2}{2R_f}\frac{1}{\gamma_u P}\frac{dP}{dt}$.

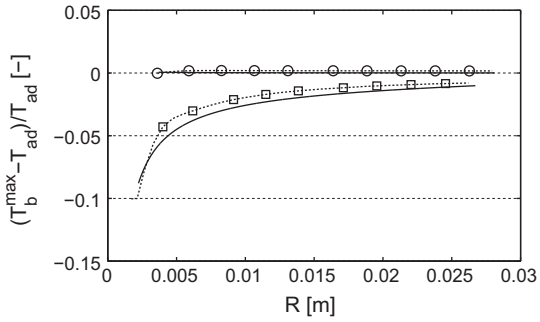

Fig. 6. Normalized burnt gases temperature $(T_b^{max} - T_{ad})/T_{ad}$ vs. the flame radius R. -□- C8H18; -○- CH4; — Theoretical expression of Clavin and Williams (Eq. (19)).

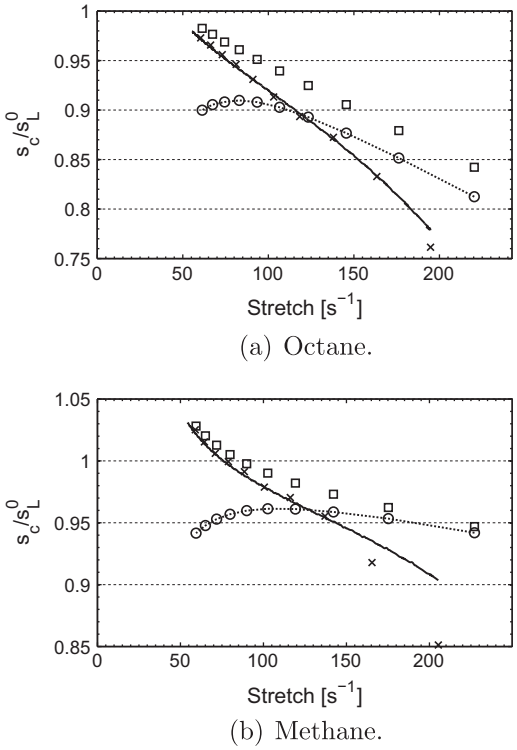

Fig. 7. Normalized consumption speed vs. stretch in a closed bomb (BOMB) with $s_L^{0,CH4} = 0.255$ m/s and $s_L^{0,C8H18} = 0.264$ m/s: — s_c (Eq. (3)); -○- $s_c^{p,expe}$ (Eq. (9)); □ s_c^p (Eq. (8)); ×s_c^f (Eq. (12)).

consumption rate (Eq. (3), solid line in Fig. 7) does not show a reduction as the flame grows. In the present configuration, for $\kappa < 150\ s^{-1}$, the departure between Eqs. (3) and (9) is significant (≃8% at low stretch).

The reason why Eq. (9) is not right here is that Eq. (9) uses the approximation $\overline{\rho_b} = \rho_{ad}$. Figure 8 displays the time variation of $\overline{\rho_b}$ is the BOMB case for octane and methane. As expected:

- for methane, at small times, curvature effects have no influence on $\overline{\rho_b}$. At later times, curvature effects decrease but confinement effects appear: pressure goes up and so does $\overline{\rho_b}$, an effect which is ignored by Eq. (9).
- for octane flames the situation is not better: curvature effects lead to an increase of $\overline{\rho_b}$ at small times and confinement effects only make it worse at later times.

The standard procedure with such data is to extrapolate the linear portion of the curve towards $\kappa = 0$. As illustrated in [27] (their

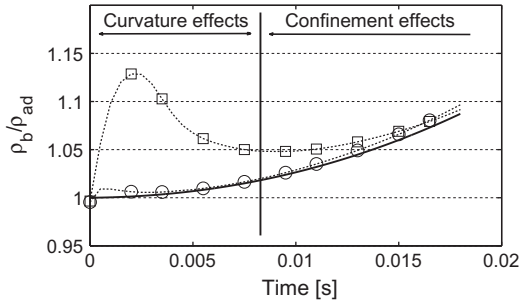

Fig. 8. Normalized burnt gases density $\overline{\rho_b}/\rho_{ad}$ vs. time. -□- C8H18; -○- CH4; — isentropic compression $(P/\overline{\rho_b}^{\gamma_b} = \text{cste})$.

Fig. 5), the length of this linear portion is greatly influenced by the size of the apparatus, i.e. by confinement. This sensitivity affects the precision of the extrapolation procedure, as shown in [29] using both linear and non-linear methods. However, the consumption speed s_c^p (Eq. (8), open squares in Fig. 7) does not match exactly the true consumption flame speed s_c (Eq. (3)) at large stretch. This can be explained by the difference between R_f and R_p, especially when the flame is very small. Indeed, replacing R_p by R_f in Eq. (8) leads to a better result. In practice, s_c^p is not used in an experiment because $d\rho_b/dt$ is not easily accessible. Conversely, the consumption speed s_c^f based on the conservation of the fuel (Eq. (12)) is easy to measure and is unaffected by the confinement as shown in Fig. 7. This expression matches perfectly the true consumption flame speed s_c.

For methane, in the early development of the flame $\kappa > 150\ s^{-1}$, s_c^f does not seem to match well the true consumption speed because the pressure increase is very small initially. At later times (the region in which we are interested and where stretch is smaller) the accuracy of Eq. (12) is very good.

Note that the simulations of Sections 3.3 and 3.4 were conducted in a 2D configuration. In a cylindrical flame, the pressure increase is much stronger than for a spherical flame so that confinement effects are overestimated in the present simulations. The first consequence is that for a spherical bomb with the same radius R_0, the diminution of s_L at low stretch would be less pronounced. Nevertheless, even with an exaggerated pressure increase, Eq. (12) is more precise than the classical formulae, which can only improve the accuracy of the extrapolation method. The second consequence is that even at moderate flame radii, the pressure and temperature increase in the fresh gases changes the flame speed. This is particularly striking for the methane flame in Fig. 7b as the normalized consumption flame speed exceeds unity at $\kappa < 70\ s^{-1}$ because the fresh gases are not in the nominal conditions any more. This peculiarity of the cylindrical flame does not affect the conclusion about the precision of Eq. (12) vs. Eq. (9).

4. Conclusion

This study addresses the issue of post-processing flame radii, obtained from spherical flames in bombs, to deduce laminar flame speeds and Markstein lengths. These experiments raise difficult questions [27]: when the flame is too small, it is influenced by curvature and non-unity Lewis number effects; when it is too large, it is affected by the confinement effect of the bomb. In the present work, the limitations of the classical formula used experimentally to construct flame speeds from flame radius measurements ($s_L = \rho_b/\rho_u\ dR/dt$) are discussed.

Two expressions for the consumption speed were derived from the conservation equation of the species, without the assumption of an infinitely-thin flame front. The first one (Eq. (8)) is the generalization of the classical formula that accounts for the temporal

evolution of the density in the fresh and burnt gases. Because this formula requires the mean burnt gases density as an input, a quantity which cannot be measured in experiments, another expression (Eq. (12)) using only the flame radius and the pressure inside the bomb (two quantities which are directly measured) is presented (existing in the literature [34] but seldom used).

A cylindrical flame computed with DNS was used to evaluate the precision of these two expressions for the consumption flame speed. In a configuration where confinement effects do not exist (propagation in an infinite medium where pressure is rigorously constant), Eq. (9) incorrectly predicts the flame speeds for non-unity Lewis number (octane) but performs correctly for methane because Lewis number is close to unity in this case. In a second configuration, corresponding to a bomb, results show that Eq. (9) incorrectly predicts flame speeds for both octane and methane/air flames because the burnt gases density increases with pressure (in addition to curvature effects for octane) while Eq. (12) captures the correct consumption speed. Since Eq. (12) only requires the knowledge of $R(t)$ and $P(t)$, it is simple to use experimentally and the present work suggests that it is a good candidate for a more precise determination of the flame speeds. The main difficulty of this method should be the measurement and treatment of the pressure signal because the pressure increase in a large bomb may be difficult to measure accurately and to post process to obtain the pressure derivative required in Eq. (12).

References

[1] E. Ranzi, A. Frassoldati, R. Grana, A. Cuoci, T. Faravelli, A. Kelley, C. Law, Prog. Energy Combust. Sci. 38 (4) (2012) 468–501.
[2] K.N.C. Bray, M. Champion, P.A. Libby, in: R. Borghi, S. Murthy (Eds.), Turbulent Reactive Flows, Lecture Notes in Engineering, vol. 40, Springer Verlag, 1989, pp. 541–563.
[3] S.B. Pope, Ann. Rev. Fluid Mech. (1994) 23–63.
[4] N. Peters, Turbulent Combustion, Cambridge University Press, 2001.
[5] D. Veynante, L. Vervisch, Prog. Energy Combust. Sci. 28 (2002) 193–266.
[6] T. Poinsot, D. Veynante, Theoretical and Numerical Combustion, third ed., 2011. <www.cerfacs.fr/elearning>.
[7] E. Mallard, H. Le Chatelier, Astron. Astrophys., Paris 93 (1881) 145.
[8] E. Mallard, H. Le Chatelier, Ann. Min. 4 (1883) 274.
[9] H. Le Chatelier, Lecons sur le carbone, la combustion, les lois chimiques, Hermann, 1907.
[10] R.V. Wheeler, J. Chem. Soc. 115 (1919) 81–94.
[11] P. Laffitte, La propagation des flammes dans les mélanges gazeux, Hermann et Cie, Actualités scientifiques et industrielles, Paris, 1939.
[12] G.I. Sivashinsky, Combust. Sci. Tech. 15 (1977) 137–146.
[13] P. Clavin, Proc. Combust. Inst. 28 (2000) 569–586.
[14] R.A. Strehlow, L.D. Savage, Combust. Flame 31 (1978) 209.
[15] S.M. Candel, T. Poinsot, Combust. Sci. Technol. 70 (1990) 1–15.
[16] F.A. Williams, Combustion Theory, Benjamin, Cummings, Menlo Park, CA, 1985.
[17] L. Selle, T. Poinsot, B. Ferret, Combust. Flame 158 (1) (2011) 146–154.
[18] M.I. Hassan, K.T. Aung, G.M. Faeth, Combust. Flame 115 (4) (1998) 539–550.
[19] D.R. Dowdy, D.B. Smith, S.C. Taylor, in: 23rd Symp. (Int.) Combust., The Combustion Institute., Pittsburgh, 1990, pp. 325–332.
[20] T. Poinsot, Combust. Flame 113 (1998) 279–284.
[21] F. Halter, T. Tahtouh, C. Mounaïm-Rousselle, Combust. Flame 157 (10) (2010) 1825–1832.
[22] K. Eisazadeh-Far, A. Moghaddas, J. Al-Mulki, H. Metghalchi, Proc. Combust. Inst. 33 (1) (2011) 1021–1027.
[23] E. Varea, V. Modica, A. Vandel, B. Renou, Combustion and Flame. 159 (2012) 577–590.
[24] J. Tien, M. Matalon, Combust. Flame 84 (3–4) (1991) 238–248.
[25] J.K. Bechtold, M. Matalon, Combust. Flame 127 (1–2) (2001) 1906–1913.
[26] H.G. Im, J.H. Chen, Int. Symp. Combust. 28 (2000) 1833–1840.
[27] A. Kelley, C. Law, Combust. Flame 156 (9) (2009) 1844–1851.
[28] Z. Chen, Combust. Flame 157 (12) (2010) 2267–2276.
[29] Z. Chen, Combust. Flame 158 (2) (2011) 291–300.
[30] D. Bradley, A. Mitcheson, Combust. Flame 32 (1978) 221–236.
[31] D. Bradley, A. Mitcheson, Combust. Flame 32 (1978) 237–255.
[32] A.P. Kelley, J.K. Bechtold, C.K. Law, in: 7th US National Technical Meeting of the Combustion Institute, 2011, pp. 1–24.
[33] D. Bradley, P.H. Gaskell, X.J. Gu, Combust. Flame 104 (1–2) (1996) 176–198.
[34] D. Bradley, A. Mitcheson, Combust. Flame 26 (1976) 201–217.
[35] N. Gourdain, L. Gicquel, G. Staffelbach, O. Vermorel, F. Duchaine, J.-F. Boussuge, T. Poinsot, Comput. Sci. Discovery 2 (1) (2009) 015004.
[36] O. Colin, M. Rudgyard, J. Comput. Phys. 162 (2) (2000) 338–371.
[37] L. Selle, G. Lartigue, T. Poinsot, R. Koch, K.-U. Schildmacher, W. Krebs, B. Prade, P. Kaufmann, D. Veynante, Combust. Flame 137 (4) (2004) 489–505.
[38] S. Jerzembeck, N. Peters, P. Pepiot-Desjardins, H. Pitsch, Combust. Flame 156 (2) (2009) 292–301.
[39] T. Poinsot, S. Lele, J. Comput. Phys. 101 (1) (1992) 104–129.
[40] C.K. Law, P. Cho, Int. Symp. Combust. (1986) 1803–1809.
[41] P. Clavin, F. Williams, J. Fluid Mech. 116 (1982) 251–282.

APPENDIX B

COMPUTERS AND FLUIDS, VOL. 101, PP. 183-193 (2014)

Computers & Fluids 101 (2014) 183–193

Contents lists available at ScienceDirect

Computers & Fluids

journal homepage: www.elsevier.com/locate/compfluid

A parallel multidomain strategy to compute turbulent flows in fan-stirred closed vessels

A. Bonhomme [a,*], F. Duchaine [c], G. Wang [d,1], L. Selle [a,b], T. Poinsot [a,b]

[a] Université de Toulouse, INPT, UPS, IMFT (Institut de Mécanique des Fluides de Toulouse), Allée Camille Soula, F-31400 Toulouse, France
[b] CNRS, IMFT, F-31400 Toulouse, France
[c] CERFACS, GlobC Team, 42 Avenue Gaspard Coriolis, 31057 Toulouse Cedex 01, France
[d] CERFACS, CFD Team, 42 Avenue Gaspard Coriolis, 31057 Toulouse Cedex 01, France

ARTICLE INFO

Article history:
Received 30 December 2013
Received in revised form 15 May 2014
Accepted 6 June 2014
Available online 20 June 2014

Keywords:
Code coupling
Fan-stirred vessel
Homogeneous isotropic turbulence
Turbulent flame speed

ABSTRACT

This paper presents a parallel multidomain strategy to compute the turbulent flow in a closed vessel stirred by six fans. The method is based on running multiple instances of the same solver, working on different subdomains and communicating through small overlapping zones where interpolations allow to handle moving meshes. First the accuracy of this Multi Instances Solver Coupled on Overlapping Grids (MISCOG) approach is evaluated for the convection of a single vortex. Load balancing issues on parallel machines are discussed and a performance model is proposed to allocate cores to each code instance. Then, the method is applied to the LES of a closed vessel stirred by six fans. Mean and fluctuating fields obtained by the LES are compared to experimental data. Finally, the structure of the turbulence generated at the center of the vessel is studied and the mechanisms allowing turbulence to travel from the fans to the center of the vessel are analyzed.

1. Introduction

Turbulence has been studied for decades in its most canonical form: homogeneous isotropic turbulence (HIT) [1–7]. This limit case is the cornerstone of multiple theoretical approaches as well as the building brick of Large Eddy Simulation (LES) models where the Kolmogorov cascade assumption allows to model the effects of small scales from information available for the resolved ones [8,9]. HIT is also the only generic case where the interaction of other phenomena with turbulence can be defined using a limited number of parameters: evolution of large droplets in HIT [10–12], interaction of evaporating droplets with HIT [13], flame/turbulence interaction [14–16].

While defining HIT theoretically or numerically is a reasonably simple and clear task, creating HIT experimentally is more challenging. This paper focuses on one classical technique used to generate HIT: fan-stirred closed vessels. Sometimes these apparatus are called 'bombs', a denomination that will be used in this paper. Stirring vessels with fans to study turbulent flame propagation has been used for more than a century (see Laffitte's book [17]). A classical paper where this turbulence was qualified as HIT is due to Semenov [18] who showed that properly designed bombs with multiple fans were able to generate reasonable HIT in a zone located near the center of the chamber where the mean flow is almost zero and turbulence is homogeneous and isotropic. A significant amount of work has been based on correlations obtained in such bombs. The most famous example is probably the quest for 'turbulent flame speed' correlations in which the speed s_T of premixed turbulent flames is expressed as a function of the initial turbulent velocity u'. Such correlations continue to be frequently published [19–23] and interestingly, few of them agree. One reason for this may be that the notion of a generic turbulent flame speed depending only on a limited number of flow and flame parameters may not be relevant [14]. Another one could be that the initial turbulence in such bombs is not really close to HIT and that more parameters should be taken into account. Therefore, since most models are based on measurements performed in bombs, an interesting question is to study whether the flow created in a fan-stirred bomb really mimics HIT and over which spatial extent. This question has been investigated experimentally [18,24,25] but using CFD would be a useful addition.

Even though the largest CFD simulations to date have been published for HIT with meshes up to 64 billion points [26], all of them were performed in simple cubic meshes, initialized with a flow which has all the properties of theoretical HIT. None of these

* Corresponding author. Tel.: +33 0534322893.
E-mail addresses: adrien.bonhomme@imft.fr (A. Bonhomme), laurent.selle@imft.fr (L. Selle), thierry.poinsot@imft.fr (T. Poinsot).
[1] Now at Sherbrooke University.

http://dx.doi.org/10.1016/j.compfluid.2014.06.010
0045-7930/

simulations address the question of how HIT is created (if it is) in a real fan-stirred bomb. This question is much more complicated and existing experimental diagnostics are not always sufficient to guaranty that the flow in this situation matches all properties of theoretical HIT: in a bomb, fans obviously induce a strong mean, pulsated flow. In the center of the vessel, the mean flow is expected to be zero and turbulence assumed to diffuse to a central zone where HIT is expected. This involves a series of questions which are rarely addressed:

- By which mechanisms does turbulence transfer from the fan region to the central zone?
- Since the number of fans is usually limited, are there preferential straining axes in the bomb which could affect isotropy near its center?
- The fans flow being by nature unsteady, is turbulence at the center of the apparatus sensitive to the pulsating nature of the flow created by the blades rotation?
- How large is the zone where HIT is obtained?

The objective of this paper is to show how the turbulent flow in a fan-stirred vessel can be studied using high-resolution LES to complement experimental diagnostics. To reach this objective, the simulation code must satisfy three criteria:

- Considering the complexity of the objects to mesh, the need to correctly capture the blade geometry and the necessity to handle moving objects, unstructured meshes are required so that classical DNS codes used for HIT (spectral methods [27,28], high-order compact schemes [29–31]) cannot be used.
- The configuration includes a large number of moving objects (the fans) close to each other. Classical techniques such as ALE (Arbitrary Lagrangian Eulerian) [32–34] are difficult to implement for a flow with multiple fans because of meshing issues. Immersed Boundary methods [35–37] are easier to develop for moving objects but are usually associated to a low order of accuracy which is not acceptable in a LES framework. Here, a new multidomain high-order LES technique with mesh overlapping developed by Wang et al. [38,39] is used on a real configuration.
- To resolve turbulent structures accurately, a high-fidelity explicit (in time) LES solver is needed and the corresponding CPU cost is expected to be large so that the implementation of the multidomain method must be fully parallel.

This paper is organized as follows: first, the numerical methodology is described in Section 2. It is based on the simultaneous execution of multiple instances of the same solver, called MISCOG for Multi Instances Solver Coupled on Overlapping Grids. These instances are coupled on parallel computers using the OpenPalm coupler [40,41]. This coupler is well suited for this task, however, one limitation is that only two instances can exchange at the same time so that the balancing strategy becomes much more complex than it was for a single instance, which is also discussed in Section 2.

A validation test case of the MISCOG approach is presented in Section 3. It consists in propagating a single vortex across two overlapping computational domains. It is thought as an elementary validation of the ability to convect turbulent structures. The method is then applied to a fan-stirred bomb experiment developed in Orléans [42], where 7 instances are required to compute the bomb and the six fans. Section 4 describes this configuration, the numerical set-up and the parallel efficiency of the global simulation.

Flow results are discussed in Section 5: quantities that can be obtained both from LES and PIV are first compared (mean flow fields and RMS values for all three velocity components). LES results are used to analyze quantities which cannot be obtained experimentally such as the velocity tensor – to identify the structure of the turbulence – or the budget of turbulent kinetic energy in order to understand how turbulence reaches the center of the vessel.

2. Numerical methodology

The filtered LES unsteady compressible Navier–Stokes equations that describe the spatially filtered mass, momentum and energy conservation are solved by the unstructured compressible LES solver, AVBP [43]. These equations can be written in the conservative form:

$$\frac{\partial \mathbf{W}}{\partial t} + \vec{\nabla} \cdot \vec{\mathbf{F}} = 0 \tag{1}$$

where $\mathbf{W}$ is the vector containing the conservative variables $(\rho, \rho U, \rho E)^T$ and $\vec{\mathbf{F}} = (\mathbf{F}, \mathbf{G}, \mathbf{H})^T$ is the flux tensor. The flux is divided into two components: the convective flux depending only on $\mathbf{W}$ and the viscous flux depending on both $\mathbf{W}$ and its gradient $\nabla\mathbf{W}$. The contributions of Sub-Grid Scale (SGS) turbulence models are included in the viscous flux through the addition of the so called turbulent viscosity ν_t. Two schemes are used in this study: Lax–Wendroff [44] (LW, with 2nd-order accuracy in time and space) and the two-step Taylor–Galerkin finite element scheme TTGC [45] (3rd-order in time and space). The LW scheme, which is faster than TTGC is used for transient phases while all statistics are gathered (when steady state is reached) using the TTGC scheme.

To compute the whole configuration and the flow created by the fans the code must be able to deal with moving parts (in this case, six rotating fans). Immersed Boundaries Methods [35,36] were tested but were not able to represent correctly the blade geometry of the fan because the entire zone spanned by the fans must be meshed with a very fine grid size leading to a prohibitive cost in term of CPU time. ALE methods with mesh deformation [46,47,34] were also considered but introduced excessive deformation of cells and frequent interpolation phases [48].

To solve this problem, the MISCOG approach, developed initially for turbomachinery [38,39], was extended to bomb configurations. In MISCOG, two or more instances of the same LES solver (namely AVBP), each with their own computational domain, are coupled through the parallel coupler OpenPALM [40,41]. For the bomb case, the whole flow domain is initially divided into 7 parts: the bomb itself has a static mesh (AVBP01) while each fan is computing in a moving framework (AVBP0i, $i \in [2;7]$). For moving parts, the code uses the ALE block rotation approach [46,47,34]: the grid is rotated without deformation. The remaining unit AVBP01 simulates the flow in the static part of the bomb in the same coordinate system. The solution retained to handle interfaces between the units involving rotating and non-rotating parts consists in reconstructing the residuals using an overset grid method and exchanging by interpolation the multidomain conservative variables wherever needed. To do so an efficient distributed search algorithm is implemented in the OpenPALM coupler to locate the points in parallel partitioned mesh blocks and a linear method is used to interpolate residuals (the interpolation is of 2nd order). This coupling phase is implemented outside the CFD instances in conjunction with second order interpolation.

The computational domain corresponding to the experiment of Orléans is displayed in Fig. 1: six cylindrical rotating domains (i = 2–7) are used for each fan zone while one domain ($i = 1$) is used for the rest of the bomb. In general, the number of cells used for each domain can be different. Here the grids for the six fans (AVBP02–AVBP07) have the same number of cells but the bomb

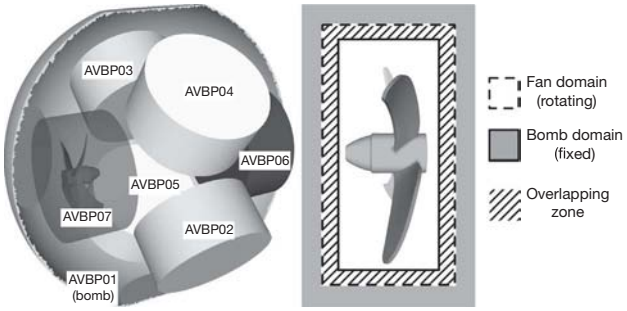

Fig. 1. MISCOG decomposition for a fan-stirred vessel. Six cylindrical rotating domains (AVBP02–AVBP07) for the fans and one fixed domain (AVBP01) for the rest of the bomb.

grid (AVBP01) is different so that load balancing becomes immediately an issue which will be discussed in Section 4.2. The timetable used in the MISCOG approach for each iteration is the following:

1. All AVP0*i* ($i \in [1;N]$) entities run.
2. When AVBP01 and AVBP02 have computed one iteration, they exchange conservative variables in the buffer zone of regions 1 and 2. After this exchange, AVBP02 starts to compute the next iteration.
3. When AVBP03 finishes its iteration and AVBP01 has also finished exchanging with AVBP02, AVBP01 and AVBP03 start to exchange, otherwise AVBP01 waits. This is repeated for all AVBP0*i* instances ($i \in [2;N]$).

Note that AVBP01 starts to compute the next iteration as soon as it has exchanged residuals with the last instance AVBP0*N*.

3. Validation test cases

Many academic test cases have been performed to validate the MISCOG approach in configurations where a single domain computation or an analytical solution can be used as the reference solution. For example, acoustic wave and two-dimensional vortex propagation cases were tested successfully using MISCOG by Wang et al. [38,39]. These results showed good performances of the MISCOG approach and a negligible accuracy loss through the overlapping zone thanks to the second-order interpolation. Here a new three-dimensional vortex case closer to the Orléans bomb geometry was tested by propagating a vortex with the TTGC scheme in the box of Fig. 2.

The computational domain consists in a tri-periodic cubic box where a cylindrical grid is inserted. This cylinder is rotated at 10,000 rpm corresponding to the rotation speed of the fans in the real bomb. The mean flow goes from left to right at U_0. In this test case, the vortex must travel through interfaces without being affected by the inner rotating mesh so that the exact solution is simple to derive as a reference. This test case is representative of the target configuration where fans are encapsulated in finite cylinders: vortices created by the fan blades must travel through the coupling interface. This case is simulated both with the MISCOG approach and with a single domain AVBP computation. Fig. 3(a) presents the time evolution of the axial velocity at the center of the rotating cylinder while Fig. 3(b) shows a cut of the pressure field after two convection times. A very good agreement is found between the analytical solution, the single domain computation and the MISCOG approach. The vortex is convected at the expected speed U_0 (no dispersion) and its structure is preserved (no dissipation). Note that formally, when the vortex goes through the overlapping zone, the third order of the TTGC scheme is lost since the current interpolation is of 2nd order. However, the pressure and the velocity profiles are both well convected.

This test case demonstrates the ability of the MISCOG approach to convect a 3D vortex through different interfaces and confirms the accuracy of this approach for coupled LES. On the long term, it is clear that the interpolation method used in the overlapping zone combined with the numerical scheme in each domain leads to global dispersion and dissipation properties which would require a much more precise analysis. This is left for further studies to concentrate here on the fan-stirred bomb simulations.

4. Numerical set-up and parallel efficiency of the MISCOG approach on a six-fan stirred vessel

This section describes the bomb configuration and the numerical set-up. The parallel efficiency of the global MISCOG simulation is discussed because it raises new questions compared to classical load balancing issues in a single instance solver.

4.1. Description of the bomb configuration and numerical set-up

The configuration is the bomb experiment of the PRISME laboratory in Orléans [42]. This spherical vessel is stirred by six fans. The radius of the closed vessel R_0 is 100 mm and it has six windows for visualization (see Fig. 4(a)). Fans are axial fans with an external diameter of 60 mm. All characteristics of the fans are presented by Fig. 4(b).

Simulations used to gather statistics are performed with the TTGC scheme. The sub-grid scale (SGS) model is WALE [49] which was developed for wall bounded flows. All boundary conditions are no-slip and adiabatic walls (fans and closed vessel).

Experimental results obtained in the PRISME laboratory, give values for the RMS velocity $\mathbf{u}_{\mathbf{rms},\mathrm{exp}}$ and the integral length scale $L_{\tau,exp}$ at the bomb center: $\mathbf{u}_{\mathbf{rms},\mathrm{exp}} \simeq 3$ m/s and $L_{\tau,exp} \simeq 3$ mm. The time scale associated to the integral length scale τ is $\tau = L_{\tau,exp}/\mathbf{u}_{rms,exp} \simeq 1$ ms. Knowing the viscosity $\nu = 1.78.10^{-5}$ m^2 s^{-1} the turbulent Reynolds number can be evaluated $Re_{t,exp} = \mathbf{u}_{\mathbf{rms},\mathrm{exp}} L_{\tau,exp}/\nu \simeq 600$. The experimental Kolmogorov length scale η_{exp} can be estimated with the relation:

$$\eta_{exp} = L_{\tau,exp}/Re_{t,exp}^{3/4} \tag{2}$$

giving a value of the order of $\eta_{exp} \simeq 40$ μm. All theses information are summarized in Table 1. The computation with a constant mesh size in the whole bomb of $\Delta x = 1$ mm in the closed vessel gives a ratio $\Delta x/\eta_{exp} \simeq 25$ corresponding to a mesh of 21 million of cells for AVBP01. Even though the computation is a LES, this resolution leads almost to a DNS-like computation because very few intense structures actually exist between the Kolmogorov scale η and a length of the order of 20η [5]. For the mesh of the fan, a fine discretization at the blade-walls is used to capture the flow generated by fans (Fig. 5): four prism layers are added on all blade-walls to describe the boundary layer [50]. The typical thickness of the prism layers is about 0.05 mm, so that the maximum wall $y+$[2] on the first grid point near the blade wall is 10 and is located at the leading edge of the blade (see Fig. 6). The mesh size around the fan (away from the walls) is 1 mm leading to a mesh of 3.3 million cells for each fan instance AVBP02 to AVBP07. Thus the full mesh including the bomb-mesh and the six fan-meshes contains 41 million cells.

[2] The normalized wall distance y^+ is defined by $u^+ = yu_\tau/\nu$ where u_τ is the friction velocity. u_τ is defined by $u_\tau = \sqrt{\tau_{wall}/\rho}$.

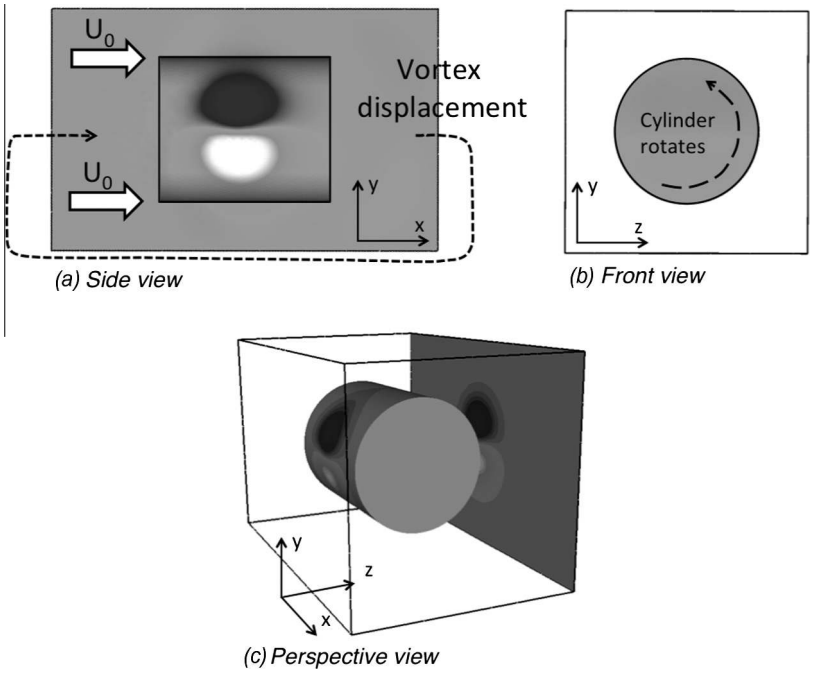

Fig. 2. Sketch of the 3D convection vortex test case: a rotating cylinder is placed inside a tri-periodic box. Views are colored by the velocity field.

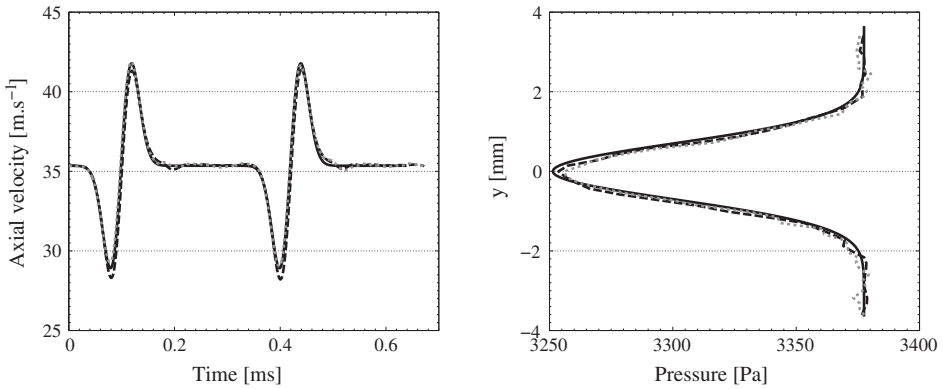

(a) Axial velocity at center of the cylinder versus time.

(b) Pressure along y-axis after two convection times.

Fig. 3. Comparison between a single domain AVBP computation and the MISCOG approach. ——: analytical solution; - - -: single mesh approach; ····: MISCOG.

4.2. Efficiency of the MISCOG approach

The load balancing of the MISCOG approach strategy raises much more questions than the usual optimization of single instance codes on parallel systems: the present configuration requires the coupling of 7 AVBP entities (one for the bomb and 6 six for the fans). Timers were added to measure the times needed for (1) computation, T_c, (2) exchange, T_e and (3) waiting, T_w.

Defining a waiting time T_w in a multiple instances run requires caution. Here we define T_w using the following convention: T_w is negative when fans (AVBP02–AVBP07) wait while it is positive if the bomb (AVBP01) waits. Note that T_e corresponds to exchanges between AVBP01 and individual fans: communication times between cores inside each instance are included in the computation time. Two computation times are defined: T_c^f and T_c^b, the fan and the bomb standalone computational times, respectively.

A theoretical model of performance for MISCOG can be derived using simple relations. Two limit cases are considered. The bomb-limited case (BL) where fans have to wait – corresponding to $T_w < 0$ – and the fan-limited case (FL) where the bomb has to wait – corresponding to $T_w > 0$ –. Timetables of BL and FL cases are displayed in Figs. 7 and 8, respectively. According to timetables presented in Figs. 7 and 8 and using the convention previously proposed for the waiting time, leads to an expression for T_w, which is valid for all cases:

$$T_w = (T_c^f - T_c^b) - (N-2)T_e \tag{3}$$

The exchange time, T_e, cannot be estimated simply (its dependance on load balancing is not easy to evaluate) and it was measured in the solver. The total time for one iteration T_{it} can be expressed using two relations: communications between instances in MISCOG approach are sequential so that (except for the first iteration) the time needed by the bomb (AVBP01) to compute one iteration T_{it}^b is equal to the time needed by each fan (AVBP02–AVBP07) to compute one iteration T_{it}^f (Figs. 7 and 8). This leads to two expressions for T_{it}:

$$T_{it} = \underbrace{(N-1)T_e + T_c^b + \max(0, T_w)}_{T_{it}^b} = \underbrace{T_e + T_c^f - \min(0, T_w)}_{T_{it}^f} \tag{4}$$

(a) Sketch of the geometry. $|\nabla \vec{u}|$ instantaneous field in the central plane and iso-surfaces of vorticity in fan regions (for 2 fans only).

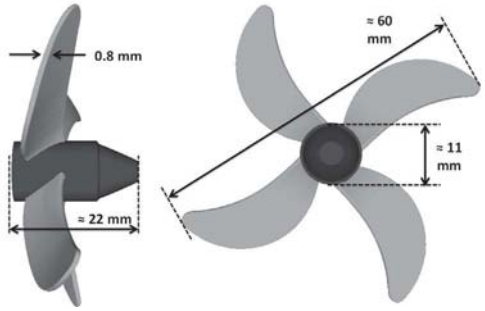

(b) Characteristics of the fan used to stir the vessel.

Fig. 4. Sketch of the geometry (top) and fan characteristics (bottom) (configuration setup at the PRISME laboratory, Orléans).

Table 1
Experimental data about the flow at the bomb center.

$\mathbf{u}_{\mathbf{rms},\mathrm{exp}}$	3 m/s
$L_{\tau,exp}$	3 mm
τ	1 ms
$Re_{t,exp}$	600
η_{exp}	40 μm

To validate this model, computations were performed where the total number of cores was fixed (400 on SGI Altix ICE 8200) and the ratio $R_c = N_c^b/N_c^f$ of the number of cores allocated to the bomb instance AVBP01 (N_c^b) to the number of cores allocated to fan instances AVBP02 to AVBP07 (N_c^f) was varied (all fan instances have the same number of cores). Table 2 summarizes the computations performed to evaluate the performance of MISCOG. Fig. 9 compares the model (Eqs. (3) and (4)) to waiting and total times measured in simulations. Fig. 9(a) shows the waiting times. When Rc is increased (more cores are allocated to the bomb instance AVBP01), the waiting time is expected to go from negative (fans wait) to positive (bomb waits) values as shown by Eq. (3). A good agreement is found while Rc is less than 20. For large Rc values, the trend is good but values differs slightly: in simulations the waiting time goes to zero but remains negative. When there are extreme differences in load balancing between AVBP01 and AVBP02 ($R_c > 20$) the behavior of MISCOG is not well understood yet. According to Eq. (3), in order to cancel the waiting time ($T_w = 0$), the load balancing must be chosen such as $T_c^f = T_c^b + (N-2)T_e$. This leads here to a ratio $Rc \simeq 19$, where 303 cores are allocated to AVBP01 (the bomb) and 16 cores are used for each fan domain. Fig. 9(b) displays the absolute execution time of the code for one time-iteration. The agreement with Eq. (4) is reasonable.

In an ideal computation, the minimum computing cost of such a simulation is obtained when $T_w = 0$. In practice, the R_c range which minimizes the total time for one iteration is $R_c \in [10; 20]$ showing that the MISCOG efficiency is weakly dependent on this ratio. In this range, T_w is closed to zero but can be negative showing that the optimal performance of MISCOG can be obtained in a situation where fans wait.

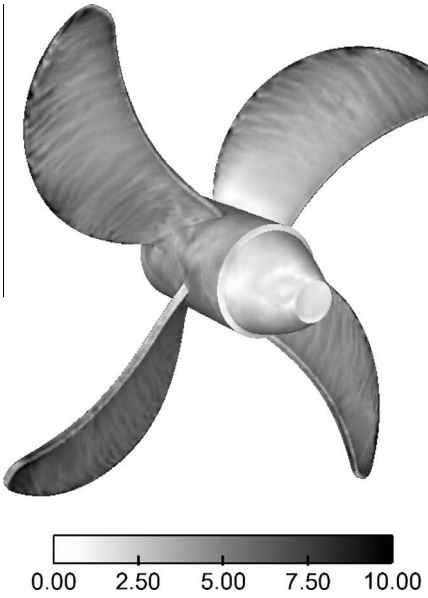

Fig. 6. y^+ field on the fan walls.

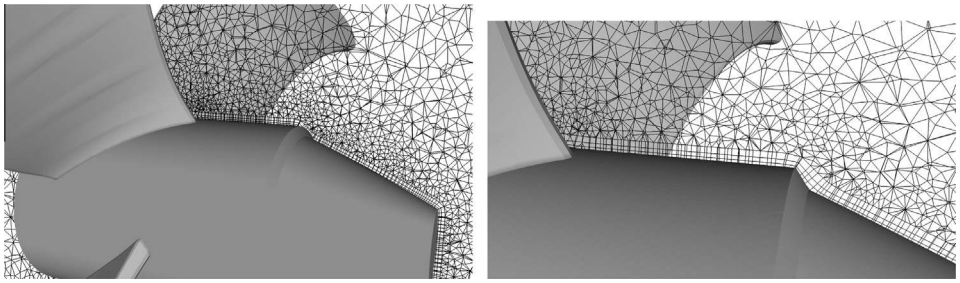

Fig. 5. Mesh of the fan. Four prism layers were added near blade-walls.

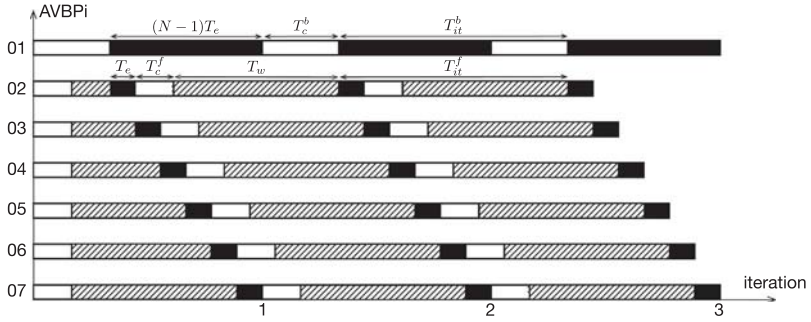

Fig. 7. Timetable of the operations performed in the MISCOG approach for the BL case (only fans wait). ▭: Computing; ▨: waiting; ■: exchanging.

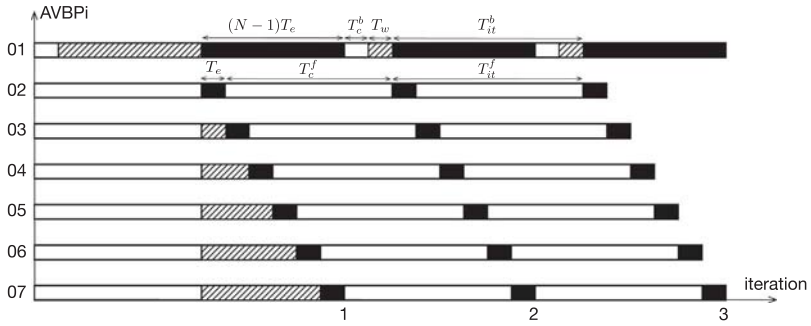

Fig. 8. Timetable of the operations performed in the MISCOG approach for the FL case (only bomb waits). ▭: Computing; ▨: waiting; ■: exchanging.

Table 2
Simulations performed to evaluate the performance of MISCOG. The ratio R_c is increased for MISCOG 1–5. All times are given in seconds per iteration.

Name	R_c	T_e	T_w	T_{it}
MISCOG 1	2	0.593	−4.35	6.19
MISCOG 2	4.5	0.345	−2.42	4.37
MISCOG 3	9.9	0.347	−1.28	3.93
MISCOG 4	19	0.423	−0.34	4.03
MISCOG 5	34	0.606	−0.25	7.84

5. Characterization of turbulent flow inside the fan-stirred bomb

In the experimental set-up, many operating points have been studied: four fan geometries have been tested, the fan rotation speed ω_{fan} was varied from 1,000 rpm to 15,000 rpm, the pressure P_0 from 1 bar to 10 bar and the temperature T_0 from 323 K to 473 K. Only one operating point is studied numerically: $P_0 = 101325$ Pa and $T_0 = 323$ K. The fans rotation speed is $\omega_{fan} = 10,000$ rpm (the corresponding rotation period is $T_{fan} = 6$ ms). The Reynolds number, based on the blade tip radius (30 mm) and speed (31.5 m/s) is about 60,000. A normalized time t^* giving the number of fan rotations that are computed is defined as $t^* = t/T_{fan}$, where t is the physical time.

To reach steady state, a first computation is performed on a coarse grid. Fig. 10 shows the evolution of the mean resolved kinetic energy in the computational domain $E_k = 1/V \iiint_V \mathbf{u}^2 dV$. This quantity is a relevant diagnostic to quantify the temporal convergence of the flow inside the vessel. In this configuration, the flow is established after about 20 rotations. From $t^* = 0$–45, the LW scheme is used. Then from $t^* = 45$–95, the TTGC scheme is used. Finally from $t^* = 95$–165, the computation is performed on the fine grid with the TTGC scheme. The resolved mean kinetic energy E_k

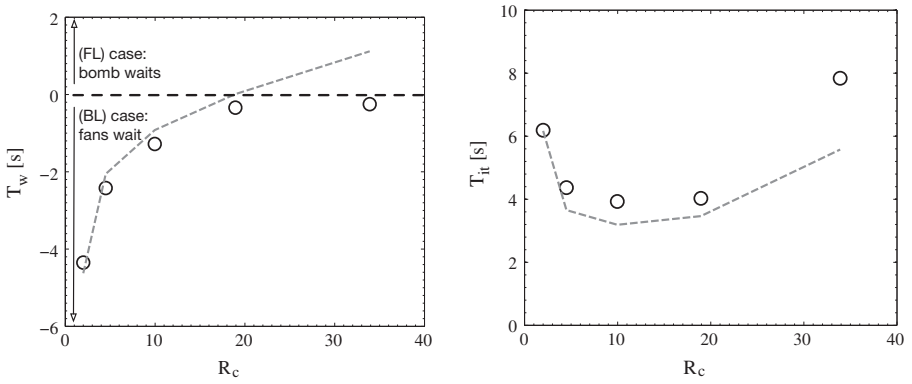

(a) Waiting time T_w. (b) Total time for one iteration T_{it}.

Fig. 9. Performance of MISCOG. ○: Computations; – – –: model.

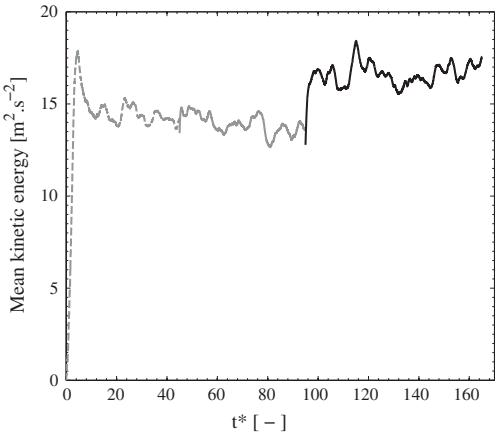

Fig. 10. Mean kinetic energy in the closed vessel versus the number of fan rotations t^*. – – – –: coarse grid LW; ———: coarse grid TTGC; ——: fine grid TTGC.

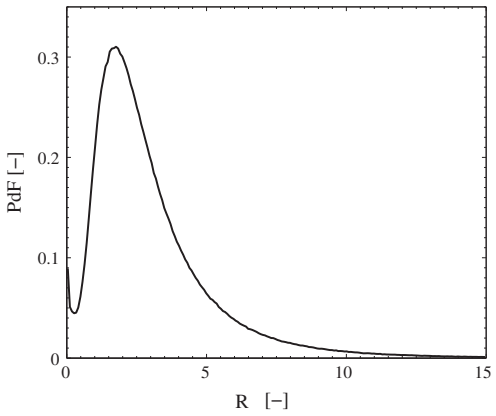

Fig. 11. Ratio R_μ of the turbulent viscosity μ_t on laminar viscosity μ_l : $R_\mu = \mu_t/\mu_l$.

increases slightly when the fine grid is introduced because new structures are created. However the new steady state is reached quickly and diagnostics are performed from t^* = 105–165.

To check the quality of the LES, the ratio R_μ of turbulent viscosity μ_t (created by the subgrid-scale model) over laminar viscosity μ_l was computed: Fig. 11 shows a probability density function (PdF) of R_μ over all grid nodes. The maximum value of R_μ reaches 15 times the laminar viscosity but is much less at most points. This diagnostic shows that a large portion of the turbulence is resolved on the mesh and not modeled.

5.1. Velocity at the bomb center

Fig. 12 presents the temporal evolution of the three velocity components $\mathbf{u} = (u, v, w)$ at the center of the vessel. The signal recorded by the probe is zero until $t^* = 6$. This time represents the time needed by large turbulent scales generated by fans to reach the center of the vessel. The distance between the fan blades to the center of the vessel is $L_{fv} = 65$ mm. A velocity V_s can be estimated by the relation $V_s = L_{fv}/t^* \simeq 2$ m/s. This velocity is very small compared to the flow velocity at the blade tip $V_{bt} \simeq 30$ m/s. The mechanism by which turbulence goes from fan regions to the bomb center is described in Section 5.4.

The RMS velocity values[3] at the center of the vessel are respectively 2.3, 2.0 and 2.1 m/s. Probability density functions of

[3] The RMS values are defined as $u_{rms} = \sqrt{\sum_{n=1}^{Ns} u_n'^2/N_s}$ where N_s is the number of samples and $u' = u - \bar{u}$. They do not include the SGS contribution.

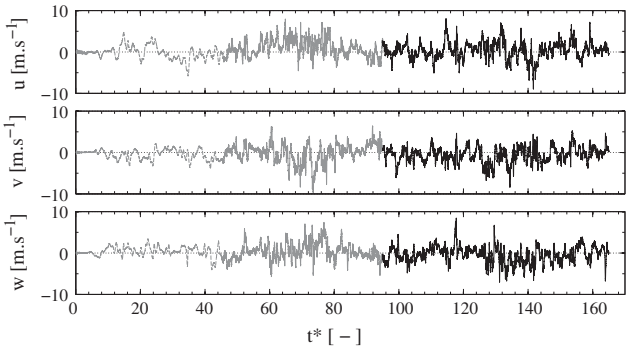

Fig. 12. Velocity components versus number of fan rotations t^* at the center of the vessel. – – – –: coarse grid LW; ———: coarse grid TTGC; ——: fine grid TTGC.

the velocity fluctuations components $\mathbf{u}'$ are plotted on Fig. 13. The pdf's of u', v' and w' are compared to a Gaussian distribution which characterizes random processes. A good agreement is found between a Gaussian distribution and the distribution of the velocity components at the bomb center. These first results suggest that turbulence at the center is close to HIT which is the objective of this experimental set-up.

5.2. Mean and RMS velocities in the closed vessel

A second diagnostic is to compare average $\bar{\mathbf{u}}$ and fluctuating $\mathbf{u_{rms}}$ velocities measured experimentally to those computed by LES. These statistics are performed oven 60 fan rotations ($t^* \in [105; 165]$). Fig. 14 shows fields of the magnitude of the average and fluctuating velocities in the closed vessel. As expected, the average velocity is close to zero at the bomb center. To compare these results to experimental data, Fig. 15 presents x-axis cuts of average velocity components. As previously observed on Fig. 14, average velocities are near zero at the bomb center. The agreement between experimental data and LES calculation is reasonable. Moreover the 'S' shape of the $\bar{u}$ and $\bar{v}$ curves observed experimentally is fairly well predicted by the computation. The domain where the average velocity is near zero is a sphere with a radius of about 3 cm. Fig. 16 presents x-axis cuts of fluctuating velocities components. Once again the agreement between experimental data and LES is quiet good. The u_{rms} and v_{rms} profiles are well captured. The LES results slightly under-estimate the velocity fluctuations since only the resolved fluctuations are plotted. Considering the complexity of this simulation, capturing most of the trends observed in the measurements is already challenging and we think that results are sufficiently good to show that the whole approach is promising.

5.3. Turbulence structure

To study the structure of the turbulence, the time average invariants defined by Lumley [51,52] are a useful tool. According to this theory an anisotropy invariant map within which all realizable Reynolds stress invariants must lie can be defined. The borders of this domain describe different states of the turbulence. This theory is based on the analysis of the non-dimensional form of the anisotropy tensor given by:

$$b_{ij} = \frac{\overline{\tau_{ij}}}{\overline{\tau_{kk}}} - \frac{1}{3}\delta_{ij} \tag{5}$$

with $\overline{\tau_{ij}} = \overline{u_i' u_j'}$ the average Reynolds stress tensor. The principal components of the anisotropy tensor may be found by solving the relation:

$$\det[b_{ij} - \sigma\delta_{ij}] = 0. \tag{6}$$

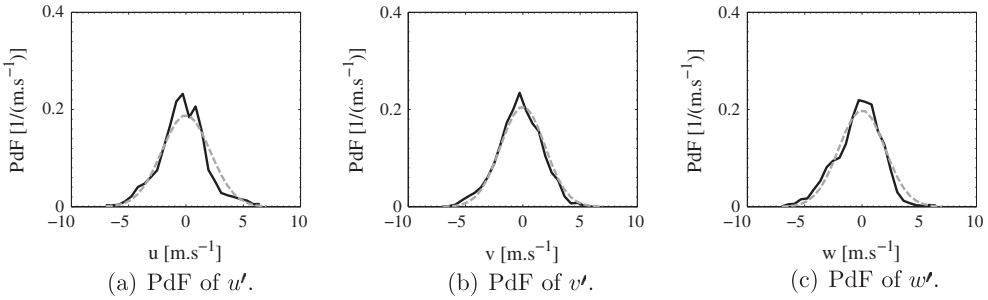

(a) PdF of u'. (b) PdF of v'. (c) PdF of w'.

Fig. 13. Local velocity fluctuations distributions at the bomb center. - - -: Gaussian distribution; ——: LES.

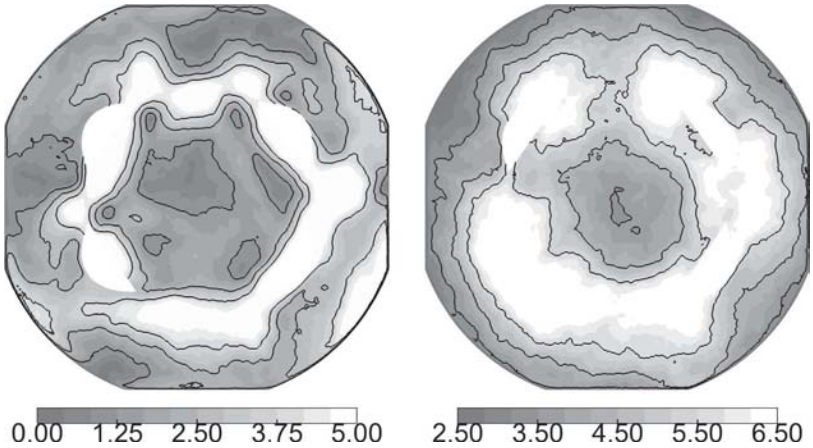

(a) Average velocity (modulus). (b) RMS velocity (modulus).

Fig. 14. Average and RMS velocity fields. (Statistics performed on 60 fan rotations, $t^* \in [105; 165]$.)

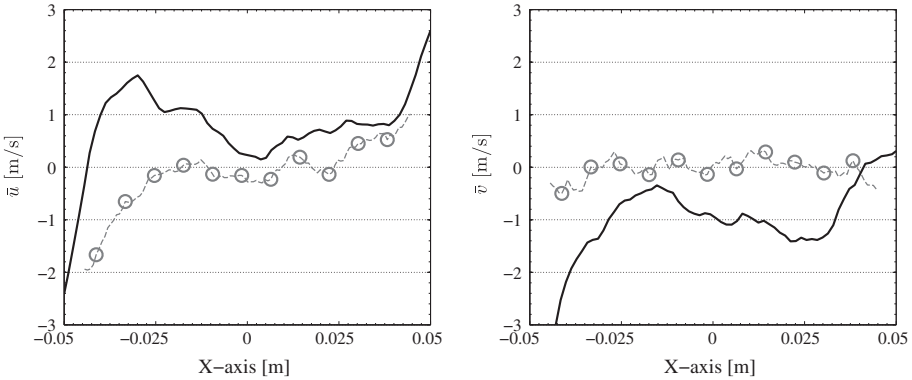

(a) $\bar{u}$. (b) $\bar{v}$.

Fig. 15. Comparison of the average velocities $\bar{u}$ and $\bar{v}$ along the x-axis. -⊖-: experimental data (PIV); ——: LES. (Statistics performed on 60 fan rotations, $t^* \in [105; 165]$.)

where σ are the eigenvalues (i.e. the principal stresses) of $\mathbf{b}$. Eq. (6) expands to the following third-order equation for:

$$\sigma^3 - I_1\sigma^2 + I_2\sigma - I_3 = 0 \tag{7}$$

where I_1, I_2 and I_3 are respectively the first, second, and third invariants of the tensor b_{ij}. These invariants are related to the tensor terms according to the relations:

$$\begin{aligned} I_1 &= \text{trace}(\mathbf{b}) = b_{kk} \\ I_2 &= \frac{1}{2}\left([\text{trace}(\mathbf{b})]^2 - \text{trace}(\mathbf{b^2})\right) = -\frac{1}{2}b_{ij}b_{ji} \\ I_3 &= \det(\mathbf{b}) \end{aligned} \tag{8}$$

I_1 is zero for incompressible flows and is not used here. The anisotropy invariant map is constructed by plotting $-I_2$ versus I_3. Isotropic turbulence is found at the origin ($I_2 = I_3 = 0$). When I_2 or I_3 differ from zero, they quantify the type of turbulence which is found locally (1, 2 or 3 components, axi-symmetry, etc.). The I_2 and I_3 invariants were computed locally (which means that the $\bar{\cdot}$ operator in Eq. (5) is a temporal averaging operator) in the LES on the fine mesh during the established phase ($t^* > 105$). This analysis has been done on the x, y and z-axis (20 points in each direction) of the closed vessel and results are reported in Fig. 17. Each point is colored by its distance r to the center of the bomb.

Fig. 17 shows that at the bomb center ($x \in [-30; +30]$ mm), turbulence can be assumed to be isotropic. In this spherical domain all

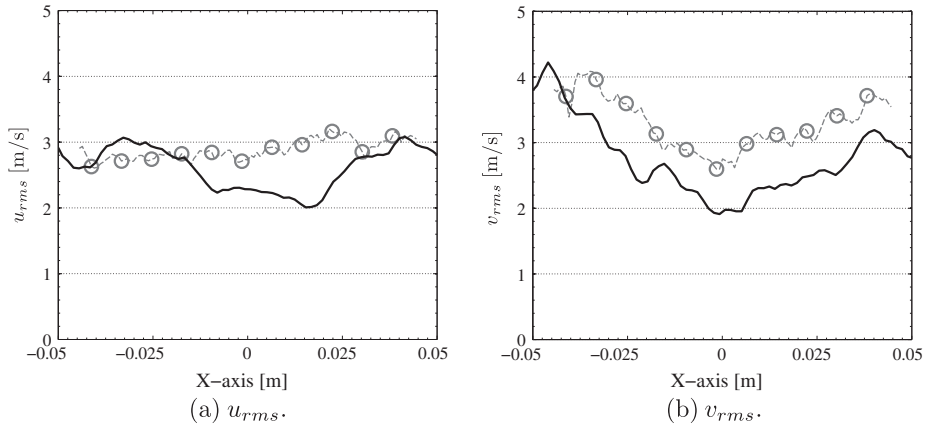

Fig. 16. Comparison of the fluctuating velocities u_{rms} and v_{rms} along the x-axis. -⊖-: experimental data (PIV); ——: LES. (Statistics performed on 60 fan rotations, $t^* \in [105; 165]$.)

structures generated by the six fans impact and mix (by diffusion) leading to an homogenous turbulence. Outside this spherical domain where turbulence is isotropic, the presence of the fans affects the structure of the turbulence: at a distance of more than 30 mm of the bomb center, turbulence becomes 'rod-like'. This loss of isotropy is confirmed by results obtained experimentally. Fig. 18 presents the evolution of the ration u_{rms}/v_{rms} versus the x-axis showing that turbulence is isotropic at the bomb center. The agreement between LES and experimental measurements is good. Note that Fig. 18 is consistent with Fig. 17

5.4. Kinetic energy balance

The objective in this section is to show how turbulence is transferred from the fans regions to the bomb center. A relevant quantity to characterize the turbulence inside the vessel in terms of production, dissipation and transport is the mean turbulent kinetic energy (TKE) $\bar{e} = 1/2\overline{u_i' u_i'}$. The budget of $\bar{e}$ is given by Hinze [3]:

$$\underbrace{-\overline{u_i}\frac{\partial \bar{e}}{\partial x_i}}_{\text{Convection}} \underbrace{-\frac{\partial}{\partial x_i}\left(\overline{p' u_i'}\right)}_{\text{Pressure diffusion}} \underbrace{-\frac{\partial}{\partial x_i}\left(\overline{e u_i'}\right)}_{\text{Turbulent diffusion}} \underbrace{+\frac{\partial}{\partial x_j}\left(2\overline{(\nu+\nu_t)s_{ij}' u_i'}\right)}_{\text{Viscous diffusion}}$$
$$\underbrace{-2\overline{(\nu+\nu_t)s_{ij}' s_{ij}'}}_{\text{Dissipation}} \underbrace{-\overline{u_i' u_j'}\frac{\partial \overline{u_i}}{\partial x_j}}_{\text{Production}} = 0 \qquad (9)$$

where p' is the pressure fluctuation, e is the instantaneous turbulent kinetic energy $e = 1/2 u_i' u_i'$ and $s_{ij}' = 1/2\left(\partial u_i'/\partial x_j + \partial u_j'/\partial x_i\right)$ is the deformation tensor [53,4,54,55]. The turbulent viscosity $\nu_t = \mu_t/\rho$ is taken into account in the budget of $\bar{e}$. Terms in Eq. (9) are calculated over 60 solutions: 1 solution is stored at each fan rotation from $t^* = 105$ to $t^* = 165$. These solutions are uncorrelated since the time between two solutions is 6 ms and the time scale associated to the integral length scale τ is around 1 ms (convergence was checked). These terms are then averaged spatially assuming spherical symmetry so that they are plotted as a function of the bomb radius r_b ($r_b = 0$ at the bomb center). Only terms of interest are plotted here: Fig. 19 displays the convection, turbulent diffusion, dissipation and the production terms (resolved quantities). A fan is superimposed to the graph to show its position in the bomb. The dissipation rate found in this work is about 100 m^2/s^3 in the region of the bomb center. This value is in agreement with the dissipation rate measured experimentally by De Jong et al. [56] in an eight-fan cubic turbulence box. The production term is maximum at $r_b/R_0 \simeq 0.5$: the turbulent kinetic energy is produced by fans which are located at this position. Finally, over a central region of

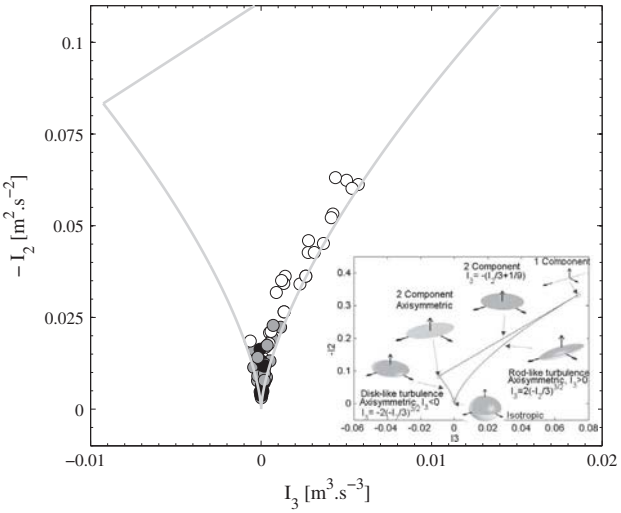

Fig. 17. Anisotropy invariant map (Lumley triangle). Each point is colored by its distance r to the center of the bomb. ●: $r < 15$ mm; ●: $r \in [15; 30]$ mm; ○: $r > 30$ mm. The figure in the bottom-right hand side is taken from [52].

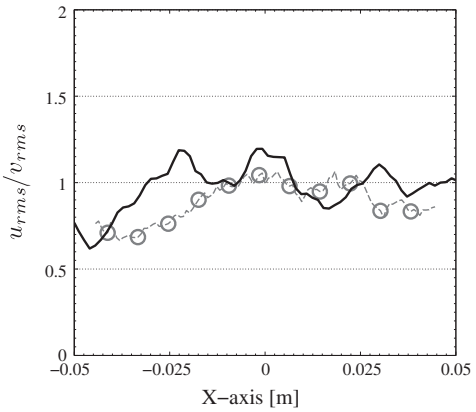

Fig. 18. Isotropy along the x-axis. -⊖-: experimental data (PIV); ——: LES. (Statistics performed on 60 fan rotations, $t^* \in [105; 165]$.)

diameter 30 mm, turbulent diffusion dominates convection as expected: the mean flow is around zero in this region (see Fig. 15), confirming that turbulence is not convected but diffused towards the bomb center from the fan regions.

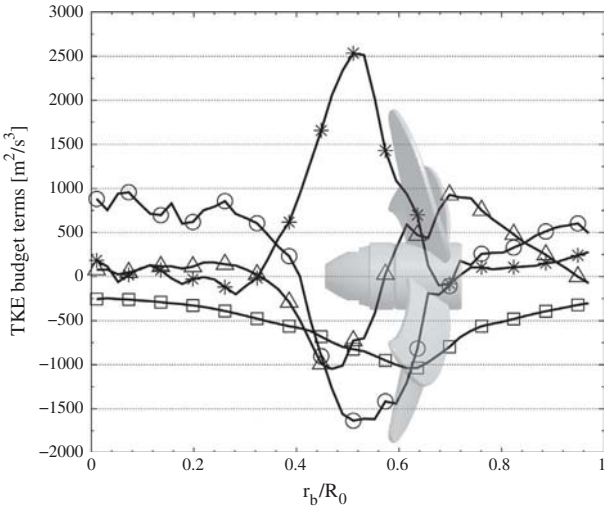

Fig. 19. Budget of resolved TKE terms versus the normalized bomb radius r_b/R_0. —◁—: Convection; —○—: turbulent diffusion; —□—: dissipation; —✳—: production.

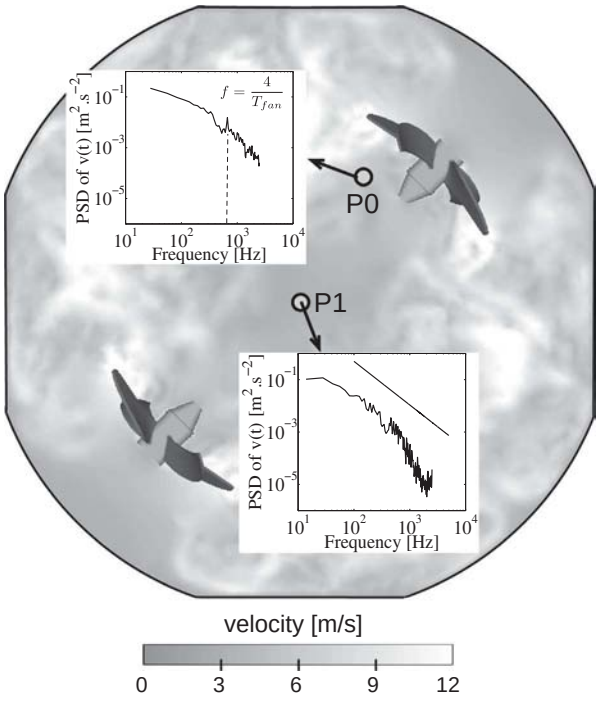

Fig. 20. Velocity spectra close to a fan and at the bomb center.

5.5. Spectra

The flow generated by fans is, by nature, a pulsating flow. Because fans have four blades, this flow is expected to exhibit a mode at a frequency f_p equal to four times the fan rotation frequency ($f_p = 4/T_{fan}$). To check if turbulence at the center of the bomb is affected by the pulsated flow created by the blades rotation, Power Spectral Density (PSD) of the velocity can be computed to track the existence of harmonic oscillations at f_p.

Fig. 20 shows the bomb configuration and the position where PSD are performed. Two points in the domain are analyzed: close to a fan (point P0) and at the bomb center (point P1). At P0, the PSD exhibits a mode at a frequency exactly equal to four times the frequency of the fan rotation as expected. On the other hand, at the bomb center, this mode vanishes and the spectrum follows the Kolmogorov theory [57]. Here the slope of the spectrum is near the $-5/3$ theoretical slope. This confirms that the turbulence at the bomb center is not affected by the periodicity of the flow generated by fans. Moreover, PSD results show that more energy is contained in the spectrum at point P0 than at point P1 (showing that turbulence decays between these two points).

6. Conclusion

This study presents a computation of a spherical vessel stirred by six fans. This configuration corresponds to an experiment conducted at the PRISME laboratory in Orléans to study the propagation of turbulent premixed flames in homogeneous isotropic turbulence. In this paper, only the non-reacting flow is studied, just before ignition. At this instant, the Reynolds number associated to the fans is 60,000 while the Reynolds number based on the integral length and RMS speed is of the order of 600 at the bomb center.

An approach first developed for turbomachinery simulations called MISCOG, has been adapted here to handle six fans inside the vessel. This method couples multiple instances of the same code, exchanging residuals on small overlapping zones. A first test case shows that the MISCOG approach is able to convect vortices with limited dispersion and dissipation effects. The parallel efficiency of MISCOG is discussed too.

A well resolved LES of the full geometry is then performed with the unstructured compressible code AVBP. Average and fluctuating fields match experimental data reasonably well. Finally the structure of the turbulence is studied and it is shown that turbulence is almost homogeneous and isotropic at the bomb center in a region of around 6 cm of diameter. The budget of mean turbulent kinetic energy is performed too and shows that turbulence is not convected from fans to the bomb center but diffused since the average velocities are near zero at this location. The trace of the blade passage frequency disappears near the bomb center.

Acknowledgments

Authors acknowledge F. Halter, F. Foucher and B. Galmiche from PRISME laboratory for their experimental results. This work was granted access to the high-performance computing resources of CINES under the allocation x20132b6607 made by Grand Equipement National de Calcul Intensif.

References

[1] Tennekes H. Simple model for the smallscale structure of turbulence. Phys Fluids 1968;11(3):669–70.
[2] Tennekes H, Lumley JL. A first course in turbulence. Cambridge: M.I.T. Press; 1972.
[3] Hinze JO. Turbulence. New-York: McGraw-Hill; 1975.
[4] Risso F, Fabre J. Diffusive turbulence in a confined jet experiment. J Fluid Mech 1997;337:233–61.
[5] Pope SB. Turbulent flows. Cambridge University Press; 2000.
[6] Sagaut P. Large eddy simulation for incompressible flows. Springer; 2002.
[7] Garnier E, Mossi M, Sagaut P, Comte P, Deville M. On the use of shock-capturing schemes for large-eddy simulation. J Comput Phys 1999;153(2):273–311.
[8] Lenormand E, Sagaut P, Phuoc LT, Comte P. Subgrid-scale models for large-eddy simulations of compressible wall bounded flows. AIAA J 2000;41(6):1340–50.
[9] Moin P, Squires KD, Cabot W, Lee S. A dynamic subgrid-scale model for compressible turbulence and scalar transport. Phys Fluids A 1991;3(11):2746–57.
[10] Mashayek F, Jaberi FA, Miller RS, Givi P. Dispersion and polydispersity of droplets in stationary isotropic turbulence. Int J Multiphase Flow 1997;23(2):337–55.
[11] Aliseda A, Cartellier A, Hainaux F, Lasheras JC. Effect of preferential concentration on the settling velocity of heavy particles in homogeneous isotropic turbulence. J Fluid Mech 2002;468:77–105.
[12] Salazar JPLC, De Jong J, Cao L, Woodward SH, Meng H, Collins LR. Experimental and numerical investigation of inertial particle clustering in isotropic turbulence. J Fluid Mech 2008;600:245–56.

[13] Birouk M, Gokalp I. Current status of droplet evaporation in turbulent flows. Prog Energy Comb Sci 2006;32(4):408–23.
[14] Poinsot T, Veynante D. Theoretical and numerical combustion, 3rd ed.; 2011 <http://www.cerfacs.fr/elearning>.
[15] Peters N. Turbulent combustion. Cambridge University Press; 2001.
[16] Girimaji SS, Pope SB. Propagating surfaces in isotropic turbulence. J Fluid Mech 1992;234:247–77.
[17] Laffitte P. La propagation des flammes dans les mélanges gazeux, Hermann et Cie. Actualités scientifiques et industrielles, Paris; 1939.
[18] Semenov E. Measurement of turbulence characteristics in a closed volume with artificial turbulence. Combust Expl Shock Waves 1965;1(2):57–62.
[19] Abdel-Gayed RG, Bradley D, Hamid MN, Lawes M. Lewis number effects on turbulent burning velocity. Proc Combust Inst 1984;20:505–12.
[20] Gulder O. Turbulent premixed flame propagation models for different combustion regimes. In: 23rd Symposium (International) on Combustion, vol. 23(1); 1991. p. 743–50.
[21] Chen JH, Im HG. Correlation of flame speed with stretch in turbulent premixed methane/air flames. In: 27th Symposium (International) on Combustion, vol. 1; 1998. p. 819–26.
[22] Shy SS, Lin WJ, Wei JC. An experimental correlation of turbulent burning velocities for premixed turbulent methane–air combustion. Proc R Soc Lond A 2000;456(2000):1997–2019.
[23] Liao S, Jiang D, Huang Z, Zeng K, Cheng Q. Determination of the laminar burning velocities for mixtures of ethanol and air at elevated temperatures. Appl Therm Eng 2007;27(2–3):374–80.
[24] Birouk M, Sarh B, Gökalp I. An attempt to realize experimental isotropic turbulence at low Reynolds number. Flow Turb Combust 2003;70(1–4):325–48.
[25] Hwang W, Eaton JK. Creating homogeneous and isotropic turbulence without a mean flow. Exp Fluids 2004;36(3):444–54.
[26] Brachet ME, Bustamante MD, Krstulovic G, Mininni PD, Pouquet A, Rosenberg D. Ideal evolution of MHD turbulence when imposing Taylor–Green symmetries. Phys Rev E 2013;87:1–16.
[27] Spalart PR, Moser RD, Rogers MM. Spectral methods for the Navier–Stokes equations with one infinite and two periodic directions. J Comput Phys 1991;96(2):297–324.
[28] Moser RD, Moin P, Leonard A. A spectral numerical method for the Navier–Stokes equations with applications to Taylor–Couette flow. J Comput Phys 1983;52(3):524–44.
[29] Lele S. Compact finite difference schemes with spectral like resolution. J Comput Phys 1992;103(1):16–42.
[30] Berland J, Bogey C, Marsden O, Bailly C. High-order, low dispersive and low dissipative explicit schemes for multiple-scale and boundary problems. J Comput Phys 2007;224(2):637–62.
[31] Marié S, Ricot D, Sagaut P. Comparison between lattice Boltzmann method and NavierStokes high order schemes for computational aeroacoustics. J Comput Phys 2009;228(4):1056–70.
[32] Moureau V. Simulation aux grandes échelles de l'aérodynamique interne des moteurs à piston. Ph.D. thesis, Ecole Centrale Paris; 2004.
[33] Moureau V, Barton I, Angelberger C, Poinsot T. Towards large eddy simulation in internal-combustion engines: simulation of a compressed tumble flow. In: SAE 113 (2004-01-1995); 2004. p. 1315–24.
[34] Moureau V, Lartigue G, Sommerer Y, Angelberger C, Colin O, Poinsot T. Numerical methods for unsteady compressible multi-component reacting flows on fixed and moving grids. J Comput Phys 2005;202(2):710–36.
[35] Peskin CS. The immersed boundary method. Acta Numer 2002:479–517.
[36] Verzicco R, Mohd-Yusof J, Orlandi P, Haworth D. Large eddy simulation in complex geometric configurations using boundary body forces. AIAA J 2000;38(3):427–33.
[37] Mittal R, Iaccarino G. Immersed boundary methods. Ann Rev Fluid Mech 2005;37(1):239–61.
[38] Wang G, Papadogiannis D, Duchaine F, Gourdain N, Gicquel LYM. Towards massively parallel large eddy simulation of turbine stages. In: ASME Turbo Expo 2013. San Antonio (TX), USA; 2013.
[39] Wang G, Moreau S, Duchaine F, Gourdain N, Gicquel LYM. Large eddy simulations of the MT1 high-pressure turbine using TurboAVBP. In: Proceeding of 21st annual conference of the CFD society of Canada. Sherbrooke, Quebec, Canada; 2013.
[40] Piacentini A, Morel T, Thévenin A, Duchaine F. Open-palm an open source dynamic parallel coupler. In: IV International conference on computational methods for coupled problems in science and engineering; 2011.
[41] Duchaine F, Jauré S, Poitou D, Quémerais E, Staffelbach G, Morel T, et al. High performance conjugate heat transfer with the OpenPALM coupler. In: V International conference on coupled problems in science and engineering – coupled problems. Ibiza, Spain; 2013.
[42] Galmiche B, Halter F, Mazellier N, Foucher F. Turbulent flow field measurements in a fan-stirred combustion vessel. In: European turbulence conference; 2013.
[43] Schønfeld T, Rudgyard M. Steady and unsteady flows simulations using the hybrid flow solver avbp. AIAA J 1999;37(11):1378–85.
[44] Lax PD, Wendroff B. Difference schemes for hyperbolic equations with high order of accuracy. Commun Pure Appl Math 1964;17:381–98.
[45] Colin O, Rudgyard M. Development of high-order Taylor–Galerkin schemes for unsteady calculations. J Comput Phys 2000;162(2):338–71.
[46] Hirt CW, Amsden A, Cook JL. An arbitrary Lagrangian–Eulerian computing method for all flow speeds. J Comput Phys 1974;131(4):371–85.
[47] Moureau VR, Vasilyev OV, Angelberger C, Poinsot TJ. Commutation errors in Large Eddy simulations on moving grids: application to piston engine flows. In: Proceedings of the summer program, center for turbulence research. NASA AMES/Stanford University, USA; 2004. p. 157–68.
[48] Enaux B, Granet V, Vermorel O, Lacour C, Pera C, Angelberger C, et al. Les and experimental study of cycle-to-cycle variations in a spark ignition engine. Proc Combust Inst 2011;33:3115–22.
[49] Ducros F, Nicoud F, Poinsot T. Wall-adapating local eddy-viscosity models for simulations in complex geometries. In: Baines MJ, editor. ICFD; 1998. p. 293–300.
[50] Boileau M, Duchaine F, Jouhaud J-C, Sommerer Y. Large-Eddy simulation of heat transfer around a square cylinder using unstructured grids. AIAA J 2013;51(2):372–85.
[51] Lumley J. Computational modelling of turbulent flows. Advan Appl Mech 1978;18:123–76.
[52] Simonsen AJ, Krogstad P-A. Turbulent stress invariant analysis: clarification of existing terminology. Phys Fluids 2005;17(8):088103.
[53] Dwyer MJ, Patton EG, Shaw RH. Turbulent kinetic energy budgets from a large-eddy simulation of airflow above and within a forest canopy. Bound-Layer Meteorol 1997;84(1):23–43.
[54] Liu X, Thomas FO. Measurement of the turbulent kinetic energy budget of a planar wake flow in pressure gradients. Exp Fluids 2004;37(4):469–82.
[55] Sideridis A, Yakinthos K, Goulas A. Turbulent kinetic energy balance measurements in the wake of a low-pressure turbine blade. Int J Heat Fluid Flow 2011;32(1):212–25.
[56] De Jong J, Cao L, Woodward SH, Salazar JPLC, Collins LR, Meng H. Dissipation rate estimation from PIV in zero-mean isotropic turbulence. Exp Fluids 2008;46(3):499–515.
[57] Kolmogorov AN. The local structure of turbulence in incompressible viscous fluid for very large reynolds numbers. C R Acad Sci, USSR 1941;30:301.